UNIVERSIDAD COMPLUTENSE DE MADRID

FACULTAD DE CIENCIAS FÍSICAS

Departamento de Óptica

TESIS DOCTORAL

Interacción de luz y materia en la nanoescala

Light-matter interaction at the nanoscale

MEMORIA PARA OPTAR AL GRADO DE DOCTOR

PRESENTADA POR

Alejandro Manjavacas Arévalo

Director

Francisco Javier García de Abajo

Madrid, 2013

Universidad Complutense de Madrid
Facultad de CC. Físicas
Departamento de Óptica

Interacción de luz y materia en la nanoescala

Tesis Doctoral

Memoria presentada por
Alejandro Manjavacas Arévalo
Para optar al grado de Doctor

Director: Prof. Francisco Javier García de Abajo

Grupo de Nanofotónica
Instituto de Química Física "Rocasolano"
Consejo Superior de Investigaciones Científicas (CSIC)
Madrid. Abril de 2013

Universidad Complutense de Madrid
Facultad de CC. Físicas
Departamento de Óptica

Light-matter interaction at the nanoscale

Doctoral thesis

Dissertation submitted by
Alejandro Manjavacas Arévalo
for the degree of Doctor of Philosophy

Supervisor: Prof. Francisco Javier García de Abajo

Nanophotonics group
Instituto de Química Física "Rocasolano"
Consejo Superior de Investigaciones Científicas (CSIC)
Madrid. April 2013

CSIC nanophotonics.es

La presente tesis doctoral se ha realizado en el grupo de Nanofotónica del CSIC en:

- Instituto de Óptica "Daza de Valdés", Serrano 121, 28006, Madrid, (2009-2011),
- Instituto de Química-Física "Rocasolano", Serrano 119, 28006, Madrid, (2011-2013),

gracias a la financiación de una beca predoctoral del programa FPU del Ministerio de Educación (Ref. AP2008-00051).

A la memoria de Pedro Mejías

A mis padres y a Rocío

Cada uno es hijo de sus obras
Miguel de Cervantes

Agradecimientos

Esta tesis no puede entenderse únicamente como un conjunto de resultados científicos, es también el fruto de un montón de experiencias acontecidas durante los últimos cinco años que, sin lugar a dudas, ya forman parte de mí. Es por ello que quisiera agradecer aquí a todos los que, de una manera u otra, han sido partícipes y responsables de dichas experiencias y que, por tanto, han hecho posible esta tesis.

En primer lugar, me gustaría agradecer a Javier todo su esfuerzo y dedicación a lo largo de estos años, la confianza que me ha demostrado en todo momento y el entusiasmo por la investigación que ha sabido transmitirme. Con su ejemplo constante me ha enseñado a valorar y respetar la ciencia. Sin duda, ha sido un privilegio haber podido crecer como científico y como persona bajo su tutela. Él es el gran responsable de la existencia de esta tesis y de los pequeños éxitos que haya podido alcanzar en estos años.

Me gustaría también dar las gracias a Rosario Martínez-Herrero y Pedro Mejías por cruzarse en mi vida. Ellos fueron los primeros en darme la oportunidad de iniciarme en la investigación científica. Pero fundamentalmente quisiera agradecerles el haber estado a mi lado siempre que los he necesitado, dispuestos a ayudarme y aconsejarme desde el cariño más sincero.

No quisiera tampoco olvidarme de Alberto Pérez, quien, hace ya unos cuantos años, supo despertar en mí la curiosidad y la pasión necesarias para estudiar Física.

Una parte importante de esta tesis y de mi formación ha sido posible gracias a la generosidad de Peter Nordlander e Ignacio Cirac. I would like to thank Peter for his hospitality and for sharing with me his vast knowledge, always with a smile on his face. Igualmente, quisiera darle las gracias a Ignacio por darme la oportunidad de pasar tres meses en Múnich trabajando y aprendiendo en uno de los mejores entornos científicos que uno pueda imaginar.

Gran parte de la culpa de que esta tesis llegue a buen puerto la tienen mis compañeros de fatigas del grupo de Nanofotónica. Ellos son los responsables de haber creado un entorno irrepetible, lleno de buen humor y grandes momentos para el recuerdo. Durante estos años hemos compartido viajes, congresos, cenas y discusiones interminables, sin las cuales esta tesis hubiera sido mucho más difícil. Por todo ello, quiero dar las gracias a Viktor, Rebeca, Xesús, Isabel, Ana, Christin, Johan, Suko e Iván. Creo que puedo decir sin miedo a equivocarme que me llevo un gran grupo de amigos. Espero que os vaya genial allá donde acabéis.

I am also in debt to all my colleges from Houston and Munich that made my stay in those cities so wonderful, and from whom I learnt a lot.

Me gustaría también dar las gracias a todo el personal científico y de administración de los Institutos de Óptica y de Química-Física del CSIC, y del departamento de Óptica de la Universidad Complutense por haberme ayudado siempre que lo he necesitado.

Más allá de la ciencia, quisiera agradecer a toda mi gente de Cabezas, Arévalo y Vicálvaro el haber estado a mi lado todos estos años aguantando mis historias de científicos y por haber conseguido que nunca me olvidase de las cosas importantes de la vida.

Por último quisiera terminar dando las gracias a mi familia, sin cuyo apoyo jamás habría conseguido llegar hasta aquí:

Gracias a Rocío por haberme acompañado en este viaje, por haber estado siempre dispuesta a animarme, por cuidar de Dora y de mí sin descanso, por todo lo que he aprendido de ti y por ser tan maravillosa. Siento haberte robado tantas horas.

Gracias a mis padres y a mi hermano por su ejemplo diario. A ellos les debo todo lo que soy y nunca me cansaré de agradecerles el haber luchado siempre para que consiguiera alcanzar todos mis sueños.

Contents

List of Figures

List of Acronyms

SPP Surface plasmon polariton

TM Transverse magnetic mode

LSP Localized surface plasmon

BEM Boundary element method

IR Infrared

RPA Random-phase approximation

FDT Fluctuation-dissipation theorem

LDOS Local density of optical states

DOS Total density of optical states

RHT Radiative heat transfer

EMCT Electromagnetic crossed terms

HTC Heat transfer coefficient

Resumen

En los últimos años hemos sido testigos de un crecimiento espectacular del campo de la nanofotónica. Este campo se focaliza en el estudio de la interacción de la luz con objetos cuyas dimensiones están en el rango de los nanómetros, y por tanto, son comparables en tamaño a la longitud de onda del espectro visible. Esta coincidencia, entre el *tamaño* de la luz y las dimensiones de las estructuras materiales, da lugar a interacciones complejas que nos permiten diseñar nuevos procedimientos para controlar la luz hasta límites anteriormente insospechados. Es precisamente en este contexto donde la plasmónica encuentra su razón de ser, erigiéndose como uno de los frentes de investigación más prometedores de la actualidad. Los plasmones de superficie, que son excitaciones colectivas de los electrones de conducción en nanoestructuras metálicas, nos proporcionan las herramientas necesarias para confinar y manipular el campo electromagnético hasta dimensiones muy por debajo del límite de difracción de la luz. Con secciones eficaces extraordinariamente grandes, las nanoestructuras plasmónicas son capaces, por ejemplo, de incrementar de forma extraordinaria la captación de luz en dispositivos de energía solar o de focalizar la luz creando lo que se conoce como *puntos calientes*, o en inglés *hot spots*, en los que la existencia de efectos no-lineales permite diseñar sondas para investigar la estructura electrónica y vibracional de la materia, y a la vez ofrece gran potencial para el diseño de futuros dispositivos de conmutación óptica a escala nanométrica

Los plasmones de superficie existentes en intercaras metal-dieléctrico pueden usarse para guiar señales con frecuencias en el infrarrojo y el visible. El alto grado de confinamiento que exhiben estas excitaciones permite concentrar las señales guiadas en secciones transversales con dimensiones muy por debajo del límite de difracción. Esto hace que las guías de onda plasmónicas sean una alternativa prometedora para

el desarrollo de dispositivos de procesamiento de información capaces de combinar las frecuencias operacionales y los anchos de banda de los dispositivos fotónicos con el alto grado de integración alcanzado por la tecnología de semiconductores.

En los últimos años, se han propuesto diferentes diseños de guías de onda plasmónicas incluyendo sistemas continuos compuestos por elementos metálicos, con sección eficaz finita, emparedados en entornos dieléctricos simétricos o antisimétricos, o canales y crestas esculpidas en superficies planas. Otros sistemas formados por conjuntos ordenados de nanopartículas, o basados en estructuras con bandas prohibidas, también han sido objeto de estudio, así como, sistemas híbridos compuestos por nanohilos dieléctricos y superficies metálicas.

En la primera parte de esta tesis, estudiamos y caracterizamos la respuesta de pares de nanohilos de plata, situados en matrices de sílice, con el objetivo de diseñar un nuevo tipo de guía de onda plasmónica. Estas estructuras admiten plasmones de hueco altamente concentrados en la región situada entre los nanohilos, los cuales emergen como resultado de la hibridación de los modos de los nanohilos individuales. Las propiedades de guiado asociadas a estos modos se pueden ajustar variando la distancia entre los nanohilos. Esto permite alcanzar una solución de compromiso óptima entre el grado de confinamiento y la longitud de propagación. A través del análisis de una figura de mérito asociada al nivel de integración alcanzable, demostramos las propiedades excepcionales de estas guías de onda, comparándolas con otros mecanismos de guiado plasmónicos propuestos en la literatura. Al mismo tiempo, analizamos el grado de robustez de los modos de hueco demostrando que pueden tolerar giros con radios menores que la longitud de onda y asimetrías en el diámetro de los nanohilos.

Con el objetivo de diseñar circuitos plasmónicos tridimensionales, estudiamos la interacción entre los modos de hueco en sistemas compuestos por más de dos nanohilos. Comenzando con el elemento básico que define un modo de hueco, es decir, el par de nanohilos, estudiamos el desdoblamiento en energías y las propiedades de simetría de los modos híbridos resultantes de la interacción entre dos pares de hilos. Además, mostramos como este sistema presenta cruces no evitados y evoluciona a cortas distancias hacia un sistema degenerado, formado por cuatro nanohilos dispuestos en los vértices de un cuadrado, en el que dos nuevos modos de hueco surgen a partir de modos de mayor energía. De igual forma, estudiamos los

modos de hueco de un sistema formado por tres nanohilos, analizando su evolución desde una configuración coplanar hasta una distribución en forma de triángulo equilátero.

Gracias a este análisis, demostramos que la interacción entre pares de nanohilos es lo suficientemente débil como para prevenir la transferencia de la señal plasmónica de un par a otro, lo cual es beneficioso para prevenir la diafonía, pero no limita el diseño de acopladores eficientes. Introduciendo un hilo de sección rectangular en la región existente entre dos pares de nanohilos, comprobamos que el acoplamiento entre los pares de nanohilos aumenta de forma considerable. Esto nos permite diseñar un acoplador de plasmones de hueco capaz de transferir la práctica totalidad de la señal de una guía a otra en distancias por debajo de la longitud de propagación. Con esto completamos el análisis de los elementos básicos necesarios para fabricar un circuito plasmónico tridimensional.

El extraordinario incremento del campo asociado a la excitación de plasmones en nanopartículas metálicas constituye otro aspecto relevante de estos modos ópticos que hace posible su interacción con emisores cuánticos (por ejemplo, átomos, moléculas o puntos cuánticos) situados en su vecindad. Basándonos en esta interacción, es posible diseñar sistemas híbridos plasmón-emisor con propiedades ópticas extraordinarias resultantes de la combinación del carácter bosónico de los plasmones y el carácter fermiónico de los emisores. Sin embargo, para poder explotar estas propiedades es necesario desarrollar herramientas teóricas capaces de describir, a un nivel cuántico, los procesos de acoplamiento e interferencia asociados a la interacción entre los diferentes elementos de estos sistemas.

La segunda parte de esta tesis comienza con la descripción de un nuevo procedimiento para estudiar la respuesta óptica de sistemas híbridos plasmón-emisor, basado en las funciones de Green de Zubarev. A pesar de su simplicidad, esta metodología nos permite ir más allá del tratamiento perturbativo de la interacción plasmón-emisor, incorporando, al mismo tiempo, el decaimiento de estas excitaciones. A modo de ejemplo, aplicamos este método al análisis del espectro de absorción de un sistema formado por un emisor cuántico situado entre dos nanopartículas metálicas. Asumiendo valores realistas para los diferentes parámetros del sistema, obtenemos un espectro de absorción complejo, originado por la interacción emisor-plasmón, que exhibe resonancias de Fano con frecuencias y tamaños determinados

por el estado cuántico del emisor.

En otra vertiente, el reciente descubrimiento de un método sencillo para la síntesis controlada de láminas de grafeno ha abierto nuevas líneas de investigación en el campo de la plasmónica. Este material, formado por una sola capa plana de átomos de carbono dispuestos en una red hexagonal, admite la existencia de plasmones cuando está dopado, ya sea con un exceso de electrones o de huecos. Comparados con los plasmones de estructuras metálicas, los plasmones existentes en nanoestructuras de grafeno presentan propiedades interesantes e inusuales. En particular, son capaces de confinar la luz en volúmenes considerablemente más pequeños y, al mismo tiempo, presentan factores de calidad y tiempos de vida mucho mayores. Además, los plasmones del grafeno se pueden sintonizar cambiando el nivel de dopaje de la nanoestructura que los soporta, lo cual se puede conseguir empleando métodos químicos, o de forma electrostática, aplicando un potencial externo. Estas propiedades extraordinarias convierten a las nanoestructuras de grafeno en plataformas ideales para la observación y el estudio de efectos cuánticos plasmónicos.

Con el objetivo de aprovechar las excelentes propiedades de los plasmones del grafeno, estudiamos la respuesta de sistemas híbridos compuestos por emisores cuánticos y nanoestructuras de grafeno. Gracias a este análisis, predecimos la existencia de un efecto de bloqueo plasmónico originado por la interacción de un emisor cuántico con un nanodisco de grafeno. Este efecto, el cual es una consecuencia directa de alcanzar un régimen de acoplamiento fuerte en la interacción entre los dos elementos del sistema, consiste en la transferencia del carácter fermiónico del emisor a los plasmones del grafeno a través de la generación de estados híbridos. Esto es posible gracias al extraordinario grado de confinamiento y tiempo de vida de los plasmones del grafeno. Como resultado del bloqueo plasmónico, el nanodisco de grafeno presenta una sección eficaz de absorción fuertemente no-lineal. Al mismo tiempo, los plasmones exhiben una estadística no-clásica, que estudiamos a través del análisis de la función de correlación de segundo orden a tiempos iguales $g^{(2)}(0)$. Esta magnitud, que para estados clásicos permanece por encima de 1, toma valores cercanos a 0 debido al bloqueo plasmónico, revelando de este modo la existencia de estados plasmónicos no-clásicos. Gracias a que los plasmones de las nanoestructuras de grafeno son sintonizables, el acoplamiento plasmón-emisor y, por tanto, el efecto

de bloqueo plasmónico se pueden controlar modulando el nivel de dopaje del nanodisco de grafeno. Por último, es necesario destacar que este efecto es análogo al fenómeno de bloqueo fotónico, el cual ha sido estudiado extensivamente y observado experimentalmente en el contexto de la electrodinámica cuántica en cavidades.

La posibilidad de controlar la evolución temporal de un emisor cuántico usando señales clásicas constituye un gran avance hacia la realización de dispositivos de información cuántica escalables. En este contexto, la aparición del grafeno como un material plasmónico sintonizable, en el que los plasmones se pueden, literalmente, encender y apagar aplicando potenciales externos, abre una vía natural para controlar la evolución de sistemas pequeños a través de interacciones mediadas por plasmones, las cuales, a su vez, se pueden modular por medio de campos y potenciales eléctricos externos. En esta tesis exploramos esta posibilidad analizando, de nuevo, un sistema compuesto por un emisor cuántico situado cerca de un nanodisco de grafeno. A través de la realización de simulaciones realistas demostramos un control excelente sobre la evolución temporal de emisores, tanto individuales como en interacción. Basándonos en la rápida modulación electro-óptica del grafeno, comprobamos que es posible conseguir cualquier perfil temporal para la evolución de los emisores. Además, usando este esquema de control, podemos también modular la emisión de sistemas compuestos por conjuntos de emisores, en los cuales es posible producir, de forma controlada, un estado de superradiancia.

Uno de los objetivos fundamentales de la investigación en plasmónica es el diseño de sistemas capaces de confinar el campo electromagnético en regiones con el mínimo tamaño posible. Con este objetivo en mente, exploramos la posibilidad de trasladar las excelentes propiedades mostradas por las nanoestructuras de grafeno consideradas hasta ahora, las cuales contienen millones de átomos de carbono, a sistemas mucho más pequeños compuestos tan sólo por cientos de átomos. La reducción de las dimensiones de las nanoestructuras produce un corrimiento de las frecuencias plasmónicas hacia longitudes de onda más pequeñas, y por tanto más cercanas al visible. Además, el carácter discreto del espectro electrónico de estos sistemas implica que alcanzar los valores típicos de dopaje solo requiera añadir o extraer unos pocos electrones. Debido a su tamaño, estos sistemas deben ser estudiados usando modelos microscópicos capaces de describir los efectos de borde y de confinamiento cuántico, los cuales, como se ha demostrado en la literatura,

juegan un papel central en nanoestructuras con un número de átomos inferior a $\sim 10^4$.

En la tercera parte de esta tesis, estudiamos nanotriángulos de grafeno a través de un análisis basado en la combinación de un método de enlace-fuerte para la descripción de la estructura electrónica, y la aproximación de fase aleatoria para la respuesta dieléctrica. Mediante estas técnicas demostramos que el añadir un sólo electrón al nanotriángulo hace posible la excitación de plasmones en el infrarrojo que no existían en la configuración neutra, lo cual constituye un resultado destacable teniendo en cuenta que los nanotriángulos estudiados contienen cientos de electrones. Además, cada electrón extra que se añade al sistema produce un corrimiento significativo de la frecuencia plasmónica. Este fenómeno es muy sensible al tipo de bordes que presenta la nanoestructura. En particular, los nanotriángulos con bordes tipo *brazo de silla* exhiben resonancias plasmónicas estrechas, asociadas a un incremento extraordinario del campo cercano, así como a secciones eficaces de absorción mayores que el área geométrica de la nanoestructura. Por el contrario, los nanotriángulos con borde tipo *zigzag* no presentan este comportamiento debido a la existencia de estados de energía nula que no participan en la respuesta plasmónica.

En un frente muy distinto, las fluctuaciones térmicas y de vacío del campo electromagnético, así como de la polarización de la materia, originan diversos fenómenos que juegan un papel central en la dinámica de las nanoestructuras. Como ejemplos de ello podemos citar las interacciones de van der Waals y de Casimir, o la transferencia radiativa de calor. Durante los últimos años se ha dedicado un tremendo esfuerzo científico a la descripción de estos fenómenos. En particular, la transferencia radiativa de calor entre nanoestructuras ha sido ampliamente estudiada debido a su importancia crucial para el desarrollo de aplicaciones en nanotecnología.

La última parte de esta tesis comienza con el desarrollo de un modelo, basado en el teorema de fluctuación-disipación, para describir la transferencia radiativa de calor entre dos nanopartículas. Este modelo, a diferencia de descripciones anteriores, incluye la respuesta electromagnética completa de las nanopartículas, el intercambio con el entorno, y correcciones radiativas, tanto en la dependencia con la distancia de los campos como en los coeficientes de absorción de las nanopartículas. Gracias a este análisis, demostramos que los términos cruzados de polarizaciones eléctrica y magnética dominan la transferencia entre partículas de oro y SiC, mientras que las

correcciones radiativas reducen dicha transferencia en varios órdenes de magnitud, incluso para separaciones relativamente pequeñas. Al mismo tiempo, mostramos que es posible suprimir o incrementar la transferencia al entorno, dependiendo de la temperatura de las partículas. Todos estos efectos han de ser tenidos en cuenta para obtener una descripción precisa del intercambio radiativo de calor en entornos nanoestructurados.

La interacción de las fluctuaciones térmicas y de vacío del campo con objetos en movimiento da lugar a fuerzas que modifican la dinámica de éstos últimos. Un claro ejemplo de ello es el efecto de Casimir dinámico. En la última parte de la tesis, estudiamos la dinámica de una nanopartícula que rota en el vacío, prediciendo la existencia de un torque generado por las fluctuaciones del campo electromagnético y de su polarizabilidad. Como resultado de este análisis, obtenemos expresiones analíticas para el torque y la potencia radiada por la nanopartícula durante el proceso de fricción en función de su velocidad, su temperatura, y la del entorno. La metodología empleada se basa en dos procedimientos diferentes: (i) un cálculo semiclásico derivado del teorema de fluctuación-disipación y (ii) una descripción estrictamente cuántica, en la que asumimos que la respuesta de la nanopartícula está gobernada por excitaciones bosónicas tales como fonones y plasmones. Ambos procedimientos convergen a las mismas expresiones finales, confirmando de este modo la idoneidad del teorema de fluctuación-disipación para tratar sistemas aparentemente fuera del equilibrio, y proporcionando, al mismo tiempo, una visión más amplia de los procesos físicos subyacentes a la fricción térmica y de vacío. Usando el modelo desarrollado, calculamos la temperatura de equilibrio de la nanopartícula durante el proceso de fricción, mostrando que dicho proceso puede producir tanto calentamiento como enfriamiento de la nanopartícula relativos a la temperatura del entorno. Finalmente, estudiamos el tiempo de frenado de nanopartículas de grafito, discutiendo sus posibles implicaciones en el comportamiento del polvo cósmico.

Abstract

In recent years we have witnessed an almost explosive growth of the field of nanophotonics: the interaction of light with structures whose dimensions lie at the nanometer scale. The matching between the *size* of light (*i.e.*, its wavelength) and the dimensions of the structures under consideration gives rise to non-trivial interactions, which enable new approaches for manipulating and controlling light. Plasmonics has emerged as one of the most promising research topics in this field. Surface plasmons (*i.e.*, collective oscillations of the conduction electrons of metallic nanostructures) provide a tool for confining and manipulating electromagnetic fields at length scales well below the diffraction limit of light. With their extremely large excitation cross-sections, plasmonic nanostructures provide the means for enhanced light harvesting and light focusing to intense *hot spots*, where non-linear optical effects can be exploited to probe the electronic and vibrational structure of matter.

Surface plasmons existing at metal-dielectric interfaces can be used to guide electromagnetic signals at infrared and visible frequencies. The large degree of confinement displayed by these excitations enables the concentration of the guided signals in transversal areas with dimensions well below the diffraction limit. This renders plasmonic waveguides as a promising alternative to develop novel information processing devices capable of combining the operating frequencies and bandwidths of photonic devices with the large degree of integration achieved by current semiconductor technologies.

Several designs of plasmonic waveguides have been proposed in the last years, including continuous systems composed of metallic elements of finite cross-section sandwiched in symmetric and asymmetric dielectric environments, or channels and ridges patterned into flat surfaces. Systems consisting of periodic arrangements of nanoparticles, or composed of plasmon-band-gap structures, have been also studied,

as well as hybrid devices combining dielectric wires and metallic planar surfaces.

In the first part of this thesis, we study and characterize the response of pairs of silver nanowires placed in silica with the aim of designing novel robust plasmonic waveguides. These structures can support gap plasmons, which emerge from the hybridization of the individual wire modes and are highly concentrated in the gap region between the wires. The guiding properties associated with these modes can be tuned by adjusting the distance between the wires. This enables the optimization of the tradeoff between the degree of confinement and the propagation length existing in all plasmonic waveguides. We demonstrate the outstanding performance of this guiding scheme by comparing it with other proposed plasmonic waveguides in terms of a figure of merit associated with the degree of allowed integration. We also analyze the robustness of the gap plasmon, showing that it can tolerate sharp turns of subwavelength radius, as well as asymmetries in the wire diameter.

With the objective of designing three dimensional plasmonic circuits, we analyze the interaction between gap plasmons in systems composed of more than two wires. Starting with the basic element defining a gap plasmon (*i.e.*, the wire pair) we study the energy splitting and symmetry properties of the hybridized gap modes resulting from the interaction between two wire pairs. This system is shown to display non-avoided crossings of hybridized modes, and it evolves at short distances towards a degenerate system consisting of four wires arranged in a square, where two new gap plasmons emerge from redshifted higher-energy modes. The gap modes of three neighboring wires are also described in a continuous transition from a coplanar configuration to an equilateral triangle arrangement.

The interaction between wire pairs is shown to be weak enough to prevent efficient transfer of plasmon signals from one pair to the other, which is beneficial to avoid crosstalking, but it still allows the design of waveguide couplers. The coupling is significantly increased by placing a wire of rectangular cross-section in between the wire pairs, thus allowing us to design a gap plasmon coupler capable of achieving large plasmon-signal transfers within propagation distances below the attenuation length, and therefore, completing the analysis of the basic elements needed to built a three dimensional plasmonic circuit.

The large field enhancements associated with the excitation of plasmons in metallic nanoparticles permit them to interact with quantum emitters (*e.g.*, atoms,

molecules, or quantum dots) placed in their vicinity. This interaction allows us to design new hybrid plasmon-emitter systems with extraordinary optical properties resulting from the combination of the bosonic character of plasmons and the fermionic behavior of emitters. However, in order to exploit these extraordinary properties, we need to develop new theoretical tools capable of describing, at the quantum level, the coupling and the interference processes associated with the interaction of the different system elements.

The second part of this thesis starts with the description of a novel approach, based on Zubarev's Green functions, to study the optical response of hybrid plasmon-emitter systems. Despite its simplicity, this methodology allows us to go beyond the perturbative regime in the plasmon-emitter interaction, incorporating, at the same time, the finite lifetimes of these excitations. We illustrate this method by applying it to the analysis of the optical absorption spectrum of a system consisting of a quantum emitter placed in the gap of a metallic dimer. Using realistic parameters, we show that, as a result of the interaction between the emitter and the dimer plasmons, the absorption spectrum of the latter can exhibit narrow Fano resonances whose position and size directly depend on the state of the emitter.

The recent discovery of the facile synthesis of single sheet graphene structures has opened up several highly promising new directions in plasmonics. This material, that consists in a flat monolayer of carbon atoms arranged in a two-dimensional honeycomb lattice, can support surface plasmons when doped, either by electrons or by holes. Plasmons supported by graphene nanostructures display interesting and unusual properties, quite different from the equivalent excitations in metallic structures. In particular, they can confine light down to substantially smaller volumes, and at the same time, provide longer plasmon lifetimes and higher Q-factors. Furthermore, graphene plasmons can be tuned through the modification of the doping level of graphene. This can be accomplished using chemical methods, and also electrostatically, using an applied potential. These extraordinary properties make of graphene nanostructures a very suitable platform to observe and study quantum plasmonic effects.

In an attempt to take advantage of the excellent properties of graphene plasmons, we study the plasmonic response of hybrid systems composed of quantum emitters and graphene nanostructures. Thanks to this analysis, we predict the existence of a

plasmon blockade effect arising from the coupling between a quantum emitter and a graphene nanodisk. This effect, which is a direct consequence of reaching the strong-coupling regime in the interaction between the two elements of the system, arises from the transfer of the fermionic character of the emitter to the graphene plasmons through the generation of hybridized states. This is only possible thanks to the extraordinary confinement and lifetime of graphene plasmons. As a result of the plasmon blockade effect, the absorption cross-section of the graphene nanodisk becomes strongly non-linear. Furthermore, the statistics of the supported plasmons turns out to be non-classical. We characterize this phenomenon by analyzing the equal-time second-order correlation function $g^{(2)}(0)$. This magnitude, which for classical states remains above 1, drops to values close to 0 as a consequence of the blockade effect, thus revealing the existence of non-classical plasmon states. Thanks to the tunability of graphene plasmons, the plasmon-emitter coupling, and therefore, the plasmon blockade, can be efficiently controlled by tuning the doping level of the graphene nanodisk. This effect is analogous to the photon blockade that has been extensively studied and experimentally observed in the context of the field of cavity quantum electrodynamics.

Controlling the temporal evolution of a quantum emitter by means of classical signals represents a significant step forward towards the realization of scalable quantum information devices. In this context, the emergence of graphene as a tunable plasmonic material, in which plasmons can be literally switched on and off by applying external potentials, opens a natural way to control the quantum evolution of small systems through plasmon-mediated interactions, which are in turn modulated by external fields. Here, we explore this possibility by analyzing again a system composed of a quantum emitter placed close to a graphene nanodisk. We provide realistic simulations demonstrating excellent control over the temporal evolution of individual and interacting quantum dots. Any desired temporal profile can be produced by resorting on the unprecedentedly fast electro-optical modulation of graphene. Furthermore, we also demonstrate that, using this scheme, it is possible to modulate the emission in systems consisting of many emitters, in which superradiance can be produced and controlled electrostatically.

One of the ultimate goals of plasmonic research is to design systems capable of confining the electromagnetic field in the smallest possible volume. With this

objective in mind, we explore the possibility of transferring the excellent properties displayed by the graphene nanostructures considered so far, containing millions of carbon atoms, to smaller systems composed of just hundreds of atoms. The reduction of the nanostructure dimensions produces an interesting blueshift of the plasmonic frequencies towards the visible range. Furthermore, as a result of the discrete character of the electronic spectrum of these systems, the addition or the removal of just a few electrons is sufficient to reach doping values compatible with the existence of plasmons. Due to their small sizes, these systems must be studied using microscopic models capable of accounting for edge and quantum confinement effects, which, as it has been shown in the literature, play a central role in structures containing less than $\sim 10^4$ carbon atoms.

In the third part of this thesis we study small graphene nanotriangles using a combination of a tight-binding model for the electronic structure and the random-phase approximation for the dielectric response. We show that the addition of a single electron switches on infrared plasmons that were previously absent from the uncharged structure. This is a remarkable result, since the nanotriangles considered contain hundreds of electrons in their valence band. Moreover, the addition of each further electron produces a dramatic frequency shift of the plasmonic resonance. These phenomena are highly sensitive to carbon edges. Specifically, armchair nanotriangles display sharp plasmons that are associated with intense near-field enhancement, as well as absorption cross-sections exceeding the geometrical area occupied by the graphene. In contrast, zigzag triangles do not support these plasmons due to the existence of zero-energy states that do not participate in the plasmonic response.

Thermal and vacuum fluctuations of the electromagnetic field and the polarization of matter are at the origin of several phenomena playing a central role in the dynamics of nanoscale objects. Examples of this include the van der Waals and the Casimir interactions, as well as the so-called radiative heat transfer. In recent years, a tremendous amount of work has been devoted to understand these phenomena. In particular, the radiative heat transfer between nanostructures has been extensively investigated due to its crucial implications for technological applications.

The last part of this thesis starts with the derivation of a model, based on the fluctuation-dissipation theorem, to explain the radiative heat transfer between

two nanoparticles. Our model includes the full electromagnetic particle response, heat exchange with the environment, and important radiative corrections, both in the distance dependence of the fields and in the particle absorption coefficients, which where ignored in previous studies. We find that crossed terms of electric and magnetic interactions dominate the transfer rate between gold and SiC particles, whereas radiative corrections reduce it by several orders of magnitude even at small separations. We further show that the amount of radiation leaking away from the system can be strongly suppressed or enhanced at low and high temperatures, respectively. These effects must be taken into account for an accurate description of radiative heat transfer in nanostructured environments.

The interaction of the thermal and vacuum field fluctuations with moving objects produce forces that modify the dynamics of the latter, as it happens in the dynamical Casimir effect. We finish the last part of this thesis by studying the stopping of spinning particles in vacuum. We predict a torque produced by fluctuations of the electromagnetic field and the particle polarization. We obtain expressions for the frictional torque and the power radiated by the particle as a function of rotation velocity and the temperatures of the particle and the surrounding environment. We solve this problem following two different approaches: (i) a semiclassical calculation based upon the fluctuation-dissipation theorem; and (ii) a fully quantum-mechanical theory within the framework of quantum electrodynamics, assuming that the response of the particle is governed by bosonic excitations such as phonons and plasmons. Both calculations lead to identical final expressions, thus corroborating the suitability of the fluctuation-dissipation theorem to deal with systems that are apparently out of equilibrium, and also providing comprehensive insight into the physical processes underlying thermal and vacuum friction. Using the developed model we calculate the equilibrium temperature of the particle during the friction process. We find that thermal and vacuum friction can produce heating but also cooling of the particle relative to the environment. Finally, we study the stopping time of graphite nanoparticles and discuss its possible implications for the rotational dynamics of cosmic dust.

Chapter 1

Introduction

The interaction between light and matter is at the origin of many phenomena that form part of our daily experience. The desire of humanity for controlling this interaction has been a powerful engine to develop new tools that have served to improve our adaptation to the environment. Examples of this advance bring us from the lenses that Galileo used in his telescope, which allowed him to observe the moons of Jupiter, to the latest developments in laser technology contained in so many of the devices that surround us nowadays.

In the last decades, we have witnessed the emergence of the novel field of nanophotonics [1]. This field is devoted to the study of the interaction between light and material structures with relevant lengths comparable to the wavelength of visible light (*i.e.*, of the order of hundreds of nanometers). This matching between the *size* of light and the dimensions of matter leads to unexpected extraordinary optical properties. A paradigmatic example is the absorption and scattering spectra of colloidal gold, which are completely different from those of bulk gold [2], and that can be tuned by tailoring the size and the shape of the gold nanoparticles [3].

In this context, collective oscillations of the conduction electrons of a metal, known as surface plasmons [4], have emerged as key elements that provide the means to confine electromagnetic energy down to nanometer scales, well below the diffraction limit of light, and to consequently enhance the light intensity relative to the external supplied illumination [5]. More recently, the discovery and synthesis of graphene [6], a flat monolayer of carbon atoms arranged in a two-dimensional

honeycomb lattice, have opened an alternative path in nanophotonics with an extraordinary potential for novel applications based on the excellent properties of the plasmons supported by graphene nanostructures [7].

The research in nanophotonics has already led to important applications in areas as diverse as ultrasensitive biosensing, in which the development of surface enhanced Raman scattering (SERS) has played a pivotal role [8, 9, 10]. Plasmon-enhanced photodetection [11], improved photovoltaics [12, 13], and photothermal cancer therapy [14, 15] are other examples of applications that are already benefiting society. Additionally, an extensive research program is being carried out to find potential applications to information technologies [16].

Framed in this context, the purpose of this thesis is to contribute to a better understanding of the interaction between light and matter at the nanoscale from a fundamental perspective, but with the view to developing novel applications for technology.

1.1 Classical electromagnetism

In a classical and macroscopic framework, light is described as an electromagnetic wave, while at the same time, matter is assumed to be a continuous medium in which the singular character of charges and currents is avoided by considering charge ρ and current $\mathbf{J}$ densities. Within these prescriptions, light-matter interaction is described by Maxwell's macroscopic equations[1] [17, 18]

$$\begin{aligned}
\nabla \times \mathbf{E}(\mathbf{r},t) &= -\frac{1}{c}\frac{\partial}{\partial t}\mathbf{B}(\mathbf{r},t), \\
\nabla \times \mathbf{H}(\mathbf{r},t) &= \frac{1}{c}\frac{\partial}{\partial t}\mathbf{D}(\mathbf{r},t) + \frac{4\pi}{c}\mathbf{J}(\mathbf{r},t), \\
\nabla \cdot \mathbf{D}(\mathbf{r},t) &= 4\pi\rho(\mathbf{r},t), \\
\nabla \cdot \mathbf{B}(\mathbf{r},t) &= 0,
\end{aligned} \tag{1.1}$$

where $\mathbf{E}$ is the electric field, $\mathbf{H}$ is the magnetic field, $\mathbf{D}$ is the electric displacement, and $\mathbf{B}$ is the magnetic induction. Maxwell's equations determine how fields are generated by charges and currents, but they do not determine how charges and

[1] Gaussian electromagnetic units are used throughout this thesis.

currents are induced by fields. Therefore, in order to get a self-consistent solution of Maxwell's equations, we must supplement them with adequate constitutive relations. Here, we limit ourselves to materials that are linear, homogeneous, isotropic, and non-magnetic, and thus, the constitutive relations can be written as

$$\mathbf{D}(\mathbf{r},t) = \int d\mathbf{r}'dt'\varepsilon(\mathbf{r}-\mathbf{r}',t-t')\,\mathbf{E}(\mathbf{r}',t'), \qquad \mathbf{B}(\mathbf{r},t) = \mathbf{H}(\mathbf{r},t), \tag{1.2}$$

where, ε is the dielectric function of the medium. The first of these equations shows that the electric displacement $\mathbf{D}$ at certain position $\mathbf{r}$ and time t depends on the value of the electric field $\mathbf{E}$ at all positions $\mathbf{r}'$ and times $t' < t$. When this happens, we talk about spatial and temporal dispersion. The latter is a very common behavior for numerous materials in the visible spectrum and leads to frequency-dependent dielectric permittivities if we perform a spectral decomposition of the fields. On the contrary, spatial dispersion, known also as non-locality, is relevant only under extreme conditions, such as for metallic structures whose size is comparable to the mean-free path of the electrons, or in gaps in which electron tunneling is significant [19, 20]. In general, a proper description of non-locality requires the use of microscopic models, from which, in some cases, it is possible to extract useful effective prescriptions.

If we shift to the frequency domain, we can write the spectrum of an arbitrary time-dependent field using the Fourier transform

$$\mathbf{E}(\mathbf{r},\omega) = \int dt\mathbf{E}(\mathbf{r},t)\,e^{i\omega t}. \tag{1.3}$$

Since $\mathbf{E}(\mathbf{r},t)$ is a real field, its spectrum must satisfy the relation $\mathbf{E}(\mathbf{r},-\omega) = \mathbf{E}^*(\mathbf{r},\omega)$. Maxwell's equations [see Eq. (1.1)] can be transformed in the same way to obtain

$$\begin{aligned}
\nabla\times\mathbf{E}(\mathbf{r},\omega) &= ik\mathbf{B}(\mathbf{r},\omega),\\
\nabla\times\mathbf{H}(\mathbf{r},\omega) &= -ik\mathbf{D}(\mathbf{r},\omega) + \frac{4\pi}{c}\mathbf{J}(\mathbf{r},\omega),\\
\nabla\cdot\mathbf{D}(\mathbf{r},\omega) &= 4\pi\rho(\mathbf{r},\omega),\\
\nabla\cdot\mathbf{B}(\mathbf{r},\omega) &= 0,
\end{aligned} \tag{1.4}$$

where $k = \omega/c$ is the light wave vector. In addition, the constitutive relations given in Eq. (1.2) can be written in the frequency domain as

$$\mathbf{D}(\mathbf{r},\omega) = \varepsilon(\omega)\,\mathbf{E}(\mathbf{r},\omega), \qquad \mathbf{B}(\mathbf{r},\omega) = \mathbf{H}(\mathbf{r},\omega),$$

where $\varepsilon(\omega)$ is the frequency-dependent dielectric permittivity. Here, we have neglected any non-locality of the material.

When the physical problem involves more than one material, the fields must satisfy some conditions at the boundaries that separate them. These conditions, which are derived from Maxwell's equations, can be expressed as follows

$$\begin{aligned}
\mathbf{n}\times(\mathbf{E}_i-\mathbf{E}_j) &= 0,\\
\mathbf{n}\times(\mathbf{H}_i-\mathbf{H}_j) &= \frac{4\pi}{c}\mathbf{K},\\
\mathbf{n}\cdot(\mathbf{D}_i-\mathbf{D}_j) &= 4\pi\eta,\\
\mathbf{n}\cdot(\mathbf{B}_i-\mathbf{B}_j) &= 0,
\end{aligned} \tag{1.5}$$

where $\mathbf{K}$ and η are the surface current and surface charge densities on the boundary, respectively. From these expressions we can work out the so-called Fresnel coefficients [1], which relate the fields transmitted and reflected by a planar boundary with the incident field. These coefficients depend on the polarization of the field. For a p-polarized electric field (*i.e.*, a field parallel to the plane of incidence) we have

$$r_{\mathrm{p}} = \frac{\varepsilon_2 k_{1\perp} - \varepsilon_1 k_{2\perp}}{\varepsilon_2 k_{1\perp} + \varepsilon_1 k_{2\perp}}, \qquad t_{\mathrm{p}} = \sqrt{\frac{\varepsilon_2}{\varepsilon_1}}\frac{k_{1\perp}}{k_{2\perp}}\left[1 - r_{\mathrm{p}}\right], \tag{1.6}$$

where $k_{i\perp}$ is the component of the wave vector in medium i perpendicular to the interface. This component is defined as $k_{\mathrm{i}\perp} = \sqrt{k_i^2 - k_\parallel^2}$ in terms of the total wave vector in that medium $k_i = \sqrt{\varepsilon_i}k$, and the parallel component $k_\parallel$, which is the same for both media. In a similar way, we have for a s-polarized field (*i.e.*, a field perpendicular to the plane of incidence) the following expressions

$$r_{\mathrm{s}} = \frac{k_{1\perp} - k_{2\perp}}{k_{1\perp} + k_{2\perp}}, \qquad t_{\mathrm{s}} = 1 + r_{\mathrm{s}}. \tag{1.7}$$

1.1.1 Surface plasmons polaritons

Surface plasmons polaritons (SPPs) are surface modes that propagate at metal-dielectric interfaces and decay in the direction perpendicular to them. They are originated from collective excitations of the conduction electrons of a metal coupled to an external electromagnetic field. From a more theoretical point of view, these excitations can be understood as the electromagnetic eigenmodes[2] of the metal-dielectric interfaces. This means that they are solutions of Maxwell's equations in the absence of external excitations. Therefore, we can obtain the dispersion relation of SPPs from the poles of the Fresnel coefficients. If we start by analyzing the pole of r_{s} [see Eq. (1.7)], we arrive to the condition $k_{1\perp} = -k_{2\perp}$, which cannot be satisfied by any physical system[3]. Then, SPPs have always p-polarization [*i.e.*, they are transverse magnetic modes (TM)] and their dispersion relation, derived from the pole of r_{p} [see Eq. (1.6)], reads

$$k_{\mathrm{spp}} = \frac{\omega}{c}\sqrt{\frac{\varepsilon_{\mathrm{m}}\varepsilon_{\mathrm{d}}}{\varepsilon_{\mathrm{m}}+\varepsilon_{\mathrm{d}}}}, \tag{1.8}$$

where $\varepsilon_{\mathrm{m}}(\omega)$ and $\varepsilon_{\mathrm{d}}(\omega)$ are the dielectric functions of the metal and the dielectric medium, respectively, which must fulfill $\varepsilon_{\mathrm{m}}(\omega)\,\varepsilon_{\mathrm{d}}(\omega) < 0$ and $\varepsilon_{\mathrm{m}}(\omega) + \varepsilon_{\mathrm{d}}(\omega) < 0$. These conditions are satisfied by noble metals at frequencies below the plasma frequency ω_{p} surrounded by a dielectric or vacuum. This magnitude, which is defined in terms of the electron density n, mass m_{e}, and charge e, as

$$\omega_{\mathrm{p}} = e\sqrt{\frac{4\pi n}{m_{\mathrm{e}}}},$$

determines the frequency above which a metal starts displaying a dielectric behavior (positive permittivity) because its conduction electrons cannot follow anymore the rapid variation of the external fields.

The dielectric function of a noble metal can be approximated using the Drude

[2]Rigorously speaking, we should talk about quasi-eigenmodes due to the fact that all systems considered in this thesis present Ohmic losses and, very often, the modes in which we focus are coupled to radiation.

[3]Nonetheless, s-polarized surface waves can exist in artificial metamaterials that sustain nontrivial magnetic response.

model [21]

$$\varepsilon(\omega) = \varepsilon_{\mathrm{b}} - \frac{\omega_{\mathrm{p}}^2}{\omega(\omega + i\gamma)}, \tag{1.9}$$

where $\gamma \ll \omega_{\mathrm{p}}$ is the electron collision rate responsible for the metal losses, and ε_{b} accounts for the electron screening due to inner shells polarization and interband transitions. From this expression, we verify that the dielectric function of a noble metal is predominantly real and negative for $\gamma \ll \omega < \omega_{\mathrm{p}}/\sqrt{\varepsilon_{\mathrm{b}}}$, while it becomes positive (*i.e.*, the metal behaves as a dielectric) for $\omega > \omega_{\mathrm{p}}/\sqrt{\varepsilon_{\mathrm{b}}}$. If we use this expression into Eq. (1.8), we can obtain the dispersion relation of SPPs.

Figure 1.1 represents the dispersion relation for a gold-vacuum interface showing explicitly the real (red curve) and the imaginary (green curve) parts of k_{spp}. We describe the dielectric function of gold using the Drude model [see Eq. (1.9)] with the following values for the different parameters: $\varepsilon_{\mathrm{b}} = 9.5$, $\hbar\omega_{\mathrm{p}} = 9.06\,\mathrm{eV}$ and $\hbar\gamma = 0.071\,\mathrm{eV}$ [22]. These values are chosen to fit correctly the experimental data from Ref. [23]. For frequencies below $\omega_{\mathrm{p}}/\sqrt{1+\varepsilon_{\mathrm{b}}}$ (see black dotted curve), SPPs propagate along the metal-dielectric interface with a wave vector larger than that corresponding to a plane wave of the same energy (*i.e.*, $\mathrm{Re}\{k_{\mathrm{spp}}\} > k = \omega/c$). Since $k_{\mathrm{i}\perp} = \sqrt{\varepsilon_i k^2 - k_{\mathrm{spp}}^2}$, this means that the perpendicular component of the wave vector both in vacuum and in gold has a dominant imaginary part related to $\mathrm{Re}\{k_{\mathrm{spp}}\}$. Therefore, the fields associated with the SPP decay in the direction perpendicular to the metal, thus confining the electromagnetic energy to a region localized around the interface. The degree of confinement is proportional to the real part of k_{spp}, and, hence, it increases as the frequency approaches $\omega_{\mathrm{p}}/\sqrt{1+\varepsilon_{\mathrm{b}}}$. The fact that SPPs lie outside of the light cone also implies that they cannot couple to free radiation due to momentum mismatch (*i.e.*, $\mathrm{Re}\{k_{\mathrm{spp}}\} \neq k = \omega/c$).

If we analyze the results obtained assuming $\gamma = 0$ (see blue dotted curve), we observe that the inclusion of losses establishes a limit to the value of $\mathrm{Re}\{k_{\mathrm{spp}}\}$, and therefore, to the maximum achievable degree of confinement. On the other hand, the propagation length of a SPP is determined by the imaginary part of the SPP wave vector $L = 1/2\mathrm{Im}\{k_{\mathrm{spp}}\}$. This magnitude is defined as the distance at which the SPP intensity decays by a factor $1/e$ of the initial value and, as extracted from the green curve of Fig. 1.1, it becomes minimum at the frequency for which the real

part of the wave vector reaches its maximum. This results in a tradeoff between the degree of confinement and the propagation length that is inherent to SPPs.

For frequencies above $\omega_p/\sqrt{\varepsilon_b}$ we observe a second mode lying inside the light cone, which indicates that it is not a bounded mode. Actually, as discussed above, gold behaves as a dielectric in that spectral region, and therefore, this mode corresponds to incident light satisfying the Brewster condition (*i.e.*, $r_p = 0$).

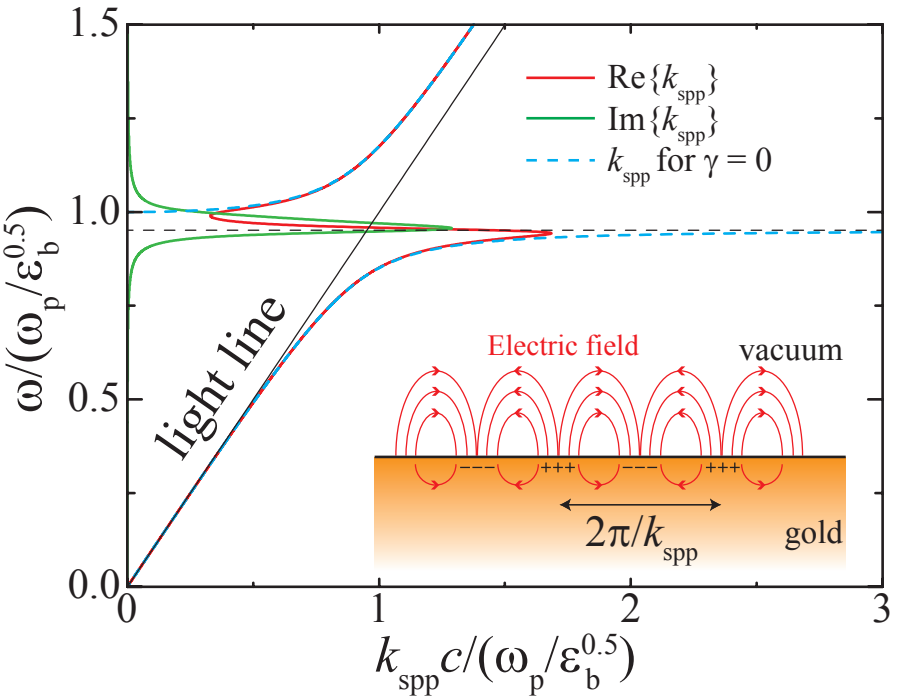

Figure 1.1: Dispersion relation of a surface plasmon polariton propagating along a gold-vacuum interface. We show explicitly the real (red curve) and the imaginary (green curve) parts of the SPP wave vector k_{spp}. The dielectric function of gold is described using the Drude model with $\varepsilon_b = 9.5$, $\hbar\omega_p = 9.06\,\text{eV}$ and $\hbar\gamma = 0.071\,\text{eV}$. These values fit correctly the experimental data from Ref. [23]. For comparison we also include k_{spp} for the case in which losses are neglected (*i.e.*, $\gamma = 0$) (blue dotted curve). The inset shows a schematic representation of the interface with the electric field associated with the SPP.

1.1.2 Localized surface plasmons

A finite system such as a metallic nanoparticle can also support surface plasmons [5]. In this case, due to the lack of translational invariance, the plasmons are confined in the three dimensions of space and, therefore, we talk about localized surface plasmons (LSPs). As we did with SPPs, we can understand these excitations as the electromagnetic eigenmodes of the nanoparticle. They can be calculated by solving Maxwell's equations as follows. First of all, in the absence of external charges and currents, we can rearrange the first two expressions of Eq. (1.4) to obtain [1]

$$\begin{aligned} \nabla \times \nabla \times \mathbf{E} - k^2 \varepsilon \mathbf{E} = 0, \\ \nabla \times \varepsilon^{-1} \nabla \times \mathbf{H} - k^2 \mathbf{H} = 0, \end{aligned} \tag{1.10}$$

which are the wave equations for the electric and the magnetic fields. With the appropriate boundary conditions, which of course depend on the particular geometry of the nanoparticle, we can solve these equations to obtain the frequency and the spatial distributions of the fields associated with the LSP. Unfortunately, even for the simple spherical geometry the solution of these equations is not a trivial problem. However, when the size of the particle is much smaller than the light wavelength, the electromagnetic interaction between different parts of the metal is almost instantaneous (*i.e.*, the speed of light can be taken as infinite). This is known as the quasi-static approximation. Within this approximation, the electric and magnetic fields are decoupled [*i.e.*, the first and the second expressions of Eq. (1.4) become $\nabla \times \mathbf{E} = 0$ and $\nabla \times \mathbf{H} = 0$, respectively], and therefore we can write the former as the gradient of a scalar potential $\mathbf{E} = -\nabla \Phi$. This in turn implies that, within this level of approximation, solving the wave equation given in Eq. (1.10) is equivalent to finding the solution of the following equation for the scalar potential with the appropriate boundary conditions

$$\nabla \cdot \varepsilon \nabla \Phi = 0.$$

Solving this equation for the case of a spherical particle in vacuum and a uniform external field, we find that it behaves as an electric point dipole, with a polarizability

given by

$$\alpha_{\mathrm{E}} = R^3 \frac{\varepsilon_{\mathrm{p}} - 1}{\varepsilon_{\mathrm{p}} + 2}, \tag{1.11}$$

where R is the particle radius, and ε_{p} is the particle dielectric function. As we did in the previous section, we can obtain the LSP frequency by analyzing the pole of this expression. By doing so, we obtain the condition $\varepsilon_{\mathrm{p}} = -2$, which can be satisfied by metallic particles. Indeed, if we describe the dielectric function of the metal nanoparticle using the Drude model [see Eq. (1.9)], we arrive at the following expression for the LSP frequency:

$$\omega = \frac{\omega_{\mathrm{p}}}{\sqrt{\varepsilon_{\mathrm{b}} + 2}}. \tag{1.12}$$

An important characteristic of LSPs is the fact that, contrary to SPPs, they couple to free radiation. This means that the excitation of the LSP of a certain nanoparticle enhances its absorption and scattering properties. For this reason, a very suitable way of studying the LSP is through the analysis of its absorption and scattering cross-sections [3]. In the case of an electric dipole we can write these magnitudes in terms of the electric polarizability as

$$\begin{aligned} \sigma_{\mathrm{abs}} &= 4\pi k \mathrm{Im}\left\{\alpha_{\mathrm{E}}\right\} - \sigma_{\mathrm{sc}}, \\ \sigma_{\mathrm{sc}} &= \frac{8\pi}{3} k^4 \left|\alpha_{\mathrm{E}}\right|^2, \end{aligned} \tag{1.13}$$

From these expressions we can clearly see that the absorption cross-section is proportional to the volume of the particle [see Eq. (1.11)], and therefore, for small particles, it dominates over the scattering cross-section, which scales as R^6.

When the size of the nanoparticle is not deep subwavelength, the quasi-static approximation breaks down and we need to explicitly solve Eq. (1.10). This was done by Gustav Mie in 1908 for the case of spherical particles [24]. He obtained an analytical solution, known nowadays as Mie theory [25], based on describing the fields and the optical response of particles in terms of an infinite series of multipolar modes. This theory predicts that a spherical metallic nanoparticle can support an infinite number of LSP resonances, corresponding to multipoles of different order (*e.g.*, dipole, quadrupole, hexapole, etc.). These resonances are determined by the

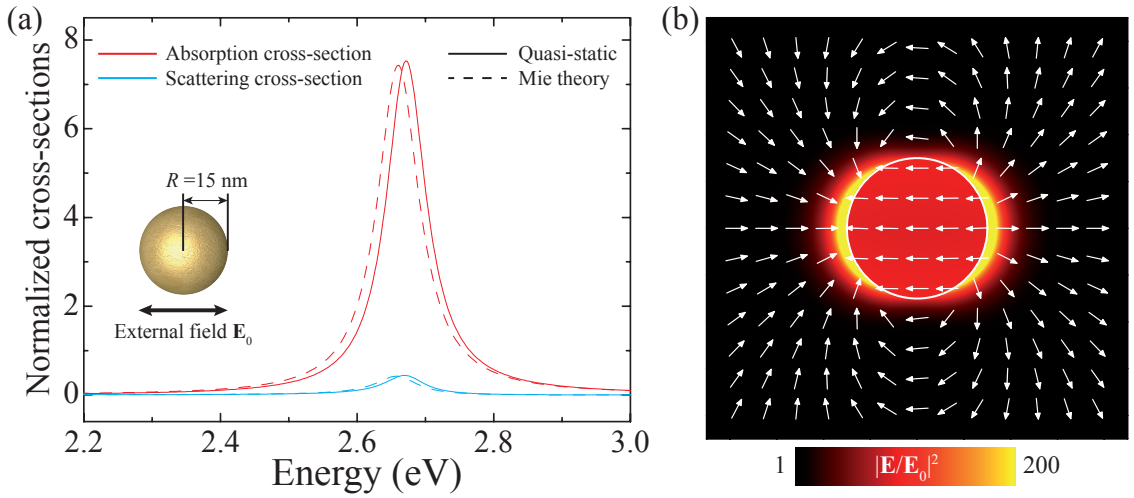

Figure 1.2: Localized surface plasmon supported by a gold nanoparticle. (a) Absorption (red curve) and scattering (blue curve) for a gold nanoparticle of radius $R = 15\,\text{nm}$ in vacuum (see inset). The cross-sections are normalized to the projected area of the particle (πR^2). The dielectric function of gold is approximated with the Drude model as in Fig. 1.1. We compare the results obtained within the quasi-static approximation (solid lines) [see Eqs. (1.11) and (1.13)] with exact calculations based on Mie theory (dashed curves). (b) Enhancement of the electric field intensity ($|\mathbf{E}/\mathbf{E}_0|^2$, background contour plot), and orientation of the induced electric field (white arrows) calculated at the energy of maximum absorption cross-section (2.66 eV) by solving Maxwell's equations using the boundary element method (BEM) (see main text).

poles of the electric scattering coefficient [26]

$$t_l^{\mathrm{E}} = \frac{\varepsilon_{\mathrm{p}} \left[j_l(\rho) + \rho j_l'(\rho) \right] j_l(\rho_{\mathrm{p}}) - \left[j_l(\rho_{\mathrm{p}}) + \rho_{\mathrm{p}} j_l'(\rho_{\mathrm{p}}) \right] j_l(\rho)}{i h_l^{(1)}(\rho) \left[j_l(\rho_{\mathrm{p}}) + \rho_{\mathrm{p}} j_l'(\rho_{\mathrm{p}}) \right] - \varepsilon_{\mathrm{p}} \left[i h_l^{(1)}(\rho) + \rho i h_l^{(1)'}(\rho) \right] j_l(\rho_{\mathrm{p}})}, \tag{1.14}$$

where we have assumed a vacuum environment, l denotes the multipole order (*e.g.*, $l = 1$ for the dipole), $\rho = kR$, $\rho_{\mathrm{p}} = kR\sqrt{\varepsilon_{\mathrm{p}}}$, j_l ($h_l^{(1)}$) is the spherical Bessel (Hankel) function of first kind, and the primes stand for derivatives with respect to the argument. Interestingly, non-metallic particles with high dielectric functions can also support these kinds of resonances, although in that case they are not associated with LSPs [27]. Furthermore, Mie theory predicts the existence of magnetic resonances, even for non-magnetic materials (*i.e.*, materials with $\mu = 1$), associated with the

poles of the magnetic scattering coefficient [26]

$$t_l^{\mathrm{M}} = \frac{\rho j_l'(\rho)\, j_l(\rho_{\mathrm{p}}) - \rho_{\mathrm{p}} j_l(\rho)\, j_l'(\rho_{\mathrm{p}})}{\rho_{\mathrm{p}} i h_l^{(1)}(\rho)\, j_l'(\rho_{\mathrm{p}}) - \rho i h_l^{(1)\prime}(\rho)\, j_l(\rho_{\mathrm{p}})}. \tag{1.15}$$

These resonances can play an important role in the optical response of metallic nanoparticles in the infrared (IR) part of the spectrum [28]. Finally, it is important to remark here that the dipolar electric (magnetic) scattering coefficient is directly related to the electric (magnetic) polarizability through the following expression

$$\alpha_{\mathrm{E,M}} = \frac{3}{2k^3} t_1^{\mathrm{E,M}}.$$

As an example to illustrate the discussion of LSPs, Fig. 1.2(a) shows the absorption (red curves) and scattering (blue curves) cross-sections of a gold nanoparticle of 15 nm of radius placed in vacuum. The dielectric function of gold is described using the Drude model with the parameters given in Fig. 1.1. Solid curves are used to represent the absorption and scattering cross-sections calculated within the quasi-static approximation, which are in good agreement with the results based on Mie theory (dashed curves). Panel (b) shows the enhancement of the field intensity $|\mathbf{E}/\mathbf{E}_0|^2$, relative to the incident field amplitude $\mathbf{E}_0$, associated with the excitation of the LSP. Such enhancement reaches values larger than 200 near the surface of the particle. The orientation of the induced electric field is indicated with white arrows and, as expected from the small size of the particle, resembles exactly the field generated by a point dipole.

So far, we have focused on spherical nanoparticles for which, as discussed above, an analytical solution exists. However, when dealing with more complex shapes we need to rely on numerical methods to study the properties of LSPs. In this thesis, we employ the boundary element method (BEM) [29, 30]. This method is based on expressing the electromagnetic field in terms of boundary charges and currents, and imposing the customary boundary conditions [see Eq. (1.5)] to get a system of surface-integral equations equivalent to Maxwell's equations. Then, this system is solved by discretizing the integrals using a set of N representative points distributed along the boundaries. In this way, we obtain a linear system of equations that can be solved numerically by standard linear-algebra techniques.

1.1.3 Surface plasmons in graphene

In the last years, graphene has emerged as a very promising material displaying a wide range of extraordinary mechanical, electrical, and optical properties, associated with its particular structure [6]. This structure, which consists of a flat monolayer of carbon atoms arranged in a two-dimensional honeycomb lattice [see Fig. 1.3(a)], is associated with a band diagram in which the conduction and the valence bands touch each other at certain singular points known as Dirac points [31]. Around those points, at which the density of electronic states vanishes, the conduction and valence bands of graphene are symmetric and linear [see Fig. 1.3(b)]. This results in charge carriers with zero effective mass (the so-called Dirac fermions [32]) that can travel for micrometers without scattering, even at room temperature.

Graphene, in its neutral state, presents a completely filled valence band, and a completely empty conduction band. Under such conditions, the Fermi level of this material lies exactly at the Dirac point. When extra electrons are added to the conduction band, the Fermi level moves up, and therefore the associated Fermi energy E_{F} (measured relative to the Dirac point) takes a finite positive value [see Fig. 1.3(b)] given by $E_{\mathrm{F}} = \hbar v_{\mathrm{F}} \sqrt{\pi n}$, where $v_{\mathrm{F}} \approx c/300$ is the Fermi velocity, and n is the density of extra electrons. This process of changing the Fermi energy of graphene is known as doping, and due to the symmetry of the bands, it can be also carried out by removing electrons from the valence band. Experimentally, graphene doping is usually achieved by electrostatic gating or with chemical methods [33, 34, 35].

Doped graphene, as noble metals, presents conduction electrons that allow it to support SPPs [36]. This has been experimentally demonstrated using different techniques, such as terahertz [37] and IR [38, 39, 40] optical spectroscopies, or in a more direct way, through direct near-field spatial imaging [34, 35]. However, due to its particular band structure, the SPPs supported by graphene present some interesting advantages as compared to SPPs supported by noble metals. First of all, the wavelength of graphene SPPs is much smaller than the wavelength of metal SPPs [*cf.*, the distance between the SPP wave vector and the light line in Figs. 1.1 and 1.3(c)], which results in a larger degree of confinement. Furthermore, the relatively large conductivity of graphene translates into long optical relaxation times reaching values of $\tau \approx 10^{-13}$ s, compared to 10^{-14} s in gold, thus providing a plausible

solution to the long-standing problem of dissipation in plasmonics. Finally, as we have discussed above, graphene must be doped in order to be able to support SPPs, therefore, by changing the doping, or equivalently, E_F it is possible to control the properties of the supported SPPs.

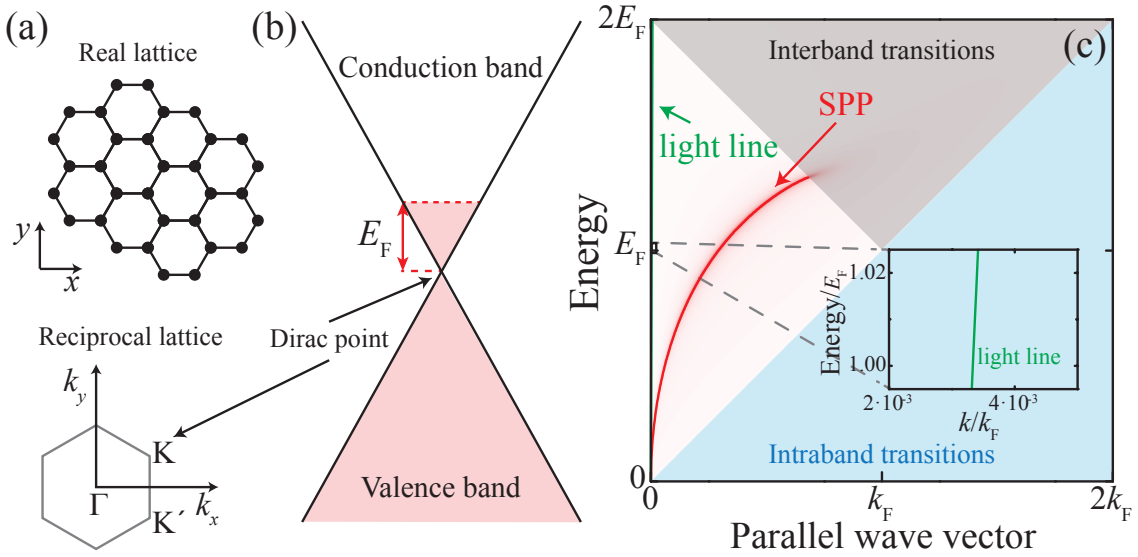

Figure 1.3: Surface plasmons in graphene. (a) Graphene real and reciprocal lattices. (b) Conduction and valence bands of graphene near the Dirac point. We have assumed a certain level of doping corresponding to a finite value of the Fermi energy E_F. (c) Dispersion relation of the SPPs supported by graphene (red curve). The light line is shown in green, and it appears almost vertical in this scale (see inset) due to the extraordinary degree of confinement of the graphene SPPs. Here, k_F represents the Fermi wave vector defined as $k_F = E_F/\hbar v_F$, being $v_F \approx c/300$ the Fermi velocity. The shaded areas represent the energies and wave vectors for which interband and intraband transitions are allowed.

As in the case of a metal-dielectric interface, the dispersion relation of SPPs can be derived from the pole of the p-polarized Fresnel reflection coefficient[4], which in the particular case of graphene, due to its intrinsic two-dimensional character, reads [7]

[4]It is important to remark that graphene, contrary to metal-dielectric interfaces, can also support s-polarized surface modes [41].

$$r_{\mathrm{p}} = \frac{\varepsilon_2 k_{1\perp} - \varepsilon_1 k_{2\perp} + \frac{4\pi\sigma}{\omega} k_{1\perp} k_{2\perp}}{\varepsilon_2 k_{1\perp} + \varepsilon_1 k_{2\perp} + \frac{4\pi\sigma}{\omega} k_{1\perp} k_{2\perp}}.$$

In this expression, σ is the graphene surface conductivity (see below), ε_1 and ε_2 are the dielectric functions of the mediums below and above graphene, and $k_{1\perp}$ and $k_{2\perp}$ are the corresponding wave vector components perpendicular to the graphene sheet. Analyzing the pole of this expression, we can obtain the graphene SPP dispersion relation

$$\frac{\varepsilon_1}{\sqrt{\varepsilon_1 k^2 - k_{\mathrm{spp}}^2}} + \frac{\varepsilon_2}{\sqrt{\varepsilon_2 k^2 - k_{\mathrm{spp}}^2}} = -\frac{4\pi\sigma}{\omega}.$$

This relation is plotted in Fig. 1.3(c), where we can observe that SPPs exist in the region in which interband and intraband transitions are forbidden.

Graphene sheets can be patterned to create finite structures such as nanodisks, nanotriangles, etc. These structures are the graphene analogous of metallic nanoparticles, and therefore, they can support LSP [7, 42]. Furthermore, as it happens with SPPs, graphene LSPs present interesting advantages over the LSP sustained by metallic nanoparticles. In particular, they are associated with a larger degree of confinement and with a lower level of losses than their metallic counterparts, with the additional advantage of being tunable through the modification of the Fermi energy.

Unfortunately, there exist no analytical theory to describe the plasmonic response of graphene nanostructures, and therefore, we are forced to rely on numerical approaches to analyze the properties of the graphene LSP. In our case, we employ a methodology based on rigorously solving Maxwell's equations using the BEM [7, 30]. Within this approach, graphene is modeled as a thin film of edges rounded by semicircular profiles and characterized by a dielectric function $1+4\pi i\sigma/\omega t$, where t is the film thickness and $\sigma(\omega)$ is the frequency-dependent surface conductivity. We normally use $t \sim 0.5\,\mathrm{nm}$, which is well converged with respect to the $t \to 0$ limit. But most importantly, we take $\sigma(\omega)$ from the local limit of the random-phase approximation (see next section) for extended graphene (*i.e.*, for zero parallel wave vector), which is available in analytical form in the literature [43, 44, 45], and we

reproduced it here for convenience:

$$\sigma(\omega) = \frac{2e^2T}{\pi\hbar}\frac{i}{\omega + i\tau^{-1}}\log\left[2\cosh(E_{\mathrm{F}}/2k_{\mathrm{B}}T)\right] + \frac{e^2}{4\hbar}\left[H(\omega/2) + \frac{4i\omega}{\pi}\int_0^\infty d\varepsilon\,\frac{H(\varepsilon) - H(\omega/2)}{\omega^2 - 4\varepsilon^2}\right], \tag{1.16}$$

where $H(\varepsilon) = \sinh(\hbar\varepsilon/k_{\mathrm{B}}T)/\left[\cosh(E_{\mathrm{F}}/k_{\mathrm{B}}T) + \cosh(\hbar\varepsilon/k_{\mathrm{B}}T)\right]$, and T is the temperature.

The first term in Eq. (1.16) corresponds to intra-band transitions, in which the relaxation time has been introduced to make it converge to the Drude model at $T = 0$. The second term stands for inter-band transitions and is assumed to be independent of τ. In general, we assume a relaxation time of $\tau = \mu E_{\mathrm{F}}/ev_{\mathrm{F}}^2$, where $\mu = 10,000\,\mathrm{cm}^2/(\mathrm{Vs})$ is the measured DC mobility [46]. This approach can describe accurately the plasmonic response of nanostructures with sizes down to $\approx 20\,\mathrm{nm}$, for which quantum confinement and edge effects are negligible. However, systems with smaller dimensions have to be studied using microscopic models capable of describing the dynamics of the electrons that constitute the surface plasmon (see next section).

1.2 Microscopic description of plasmonic materials: Random-phase approximation

Classical descriptions of the plasmonic response of nanostructures, based on solving Maxwell's equations using homogeneous dielectric functions, fail when the relevant dimensions of the nanostructure are comparable to the electron mean free path. In such cases, as we anticipated in previous sections, it is necessary to employ microscopic descriptions in which the plasmonic response of the system is built from the electronic wave functions. Among the different microscopic approaches that one can find in the literature, those based on the random-phase approximation (RPA) [47, 48] can be readily applied to low-dimensionality systems such as nanostructures created from graphene or noble metal monolayers.

Within linear response theory, the reaction of the electrons of a certain nano-

structure to an external perturbation can be characterized by the susceptibility χ [47, 48], which relates the induced charge density ρ^{ind} to the applied external potential Φ^{ext} as

$$\rho^{\text{ind}} = \chi \Phi^{\text{ext}}.$$

The susceptibility χ includes the effect of the interaction between the electrons of the system, and therefore, must be constructed using many-body wave functions. In practice, this is a hard task even for systems involving a small number of electrons. Instead of this, we choose to work with the non-interacting susceptibility χ_0, which is constructed from the single particle wave functions $\psi_i(\mathbf{r})$ as

$$\chi_0(\mathbf{r}, \mathbf{r}', \omega) = -2e \sum_{ij} (f_i - f_j) \frac{\psi_i(\mathbf{r}) \psi_i^*(\mathbf{r}') \psi_j^*(\mathbf{r}) \psi_j(\mathbf{r}')}{\hbar\omega - \varepsilon_i + \varepsilon_j + i\hbar/2\tau}, \tag{1.17}$$

where ε_i is the energy of state i, $\hbar\tau^{-1}$ is a phenomenological width that accounts for the finite lifetime of the electronic excitations, and

$$f_i = \frac{1}{e^{(\varepsilon_i - E_{\text{F}})/k_{\text{B}}T} + 1}$$

is the Fermi-Dirac distribution at a temperature T and a Fermi energy E_{F}. Using χ_0, the induced charge density is given by

$$\rho^{\text{ind}} = \chi_0 \Phi.$$

In this expression $\Phi = \Phi^{\text{ext}} + \Phi^{\text{ind}}$ is the total potential resulting from the sum of the external potential and the potential induced by the electrons. The latter can be written using the Coulomb interaction $v(\mathbf{r}, \mathbf{r}', \omega) = 1/|\mathbf{r} - \mathbf{r}'|^{-1}$ as

$$\Phi^{\text{ind}} = v\rho^{\text{ind}} = v\chi_0\Phi.$$

Combining the expressions given above, the total potential reads

$$\Phi = [1 - v\chi_0]^{-1} \Phi^{\text{ext}},$$

and therefore, the induced charge is finally given by

$$\rho^{\mathrm{ind}} = \chi_0 \left[1 - v\chi_0\right]^{-1} \Phi^{\mathrm{ext}}.$$

Once the induced charge is known, the induced dipole, and therefore, the absorption cross-section can be readily calculated.

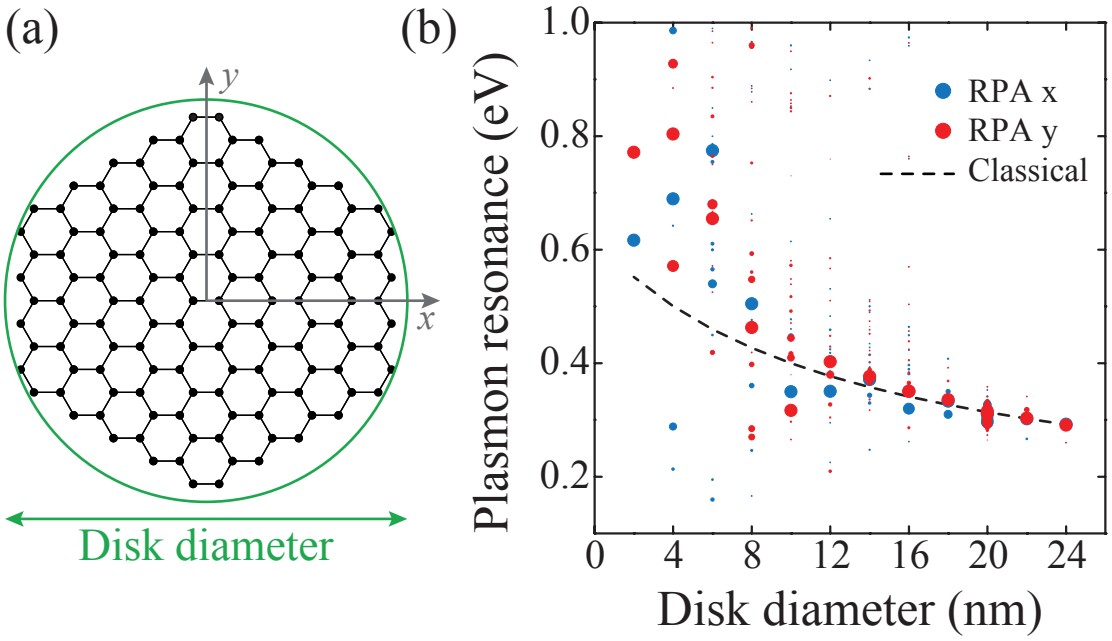

Figure 1.4: Microscopic description of plasmons in graphene nanodisks (adapted from Ref. [49]). (a) Real geometry of a graphene nanodisk obtained after eliminating the edge atoms connected by dangling bonds. (b) Spectral features in the extinction spectra (symbols) compared with the classical electromagnetic dipole plasmon energy (dashed curve) as a function of disk diameter. The symbol sizes are scaled with the strength of the spectral peaks. The Fermi energy is $E_{\mathrm{F}} = 0.4\,\mathrm{eV}$ in all cases.

The electronic wave functions and the corresponding energies needed to construct χ_0 [see Eq. (1.17)] are obtained from the diagonalization of the Hamiltonian describing the dynamics of the non-interacting electrons. In the particular case of graphene nanostructures, the optical response is dominated by excitations of the π valence band, formed by electrons residing in the carbon 2p orbitals oriented perpendicularly with respect to the local carbon bonds and populated on average

with one electron per carbon site. The σ band lies deeper in energy and only contributes with a nearly uniform background polarization. Excited states are formed when π electrons hop between neighboring sites, and thus, it is natural to study the π band within a tight-binding model, in which one-electron states are linear combinations of carbon 2p orbitals obtained, together with their associated energies, from the diagonalization of the corresponding tight-binding Hamiltonian [50, 43, 31].

As an illustrative example of the application of this methodology, we show in Fig. 1.4(b) (adapted from Ref. [49]) a summary of the plasmonic spectra of graphene nanodisks, obtained using the combination of the tight-binding Hamiltonian and the RPA methodology, and plotted as a function of disk diameter for polarizations either along x or y [see Fig. 1.4(a)]. The Fermi energy of the nanodisks is $E_{\mathrm{F}} = 0.4\,\mathrm{eV}$. For each value of the diameter, this plot contains several symbols indicating the different peaks that show up in the spectra. The size of each symbol is roughly proportional to the strength of the corresponding peak. As the diameter increases, we observe a clear trend of convergence of spectral features toward the plasmon predicted by the classical methodology explained at the end of Section 1.1.3. Interestingly, this convergence is nearly achieved for nanodisks with diameters above $\approx 20\,\mathrm{nm}$, for which, therefore, a classical description is valid. For smaller sizes, the strength of the plasmon is generally situated at larger energies (*i.e.*, it is blue-shifted) compared to the classical calculation [49].

1.3 Quantum electromagnetism

In Section 1.1 we have described light as an electromagnetic wave. Although this description explains correctly many of the physical phenomena happening at the nanoscale, it fails in situations in which light reveals its corpuscular behavior and, therefore, we are forced to talk about photons instead of electromagnetic waves. Typical examples of these situations are the spontaneous emission, the Lamb shift, the laser linewidth, or the Casimir effect [51, 52, 53]. In general, the corpuscular behavior of light becomes more important as the wavelength and the intensity decreases, or, in other words, as the number of photons involved in the problem becomes small. When this happens we need to employ a quantum description of

light, which involves the quantization of the electromagnetic field.

In general, the process of field quantization starts with an expansion of the field in a basis consisting of a complete set of functions (*e.g.*, plane waves). These functions or modes are interpreted as independent harmonic oscillators that can be quantized following the canonical procedure. As a result of this, the expansion coefficients are promoted from ordinary numbers to operators that create or annihilate a photon (*i.e.*, the quanta of the electromagnetic field) of a given mode. After this process, the quantized field reads [51, 53]

$$\hat{\mathbf{E}}(\mathbf{r}) = i \sum_{\mathbf{k}\varsigma} \sqrt{\frac{2\pi\hbar\omega_{\mathbf{k}}}{V}} \mathbf{e}_{\mathbf{k}\varsigma} \left[\hat{a}_{\mathbf{k}\varsigma} e^{i\mathbf{k}\cdot\mathbf{r}} - \hat{a}^{+}_{\mathbf{k}\varsigma} e^{-i\mathbf{k}\cdot\mathbf{r}} \right], \tag{1.18}$$

where the sum runs over the modes with wave vector $\mathbf{k}$ and polarization ς. In this expression, $\mathbf{e}_{\mathbf{k}\varsigma}$ is the polarization vector, $\omega_{\mathbf{k}}$ is the frequency, and V is the quantization volume. Furthermore, $\hat{a}^{+}_{\mathbf{k}\varsigma}$ ($\hat{a}_{\mathbf{k}\varsigma}$) is the creation (annihilation) operator of photons in the mode $\mathbf{k}\varsigma$. These operators must obey the commutation relations typical from bosonic operators [54, 52]

$$\left[\hat{a}_{\mathbf{k}\varsigma}, \hat{a}^{+}_{\mathbf{k}'\varsigma'} \right] = \hat{a}_{\mathbf{k}\varsigma} \hat{a}^{+}_{\mathbf{k}'\varsigma'} - \hat{a}^{+}_{\mathbf{k}'\varsigma'} \hat{a}_{\mathbf{k}\varsigma} = \delta\left(\mathbf{k} - \mathbf{k}'\right) \delta_{\varsigma\varsigma'}, \tag{1.19}$$

Furthermore, they act over the photon states as

$$\begin{aligned} \hat{a}_{\mathbf{k}\varsigma} \left| n_{\mathbf{k}\varsigma} \right\rangle &= \sqrt{n} \left| (n-1)_{\mathbf{k}\varsigma} \right\rangle, \\ \hat{a}^{+}_{\mathbf{k}\varsigma} \left| n_{\mathbf{k}\varsigma} \right\rangle &= \sqrt{n+1} \left| (n+1)_{\mathbf{k}\varsigma} \right\rangle, \end{aligned}$$

where $|n_{\mathbf{k}\varsigma}\rangle$ represents a state with n photons in the mode $\mathbf{k}\varsigma$.

The light Hamiltonian is also expressed in terms of the creation and annihilation operators

$$\hat{H} = \sum_{\mathbf{k}\varsigma} \hbar\omega_{\mathbf{k}} \left[\hat{a}^{+}_{\mathbf{k}\varsigma} \hat{a}_{\mathbf{k}\varsigma} + \frac{1}{2} \right].$$

The factor 1/2 in these expression accounts for the energy of the vacuum state $|0\rangle$, also known as zero-point energy. Although it may seem to be the contrary, this factor does not lead to any divergence because the energies are always measured

relative to vacuum. However, the vacuum state has real physical consequences. If we calculate the expected value of the field intensity for a certain state $|n_{\kappa\varsigma}\rangle$, we obtain

$$\langle n_{\kappa\varsigma}|\,\hat{\mathbf{E}}(\mathbf{r})\cdot\hat{\mathbf{E}}^{+}(\mathbf{r})\,|n_{\kappa\varsigma}\rangle = \frac{2\pi\hbar\omega_{\mathbf{k}}}{V}\mathbf{e}^{2}_{\mathbf{k}\varsigma}\left[\langle n_{\kappa\varsigma}|\,\hat{a}^{+}_{\mathbf{k}\varsigma}\hat{a}_{\mathbf{k}\varsigma}\,|n_{\kappa\varsigma}\rangle + \langle n_{\kappa\varsigma}|\,\hat{a}_{\mathbf{k}\varsigma}\hat{a}^{+}_{\mathbf{k}\varsigma}\,|n_{\kappa\varsigma}\rangle\right],$$

which particularized for the case of the vacuum state $|0_{\mathbf{k}\varsigma}\rangle$ results in the finite value

$$\langle 0_{\mathbf{k}\varsigma}|\,\hat{\mathbf{E}}(\mathbf{r})\cdot\hat{\mathbf{E}}^{+}(\mathbf{r})\,|0_{\mathbf{k}\varsigma}\rangle = \frac{2\pi\hbar\omega_{\mathbf{k}}}{V}\mathbf{e}^{2}_{\mathbf{k}\varsigma}.$$

This result does not have a classical analogue and, therefore, is at the origin of many of the phenomena that cannot be described within a classical electromagnetism framework such as the spontaneous emission, the Lamb shift, or the Casimir effect [52, 53].

Surface plasmons can also be quantized. In the case of SPPs, the quantization scheme is analogous to the photon quantization depicted above. The fundamental difference is that, now, the expansion of the field must be done using the eigenmodes of the metal-dielectric interface [55, 56]. On the other hand, the LSPs supported by a certain nanoparticle can be quantized directly by treating them as harmonic oscillators. By doing this, we can write the Hamiltonian of the quantized LSPs as

$$\hat{H} = \sum_{i}\hbar\omega_{i}\left[\hat{b}^{+}_{i}\hat{b}_{i} + \frac{1}{2}\right],$$

where $\hat{b}_i$ and $\hat{b}^{+}_{i}$ are the annihilation and creation operators for a LSP in the mode i that satisfy the commutation relations given in Eq. (1.19). In the same way, we can write the particle dipole operator as

$$\hat{\mathbf{p}}_{\mathrm{pl}} = \sum_{i}\mathbf{p}_{\mathrm{pl},i}\left[\hat{b}_{i} + \hat{b}^{+}_{i}\right], \tag{1.20}$$

where, $\mathbf{p}_{\mathrm{pl},i}$ is the dipole moment associated with the LSP of mode i.

In many of the physical systems studied in this thesis, plasmons and photons interact with quantum emitters such as atoms, molecules, or quantum dots. Here, we describe those systems as composed of two levels ($|\uparrow\rangle$ and $|\downarrow\rangle$) separated by a certain

energy ε_0. Furthermore, we consider that these levels cannot be doubly populated, which is equivalent to assuming a fermionic behavior. With these assumptions, the dynamics of a quantum emitter can be described using creation $\hat{c}^+$ and annihilation $\hat{c}$ operators that satisfy anticommutation relations

$$\left[\hat{c}, \hat{c}^+\right] = \hat{c}\hat{c}^+ + \hat{c}^+\hat{c} = 1.$$

The action of these operators over the states of the emitter is $\hat{c}^+ |\downarrow\rangle = |\uparrow\rangle$ and $\hat{c} |\uparrow\rangle = |\downarrow\rangle$, while $\hat{c} |\downarrow\rangle = \hat{c}^+ |\uparrow\rangle = 0$. Therefore, the Hamiltonian of the quantum emitter can be written as $\hat{H} = \varepsilon_0 \hat{c}^+\hat{c}$, while its dipole operator reads $\hat{\mathbf{p}}_{\text{qe}} = \mathbf{p}_{\text{qe}} [\hat{c} + \hat{c}^+]$, where $\mathbf{p}_{\text{qe}}$ is the dipole moment associated with the quantum emitter transition.

1.3.1 Interacting systems

Within the dipolar approximation, the interaction between photons, plasmons, and emitters can be described using the direct coupling Hamiltonian [53]

$$\hat{H}_{\text{int}} = -\hat{\mathbf{p}} \cdot \hat{\mathbf{E}}. \tag{1.21}$$

where $\hat{\mathbf{p}}$ and $\hat{\mathbf{E}}$ are the dipole and the electric field operators, respectively. It can be proved that this Hamiltonian leads to identical predictions for observable quantities as the minimal coupling Hamiltonian $\propto \hat{\mathbf{P}} \cdot \hat{\mathbf{A}}$, where $\hat{\mathbf{P}}$ is the canonical momentum and $\hat{\mathbf{A}}$ the vector potential [57].

Usually, we are interested in analyzing the changes in the physical properties of a system, composed of plasmons, emitters, and photons, induced by the interaction Hamiltonian $\hat{H}_{\text{int}}$. As long as this interaction can be treated as a perturbation of the total Hamiltonian, we can study the dynamics of the system through the calculation of the transition rates between the different unperturbed states of the system. These transition rates are naturally obtained using Fermi's golden rule [54]

$$P_{|f\rangle \leftarrow |i\rangle} = \frac{2\pi}{\hbar} \left| \langle f | \hat{H}_{\text{int}} | i \rangle \right|^2 \delta\left(\varepsilon_f - \varepsilon_i\right). \tag{1.22}$$

In this expression, $|i\rangle$ and $|f\rangle$ are the initial and the final states with energies ε_i

and ε_f, respectively. The delta function guarantees the conservation of energy in the process.

In the particular case in which our objective is to study the absorption spectrum of the system, there exist an alternative method based on Zubarev's Green functions [58]. This method has been successfully applied to different problems in statistical physics and linear response theory [59, 60, 61], and can be adapted to study the optical absorption properties of plasmonic systems interacting with quantum emitters. The idea is to compute the absorption spectra from the retarded Zubarev Green function of the quantum operators that mediate the photon absorption process. The time-domain Green function of two of these operators contains the information on the evolution of the quantum process that they represent, and its Fourier transform is therefore directly related to the absorption spectrum.

The retarded Zubarev Green function of two operators $\hat{R}$ and $\hat{S}$ is defined in the frequency domain as [5]

$$\langle\langle \hat{R}; \hat{S} \rangle\rangle_{\omega+i0^+} = -\frac{i}{\hbar}\int_{-\infty}^{\infty} dt e^{i(\omega+i0^+)t}\theta(t)\left\langle \left[\hat{R}(t), \hat{S}(0)\right]_\eta \right\rangle, \tag{1.23}$$

where $\hat{R}(t)$ is the Heisenberg representation [54] of operator $\hat{R}$, $\theta(t)$ is the Heaviside step function, and the brackets $[\hat{R}, \hat{S}]_\eta = \hat{R}\hat{S} - \eta\hat{S}\hat{R}$ stand for the commutator of bosonic operators ($\eta = 1$) or the anticommutator of fermionic operators ($\eta = -1$).

The absorption spectrum is then related to the retarded Zubarev Green function as

$$\sigma(\omega) \propto -\mathrm{Im}\left\{\langle\langle \hat{R}; \hat{R}^+ \rangle\rangle_{\omega+i0^+}\right\}, \tag{1.24}$$

(a derivation of this expression is given in Appendix A), where $\hat{R}$ ($\hat{R}^+$) is the annihilation (creation) operator of an excitation in the system resulting from the emission (absorption) of one photon. This type of Green function is commonly calculated by writing its equation of motion (see Appendix A)

$$\hbar\omega\langle\langle \hat{R}; \hat{R}^+ \rangle\rangle = \left\langle \left[\hat{R}, \hat{R}^+\right]_\eta \right\rangle + \langle\langle \left[\hat{R}, \hat{H}\right]; \hat{R}^+ \rangle\rangle, \tag{1.25}$$

[5] Notice that an infinitesimally small positive imaginary part is added to the frequency in order to ensure the convergence of the integral.

which depends on another Green function $\langle\langle\left[\hat{R},\hat{H}\right];\hat{R}^{+}\rangle\rangle$. Here, $\hat{H}$ is the total Hamiltonian of the system. In a similar way, the new Green function can be also calculated by writing down its equation of motion. Iterating this process, one obtains a hierarchy of equations that needs to be truncated at some point by applying a physical approximation. After doing that, we end up with a linear system of equations, from which $\langle\langle\hat{R};\hat{R}^{+}\rangle\rangle$, and therefore, the absorption spectrum, can be obtained.

1.3.2 Dissipative systems

Dissipation is at the origin of the finite lifetime of the excited states of real systems. From a physical point of view, every dissipation channel emerges from the interaction between the system and a continuum of modes that acts as a reservoir, breaking the reversibility of the system dynamics. As a result of this coupling, the excited states acquire a finite width, associated with a finite decay rate, whose inverse determines the finite lifetime. For instance, the radiative decay of the excited state of a quantum emitter is determined by the coupling with the continuum of radiative modes

$$\Gamma=\frac{2\pi}{\hbar}\sum_{\varsigma}\frac{V}{8\pi^{3}}\int d\mathbf{k}\left|\langle\downarrow|\langle 1_{\mathbf{k}\varsigma}|\,\hat{H}_{\mathrm{int}}\,|0\rangle\,|\uparrow\rangle\right|^{2}\delta\left(\varepsilon_{0}-\hbar\omega_{\mathbf{k}\varsigma}\right). \tag{1.26}$$

In this expression, ε_0 is the quantum emitter energy, and we have integrated over the continuum of photonic final states.

Within the method of Zubarev's Green functions, dissipation can be taken into account in a phenomenological way by introducing a coupling to the appropriate continuum of modes (see Section 3.2.1). However, the standard approach to treat dissipation involves the study of the density operator $\hat{\rho}$ [54, 62, 63], which contains all information about the quantum state of the system, and is defined as

$$\hat{\rho}=\sum_{ij}\rho_{ij}\,|i\rangle\,\langle j|\,.$$

Here, the diagonal matrix elements ρ_{ii} represent the probability of finding the system in state i, while the off-diagonal elements (*i.e.*, ρ_{ij} with $i\neq j$), called coherences, are related to the cross-probability between states i and j. The density operator

can describe both pure and mixed states, which are statistical ensembles of several quantum states. Furthermore, it can be used to evaluate the expected value of any operator $\hat{R}$ through the expression $\left\langle \hat{R} \right\rangle = \mathrm{Tr}\left\{ \hat{\rho}\hat{R} \right\}$, where Tr stands for the trace over all the states of the system.

The evolution of the density operator is governed by the master equation [62]

$$\frac{\partial \hat{\rho}}{\partial t} = -\frac{i}{\hbar}\left[\hat{H}, \hat{\rho}\right] + \sum_i \mathcal{L}_i\left(\hat{\rho}\right). \tag{1.27}$$

In this expression $\mathcal{L}_i\left(\hat{\rho}\right)$ is the Lindblad superoperator

$$\mathcal{L}_i\left(\hat{\rho}\right) = \frac{\Gamma_i}{2}\left[2\hat{s}_i\hat{\rho}\hat{s}_i^{+} - \hat{\rho}\hat{s}_i^{+}\hat{s}_i - \hat{s}_i^{+}\hat{s}_i\hat{\rho}\right], \tag{1.28}$$

that describes the dissipation through channel i. Here, $\hat{s}$, and $\hat{s}^{+}$ are the system operators associated with the decay process, and Γ_i the corresponding decay rate. For instance, in the case of the radiative dissipation of the excited state of a quantum emitter $\hat{s} = \hat{c}$, $\hat{s}^{+} = \hat{c}^{+}$ (*i.e.*, the annihilation and creation operators of the emitter excited state), while Γ_i is the radiative decay rate given in Eq. (1.26).

The derivation of the master equation involves the Born-Markov approximation [62] and assumes a weak coupling between the system and the reservoir, which is treated within second order perturbation theory.

1.4 Fluctuation and dissipation

Classical mechanics predicts a finite kinetic energy for a particle at finite temperature. Something similar happens with the charges existing inside of a material, which due to the finite temperature, undergo a thermal motion that generates fluctuating currents. Interestingly, these fluctuations do not disappear in the limit of zero temperature. On the contrary, as we have seen before, quantum mechanics predicts zero-point fluctuations associated with the uncertainty principle.

In the case of small objects, such as nanoparticles, the fluctuating currents result in a fluctuating dipole. The latter generates fluctuating fields that lead to dissipation via radiation, and that interact with the fluctuating dipoles of other nanoparticles. This results in a transfer of energy and momentum that can produce cooling or

heating of the object, and that generate forces, as it happens in the Casimir and the van der Waals interactions [64]. These phenomena are usually analyzed within the framework of fluctuation electrodynamics [65]. In this context, the fluctuation-dissipation theorem (FDT) allows us to relate the fluctuations of a certain magnitude to the dissipation associated with it. This theorem was first formulated by Nyquist to account for the voltage fluctuations associated with a resistor [66], and later proved by Callen and Welton [67]. In the particular case of the fluctuations of a particle dipole, the FDT reads

$$\left\langle p_i^{\mathrm{fl}}(\omega) p_j^{\mathrm{fl}}(\omega') \right\rangle = 4\pi\hbar \left[n(\omega, T) + \frac{1}{2} \right] \mathrm{Im}\left\{ \alpha_{ij}(\omega) \right\} \delta(\omega + \omega'), \tag{1.29}$$

where the indices i, j stand for the cartesian components, α_{ij} is the ij component of the particle polarizability tensor, and

$$n(\omega, T) = \frac{1}{e^{\hbar\omega/k_{\mathrm{B}}T} - 1},$$

is the Bose-Einstein distribution function for a temperature T. This factor accounts for the fluctuations of thermal origin, while the $1/2$ factor is responsible for the zero-point fluctuations (*i.e.*, the fluctuations of quantum origin). Therefore, Eq. (1.29) relates the fluctuations of the particle dipole to its dissipation expressed through the imaginary part of the polarizability, which is simply proportional to the particle absorption [see Eq. (1.13)]. A similar relation can be written for the field fluctuations

$$\left\langle E_i^{\mathrm{fl}}(\mathbf{r}, \omega) E_j^{\mathrm{fl}}(\mathbf{r}', \omega') \right\rangle = 4\pi\hbar \left[n(\omega, T) + \frac{1}{2} \right] \mathrm{Im}\left\{ \mathcal{G}_{ij}(\mathbf{r}, \mathbf{r}', \omega) \right\} \delta(\omega + \omega'). \tag{1.30}$$

Here, $\mathcal{G}_{ij}(\mathbf{r}, \mathbf{r}', \omega)$ represents the electromagnetic Green tensor, which for vacuum is given by

$$\mathcal{G}_{ij}(\mathbf{r}, \mathbf{r}', \omega) = \frac{\exp(ikR)}{R^3} \left[(k^2R^2 + ikR - 1)\, \delta_{ij} - (k^2R^2 + 3ikR - 3)\, \frac{R_i R_j}{R^2} \right], \tag{1.31}$$

with $\mathbf{R} = \mathbf{r} - \mathbf{r}'$. The derivation of the two expressions of the FDT presented here can be found in Appendix B.

As an example of application of the FDT, we can derive the net power interchanged by a nanoparticle and the environment. We choose a spherical particle

placed at $\mathbf{r}_0$, with a temperature T_1, and surrounded by vacuum at temperature T_0. Furthermore, the particle is assumed to be small enough to be described by three equal dipoles directed along the three cartesian axes. Under these conditions the net power radiated by the particle can be written as [18]

$$\begin{aligned}\mathcal{P} = & -\left\langle \mathbf{E}^{\mathrm{ind}}(\mathbf{r}_0,t)\cdot\frac{\partial \mathbf{p}^{\mathrm{fl}}(t)}{\partial t} + \mathbf{E}^{\mathrm{fl}}(\mathbf{r}_0,t)\cdot\frac{\partial \mathbf{p}^{\mathrm{ind}}(t)}{\partial t}\right\rangle \\ = & \sum_{ij}\int_{-\infty}^{\infty}\frac{d\omega d\omega'}{4\pi^2}e^{-i(\omega+\omega')t}i\omega \\ & \times\left\langle p_i^{\mathrm{fl}}(\omega)\mathcal{G}_{ij}(\mathbf{r}_0,\mathbf{r}_0,\omega')p_j^{\mathrm{fl}}(\omega') + E_i^{\mathrm{fl}}(\mathbf{r}_0,\omega')\alpha_{ij}(\omega)E_j^{\mathrm{fl}}(\mathbf{r}_0,\omega)\right\rangle,\end{aligned}$$

where we have written the induced dipole as $p_i^{\mathrm{ind}}(\omega) = \sum_j \alpha_{ij}(\omega)E_j^{\mathrm{fl}}(\mathbf{r}_0,\omega)$, and the induced field as $E_i^{\mathrm{ind}}(\mathbf{r},\omega) = \sum_j \mathcal{G}_{ij}(\mathbf{r},\mathbf{r}_0,\omega)p_j^{\mathrm{fl}}(\omega)$. Using Eqs. (1.29) and (1.30) in the expression above, and taking into account that $\lim_{\mathbf{r}\to\mathbf{r}'}\mathrm{Im}\left\{\mathcal{G}_{ij}(\mathbf{r},\mathbf{r}',\omega)\right\} = 2k^3/3\delta_{ij}$ (see Appendix B) we obtain

$$\mathcal{P} = \frac{4\hbar}{\pi c^3}\int_0^{\infty} d\omega\omega^4 \mathrm{Im}\left\{\alpha(\omega)\right\}\left[n(\omega,T_1) - n(\omega,T_0)\right].$$

Therefore, the net radiated power depends on the absorption of the particle, as well as on the temperature difference through the Bose-Einstein distribution functions $n(\omega,T_1) - n(\omega,T_0)$, and as expected, it vanishes when $T_0 = T_1$.

Chapter 2

Plasmonic waveguides

2.1 Introduction

From its beginning, computer industry has devoted strong efforts to develop smaller and faster devices. In the last years, the semiconductor technology has undergone an impressive trend in scaling electronic devices down to nanoscale dimensions, but still with operational frequencies that cannot reach values beyond gigahertzs. On the other hand, the advance of photonic technologies has enabled the development of devices based on dielectric materials that can manipulate signals at optical frequencies with an enormous bandwidth, but whose smallest size is determined by the diffraction limit. In this context, plasmonic devices emerge as a plausible candidate to fill the gap existing between the semiconductor and the photonic technologies [16].

As shown in Section 1.1.1, surface plasmons can propagate along millimeters in metal-dielectric interfaces at visible and near-IR frequencies [68, 69, 70]. These excitations are, however, confined to the interface and penetrate inside the metal only a few tens of nanometers [18]. In the case of planar geometries, plasmons extend towards the dielectric over a significant fraction of a micron at visible and near-IR frequencies, but this spreading can be limited by conveniently shaping the interface, so that the overall extension of the mode in the plane perpendicular to the propagation direction is reduced to just a few tens of nanometers in average radius. These properties make surface plasmons very attractive as carriers of information

that can be highly packed in space, thus enabling the development of devices that combine the working frequencies and bandwidths of photonic devices with the subwavelength dimensions of semiconductor devices [16, 71].

Several designs of plasmon interconnects have been prototyped in recent years, including metallic waveguides of finite cross-section in symmetric [69, 72] and asymmetric [70] environments, channels [73] and ridges [74] patterned into flat surfaces, gaps between metals [75], plasmon-band-gap structures based upon periodic corrugations [76], and plasmon hopping in arrays of nanoparticles [77, 78]. A hybrid system consisting of a dielectric wire positioned close to a silver planar surface has been also studied, providing large optical confinement and long propagation length, but with the inherent limitation of being constraint to two dimensional designs [79].

As discussed above, plasmon waveguides are advantageous over their dielectric counterparts because the metal skin depth makes them highly compact [69, 70]. This generates large light intensity concentration, which allows non-linear optics [80] and sensing [8] applications. Plasmon modes can be tuned in frequency, and their spatial distribution molded, by tailoring the geometry of metallic structures on the nanometer scale, either using direct lithographic methods [81] or chemical synthesis [82]. In particular, extreme plasmon confinement has been achieved in narrow insulator films buried inside metal [83]. Actually, buried structures provide a natural but technologically challenging approach to compact integration. In contrast, open plasmonic geometries involve electromagnetic fields extending significantly away from the metal, [69, 70, 73, 76, 77, 78] and consequently producing a substantial degree of cross-talk between neighboring waveguides [84].

In this chapter, we propose and characterize a new type of plasmonic waveguides based upon pairs of parallel metallic nanowires. These structures are shown to provide a versatile and tunable platform for highly-integrated plasmon interconnects. In the first part of this chapter, we focus on studying the guiding properties of these structures. We find that the propagation length and degree of confinement of the plasmon guided modes depend strongly on the separation between wires. Individual wire modes are recovered at large separations, while mode hybridization is observed when the spacing is reduced. As a result of this hybridization, gap modes are observed at small wire separations, highly localized in the regions between two adjacent wires. These modes present an excellent balance between the degree of

confinement and the propagation length, which is shown to depend critically on geometrical shape and separation. Furthermore, the proposed guiding mechanism is demonstrated to be tolerant to asymmetry in wire pairs and sharp turns of subwavelength radius.

The second part of the chapter is devoted to explore the hybridization of gap plasmons in structures involving more that two aligned metal wires. In particular, we study the interaction between the gap modes of two neighboring wire pairs as a function of the spacing between them. The interaction of gap modes in a system formed by three wires is also investigated. We conclude with a proposal for a gap-mode coupler consisting of an intermediate rectangular wire that can produce large transfer of the gap mode from a given wire pair to a neighboring one. This completes the characterization of the basic elements needed to built a three dimensional plasmonic circuit.

2.2 Guiding with gap plasmons

The spatial behavior of the localized plasmons sustained by our structures can be conveniently characterized using the photonic local density of states (LDOS), defined by analogy to its electronic counterpart as the combined local intensity of all eigenmodes of the system under investigation. This magnitude takes the value $\omega^2\sqrt{\varepsilon}/3\pi^2c^3$ in a homogeneous medium of permittivity ε when projected along any spatial direction [1]. Here, we decompose this quantity into the contribution of different wave vectors $k_\parallel$ along the direction of translational symmetry z. For example, in a homogeneous medium, the $k_\parallel$-resolved LDOS projected along z reduces to $(\omega/2\pi c^2)(1-k_\parallel^2/\varepsilon k^2)\theta(\sqrt{\varepsilon}k-k_\parallel)$ [85]. The LDOS is proportional to the radiative decay rate of excited atoms [86], and therefore can be obtained from the imaginary part of the self-induced electric field acting back on a dipole, which in turn we calculate by solving Maxwell's equations with the BEM [29, 30]. We obtain the dispersion relation of the structures under study by examining the $k_\parallel$-resolved density of states (DOS), which is the integral of the LDOS over the $x-y$ directions. This magnitude is also derived from the solution of Maxwell's equations for an arbitrary number of circular wires using two-dimensional multiple elastic scattering of multipole expansions of the field around the cylinders [87].

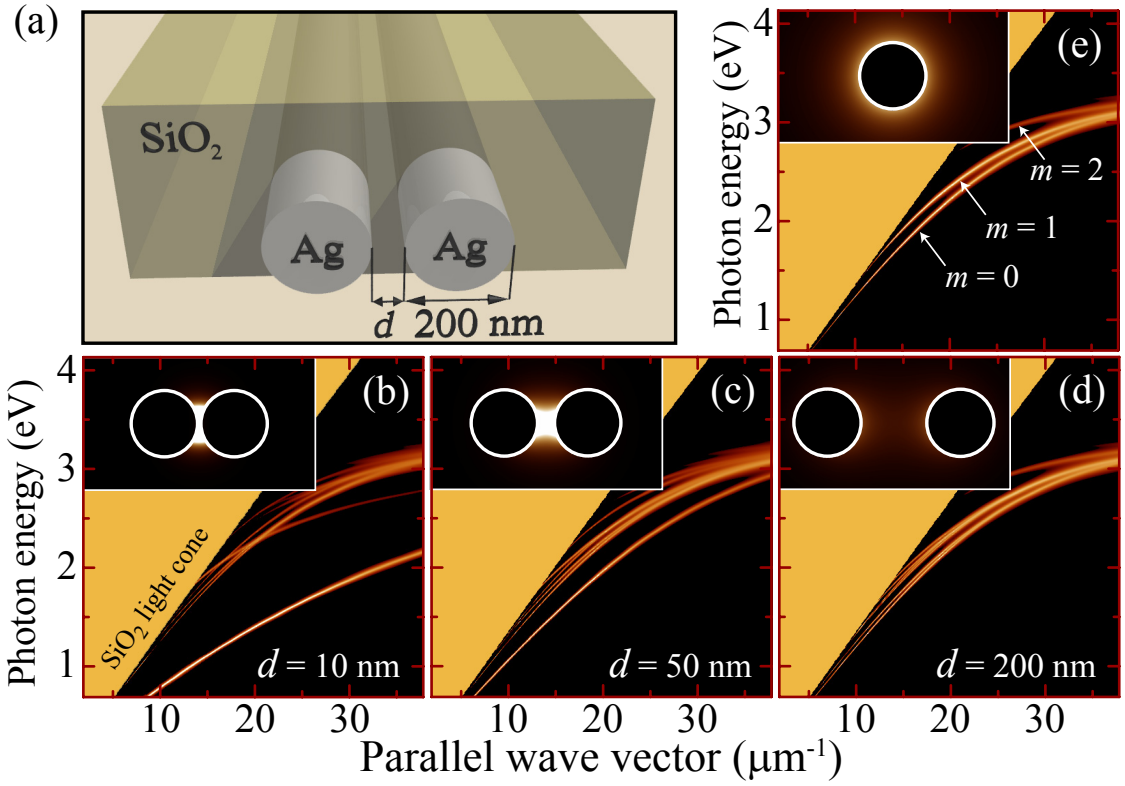

Figure 2.1: Gap plasmon modes of two parallel silver nanowires in silica. (a) Schematic view of the geometry. (b)-(d) Photonic density of states (DOS) as a function of energy and wave vector parallel to the wires for various wire pair separations d. (e) Same as (b)-(d) for the case of a single wire. The insets show the spatial distribution of the local density of states (LDOS) for the lowest-energy gap mode at a free-space light wavelength of 1550 nm. Brighter regions correspond to higher DOS and LDOS. The maximum LDOS in the inset of (b) is $\sim$ 15000 times the vacuum value.

We start by considering a wire pair formed by two 200-nm circular silver wires embedded in silica, as shown in Fig. 2.1(a). The dielectric functions of silver [23] and silica [88] have been taken from optical data. The contour plots of Fig. 2.1(b)-(d) show the DOS resolved in contributions of different wave vector $k_{\|}$ parallel to the wires for various separations between wire surfaces (d). A strongly bound mode is observed at small wire separations [Fig. 2.1(b)], with $k_{\|}$ well above $\sqrt{\varepsilon}k$, the wave vector of light in the host silica. The spatial extension of this gap mode is limited to the inter-wire region (see inset), and thus, it is expected to interact very weakly with other structures sitting in the vicinity of the wires but far from the gap. This mode evolves continuously for increasing inter-wire distance to become a hybridized monopole-monopole mode of induced-charge pattern $(+)\cdots(-)$ aligned with the wires axis [Figs. 2.1(c)-(d)]. This is in contrast to the $(+-)\cdots(+-)$ dipole-dipole plasmon in particle dimers [89], which is the lowest-energy mode according to plasmon chemistry arguments [90]. In this sense, wires are distinctly different from particles because charge neutrality is guaranteed by oscillations along the rods for finite $k_{\|}$, thus making two-dimensional monopoles possible. At sufficiently large distance, single-wire plasmons of $m = 0$ azimuthal symmetry are recovered as we observe by comparing Fig. 2.1(d) and Fig. 2.1(e). As expected, the dispersion relation of a single wire agrees with the analytical result derived elsewhere [91].

The degree of plasmon localization increases with decreasing gap distance d. This is reflected in a reduction of the phase velocity $v_{\rm phase} = c_{\rm h}\sqrt{\varepsilon}k/k_{\|}$ relative to the speed of light in silica, $c_{\rm h}$, as shown in Fig. 2.2(a). The group velocity (no shown) is also reduced, so that gap modes become considerably slower than light in silica. The propagation length is strongly-dependent on inter-wire distance [Fig. 2.2(b)]: the large confinement observed at small separations increases the relative weight of the electric field intensity inside the metal, where Ohmic losses are produced in proportion to that intensity within linear response, thus reducing the propagation length. This is a reflection of the tradeoff between confinement and propagation length intrinsic to any plasmon waveguide (see Section 1.1.1). Nevertheless, the gap mode involves electric field polarization mainly perpendicular to the wire surfaces near the gap, where light energy is concentrated, and this is beneficial to obtain longer propagation lengths because the normal electric field inside the metal is reduced by its large dielectric function to fulfill the continuity of

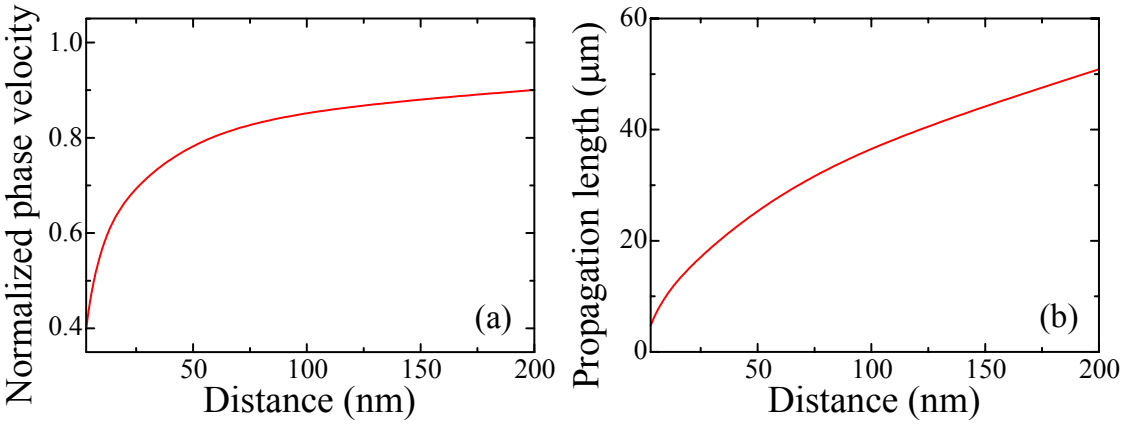

Figure 2.2: (a) Phase velocity of gap plasmon modes in silver wire pairs as a function of separation d for fixed wavelength $\lambda = 1550$ nm. (b) Propagation length L under the same conditions as in (a), obtained from $L = 1/2\mathrm{Im}\{k_\parallel\}$, where $\mathrm{Im}\{k_\parallel\}$ corresponds to the HWHM of the $k_\parallel$-dependent DOS.

the normal electric displacement. This gives rise to propagation lengths of the order of tens of microns for separations of tens of nanometers, accompanied by relatively large mode confinement.

We find it convenient to define a figure of merit F for the waveguides expressed as the ratio between the propagation length and the geometric mean of the mode diameter in the transverse directions. The quantities F^2 and F^3 should be roughly proportional to the number of logical elements that can be integrated using a given waveguiding scheme with two and three dimensional packing, respectively. We obtain $F \approx 540$ for the wire pair at a separation of 10 nm. This has to be compared with values of $F \lesssim 50$ for channel plasmon polaritons [73] and particle arrays [78], and $F \approx 100$ at 1550 nm in ridge structures [74]. High values of $F \approx 500$ can also be achieved with dielectric wires near silver [79], specifically designed for planar structures. We conclude that the wire arrays here proposed yield high values of $F \approx 540$, also improved with respect to those obtained for single wires (*e.g.*, $F \approx 100$ at 100 nm radius and 1550 nm wavelength), compatible with high integration of plasmonic circuits. The decrease in propagation length is the price to pay for plasmon confinement, but wire arrays seem to perform optimally with respect to the figure of merit F.

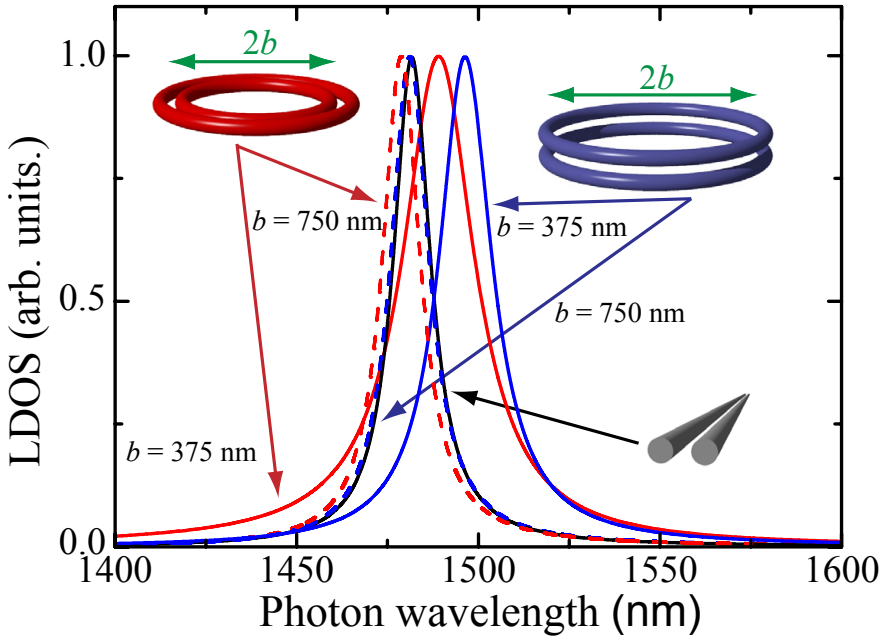

Figure 2.3: Gap mode in co-planar and co-axial bi-tori compared with a straight-wire pair for a gap distance $d = 10\,\mathrm{nm}$. Partial contributions to the LDOS are shown as a function of wavelength for a point in the center of the gap, both at fixed azimuthal number in tori ($m = 8$ for radius $b = 750\,\mathrm{nm}$ and $m = 4$ for $b = 375\,\mathrm{nm}$) and at fixed parallel wave vector in the straight-wire pair ($k_\parallel \approx 10.7\,\mu\mathrm{m}^{-1}$, such that $k_\parallel = m/b$). The curves are normalized to their maximum value.

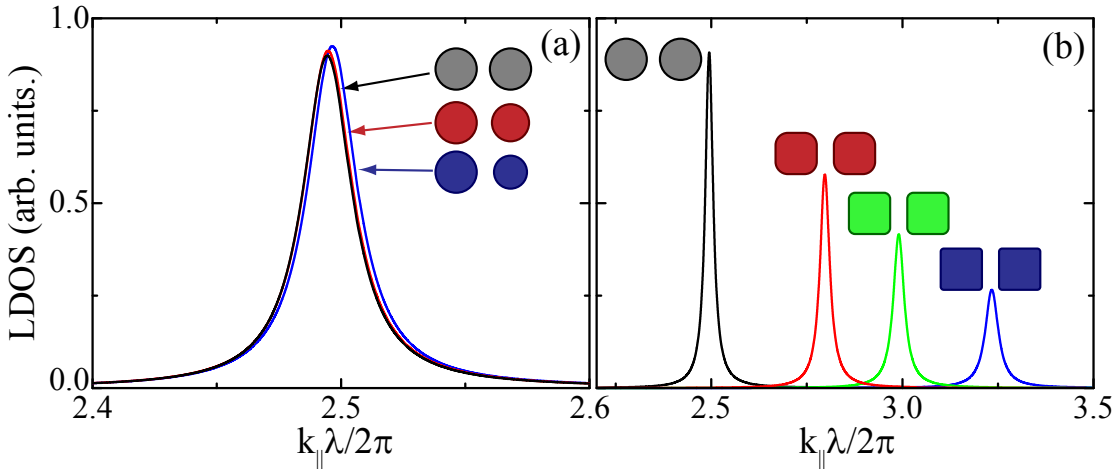

Figure 2.4: Gap mode against variations of wire radius (a) and shape (from circular to square cross-section) (b). The LDOS is represented as a function of $k_{\|}$ for a point at the center of each wire pair and a wavelength $\lambda = 1550\,\text{nm}$. One of the wires in the pairs of (a) has a fixed radius of 100 nm, while various values of the radius are considered for the neighboring wire: 100 nm, 90 nm, and 80 nm, from top to bottom. The distance between wires is $d = 10\,\text{nm}$ in all cases. The horizontal diameter of the wires in (b) is 200 nm for all cross-sections.

Reliable plasmon waveguides must be robust against fabrication imperfections and sharp turns. Next, we show that gap waveguides satisfy these requirements. In particular, curved waveguide paths produce radiative losses originating in coupling to propagating light waves when translational invariance is broken. We analyze this effect in Fig. 2.3 both for non-identical co-planar tori and for identical co-axial tori, using the prescription $k_{\|} = m/b$ to compare with straight waveguide modes, where b is the toroidal radius (see insets) and m is the azimuthal momentum number. The calculations are performed using the BEM, specialized for axially-symmetric geometries [29, 30]. Radiative losses are still small compared to absorption for $b = 750\,\text{nm}$ (*cf.* curves for straight wires and large-radius tori in Fig. 2.3, showing only $\sim 3\%$ increase in peak width of curved versus straight wires due to radiative losses in the former), but they become sizable for shaper turns (the width increases by 42% and 95% for $b = 375\,\text{nm}$ in co-axial and co-planar torii, respectively).

Guided gap plasmons are also robust against wire pair asymmetries, as shown in Fig. 2.4(a) for fixed wavelength $\lambda = 1550\,\text{nm}$ and gap distance $d = 10\,\text{nm}$. Variations

of up to 20% in the relative radius of neighboring wires produce just a small, tolerable shift in $k_{\|}$. However, wire shape is a critical parameter, which we study in Fig. 2.4(b) through the transition from circular to square cross-section. This produces a shift of the gap plasmon towards larger $k_{\|}$, consistent with the higher degree of confinement that occurs when evolving from the line-like contact of the circular wires to the planar waveguide defined by the square wires, the guided modes of which have been the subject of recent experimental investigation [83]. This increase in confinement is accompanied by peak broadening originating in larger overlap of the gap mode with the metal (Ohmic losses). Finally, although the observed sensitivity to the shape and the separation of the wires provides a large degree of tunability to the system, it also imposes severe limits to the precision required in the fabrication of the arrays in order to maintain a homogenous mode wavelength along the waveguide.

2.3 Coupling between gap plasmons

The wire pair that we have studied in the previous section constitutes the basic element defining a gap plasmon [see Fig. 2.5(a)]. The dispersion relation of this system is reproduced in Fig. 2.5(c) for a separation of $d = 10$ nm. For this small separation, the gap mode lies far apart from the light line, which is coherent with its large degree of confinement [see the inset of Fig. 2.5(c)]. Gap modes supported by two different wire pairs can interact. The simplest system in which this interaction can be observed consists in two wire pairs placed at a distance b, as depicted in Fig. 2.5(b). We investigate this system in Fig. 2.6. At large distances, the interaction between gap modes is weak and results in a small energy splitting that increases as b becomes smaller [see Fig. 2.6(a)]. This is accompanied by a significant redshift in two of the higher-energy modes. Eventually the splitting of the two gap modes decreases with decreasing b, presumably as a result of mode repulsion triggered by the approaching higher-energy modes, at there is even a non-avoided mode crossing, which is clearly resolved in the zoomed inset of Fig. 2.6(a).

It is surprising to see that gap modes undergo such a non-avoided crossing, since it is clear that they interact with each other even at relatively large distances within the range considered in Fig. 2.6. That is, their interaction is allowed by symmetry, but they still cross each other. The reason for this is that the interaction

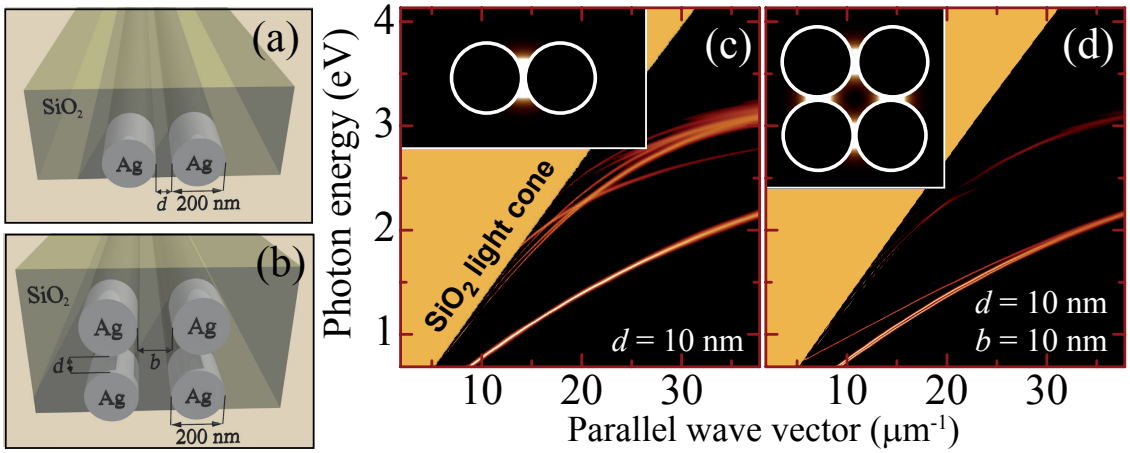

Figure 2.5: Gap plasmon modes for one and two wire pairs. (a),(b) Schematic view of the geometry. (c),(d) Photonic density of states (DOS) as a function of energy and wave vector parallel to the wires for one and two wire pairs. The inter-wire gap distance is $d = 10\,\text{nm}$ in both cases and the distance b between the two wire pairs in (d) is 10 nm. The insets show the spatial distribution of the local density of states (LDOS) for the lowest-energy gap mode at a free-space light wavelength of 1550 nm.

becomes zero exactly at the point of crossing, thus averting the typical avoided-crossing behavior described in quantum chemistry textbooks [92]. This is actually a feature associated with the interaction between line dipoles in two dimensions. Unlike the interaction between point dipoles, which is described in free space by the non-vanishing complex dipole field, line dipoles can have vanishing interaction. This is illustrated by the electric field created under the conditions of Fig. 2.7, where we represent the field due to a line dipole of the form $e^{ik_\parallel z}\hat{\mathbf{y}}$, placed in a homogeneous medium of permittivity ε and with the line oriented along z. The electric field at points along the x axis takes the form

$$\mathbf{E}(R\hat{\mathbf{x}}) = 2\left[k^2 K_0(\Gamma R) - \frac{\Gamma}{\varepsilon R} K_1(\Gamma R)\right] e^{ik_\parallel z}\hat{\mathbf{y}}, \tag{2.1}$$

where Γ is defined as $\Gamma = \sqrt{k_\parallel^2 - \varepsilon k^2}$, and K_0 and K_1 are modified Bessel functions of the second kind. The interaction is thus real for wave vectors outside the light cone of the medium (*i.e.*, $k_\parallel > \sqrt{\varepsilon}k$), except for a trivial plane wave dependence on z, and it contains a node at a distance $R = 306\,\text{nm}$ from the z axis for a wavelength

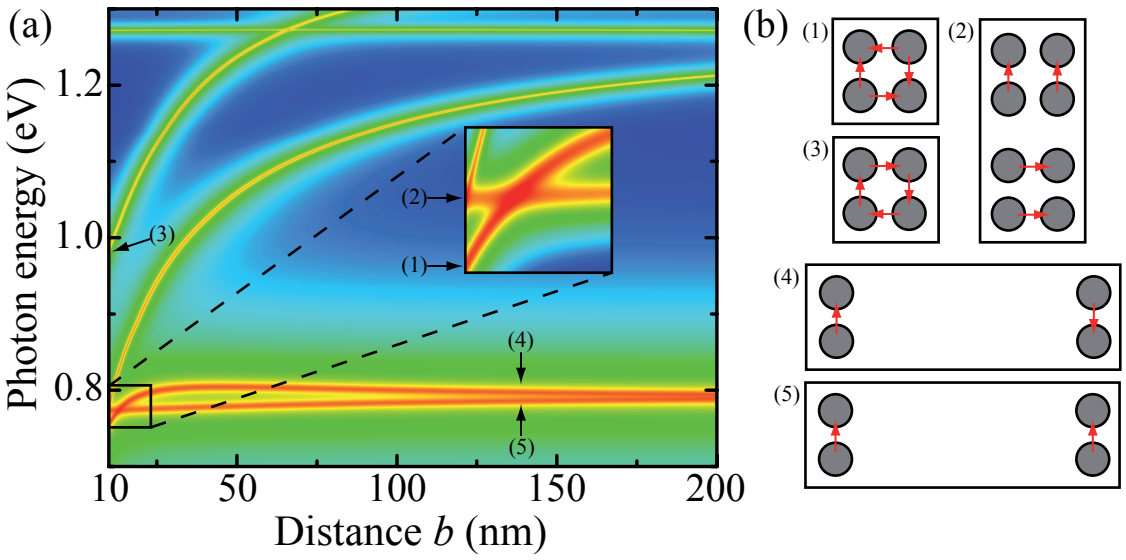

Figure 2.6: (a) Evolution of the modes in two wire pairs as a function of the distance between them for fixed $k_{\parallel} = 10\,\mu\mathrm{m}^{-1}$. The inset shows a zoom of the low-energy mode-crossing region. (b) Orientation of the electric field in the gap regions for two limiting geometries: (1-3) square symmetry ($b = d = 10\,\mathrm{nm}$) and (4,5) rectangular symmetry ($b \gg d = 10\,\mathrm{nm}$). The numerical labels correspond to the modes signalled by arrows in (a). The symmetry increase in the square configuration leads to mode degeneracy, as shown in (2).

$\lambda = 1605\,\mathrm{nm}$ ($\sim 0.77\,\mathrm{eV}$). The center-to-center distance at the crossing point in the wires of Fig. 2.6 is 213 nm. This is qualitatively consistent with the line-dipole model (see Fig. 2.7), which is an idealization of the electric field produced by a gap mode.

The orientation of the electric field in the gap regions of two interacting wire pairs is schematically represented in Fig. 2.6(b). At large distances, a characteristic binding-antibinding interplay is displayed (panels 4 and 5). Incidentally, parallel dipoles (panel 5) give rise to binding (lower energy), although this behavior is reversed at small distances due to the sign change noted in Eq. (2.1) and Fig. 2.7.

An interesting situation is presented when the distance between all wires is the same [$b = d = 10\,\mathrm{nm}$ in Fig. 2.5(d) and Fig. 2.6], so that there are four hybridized gap modes. In the evolution of different modes when two wire pairs are brought together into this configuration [Fig. 2.6(a)], we find that one of the higher-order modes

is dramatically redshifted to become degenerate with a short-distance antibinding mode [panel 2 of Fig. 2.6(b)]. The binding mode (panel 1) involves electric fields of adjacent gaps facing each other. The remaining fourth mode is provided by another redshifted higher-order mode, and displays closed electric-field lines, which make it more strongly confined. For completeness, the dispersion diagram of this degenerate system is given in Fig. 2.5(d), showing three gap-mode lines that are clearly separated from the upper-energy structure: a central line corresponding to the two degenerate modes of panel 2 in Fig. 2.6(b), flanked by two non-degenerate lines [upper and lower lines in Fig. 2.5(d), corresponding to the modes of panels 3 and 1 in Fig. 2.6(b), respectively]. This mode structure can be qualitatively described by considering the interaction of nearest-neighbors gap-plasmons described by a coupling energy Δ and leading to the interaction matrix

$$\begin{bmatrix} 0 & \Delta & 0 & \Delta \\ \Delta & 0 & \Delta & 0 \\ 0 & \Delta & 0 & \Delta \\ \Delta & 0 & \Delta & 0 \end{bmatrix},$$

which has two degenerate eigenstates $(0,-1,0,1)$ and $(-1,0,1,0)$ at the same energy as the single wire pair [these are the modes of panel 2 in Fig. 2.6(b)], a state $(-1,1,-1,1)$ shifted by -2Δ (panel 3), and another state $(1,1,1,1)$ shifted by 2Δ (panel 1, implying that $\Delta < 0$). Notice that the two degenerate eigenstates $(0,-1,0,1)$ and $(-1,0,1,0)$ form a basis of the 2-dimensional irreducible representation E of the point group C_{4v}, which characterizes the coupled square structure. In the same way, the other two eigenstates $(-1,1,-1,1)$ and $(1,1,1,1)$ form a basis of the 1-dimensional irreducible representations B_2 and A_2, respectively [93]. This means that each of those eigenstates is transformed under the symmetry operations, as each irreducible representation indicates. It should be mentioned that a systematic analysis of the modes of systems with square symmetry leads to six types of modes (two degenerate ones and four non-degenerate) [94, 95], but here we are concerned only with modes that are a combination of gap modes, and therefore, this restriction limits our number of states to just four. The coordinates in the vectors stand for the electric field in consecutive gaps of the structure (*e.g.*,

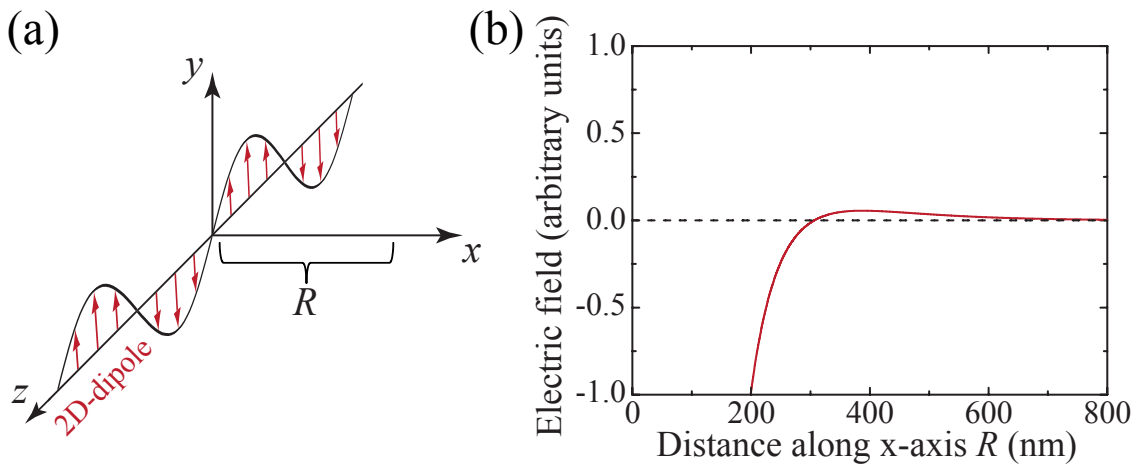

Figure 2.7: Spatial dependence of field produced by a line dipole. (a) Line of dipoles $e^{ik_\parallel z}\hat{\mathbf{y}}$ distributed along the z axis. (b) y component of the electric field produced by the dipoles of (a) along the x axis for a free-space wavelength $\lambda = 1605\,\text{nm}$ and $k_\parallel = 10\,\mu\text{m}^{-1}$, with the dipoles embedded in silica ($\varepsilon = 2.08$).

-1 and 1 correspond to clockwise and counterclockwise orientations of the field, respectively). Whereas this model predicts a symmetric disposition of the upper- and lower-energy gap states relative to the unperturbed state, the $(-1, 1, -1, 1)$ state undergoes much larger shift than the $(1, 1, 1, 1)$ state in the actual structure [Fig. 2.6(a)], which we attribute to interaction with higher other states, although the effect of second-neighbor interaction cannot be ruled out. Incidentally, this type of interaction does not change the symmetry of the states.

The hybridization of gap modes in a wire trimer is studied in Fig. 2.8. Starting from a coplanar configuration (*i.e.*, a trimer angle of 180°), the interaction increases as the angle spanned by the two gaps is reduced, thus leading to further splitting between the energies of the two resulting hybridized modes. Interestingly, the splitting reaches a maximum at an angle of $\sim 70°$, and it drops to zero in the 3-fold symmetric trimer (angle $= 60°$). A higher-order mode is redshifted with decreasing trimer angle, and becomes the third mode of the symmetric trimer. The degeneracy of two of the three gap modes is needed by symmetry in this case, as deduced from

the interaction matrix

$$\begin{bmatrix} 0 & \Delta' & \Delta' \\ \Delta' & 0 & \Delta' \\ \Delta' & \Delta' & 0 \end{bmatrix},$$

where Δ' represents the inter-mode coupling. This matrix has two degenerate eigenmodes, $(1, 0, -1)$ and $(-1, 1, 0)$, with energy shift $-\Delta'$ and a symmetric mode, $(1, 1, 1)$, shifted by $2\Delta'$. These states form a basis of the irreducible representations E (2-dimensional) and A_2 (1-dimensional) of the point group C_{3v}, which characterizes the 3-fold-symmetric trimer-structure. They are in full agreement with the orientation of the electric field at the gaps of the symmetric trimer (see the insets of Fig. 2.8), although the relative energy shift is larger for the symmetric mode in the actual structure, presumably as a result of interaction with higher-energy modes. Again, the restriction that the hybridized modes are made of gap modes limits their number to just three, rather than the four states predicted by general symmetry theory for structures with triangular symmetry [94, 95].

The coupling between gap modes in the two wire pairs of Fig. 2.5(b) is relatively weak according to Fig. 2.6(a), except at very small distances b. The crosstalk between gap plasmons is then small, also implying that it will be difficult to realize a plasmon coupler capable of transferring a plasmon signal from a given wire pair to a neighboring one (see below). We intend however to design a plasmon coupler for wire pairs, that is an important element in eventual plasmonic circuits for implementing simple logical elements such as splitters and interferometers [73].

We need to estimate how much of the signal propagating in a gap-plasmon mode is transferred to another neighboring gap plasmon over a certain propagation distance. Following Ref. [96], we note that for symmetric systems such as those considered above there exist (for any given fixed frequency) two hybridized gap modes that are symmetric and antisymmetric with respect to the center of the combined structure. We can write them as

$$\mathbf{E}_{\mathrm{s}}(\mathbf{r}) = \mathbf{e}_{\mathrm{s}}(x, y)e^{ik_{\mathrm{s}\parallel}z},$$
$$\mathbf{E}_{\mathrm{a}}(\mathbf{r}) = \mathbf{e}_{\mathrm{a}}(x, y)e^{ik_{\mathrm{a}\parallel}z},$$

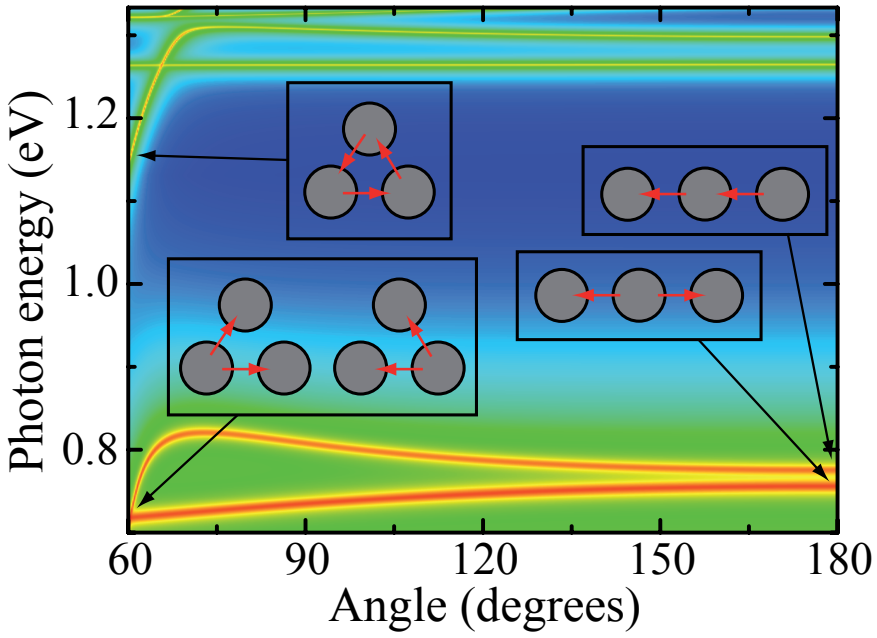

Figure 2.8: Evolution of the gap modes with the trimer angle for fixed $k_{\parallel} = 10\,\mu\mathrm{m}^{-1}$. The insets show the orientation of the electric field in the gap regions for equilateral and coplanar trimers. Two of the modes are degenerate in the 3-fold symmetric case (angle $= 60°$). The inter-wire gap distance is $d = 10\,\mathrm{nm}$ in all cases.

where $k_{\mathrm{s}\parallel}$ and $k_{\mathrm{a}\parallel}$ are the corresponding wave vectors along the direction of the wires. These two modes can be expressed as symmetric and antisymmetric combinations of the gap modes of each wire pair (1 and 2) as

$$\mathbf{e}_{\mathrm{s}} = \frac{1}{\sqrt{2}}\left[\mathbf{e}_1 + \mathbf{e}_2\right],$$
$$\mathbf{e}_{\mathrm{a}} = \frac{1}{\sqrt{2}}\left[\mathbf{e}_1 - \mathbf{e}_2\right].$$

Now, we can prepare a signal that is propagating in a combined state

$$\begin{aligned}\mathbf{E}(\mathbf{r}) =& \frac{1}{\sqrt{2}}\left[e^{ik_{\mathrm{s}\parallel}z}\mathbf{e}_{\mathrm{s}}(x,y) + e^{ik_{\mathrm{a}\parallel}z}\mathbf{e}_{\mathrm{a}}(x,y)\right] \\ =& \frac{1}{2}\left(e^{ik_{\mathrm{s}\parallel}z} + e^{ik_{\mathrm{a}\parallel}z}\right)\mathbf{e}_1(x,y) + \frac{1}{2}\left(e^{ik_{\mathrm{s}\parallel}z} - e^{ik_{\mathrm{a}\parallel}z}\right)\mathbf{e}_2(x,y).\end{aligned}$$

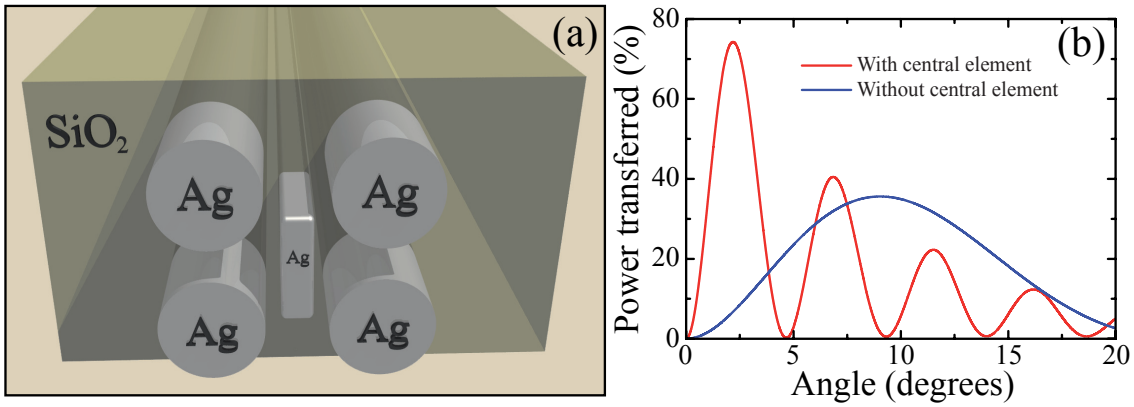

Figure 2.9: Waveguide coupler consisting of an intermediate wire of rectangular cross-section placed between the two gap-plasmon waveguides. (a) Schematic view of the geometry. (b) Fraction of power transferred between waveguides as a function of coupler length along the wires (solid curve). For comparison, we show the power transfer in two wire pairs without intermediate coupler (dashed curve) for a distance $b = 20\,\text{nm}$. The transversal dimensions of the coupler are $140\,\text{nm} \times 20\,\text{nm}$. The four circular wires are arranged as in Fig. 2.5(b) with $d = 10\,\text{nm}$ and $b = 20\,\text{nm}$.

This state is initially propagating in the gap mode 1 at $z = 0$ (the coefficient of state $\mathbf{e}_2$ vanishes at that point). The fraction of power $T(L)$ that is transferred to mode 2 after propagation over a distance L is given by the squared modulus of the coefficient multiplying $\mathbf{e}_2$ [96]:

$$T(L) = \frac{1}{4}\left|e^{ik_{\mathrm{s}\|}L} - e^{ik_{\mathrm{a}\|}L}\right|^2. \tag{2.2}$$

If we neglect absorption, $k_{\mathrm{s}\|}$ and $k_{\mathrm{a}\|}$ are real, so that Eq. (2.2) reduces to

$$T(L) = \sin^2\left[(k_{\mathrm{s}\|} - k_{\mathrm{a}\|})L/2\right],$$

which is an oscillatory function of L predicting full transfer from gap 1 to gap 2 after a propagation distance $L = \pi/|k_{\mathrm{s}\|} - k_{\mathrm{a}\|}|$. However, absorption introduces a small imaginary part in the wave vectors, leading to attenuated oscillations.

We show in Fig. 2.9(b) a representative case of the fraction of transferred power $T(L)$ between two wire pairs (dashed curve), given by Eq. (2.2) for the values of $k_{\mathrm{s}\|}$ and $k_{\mathrm{a}\|}$ obtained from the BEM with $b = 20\,\text{nm}$ and $\lambda = 1550\,\text{nm}$. The maximum

transferred-power fraction is only $T_{\max} = 35.6\%$. The remaining power is lost to absorption before full transfer between gap modes can be realized. This coupling scheme is thus of no practical use because absorption dominates over power transfer. In order to increase the coupling efficiency, we have placed a structure in between the wire pairs [see Fig. 2.9(a)], leading to a larger maximum transferred-power fraction $T_{\max} = 74.3\%$, as shown by the solid curve of Fig. 2.9(b). This geometry is not fully optimized, but it shows that by placing a structure in between the waveguides, one can increase crosstalking to achieve a significant degree of power transfer. This type of coupler can find practical application in waveguide splitters, interferometers, and other signal processing elements.

2.4 Other systems

Interestingly, alkali-halide crystals [21] display, in some regions of the mid-IR, a dielectric behavior similar to metals at visible and near-IR frequencies, characterized by large negative permittivities and small losses. The origin of such behavior lies in the excitation of optical-phonon polaritons supported by these materials. These excitations are expected to mimic the behavior of the plasmons supported by metallic nanostructures, and thus, we expect that two parallel wires made of an alkali-halide crystal can support a gap mode with the same excellent guiding properties as the gap mode observed in metallic nanowires. For instance, two wires of KCl surrounded by vacuum, with a radius of $2\,\mu$m, and separated by 500 nm display a gap mode in the spectral region of $50 - 70\,\mu$m. Similarly, wires with the same dimensions, made of LiF and embedded in a matrix of NaCl, support a gap mode for wavelengths of $20 - 40\,\mu$m [97]. These structures are a realistic alternative to processes information encoded as IR light and contribute to ease the lack of suitable devices in this regime.

Surface plasmons supported by graphene nanoribbons have been also studied and characterized as excellent candidates to guide signals [98, 99, 100]. The large degree of confinement and lifetime of these excitations enables the creation of extremely compact three-dimensional plasmonic circuits. Furthermore, the possibility of tuning the plasmon frequency through the modulation of the doping level of the ribbon adds an extra degree of control to these graphene waveguides, which can be used to design, for instance, novel tunable biosensors.

2.5 Conclusions

In conclusion, we have shown that gap plasmon modes existing in the region defined by two neighboring nanowires are excellent candidates to guide signals over tens of microns. These modes are quite robust against both unintended variations of wire cross-section and curvature in short turns, and thus, gap plasmons can be guided with minimum losses over complicated winding paths of micrometer dimensions. Furthermore, gap modes are highly confined to the gap region, so that inter-mixing between neighboring wire pairs can be minimized. This has the advantage of preventing waveguide cross-talk and allowing highly-integrated plasmonic circuits in three dimensional spaces, but makes it very difficult to completely transfer a plasmon signal between wire pairs within a distance smaller than the attenuation length.

In order to solve this problem, we have studied the interaction of gap plasmons confined to wire pairs, finding a complex structure of hybridized modes, including unavoided crossings facilitated by the vanishing of the interaction right at the point of crossing. Thanks to this insight, we have presented a design of a more efficient plasmon coupler containing an additional intermediate wire and capable of transferring 74% of the signal between wires. Optimization of geometrical parameters should allow achieving larger transfer fractions for application to signal-processing elements such as waveguide splitters, energy filters, and interferometers.

Chapter 3

Interaction between plasmons and quantum emitters

3.1 Introduction

The large fields and the high confinement associated with the plasmonic resonances supported by metallic nanoparticles [10, 101, 102] enable strong interactions with other photonic elements such as quantum emitters. This allows us to design new hybrid plasmon-emitter systems that exhibit unique optical responses [103, 104, 105, 106, 107, 108, 109, 110, 111, 112, 113], and that are capable of controlling light-matter interactions at the nanoscale. Thanks to the advance in nanofabrication techniques [114, 115, 116], we are currently approaching dimensions in which the quantum behavior of these structures emerges naturally, thus opening wide horizons for new designs and applications in the area of quantum plasmonics [117].

Understanding the physics underlying the internal interaction in these systems is important to take advantage of their quantum features such as single excitations [118], and quantum correlations and interferences [119]. The theoretical characterization of these processes requires a fully quantum mechanical framework in order to capture the quantum aspects of the optical response. This is exactly the reason why numerical simulations of Maxwell's equations, which have been successfully used to model the optical response of a vast number of systems involving metal-

lic nanostructures [3], cannot describe completely the behavior of these systems. Therefore, it is clear the necessity of developing new theoretical tools that overcome such limitations.

In the first part of this chapter, we use Zubarev's Green functions (see Section 1.3.1 and [58]) to model the optical response of plasmons interacting with quantum emitters. This results in a powerful approach that allows us to describe the internal evolution of these kinds of systems beyond the perturbative regime. Despite its simplicity, this methodology incorporates a proper account of finite lifetimes via coupling to a continuum of modes. Resonance phenomena such as Fano lineshapes are then emerging in a natural way [120, 121]. We illustrate the application of this formalism by analyzing the optical response of a system formed by a quantum emitter placed at the gap of a nanoparticle dimer [90]. These types of structures are currently attracting much attention [104, 105, 108, 109, 110, 111, 112, 113] due to its potential application as a platform for quantum information devices.

The possibility of reaching the quantum regime using plasmonic systems faces difficult challenges but offers great opportunities [117, 122, 123]. For instance, the non-linear behavior arising from the quantum nature of both a fermionic emitter and light has been extensively investigated on theoretical and experimental grounds over the last decade [124, 125]. An interesting example is the photon blockade effect [126], which has been experimentally observed in atoms coupled to cavities [127], as well as in superconducting circuits [128]. The essential ingredient of these experiments is the achievement of strong light-matter coupling, characterized by an interaction energy exceeding the damping introduced by cavity losses. Nonetheless, reaching the strong-coupling regime is a delicate task that has so far been reserved to a handful of cavity quantum-electrodynamics (QED) experiments.

The extension of this regime to quantum emitters interacting with plasmons supported by metallic nanoparticles has been recently pursued [104, 105, 108, 109, 110, 111, 112, 113] in order to realize quantum behavior in more robust and compact systems than the elaborate QED setups. However, this goal is very difficult to achieve using standard plasmonic materials such as noble metals due to the relatively large losses inherent to these materials, which limit the lifetime of the plasmons to ~ 10 optical cycles. A promising alternative approach would be to use plasmons supported by doped graphene nanodisks [36, 98, 7, 99], which, as it has been

discussed in Section 1.1.3, can confine the electromagnetic field down to smaller volumes than plasmons supported by metallic nanoparticles, having at the same time longer lifetimes ($\sim$ 100 optical cycles [36]).

In the second part of this chapter, we show that quantum effects can introduce a strong non-linear optical response in a system formed by a doped graphene nanodisk and a nearby quantum emitter. We predict a plasmon blockade effect under feasible conditions, which allows actively switching the optical properties of the resulting device in a manner analogous to the photon blockade effect that has been extensively studied in cooled atoms coupled to photonic cavities. The plasmon blockade effect produces non-classical distributions when multiple-plasmon states are generated. Additionally we show that, in contrast to photon blockade, the wavelength at which plasmon blockade takes place can be straightforwardly tuned simply by changing the charge in the graphene *via* electrostatic gating [129].

The possibility of controlling the temporal quantum evolution of a physical system by means of external macroscopic stimuli will make versatile quantum-information devices viable [130]. Various methods for quantum control have been proposed [130], and despite efforts and progress in fields such as ion traps [131, 132], scalable systems remain an open challenge. Recently, solid-state quantum devices are attracting growing interest because they provide a robust platform for implementing scalable temporal control [133, 134]. In this context, the emergence of graphene as a tunable plasmonic material, in which plasmons can be literally switched on and off by applying external potentials [34, 35], opens a natural way to control the quantum evolution of small systems through plasmon-mediated interactions, which are in turn modulated by external fields. This constitutes an interesting alternative path to the elaborate setups employed in the context of cavity-QED [130, 135, 132].

In the last part of this chapter, we show that doped graphene nanostructures combined with two-level atoms or quantum dots provide a robust platform for achieving the desired goal of full temporal quantum control. The interaction between the quantum dots is strongly mediated by plasmons in the graphene, which can be electrostatically tuned through engineered gates [136, 33]. The quantum evolution of the dots is then manipulated by modulating over time the electric potential that we apply to the gates. Specifically, we show that direct control over two-level emitters

is possible, thus allowing one to convert the excited state into a long-lived state and eliminating the need to involve additional excited or metastable states and external control fields upon which other methods are relying [130, 137]. We provide realistic simulations demonstrating excellent control over the decay of individual and interacting dots. Any desired decay profile can be produced by resorting on the unprecedentedly fast electro-optical modulation of graphene [34, 35] and its strong interaction with neighboring quantum emitters [138].

3.2 Quantum plexcitonics

3.2.1 A quantum emitter interacting with two metallic nanoparticles

We consider a system composed of two identical metallic nanoparticles with diameter of tens of nanometers separated by a gap of a few nanometers. A quantum emitter is placed in this gap, where the field-amplitude enhancement due to the plasmonic resonances of the particles can easily reach two orders of magnitude with respect to the value of an external plane wave [10]. Such a coupled plasmonic-exciton system results in hybrid plasmonic excitonic modes also referred to as Plexcitons [139]. The optical response of this system has been studied recently using classical electrodynamics methods [108, 109]. We assume each particle to be supporting just one dipolar plasmon and one quadrupolar plasmon with $m = 0$ azimuthal symmetry with respect to the dimer axis. Only modes with this symmetry can be excited because we consider the external field to be oriented along the dimer axis. In a real system, higher-order multipoles are also contributing for small separations, although the dipoles are dominant for the separations discussed below. In fact, the quadrupole can be considered to effectively account for the effects of all higher-order modes combined. The quantum emitter is described as a fermionic system with only two possible states (ground and excited). The Hamiltonian that determines the behavior of this nanostructure contains three terms

$$\hat{H} = \hat{H}_0 + \hat{H}_{\text{int}} + \hat{H}_{\text{decay}}.$$

The part describing the non-interacting evolution of the fermion and the plasmons reads

$$\hat{H}_0 = \hbar\omega_d \left[\hat{d}_1^+ \hat{d}_1 + \hat{d}_2^+ \hat{d}_2\right] + \hbar\omega_q \left[\hat{q}_1^+ \hat{q}_1 + \hat{q}_2^+ \hat{q}_2\right] + \hbar\omega_c \hat{c}^+ \hat{c},$$

where $\hat{d}_i$ and $\hat{q}_i$ ($\hat{d}_i^+$ and $\hat{q}_i^+$) are the dipolar and quadrupolar plasmon bosonic annihilation (creation) operators of particle $i = 1, 2$, respectively. Similarly, $\hat{c}$ ($\hat{c}^+$) is the annihilation (creation) operator for the quantum emitter fermion. The characteristic frequencies of these excitations are ω_d, ω_q and ω_c.

The interaction Hamiltonian $\hat{H}_{\text{int}}$ must describe all possible couplings between the different system excitations. In our particular case, the dipolar and quadrupolar plasmons of one particle can interact with the excitations of the other one via dipole-dipole (Δ_{dd}), dipole-quadrupole (Δ_{dq}), and quadrupole-quadrupole (Δ_{qq}) coupling constants [1]. In addition, the quantum emitter interacts with both the dipolar plasmons (Δ_{dc}) and quadrupolar plasmons (Δ_{qc}). Therefore, we have

$$\begin{aligned}\hat{H}_{\text{int}} = & -\Delta_{dd}\left[\hat{d}_1^+ \hat{d}_2 + \hat{d}_2^+ \hat{d}_1\right] - \Delta_{qq}\left[\hat{q}_1^+ \hat{q}_2 + \hat{q}_2^+ \hat{q}_1\right] - \Delta_{dq}\left[\hat{d}_1^+ \hat{q}_2 + \hat{q}_2^+ \hat{d}_1\right] \\ & - \Delta_{dq}\left[\hat{d}_2^+ \hat{q}_1 + \hat{q}_1^+ \hat{d}_2\right] - \Delta_{dc}\left[\hat{d}_1^+ \hat{c} + \hat{c}^+ \hat{d}_1\right] - \Delta_{dc}\left[\hat{d}_2^+ \hat{c} + \hat{c}^+ \hat{d}_2\right] \\ & - \Delta_{qc}\left[\hat{q}_1^+ \hat{c} + \hat{c}^+ \hat{q}_1\right] - \Delta_{qc}\left[\hat{q}_2^+ \hat{c} + \hat{c}^+ \hat{q}_2\right].\end{aligned}$$

In a realistic model, one has to describe the finite lifetime of the excitations of the system, which produce finite widths in the corresponding spectral resonances. Generally, such widths are the result of the inelastic interaction with a continuum of modes. For instance, a plasmon can decay radiatively by emitting one photon and non-radiatively through the generation of electron-hole pairs, phonons, etc. We describe these inelastic interactions by adding the following term to the Hamiltonian

$$\begin{aligned}\hat{H}_{\text{decay}} = & \sum_{s=d,q}\sum_{i=1,2}\int d\omega \left[\hbar\omega \hat{f}_{s_i}^+(\omega)\hat{f}_{s_i}(\omega) - \left(v_s(\omega)\hat{f}_{s_i}(\omega)\hat{s}_i^+ + v_s^*(\omega)\hat{f}_{s_i}^+(\omega)\hat{s}_i\right)\right] \\ & + \int d\omega \hbar\omega \hat{f}_c^+(\omega)\hat{f}_c(\omega) - \int d\omega \left[v_c(\omega)\hat{f}_c(\omega)\hat{c}^+ + v_c^*(\omega)\hat{f}_c^+(\omega)\hat{c}\right],\end{aligned}$$

[1] Any possible phase of the coupling constants can be reabsorbed into the definition of the creation and annihilation operators, so we can assume them to be positive real numbers without loss of generality.

where $\hat{f}_{s_i}(\omega)$ and $\hat{f}_c(\omega)$ are the annihilation operators of the continuum of modes that couple to the plasmons and the fermion, respectively. The corresponding coupling constants are $v_s(\omega)$ and $v_c(\omega)$. These terms account for all possible decay channels of the system excitations.

For particles with diameters of tens of nanometers, the quadrupoles couple only weakly to the light. Furthermore, the absorption cross-section of the nanoparticle is generally much larger than that of a molecule or a quantum dot. We therefore assume that only the dipolar plasmons couple efficiently to the external photons. (However, the extension of our calculations to include the direct coupling to the emitter and the quadrupoles is straightforward.) With this approximation, we can apply the method based on Zubarev's Green functions, described in Section 1.3.1, to calculate the optical absorption spectrum of the system under study. For doing that we just need to obtain the Green function $\langle\langle \hat{D}; \hat{D}^+ \rangle\rangle$ [see Eq. (1.24)], where $\hat{D}$ is a linear combination of the dipolar plasmon annihilation operators of particles 1 and 2 compatible with the symmetry of the external field. We choose $\hat{D} = \hat{d}_1 + \hat{d}_2$, which implies that the incident photons are absorbed at the two particles with the same phase. This represents the situation in which the external field is incident perpendicularly to the dimer axis, and therefore, only the bonding mode [90] of the dimer is excited.

Using Eq. (1.25) and the Hamiltonian derived above, the equation of motion of the Green function $\langle\langle \hat{D}; \hat{D}^+ \rangle\rangle$ reads

$$\begin{aligned}(\hbar\omega - \hbar\omega_d + \Delta_{dd}) \langle\langle \hat{D}; \hat{D}^+ \rangle\rangle = 2 - \Delta_{dq}\langle\langle \hat{Q}; \hat{D}^+ \rangle\rangle - 2\Delta_{dc}\langle\langle \hat{c}; \hat{D}^+ \rangle\rangle \\ - \int d\omega' v_d(\omega')\langle\langle \hat{f}_D(\omega'); \hat{D}^+ \rangle\rangle, \end{aligned} \tag{3.1}$$

where $\hat{Q} = \hat{q}_1 + \hat{q}_2$ and $\hat{f}_D = \hat{f}_{d_1} + \hat{f}_{d_2}$. From this expression, it is clear that we need to compute additional Green functions. In particular $\langle\langle \hat{Q}; \hat{D}^+ \rangle\rangle$, whose equation of motion is

$$\begin{aligned}(\hbar\omega - \hbar\omega_q + \Delta_{qq}) \langle\langle \hat{Q}; \hat{D}^+ \rangle\rangle = & - \Delta_{dq}\langle\langle \hat{D}; \hat{D}^+ \rangle\rangle - 2\Delta_{qc}\langle\langle \hat{c}; \hat{D}^+ \rangle\rangle \\ & - \int d\omega' v_q(\omega')\langle\langle \hat{f}_Q(\omega'); \hat{D}^+ \rangle\rangle,\end{aligned}$$

with $\hat{f}_Q = \hat{f}_{q_1} + \hat{f}_{q_2}$. Similarly, the dynamics of $\langle\langle \hat{c}; \hat{D}^+ \rangle\rangle$ is governed by

$$(\hbar\omega - \hbar\omega_c)\,\langle\langle \hat{c}; \hat{D}^+ \rangle\rangle = -\Delta_{dc}\langle\langle (1 - 2\hat{c}^+\hat{c})\hat{D}; \hat{D}^+ \rangle\rangle - \Delta_{qc}(1 - 2\hat{c}^+\hat{c})\langle\langle \hat{Q}; \hat{D}^+ \rangle\rangle - (1 - 2\hat{c}^+\hat{c}) \int d\omega' v_c(\omega')\langle\langle \hat{f}_c(\omega'); \hat{D}^+ \rangle\rangle.$$

In principle, the iteration of this process would produce an infinite hierarchy of equations of motion, however, we decide to truncated it at this point by approximating the operator $\hat{c}^+\hat{c}$ by its expectation value $\langle \hat{c}^+\hat{c} \rangle = n_c$. With this substitution, the last expression becomes

$$(\hbar\omega - \hbar\omega_c)\,\langle\langle \hat{c}; \hat{D}^+ \rangle\rangle = -\Delta_{dc}(1 - 2n_c)\langle\langle \hat{D}; \hat{D}^+ \rangle\rangle - \Delta_{qc}(1 - 2n_c)\langle\langle \hat{Q}; \hat{D}^+ \rangle\rangle - (1 - 2n_c) \int d\omega' v_c(\omega')\langle\langle \hat{f}_c(\omega'); \hat{D}^+ \rangle\rangle.$$

The presence of n_c here is the result of the fermionic character of the quantum emitter.

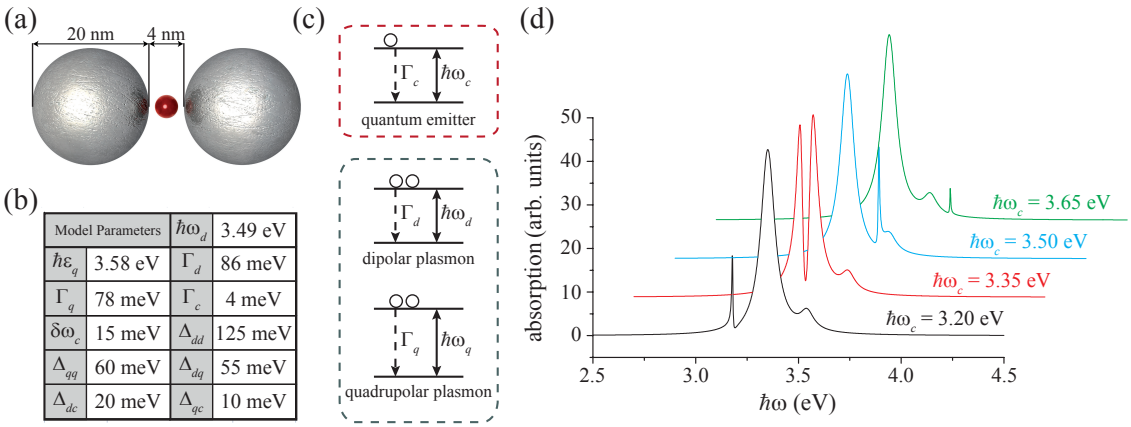

Model Parameters		$\hbar\omega_d$	3.49 eV
$\hbar\varepsilon_q$	3.58 eV	Γ_d	86 meV
Γ_q	78 meV	Γ_c	4 meV
$\delta\omega_c$	15 meV	Δ_{dd}	125 meV
Δ_{qq}	60 meV	Δ_{dq}	55 meV
Δ_{dc}	20 meV	Δ_{qc}	10 meV

Figure 3.1: Optical response of a hybrid plexcitonic system formed by a quantum emitter placed in the gap of a nanoparticle dimer. (a) Description of the system under study. (b) Values of the different model parameters (see text). (c) Energy diagrams of the quantum emitter (fermionic character), and the dipolar and quadrupolar plasmons supported by the nanoparticles (bosonic character). (d) Optical absorption spectrum of the dimer-quantum-emitter system, computed for different values of the emitter resonance energy. A Fano resonance is clearly observed as a result of the coupling between the emitter and the particle plasmons.

We still need to deal with Green functions containing information related to the inelastic decay processes: $\langle\langle \hat{f}_D(\omega'); \hat{D}^+\rangle\rangle$, $\langle\langle \hat{f}_Q(\omega'); \hat{D}^+\rangle\rangle$ and $\langle\langle \hat{f}_c(\omega'); \hat{D}^+\rangle\rangle$. Upon inspection of the Hamiltonian, we conclude that these Green functions only depend on those derived above, and can be obtained from

$$\begin{aligned}
(\hbar\omega - \hbar\omega')\,\langle\langle \hat{f}_D(\omega'); \hat{D}^+\rangle\rangle &= -v_d^*(\omega')\langle\langle \hat{D}; \hat{D}^+\rangle\rangle,\\
(\hbar\omega - \hbar\omega')\,\langle\langle \hat{f}_Q(\omega'); \hat{D}^+\rangle\rangle &= -v_q^*(\omega')\langle\langle \hat{Q}; \hat{D}^+\rangle\rangle,\\
(\hbar\omega - \hbar\omega')\,\langle\langle \hat{f}_c(\omega'); \hat{D}^+\rangle\rangle &= -v_c^*(\omega')\langle\langle \hat{c}; \hat{D}^+\rangle\rangle.
\end{aligned}$$

Substituting the first of these expressions into Eq. (3.1) and introducing the positive infinitesimal imaginary part of the frequency that appears in the definition of Zubarev's Green function [see Eq. (1.23)], we find the integral

$$\int d\omega' \frac{|v_d(\omega')|^2}{\hbar\omega' - \hbar\omega - i0^+} = \text{P.V.} \int d\omega' \frac{|v_d(\omega')|^2}{\hbar\omega' - \hbar\omega} + i\pi|v_d(\omega)|^2 = \delta\omega_d + i\frac{\Gamma_d}{2},$$

which we have evaluated using the Sokhatsky-Weierstrass theorem. Here, P.V. denotes the Cauchy principal value, $\delta\omega_d$ represents a frequency shift, and $\Gamma_d = 2\pi|v_d(\omega)|^2$ is the inelastic decay rate of the dipolar plasmons. Dealing in a similar way with the remaining decay channels, we end up with a linear system of three equations and three unknowns: $\langle\langle \hat{D}; \hat{D}^+\rangle\rangle$, $\langle\langle \hat{Q}; \hat{D}^+\rangle\rangle$, and $\langle\langle \hat{c}; \hat{D}^+\rangle\rangle$. Finally, solving this system of equations we obtain $\langle\langle \hat{D}, \hat{D}^+\rangle\rangle$, and therefore, via Eq. (1.24), the optical absorption spectrum

$$\sigma \propto \text{Im}\left\{ S_d - \frac{2\Delta_{dc}^2(1-2n_c)}{S_c} - \frac{\left[\Delta_{dq} - \frac{2\Delta_{qc}\Delta_{dc}(1-2n_c)}{S_c}\right]^2}{S_q - \frac{2\Delta_{qc}^2(1-2n_c)}{S_c}} \right\}^{-1}, \tag{3.2}$$

where we have defined $S_d = \hbar\omega - \hbar\omega_d + \Delta_{dd} + \delta\omega_d + i\frac{\Gamma_d}{2}$, $S_q = \hbar\omega - \hbar\omega_q + \Delta_{qq} + \delta\omega_q + i\frac{\Gamma_q}{2}$, and $S_c = \hbar\omega - \hbar\omega_c + (1-2n_c)\left[\delta\omega_c + i\frac{\Gamma_c}{2}\right]$.

In order to apply this model to actual dimer-quantum-emitter systems, we need to find realistic values for the different parameters involved in Eq. (3.2). We illustrate this by considering two silver nanoparticles of 10 nm radius separated by a gap of 4 nm. We take the system to be initially prepared in the ground state, so that $n_c = 0$ for the emitter placed in the dimer gap. Moreover, the frequency shifts $\delta\omega_d$

and $\delta\omega_q$ can be accounted for by renormalizing the energies of the corresponding states $\hbar\omega_d$, and $\hbar\omega_q$, respectively. Notice that we keep $\delta\omega_c$ as it cannot be reabsorbed when $n_c \neq 0$. We extract the energies and widths of the dipolar and quadrupolar plasmons from classical electromagnetic simulations of the absorption cross-section for a single silver nanoparticle using Mie theory. In a similar way, we obtain the coupling constants describing the interaction between the dipolar and quadrupolar plasmons by fitting Eq. (3.2) with $\Delta_{dc} = \Delta_{qc} = 0$ (*i.e.*, without emitter) to an electromagnetic simulation of the dimer absorption cross-section using a multiple-scattering approach [140]. The resulting values for the different parameters are given in Fig. 3.1(b).

Figure 3.1(d) shows the optical absorption spectrum of the system under study, computed from Eq. (3.2), for different energies of the quantum emitter resonance. The width of this resonance has been taken to be $\Gamma_c = 4\,\text{meV}$, which is a realistic value for actual quantum dots [141]. It is important to note that we have considered quantum emitters of resonance energy lying close to the dimer plasmons. For a given emitter energy within the $3 - 3.5\,\text{eV}$ range, the dimer plasmon frequencies can be easily tuned by selecting the size, shape, and separation of the nanoparticles [142] (*e.g.*, using nanoshells of appropriate thickness [143]).

We have calculated the strength of the coupling between the quantum emitter and the dipolar and quadrupolar plasmons, and the value of $\delta\omega_c$ by fitting Eq. (3.2) to a simulation performed using the BEM [7, 30]. In this model the quantum emitter is represented by a point dipole with a linear polarizability $\alpha(\omega) = \mu^2/(\hbar\omega_c - \omega - i\Gamma_c/2)$ [144], where μ is the transition dipole. In our particular example we assume $\mu/e = 0.3\,\text{nm}$, which is a realistic value for a quantum dot [145]. Using this transition dipole we obtain the values for the different model parameters shown in Fig. 3.1(b). Thanks to the large plasmonic fields existing in the dimer gap, this system exhibits relative large values of the coupling constants Δ_{dc} and Δ_{qc}.

As we observe in Fig. 3.1, the optical spectra exhibit three distinct features. The hybridized bonding dipolar and quadrupolar dimer modes around 3.3 ($\approx \hbar\omega_d - \Delta_{dd}$) and 3.5 eV ($\approx \hbar\omega_q - \Delta_{qq}$); and the excitonic mode, which is clearly visible as a Fano resonance with a lineshape that strongly depends on the energy $\hbar\omega_c$. The Fano resonance results from the interaction between a continuum of modes and a narrow discrete mode [121]. In our example, the quantum emitter resonance is the narrow

mode, while the dipolar and quadrupolar plasmons, with their larger widths, play the role of a continuum. As expected these resonances can be fitted approximately using the conventional Fano lineshape with $|q| << 1$. For instance, in the case of the curve of Fig. 3.1(d) corresponding to $\hbar\omega_c = 3.35\,\text{eV}$ we have $q \sim 0.07 - 0.05$.

In Fig. 3.2(a), we show how the width of the exciton influences the Fano resonance. The resonance width is an essential factor to observe Fano resonances in this type of system. Figure 3.2(a) also shows that the Fano resonance displayed for small values of Γ_c disappears as this parameter approaches the value of the dipolar plasmon width Γ_d.

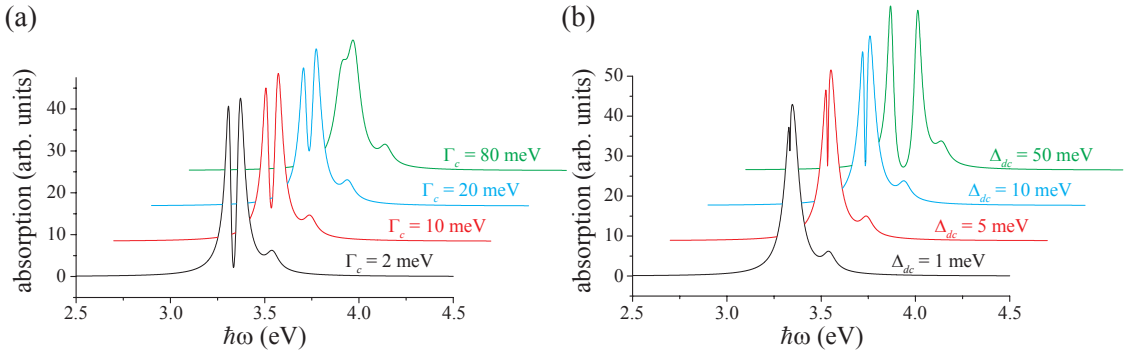

Figure 3.2: Dependence of the optical absorption spectrum on the quantum emitter resonance width Γ_c (a) and on the strength of the coupling between the dipolar plasmons and the quantum emitter Δ_{dc} (b). We take the emitter excitation energy $\hbar\omega_c = 3.35\,\text{eV}$, while the rest of the model parameters are given in Fig. 3.1(b). The Fano resonance disappears as Γ_c increases, while a dramatic dependence of the spectral shape on Δ_{dc} is observed.

In Fig. 3.2(b) we illustrate the critical role played by the strength of the coupling between the quantum emitter and the dipolar plasmon Δ_{dc} in determining the shape of the optical absorption spectrum. For small values of Δ_{dc}, the dip associated with the Fano resonance almost disappears. For increasing Δ_{dc}, the dip becomes deeper and the separation between the two resulting peaks becomes more pronounced. Actually, when this coupling constant is larger than the dipolar plasmon half width $\Gamma_d/2$ we can alternatively interpret the resulting lineshape as vacuum Rabi splitting [108].

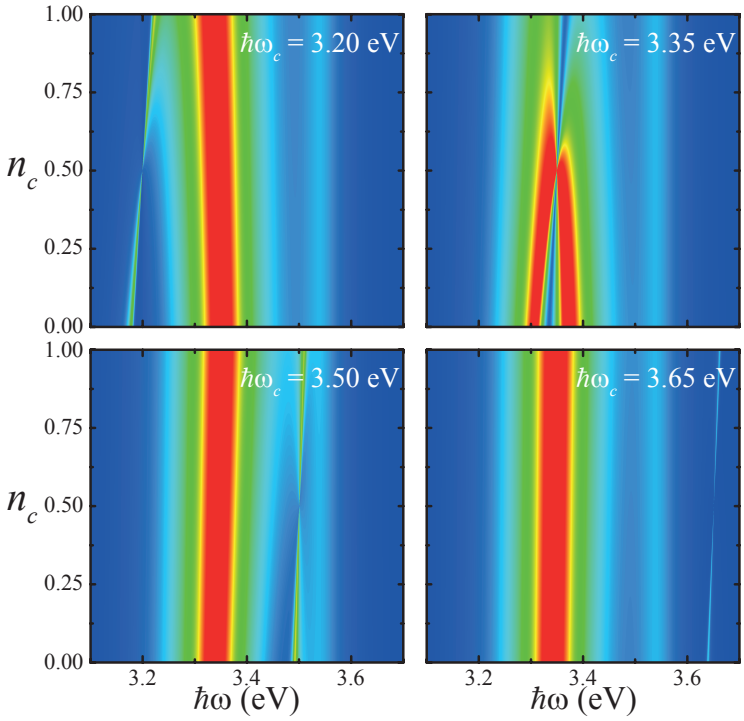

Figure 3.3: Dependence of the optical absorption spectrum on the expectation value of the emitter excited level n_c for different values of the emitter excitation energy. The rest of the model parameters are given in Fig. 3.1(b). The absorption spectrum changes dramatically as n_c changes from 0 to 1.

3.2.2 Non-linear effects and beyond

It is important to stress that our results reproduce the simulations performed in previous works [108, 109]. However, our methodology allows us to go one step forward in the understanding of the physical mechanisms governing the response of the system. First of all, we can clearly identify the origin of the peaks and other features that characterize the investigated optical absorption spectra. Furthermore, our model can capture the non-classical behavior of the different elements of the system. For instance, in a situation in which the quantum emitter is not initially prepared in its ground state, and hence, the expectation value n_c does not vanish. In such case, the optical response of the system changes dramatically [see Eq. (3.2)]. In particular, under strong optical pumping this expectation value should

be $\sim 1/2$, for which the interaction between the quantum emitter and the dipolar plasmon disappear, leading to an inhibition of the Fano resonance. Such non-linear Fano resonances have been observed in quantum-well structures and are of clear fundamental importance [103, 146]. This can be clearly observed in Fig. 3.3, which shows the dependence of the optical absorption spectrum on the expectation value n_c, for different emitter excitation energies $\hbar\omega_c$. As n_c grows from 0 to 0.5 the Fano resonance becomes weaker and finally disappears, reemerging again for higher values. At the same time, the position of the Fano resonance is shifted towards higher energies. This behavior, which is associated with the saturation of the quantum emitter, emerges from the fermionic nature of this system. For this reason, although it could be modeled a posteriori using a classical or a semiclassical approach by assuming a change in the oscillator strength, it could not be predicted a priori, unless a fully quantum approach is employed. In practical terms, saturation can be obtained with a pumping-light frequency differing from the probing frequency, but separated from it by less than the width of the emitter excitation. The non-linear response associated with this non-classical behavior opens the possibility of externally controlling the optical absorption spectrum of the system.

The Zubarev's Green functions [58] method presented in this paper is conceptually much simpler than standard Green's function or density matrix approaches since the only formalism that is required is the evaluation of simple commutation relations between operators. However, the major advantage of the present approach is that all dynamics are obtained non-perturbatively directly from the Hamiltonian. Because of this, by simply adding more terms to the Hamiltonian, it is straightforward to include more complex interactions such as the coupling to the continuum which introduced the broadening of the plasmon and exciton states already discussed. Most importantly, our method provides a simple approach for including much more complicated effects such as strong correlation, coupling between two emitters, coupling to phonons and other collective excitations. For instance, an interesting scenario is presented when two quantum emitters are placed at the gap of a particle dimer. The interaction between emitters can be affected by Coulomb repulsion, which can be incorporated into our formalism by adding a Hubbard term to the Hamiltonian as it is commonly done in the Anderson model [147]. Such a term prevents the two quantum emitters from simultaneously lying in excited states, and

may therefore introduce additional useful tunable non-linear behavior of relevance for plexciton-based quantum information devices.

3.3 Plasmon blockade

3.3.1 A quantum emitter interacting with a graphene nanodisk

As discussed in the introduction of this chapter, the extraordinary confinement and lifetime displayed by plasmons in graphene nanodisks make it possible to reach the strong-coupling regime with a nearby quantum emitter, such as a quantum dot or a molecule. In this limit, the quantum emitter can introduce a significant plasmon-plasmon interaction, which gives rise to a plasmon blockade effect. Here, we analyze this effect by studying the system depicted in Fig. 3.4. We consider a graphene nanodisk of diameter D, large enough to safely neglect edge and quantum confinement effects (see the discussion at the end of Sections 1.1.3 and 1.2), and doped to a Fermi energy E_{F} relative to the Fermi energy for the neutral disk. This graphene nanostructure supports localized surface plasmons [7] of energy $\hbar\omega_{\mathrm{p}}$. Specifically, we focus on a dipolar plasmon with polarization parallel to the disk and $m = 1$ azimuthal symmetry. The quantum emitter, which is placed 10 nm above the nanodisk, is described as a two-level system with excited and ground states $|\uparrow\rangle$ and $|\downarrow\rangle$ separated by an energy $\hbar\omega_0$. The entire system is illuminated by an external laser of frequency ω_{L}. In the absence of any losses, the dynamical evolution of the interacting system can be described by a Hamiltonian that consists of three terms: $\hat{H} = \hat{H}_0 + \hat{H}_{\mathrm{int}} + \hat{H}_{\mathrm{ext}}$. The first describes the evolution of the non-interacting system

$$\hat{H}_0 = \hbar\omega_{\mathrm{p}}\hat{b}^\dagger\hat{b} + \hbar\omega_0\hat{c}^\dagger\hat{c},$$

where $\hat{b}$ and $\hat{c} = |\downarrow\rangle\langle\uparrow|$ ($\hat{b}^\dagger$ and $\hat{c}^\dagger = |\uparrow\rangle\langle\downarrow|$) are the annihilation (creation) operators for the graphene plasmon and the excited state of the emitter, respectively. The coupling between the two excitations is described by the second term,

$$\hat{H}_{\mathrm{int}} = \hbar g\left(\hat{b}^\dagger\hat{c} + \hat{b}\hat{c}^\dagger\right),$$

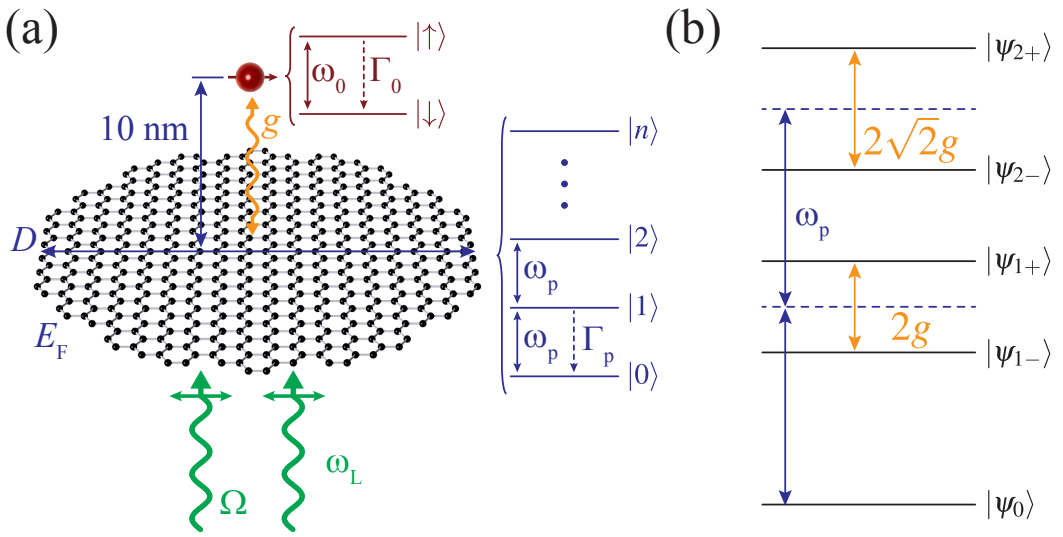

Figure 3.4: Description of the graphene-nanodisk/emitter combined system under study. (a) A quantum emitter is placed 10 nm above of a doped graphene nanodisk of diameter D and Fermi energy E_{F}. The disk can support localized surface plasmons of frequency ω_{p} and lifetime Γ_{p}^{-1}. The quantum emitter is described as a two-level system (ground state $|\downarrow\rangle$ and excited state $|\uparrow\rangle$, transition frequency ω_0, excited-state lifetime Γ_0^{-1}). The dipolar moment of the quantum emitter, taken to be parallel to the disk, interacts with the near field of the graphene plasmon with effective coupling strength g. The entire system is illuminated by an external laser of frequency ω_{L} and intensity quantified in terms of the Rabi frequency Ω. (b) Energy level diagram of the interacting system for $\omega_0 = \omega_{\mathrm{p}}$. The energy diagrams of (a) correspond to the non-interacting disk and emitter, in which the energy level spacing is constant. In contrast, the spacings between the interacting levels in (b) are different as a result of the coupling between the emitter and the graphene plasmon. This interaction introduces anharmonicity and non-linearity in the optical response.

where g is a coupling constant that determines the strength of the interaction. The last term accounts for the effect of the laser,

$$\hat{H}_{\text{ext}} = \hbar\Omega e^{-i\omega_{\text{L}}t}\hat{b}^{\dagger} + \hbar\Omega^{*} e^{i\omega_{\text{L}}t}\hat{b},$$

which operates at frequency ω_{L} with an intensity defined in terms of the Rabi frequency Ω. We neglect direct pumping of the emitter because its cross-section is generally several orders of magnitude smaller that the one of the graphene plasmon.

We incorporate dissipation *via* the master equation for the density operator, as explained in Section 1.3.2 [see Eq. (1.27)]

$$\dot{\hat{\rho}} = \frac{i}{\hbar}\left[\hat{\rho}, \hat{H}\right] + \mathcal{L}_0\left(\hat{\rho}\right) + \mathcal{L}_{\text{p}}\left(\hat{\rho}\right).$$

The first term of this expression contains the Hamiltonian and determines the coherent evolution of the system, while the Lindblad terms $\mathcal{L}_i\left(\hat{\rho}\right) = \Gamma_i/2\left[2\hat{s}_i\hat{\rho}\hat{s}_i^{\dagger} - \hat{\rho}\hat{s}_i^{\dagger}\hat{s}_i - \hat{s}_i^{\dagger}\hat{s}_i\hat{\rho}\right]$ [see Eq. (1.28)], with $i = 0, \text{p}$, account for the damping of both the excited emitter state ($\hat{s}_0 = \hat{c}$) and the graphene plasmon ($\hat{s}_{\text{p}} = \hat{b}$).

Apart from the coupling to external light, $\hat{H}$ is the well-known Jaynes-Cummings Hamiltonian [148], which has the same ground state as $\hat{H}_0\left|\psi_0\right\rangle = \left|\downarrow 0\right\rangle$, and whose excited states $\left|\psi_{n\pm}\right\rangle$ are pairs of linear combinations of $\left|\uparrow n-1\right\rangle$ and $\left|\downarrow n\right\rangle$ with eigenenergies

$$E_{n\pm} = \hbar\left(n\omega_{\text{p}} + \frac{\delta}{2} \pm \sqrt{\frac{\delta^2}{4} + ng^2}\right),$$

where $\delta = \omega_0 - \omega_{\text{p}}$. In each pair of states the sum of the number of plasmon and emitter excitations is n. As we show in Fig. 3.4(b), the interaction of the plasmon with the two-level emitter results in a non-uniform distribution of states known as Jaynes-Cummings ladder [149], in which the states of each pair are separated by an energy determined by the emitter-plasmon coupling g, the detuning δ and the quantum occupation number n. The resulting non-linear dependence of the excitation energy on n is equivalent to anharmonicity and has an important consequence: an external light source tuned to be resonant with the plasmon frequency ω_{p} becomes increasingly more detuned as the system climbs the energy

ladder and n increases. The detuning with respect to the uncoupled plasmon frequency is given by

$$\frac{1}{\hbar}\left(E_{(n+1)\pm} - E_{n\pm}\right) - \omega_{\rm p} = \pm\left(\sqrt{\delta^2/4 + (n+1)\,g^2} - \sqrt{\delta^2/4 + ng^2}\right),$$

which is maximum for $\delta = 0$ (*i.e.*, $\omega_0 = \omega_{\rm p}$). An increasing detuning obviously limits the possibility of generating an arbitrary number of plasmons. We refer to this behavior as plasmon blockade, in direct analogy to the so-called photon blockade observed in cavity QED experiments [127].

It is important to notice that the non-linear behavior associated with the plasmon blockade is only effective in systems for which the coupling g dominates over the losses $\Gamma_{\rm p}$ and Γ_0. In general, plasmonic losses are several orders of magnitude larger than quantum emitter losses ($\Gamma_{\rm p} \gg \Gamma_0$), and thus the condition for observation of an efficient plasmon blockade amounts to $g/\Gamma_{\rm p} \gg 1$. This is known as strong-coupling regime, which is difficult to reach using plasmons supported by standard metallic nanostructures [104, 105, 108, 109, 110, 111, 112, 113]. However, the coupling strength $g/\Gamma_{\rm p}$ associated with the dipolar plasmon of a graphene nanodisk of diameter $D = 100\,\text{nm}$ reaches values in the $1.5 - 3$ range for moderate Fermi energies $E_{\rm F} = 0.2 - 0.6\,\text{eV}$, and it decreases for larger D. Here, we assume typical values for the quantum emitter natural decay rate $\Gamma_0 = 5 \times 10^7\,\text{s}^{-1}$, the nanodisk diameters $D = 100 - 200\,\text{nm}$, and the Fermi energies $E_{\rm F} = 0.2 - 0.6\,\text{eV}$, for which the plasmon energy and width take values $\hbar\omega_{\rm p} \approx 0.1 - 0.25\,\text{eV}$ and $\hbar\Gamma_{\rm p} \approx 1 - 3.5\,\text{meV}$. Since the diameters under consideration are well above 20 nm we safely neglect edge and quantum confinement effects (see Section 1.2 and [49]), and compute these values following the classical approach depicted at the end of Section 1.1.3.

Figure 3.5 shows some of the main signatures of plasmon blockade in the nanodisk-emitter systems. In what follows, we present results for steady-state conditions under continuous wave illumination. In particular, Figs. 3.5(a),(b) show the population of different state pairs n under stationary conditions. We consider two different illumination intensities ($|\Omega|^2 = 0.01\,\Gamma_{\rm p}^2$ and $|\Omega|^2 = \Gamma_{\rm p}^2$), take $\omega_0 = \omega_{\rm p}$, and tune the laser frequency to be resonant with the $|\psi_0\rangle \rightarrow |\psi_{1+}\rangle$ transition. The black bars are the results for the uncoupled system (*i.e.*, in the absence of the quantum emitter), while the red bars refer to the interacting system with a coupling

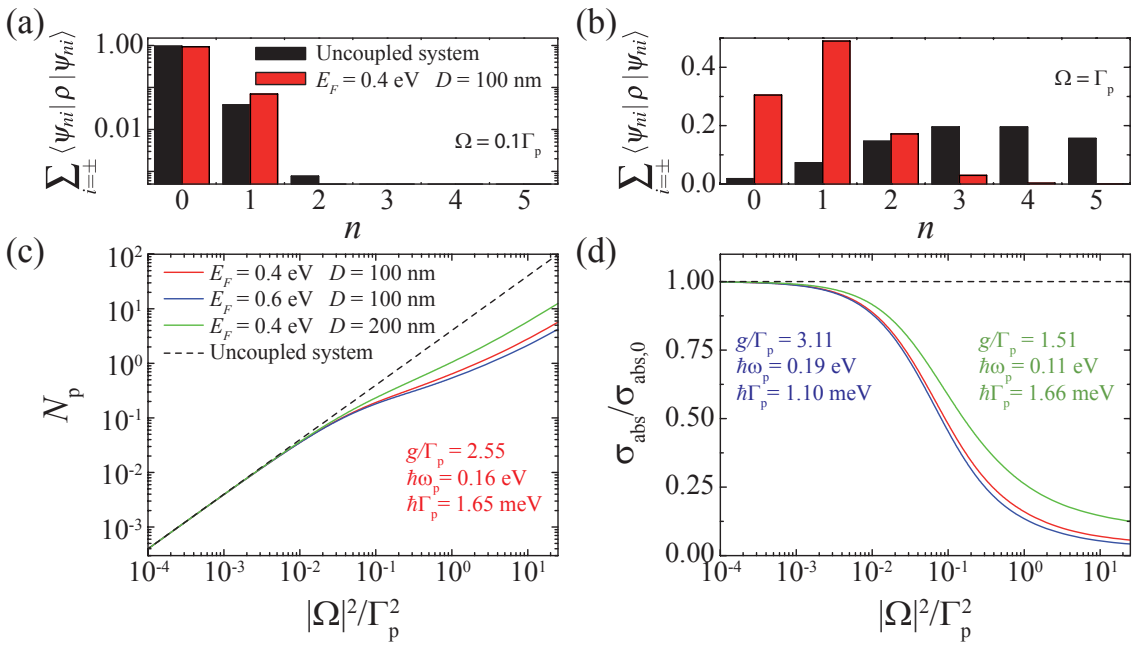

Figure 3.5: Plasmon blockade. (a),(b) Population of the different states of a graphene-nanodisk/emitter system for two different values of the external laser intensity under continuous illumination conditions. Results for interacting ($g/\Gamma_\mathrm{p} = 2.55$, red) and non-interacting ($g/\Gamma_\mathrm{p} = 0$, black) systems are contrasted. We assume resonant coupling ($\omega_0 = \omega_\mathrm{p}$) and tune the laser frequency to the $|\psi_0\rangle \rightarrow |\psi_{1+}\rangle$ transition. For this laser frequency, only $|\psi_{n+}\rangle$ states are significantly populated in the interacting system. (c) Average number of plasmons in the graphene nanodisk N_p as a function of laser intensity for different disk diameters D and Fermi energies E_F (solid curves) under the same conditions as in (a),(b). The uncoupled system (dashed line) shows a linear increase of N_p with the laser intensity. In contrast, the coupled system (solid curves) exhibits a clear non-linear behavior for $|\Omega|^2/\Gamma_\mathrm{p}^2 > 10^{-2}$. The non-linearity is more pronounced for larger graphene-nanodisk/emitter coupling g (*cf.*, red, blue, and green curves). (d) Absorption cross-section of the graphene-nanodisk/emitter coupled system normalized to the value of the uncoupled configuration as a function of laser intensity. A departure from the linear regime is observed for large laser intensities.

constant $g = 2.55\,\Gamma_{\rm p}$. For low illumination intensities [Fig. 3.5(a)], the ground state ($n = 0$) takes most of the weight, while the first excited states ($n = 1$) are only marginally populated. In contrast, for high intensity [Fig. 3.5(b)], the population of the system is distributed among different excited states, but with very different profiles for configurations with and without coupling. For the uncoupled system the population follows a broad Poisson distribution centered around $n = 4$, but for the coupled system the population is mainly concentrated in the ground ($n = 0$) and singly excited ($n = 1$) states. This is a direct consequence of the non-linearity and anharmonicity associated with the plasmon blockade, which prevents efficient plasmon excitation beyond $n = 1$.

In Fig. 3.5(c), we show the average number of plasmons $N_{\rm p} = \langle \hat{b}^\dagger \hat{b} \rangle$ supported by the graphene nanodisks as a function of external illumination intensity for different values of $E_{\rm F}$ and D (solid curves). The corresponding calculated coupling constant (g), plasmon frequency, and decay rate ($\omega_{\rm p}$ and $\Gamma_{\rm p}$) are shown in the text insets throughout Figs. 3.5(c),(d) with color codes standing for the selected values of $E_{\rm F}$ and D. Obviously, the uncoupled system ($g = 0$) presents a linear dependence on intensity, $N_{\rm p} = 4\,|\Omega|^2/\Gamma_{\rm p}^2$ (dashed curve, plotted for reference). In contrast, a significant departure from this linear behavior is observed above $|\Omega|^2/\Gamma_{\rm p}^2 \approx 10^{-2}$ in the coupled system as a signature of plasmon blockade (solid curves). As expected, the non-linearity increases with g. In the small intensity limit, the linear behavior is recovered for any value of g, as $N_{\rm p}$ is well below 1 (*e.g.*, for $|\Omega|^2/\Gamma_{\rm p}^2 < 10^{-2}$). However, even in this limit, the plasmon blockade severely modifies the plasmon statistics, as we show below.

The normalized absorption cross-section is shown in Fig. 3.5(d) as computed by assuming that the dominant dissipation channel is inelastic plasmon decay, and that the radiative part represents only a small fraction $\leq 1\%$ of the total decay rate [150]. In this limit, the absorption cross-section can be written as $\sigma_{\rm abs} = \hbar\omega_{\rm p}\Gamma_{\rm p}N_{\rm p}/I$, where $I \propto |\Omega|^2$ is the laser intensity. It is convenient to normalize the cross-section to that of the uncoupled graphene disk $\sigma_{abs,0}$ as

$$\frac{\sigma_{\rm abs}}{\sigma_{abs,0}} = \frac{N_{\rm p}}{4}\frac{\Gamma_{\rm p}^2}{|\Omega|^2}. \tag{3.3}$$

As shown in Fig. 3.5(d), the normalized absorption decreases with increasing

intensity and the nanodisk-emitter system behaves as a saturable absorber, again as a result of plasmon blockade, which is more pronounced for larger g (*cf.* green and blue curves).

3.3.2 Non-classical plasmons

Besides the plasmon blockade effect, the coupling between a graphene plasmon and a quantum emitter can also produce strong modifications in the plasmon statistics, which we characterize through the equal-time second-order correlation function, defined as $g^{(2)}(0) = \left\langle \hat{b}^\dagger \hat{b}^\dagger \hat{b} \hat{b} \right\rangle / N_{\rm p}^2$ [51]. This quantity becomes 1 for Poissonian distributions (also known as coherent states), which also characterize photons in a coherent laser source. In contrast, $g^{(2)}(0) > 1$ is associated with thermal distributions (super-Poissonian statistics), leading to bunching of photon pairs emerging from a thermal source (similar bunching is expected in thermally excited plasmons in uncoupled nanodisks). However, it is only for $g^{(2)}(0) < 1$ (sub-Poissonian statistics, leading to antibunching [151]) that a quantum description of photons or plasmons is needed, as a classical model cannot produce these values of the correlation function. Indeed, $g^{(2)}(0) = 0$ would mean the existence of a single plasmon state.

For graphene-nanodisk plasmons, $g^{(2)}(0)$ can be directly measured from the photons emitted *via* radiative plasmon decay [122]. Although less than one in a hundred plasmons decays by emitting a photon [7], even for the smallest intensities of the external illumination under consideration the resulting photon flux should allow for experimental verification of the non-classical, quantum-plasmonic regime: for instance, for a moderate incident intensity $\Omega = 0.1\,\Gamma_{\rm p}$, the rate of photon generation $\approx N_{\rm p}\,\Gamma_{\rm p,rad} \approx 4 \cdot 10^{-4}\,\Gamma_{\rm p} \approx 10^9\,{\rm s}^{-1}$ is significant.

Figure 3.6 shows $g^{(2)}(0)$ as a function of laser intensity for the different graphene nanodisks discussed in Fig. 3.5. We assume that the laser frequency is resonant with the $|\psi_0\rangle \rightarrow |\psi_{1+}\rangle$ transition, and $\omega_0 = \omega_{\rm p}$. In the absence of a quantum emitter (uncoupled system), we have $g^{(2)}(0) = 1$ (dashed line), so that plasmons are generated in coherent states, which are typical of coherent classical systems. When coupling is switched on (solid curves), $g^{(2)}(0)$ drops below one, and thus, non-classical plasmon states are generated. Furthermore, the minimum value that

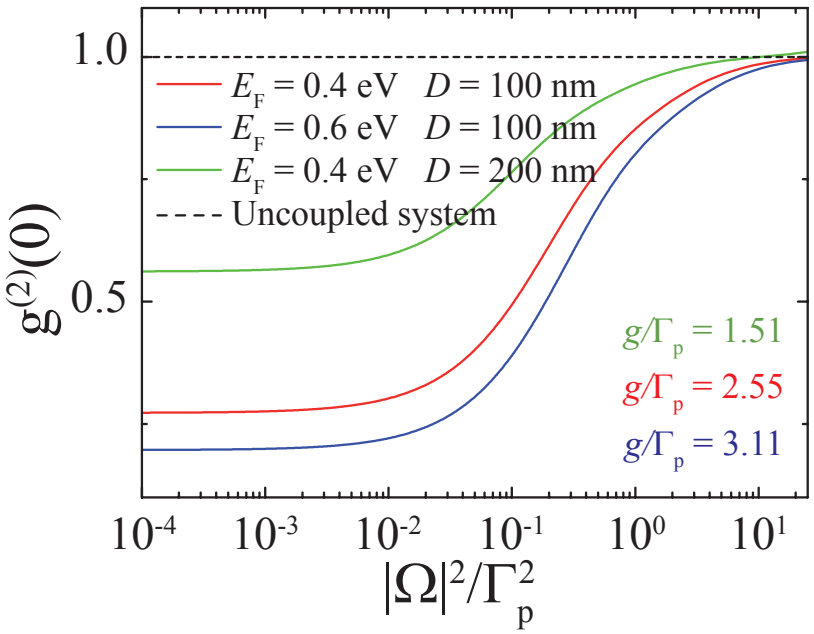

Figure 3.6: Non-classical plasmon states. We show the equal-time second-order correlation function $g^{(2)}(0) = \left\langle \hat{b}^\dagger \hat{b}^\dagger \hat{b} \hat{b} \right\rangle / N_p^2$ versus laser intensity for different disk diameters D and Fermi energies E_F (solid curves) under the same conditions as in Fig. 3.5. We also show $g^{(2)}(0) = 1$ (dashed line), as obtained for the uncoupled system. For finite coupling (solid curves) and relatively low intensity, $g^{(2)}(0)$ lies below 1 and decreases with increasing g/Γ_p, thus revealing the creation of non-classical plasmon states. For large intensity, $g^{(2)}(0)$ increases and eventually becomes larger than 1.

is reached depends on the coupling strength, decreasing with increasing g. As the laser intensity grows, $g^{(2)}(0)$ approaches the classical threshold $g^{(2)}(0) = 1$, and eventually rises above this value. This behavior can be understood by examining Figs. 3.5(a),(b), in which we see that small values of $|\Omega|^2/\Gamma_{\rm p}^2$ produce a negligible population of states above $n = 1$, therefore resulting in sub-Poissonian statistics. In contrast, for larger intensities the population of $n > 1$ states increases, thus resulting in the super-Poissonian behavior shown in Fig. 3.6 despite the plasmon-blockade.

3.3.3 Tunability of plasmon blockade

A great advantage of the plasmons supported by the graphene nanodisks is the possibility of controlling their properties by tuning the Fermi energy. This can be achieved, for instance, by introducing electrostatic doping [33], thus allowing us the tuning of both the plasmon energy and its coupling with the quantum emitter, and by extension, the modulation of the plasmon blockade effect. This is illustrated in Fig. 3.7(a), which shows the normalized absorption cross-section defined in Eq. (3.3) as a function of the graphene Fermi energy for different values of the laser intensity. The excitation energy of the quantum emitter is set to 0.16 eV, which coincides with the plasmon energy for $E_{\rm F} = 0.4\,$eV. As in the remainder of this work, the laser frequency is chosen to be resonant with the $|\psi_0\rangle \to |\psi_{1+}\rangle$ transition.

At small intensities (red curve), the normalized absorption cross-section approximately follows the same behavior as in the uncoupled system (dashed line), with a slight departure for low Fermi energies. When $|\Omega|^2$ increases (blue and green curves), the plasmon blockade effect produces significant non-linearity. The non-linearity is stronger for $E_{\rm F}$ below the resonance condition $E_{\rm F} = 0.4\,$eV. This behavior is directly connected to the evolution of $|\psi_{n\pm}\rangle$ states with detuning δ: these states are linear combinations of $|\uparrow n-1\rangle$ and $|\downarrow n\rangle$, but absorption dominates in the latter because it contains a larger number of plasmons. More precisely, the external illumination is tuned to induce transitions from the ground state to $|\psi_{1+}\rangle$. For $E_{\rm F} > 0.4\,$eV (*i.e.*, $g < |\delta|$ and $\delta < 0$), one finds that $|\downarrow 1\rangle$ has stronger weight in $|\psi_{1+}\rangle$, thus leading to higher absorption. In contrast, for $E_{\rm F} < 0.4\,$eV, where $g < |\delta|$ and $\delta > 0$, the weight of $|\downarrow 1\rangle$ is smaller and absorption is reduced. This example clearly illustrates that it is possible to enhance plasmon blockade by detuning the plasmon energy, which of

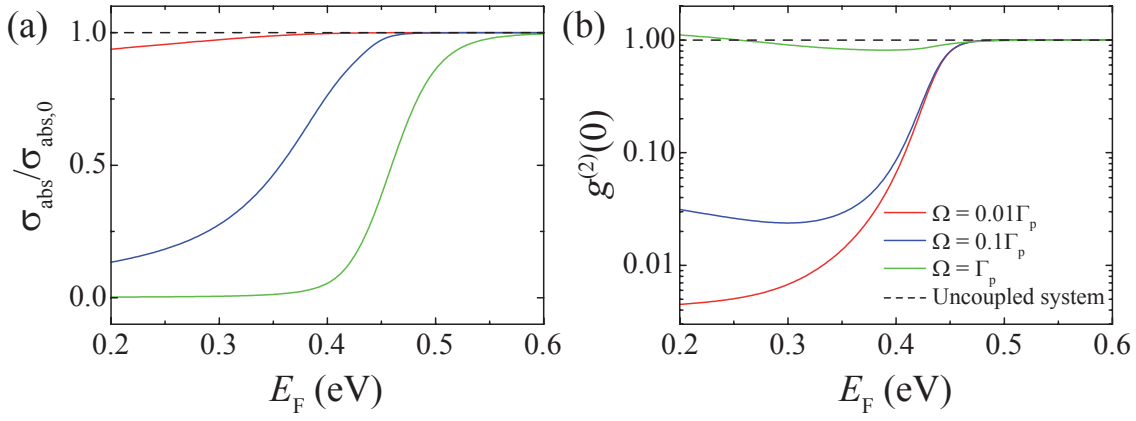

Figure 3.7: Tunability of graphene-nanodisk/emitter systems. (a) Normalized absorption cross-section of a graphene-nanodisk/emitter system as a function of graphene Fermi energy for different values of the external laser intensity. The nanodisk diameter is $D = 100\,\text{nm}$. The emitter has fixed excitation energy $\hbar\omega_0 = 0.16\,\text{eV}$, which coincides with the plasmon energy $\hbar\omega_\text{p}$ for $E_\text{F} = 0.4\,\text{eV}$. We tune the laser frequency to be resonant with the $|\psi_0\rangle \rightarrow |\psi_{1+}\rangle$ transition. The cross-section is normalized to that of the uncoupled system. At low laser intensity (red curve), the cross-sections with and without coupling are very similar. As $|\Omega|^2$ increases (blue and green curves), the cross-section becomes strongly non-linear for small E_F and essentially linear for large E_F. The transition between these two regimes is sharper for larger laser intensity. (b) Equal-time second-order correlation function $g^{(2)}(0)$ under the same conditions as in (a). For large intensity, $g^{(2)}(0)$ is found to be close to the classical value $g^{(2)}(0) = 1$. When the intensity decreases, we again observe two different regimes: for small E_F the system exhibits sub-Poissonian statistics associated with the existence of non-classical plasmons, while for larger E_F a classical behavior is recovered.

course can be controlled *via* the Fermi energy of the graphene nanodisk, provided we have coupling to a quantum emitter.

The enhancement of the plasmon blockade also influences the statistics of the generated plasmons, as shown in Fig. 3.7(b), where $g^{(2)}(0)$ is plotted as a function of the Fermi energy for the same conditions as in Fig. 3.7(a). The dashed line represents the uncoupled system (classical states). In the coupled system (solid curves) we again observe two different regions: for large values of E_F, the system approaches the classical limit ($g^{(2)}(0) \rightarrow 1$) due to the reduction in the efficiency of plasmon blockade. In contrast, for small E_F, the plasmon blockade is enhanced,

giving rise to antibunching ($g^{(2)}(0) < 1$). Clearly, the antibunching increases when the Fermi energy becomes smaller than $E_{\mathrm{F}} = 0.4\,\mathrm{eV}$, where the plasmon and the laser are on resonance. As expected, this effect is more pronounced for smaller illumination intensities (see also Fig. 3.6). Interestingly, there is an optimum value of E_{F} for which $g^{(2)}(0)$ reaches a minimum as a result of the interplay between the plasmon-emitter coupling g and the detuning δ. When the latter increases for $E_{\mathrm{F}} < 0.4\,\mathrm{eV}$, the state $|\psi_{1+}\rangle$ approaches $|\uparrow 0\rangle$, thus preventing higher n states to be populated, which results in lower $g^{(2)}(0)$. But at the same time g decreases, therefore reducing the anharmonicity of the energy ladder, which contributes to increase the value of $g^{(2)}(0)$. The tradeoff between these two effects results in an optimum value of E_{F} at which $g^{(2)}(0)$ presents a minimum.

3.4 Temporal quantum control with graphene

3.4.1 Controlled evolution of one emitter

In this section, we explore the possibility of controlling the temporal evolution of one or more quantum emitters interacting with the plasmons of a graphene nanodisk by switching on and off these plasmons through electrostatic gating. We first illustrate this concept by analyzing the interaction of a doped graphene nanodisk with a single quantum emitter (Fig. 3.8). The size of the disk is an important parameter that directly affects the plasmon frequency and the strength of the coupling to the emitter. Both of these magnitudes decrease with increasing diameter. Here, we choose a realistic nanodisk diameter of 100 nm, which is sufficiently large to ignore edge and quantum confinement effects that are otherwise important in smaller disks below 20 nm diameter (see Section 1.2 and [49]). The level of doping is characterized by the Fermi energy $E_{\mathrm{F}} = \hbar v_F \sqrt{\pi |n|}$ (see Section 1.1.3). This determines the plasmon energy $\hbar\omega_p \propto \sqrt{E_{\mathrm{F}}}$ and the plasmon decay rate $\Gamma_p \propto 1/E_{\mathrm{F}}$ [7]. The emitter is placed 60 nm above the center of the graphene nanodisk. This is a realistic geometry, considering recent advances in the control over the position and orientation of optical emitters [152, 153, 154]. One of the possibilities to facilitate such control consists in depositing a passive dielectric layer above the graphene sheet, the thickness of which determines the separation from the emitters.

Solid-state emitters based upon quantum dots or nitrogen-vacancies embedded in nanodiamond crystals offer the additional possibility of coating them with silica [155], thus providing a controlled spacing distance depending on the thickness of the coating layer. Once again, we model the emitter as a two-level system with a characteristic transition energy $\hbar\omega_0$ and a natural decay rate Γ_0. The different time scales that characterize the evolution of the system are plotted in Fig. 3.8(b). We choose a value of $\Gamma_0 \sim 10^3 - 10^4\,\mathrm{s}^{-1}$ typical of slowly emitting atoms such as erbium. When the emitter is placed close to the nanodisk, its decay rate is enhanced up to $\Gamma_{11} \sim 10^4\,\Gamma_0$ due to resonant interaction with the graphene plasmons. These decay rates are well below the frequencies at which the doping level can be modulated with currently available electronics ($\sim$ GHz), which is in turn much smaller than the plasmon frequency ω_p and the decay rate Γ_p. With this choice of parameters, we ensure that the emitter-plasmon interaction remains in the weak-coupling regime, instantaneously following any modulation of the doping level. Under such conditions, we can trace out the plasmonic degrees of freedom, and therefore the dynamics of the quantum emitter is completely described by the reduced density matrix $\hat{\rho}$, whose temporal evolution is given by [see Eq. (1.27)]

$$\dot{\hat{\rho}} = \frac{i}{\hbar}\left[\hat{\rho}, \hat{H}\right] + \frac{\Gamma_{11}}{2}\left[2\hat{c}\hat{\rho}\hat{c}^\dagger - \hat{c}^\dagger\hat{c}\hat{\rho} - \hat{\rho}\hat{c}^\dagger\hat{c}\right], \tag{3.4}$$

where $\hat{c}$ is the annihilation operator of the emitter excited state, and the Hamiltonian reduces to $\hat{H} = \hbar\omega_0\hat{c}^\dagger\hat{c}$. This is in contrast to the strong-coupling regime studied in the previous section, which can be reached for smaller emitter-graphene separations and requires a full description of the density matrix including the emitter and the plasmon modes, without tracing out the latter.

Incidentally, the electrostatic doping of the graphene nanodisk can influence the emitter spectrum by shifting the transition frequency through the Stark effect. This could be problematic in asymmetric systems, unless the shifts are small compared with the plasmon line width. However, for symmetrical configurations such as the ones that we consider here, all emitters experience the same frequency shift, and thus, this effect simply has to be taken into account when considering the graphene plasmon frequency for which the emitters are on resonance.

Figure 3.8(c) shows the normalized decay rate Γ_{11}/Γ_0 as a function of emission

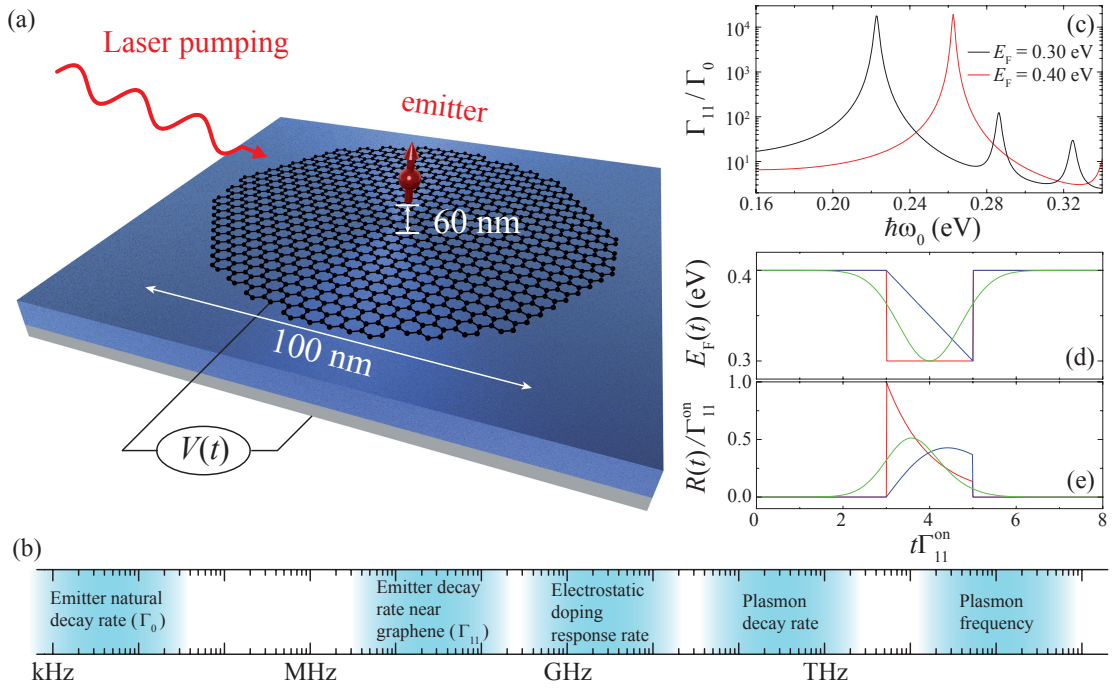

Figure 3.8: Temporal control over the quantum evolution of an optical emitter via interaction with a doped graphene nanostructure. (a) We consider a two-level optical emitter placed above a graphene nanodisk. The emitter is excited by a laser pulse. Electrical doping of the graphene through a bias potential V allows the nanodisk to support plasmons. The plasmon frequency is proportional to $\sqrt{|V|}$, and thus, it can be controlled over time by modulating $V(t)$. The coupling of the emitter to the plasmon and therefore the quantum evolution of the emitter state are both controlled by V. (b) Different time scales are involved in the evolution of the emitter-graphene system, represented here through the emitter natural decay rate Γ_0, the enhanced decay rate Γ_{11} produced by interaction with the graphene plasmons, and the plasmon decay rate and frequency typical of doped graphene. It is important to stress that the plasmon lifetime is short compared to the electric modulation rates of the doping potential, in the GHz range, which is in turn fast compared to the lifetime of the excited emitter. (c) The increase in emission rate Γ_{11}/Γ_0 is shown as a function of emission frequency for two different doping levels, quantified through the graphene Fermi energy E_F. The temporal profile of the emission rate $R(t)$ can be controlled by suitably modulating E_F over time as shown in (d) and (e) for $\hbar\omega_0 = 0.22\,\text{eV}$.

energy $\hbar\omega_0$ for two different doping levels corresponding to Fermi energies of 0.3 and 0.4 eV, respectively. Then, choosing an emitter of transition energy ≈ 0.22 eV (highest peak of black curve), we can switch the normalized decay rate from $\Gamma_{11}^{\mathrm{on}}/\Gamma_0 > 10^4$ down to $\Gamma_{11}^{\mathrm{off}}/\Gamma_0 \sim 10$, just by shifting the graphene doping level from 0.3 to 0.4 eV. This clearly shows the feasibility of controlling the temporal evolution of the quantum emitter by modulating the doping level of the graphene nanodisk between on- and off-resonance conditions. We explore this possibility in more detail in Figs. 3.8(d),(e) for three different doping modulation profiles: rectangular (red curve), triangular (blue curve) and gaussian (green curve). The emitter is initially prepared in the excited state, and we study the plasmon generation rate $R = \left\langle \Gamma_{11} \hat{c}^\dagger \hat{c} \right\rangle$, normalized to $\Gamma_{11}^{\mathrm{on}}$. This magnitude measures the number of plasmons generated per unit time, and it is calculated here neglecting decay channels others than plasmon generation. This assumption is well justified by the large values of $\Gamma_{11}^{\mathrm{on/off}}/\Gamma_0$. As shown in Fig. 3.8(e), each different doping profile results in a totally different evolution of the quantum emitter, which reflects the complete temporal control achievable with the system under study. Actually, it is not difficult to obtain the analytical relation existing between R and the single-emitter decay rate. Assuming the emitter in its excited state at time $t = t_0$, this relation reduces to

$$\Gamma_{11}(t) = \frac{R(t)}{1 - \int_{t_0}^{t} dt' R(t')}.$$

With the only constraint that $\Gamma_{11}(t) \leq \Gamma_{11}^{\mathrm{on}}$, a desired profile $R(t)$ can be achieved with the temporal evolution of $\Gamma_{11}(t)$ prescribed by this equation, which is in turn obtained by directly modulating the doping voltage, and therefore E_{F}, over time using the Lorentzian dependence of Γ_{11} on E_{F}.

3.4.2 Controlled interaction of two emitters

When a second quantum emitter is placed close to the graphene, the interaction between the two emitters can also be controlled over time. The interaction between two emitters in extended graphene and in ribbons has been recently shown to strongly enhanced or suppressed by the plasmons [157]. We investigate this possibility by studying the system depicted in Fig. 3.9(a), where two identical emitters are placed

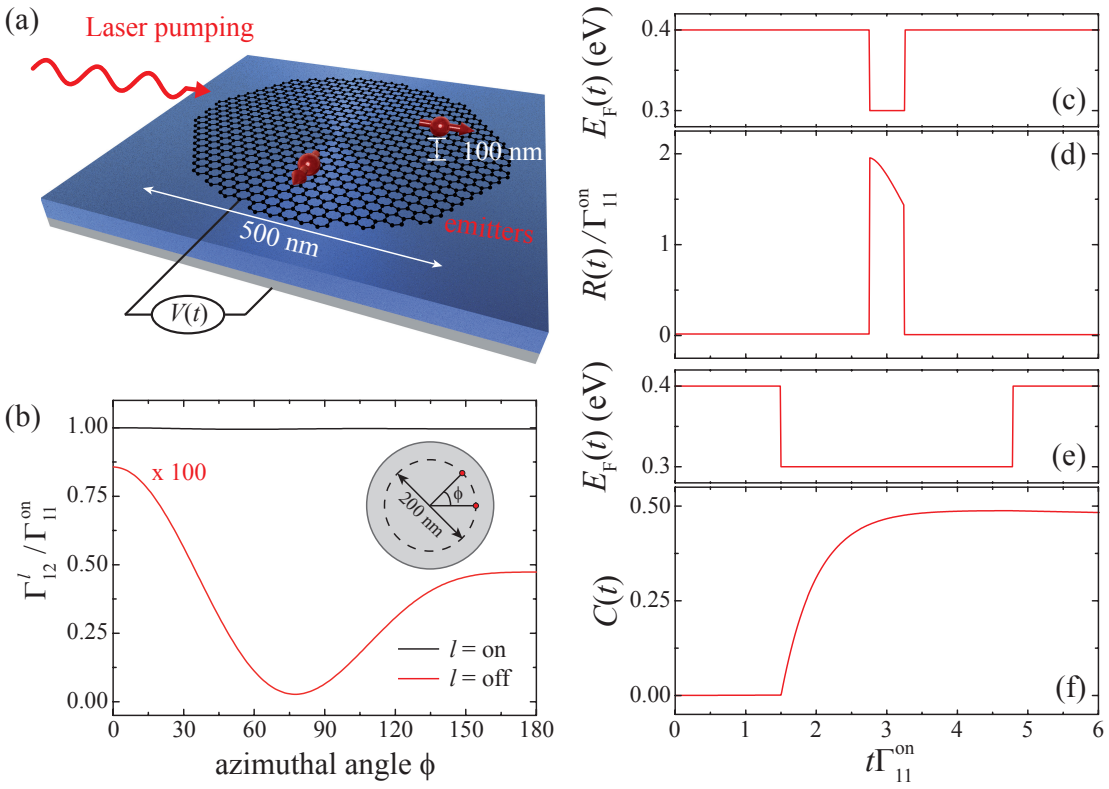

Figure 3.9: Temporal control over the interaction between quantum dots mediated by graphene. (a) Two emitters are excited and their decay and mutual interaction is modulated electrically through the plasmons of a neighboring graphene disk. (b) Interaction rate Γ_{12} as a function of the azimuthal angle between the positions of the dots (see inset) when plasmons of 0.108 eV energy (tuned to the energy of the emitters) are switched on ($E_F = 0.3$ eV) and off ($E_F = 0.4$ eV), and the emitter dipoles are along radial directions. The interaction rate is normalized to the on-resonance single-emitter decay rate Γ_{11}^{on}. The imposed temporal evolution of the doping (c) is used to control the emission rate (d) with the two emitters initially prepared in their excited states. When only one of the emitters is initially excited, the degree of entanglement for the doping profile of (e) is quantified through the Wootters concurrence (f) [156].

100 nm above a graphene nanodisk of 500 nm in diameter. The emitters are separated by a distance of $100\sqrt{2}$ nm and oriented along orthogonal radial directions, so that they can be independently excited by light plane waves linearly polarized along orthogonal directions. Their temporal evolution is determined by the generalization of Eq. (3.4),

$$\dot{\hat{\rho}} = \frac{i}{\hbar}\left[\hat{\rho}, \hat{H}\right] + \sum_{i,j=1}^{2} \frac{\Gamma_{ij}}{2}\left[2\hat{c}_i\hat{\rho}\hat{c}_j^\dagger - \hat{c}_i^\dagger\hat{c}_j\hat{\rho} - \hat{\rho}\hat{c}_i^\dagger\hat{c}_j\right], \tag{3.5}$$

where $\hat{H} = \hbar\omega_0 \sum_{i=1}^{2} \hat{c}_i^\dagger\hat{c}_i$ and $\Gamma_{12} = \Gamma_{21}$ is the interaction rate. This magnitude is plotted in Fig. 3.9(b) as a function of the azimuthal angle between the emitters, normalized to the on-resonance single-emitter decay rate Γ_{11}^{on}. When the doping level of the graphene nanodisk matches the on-resonance value, Γ_{12} remains nearly equal to Γ_{11}^{on} for all angles. In contrast, the normalized interaction rate $\Gamma_{12}/\Gamma_{11}^{\text{on}}$ drops below 0.01 when the doping is tuned to off-resonance conditions. Therefore, it is possible to switch on and off the interaction between the emitters. Fig. 3.9(d) quantifies this possibility through the temporal evolution of the plasmon generation rate $R = \left\langle \sum_{i,j=1}^{2} \Gamma_{ij}\hat{c}_i^\dagger\hat{c}_j \right\rangle$ associated with the doping profile shown in Fig. 3.9(c). The two emitters are assumed to be initially prepared in the excited state. Without interaction, they decay rather slowly and independently, resulting in a negligible value of R. This situation changes dramatically when the doping level is switched to the on-resonance condition, so that the emitters interact strongly and decay faster, producing a sudden jump in the plasmon generation rate.

The high degree of control displayed by this system can be exploited to temporally modulate different properties of the quantum emitters, such as their degree of entanglement. In Fig. 3.9(f) we plot the temporal evolution of the Wootters concurrence [156] associated with the doping profile of Fig. 3.9(e) when only one of the emitters is initially excited. The concurrence directly measures the degree of entanglement (1 for a maximally entangled state). Our system is capable of reaching a value of C close to 0.5, which is understandable because a single excited emitter can be re-written as a mixture of a symmetric (superradiant) state and anti-symmetric (subradiant) state, but the subradiant state lives for very long time, such that there is 50% chance of creating a long-lived entangled state. Larger degree of entangle-

ment can be achieved by various means, such as utilizing quantum emitters with more than two levels, heralded schemes based on photon detection, or coherent dipole-dipole interactions between the emitters.

3.4.3 Controlled superradiance of N emitters

A similar scheme can be used to control the evolution of an ensemble of emitters coupled to a graphene nanodisk. In particular, these emitters can be brought in a controlled manner to a superradiance regime [158, 159, 160, 161, 162] in which they are collectively coupled. We illustrate this possibility by studying the system depicted in Fig. 3.10(a). We consider a nanodisk of 500 nm in diameter, with N emitters periodically arranged along a co-axial circumference of 200 nm in diameter, placed 100 nm above the disk. The emitters are polarized perpendicularly to the graphene nanodisk and we assume a transition frequency $\hbar\omega_0 = 0.108\,\mathrm{eV}$, compatible with an on-resonance (off-resonance) Fermi energy of $E_\mathrm{F}^\mathrm{on} = 0.3\,\mathrm{eV}$ ($E_\mathrm{F}^\mathrm{off} = 0.4\,\mathrm{eV}$). The interaction rate between pairs of emitters Γ_{12} is plotted in Fig. 3.10(b) as a function of their relative azimuthal angle along the noted circumference, normalized to the on-resonance single-emitter decay rate Γ_{11}^on.

The temporal dynamics of the system is given by a generalized version of Eq. (3.5), with the sums extended over the N emitters. This is a straightforward task for small N, but it becomes unaffordable above $N \sim 10$ because the resulting Hilbert space grows exponentially with N. However, under perfectly symmetric coupling conditions ($\Gamma_{12} = \Gamma_{11}$ for all pairs of emitters), as it is the case in our system when $E_\mathrm{F} = E_\mathrm{F}^\mathrm{on}$, the temporal evolution is simplified because only symmetrical combinations of the single-emitter states are involved in the dynamics of the system [161]. These symmetrical states are characterized by a single quantum number M, which can take values in the interval $-N/2, \ldots, N/2$, where $M + N/2$ is the number of emitters that are in the excited state. Using this notation, it has been proved [161] that the generalization of Eq. (3.5) reduces to

$$\frac{1}{\Gamma_{11}}\dot{\hat{\rho}}_M = -\left(\frac{N}{2}+M\right)\left(\frac{N}{2}-M+1\right)\hat{\rho}_M + \left(\frac{N}{2}+M+1\right)\left(\frac{N}{2}-M\right)\hat{\rho}_{M+1},$$

which can be quickly solved for a large number of emitters. Furthermore, the small

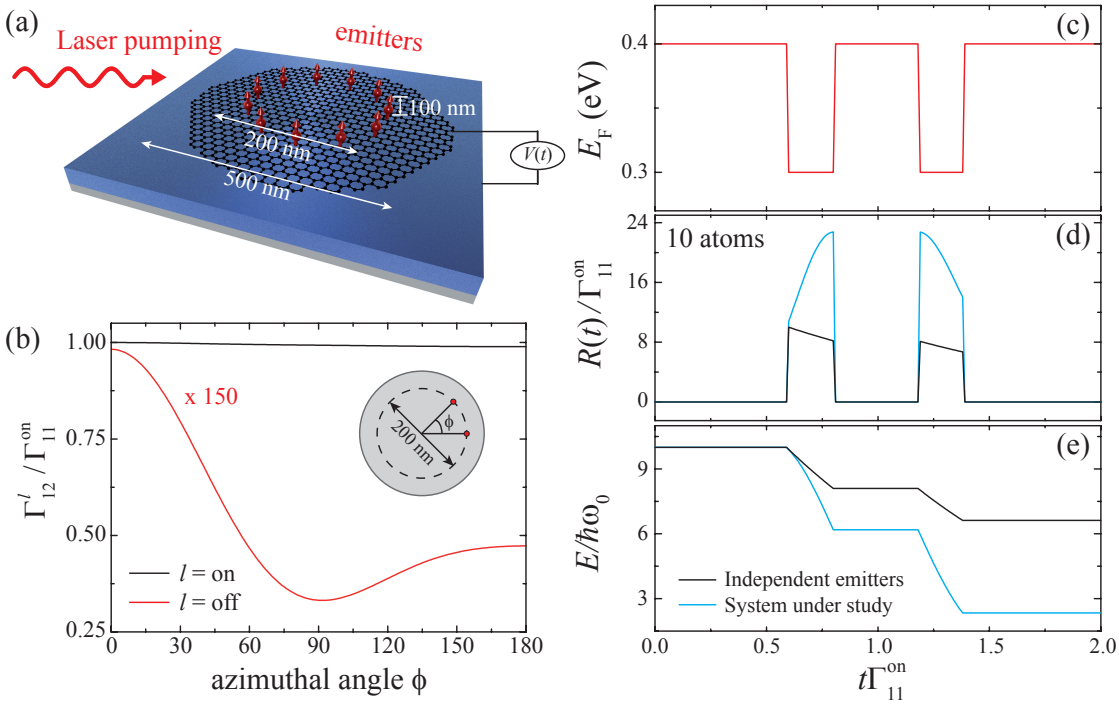

Figure 3.10: Control of the superradiance emission from an ensemble of emitters coupled to a graphene nanodisk. (a) N two-level quantum emitters are periodically arranged along a circumference of 200 nm in diameter placed 100 nm above a doped graphene nanodisk of 500 nm in diameter. The combined system possess $N-$fold rotation symmetry with the emitter dipoles oriented perpendicular to the disk. The system is pumped with an external laser that brings all emitters to the excited state at time $t = 0$. (b) Interaction rate Γ_{12} as a function of the azimuthal angle between the positions of the emitters (see inset) when plasmons of 0.108 eV energy (tuned to the energy of the emitters) are switched on ($E_{\rm F}^{\rm on} = 0.3\,{\rm eV}$) and off ($E_{\rm F}^{\rm off} = 0.4\,{\rm eV}$). The interaction rate is normalized to the on-resonance single-emitter decay rate $\Gamma_{11}^{\rm on}$. (c) Illustrative doping level of the graphene nanostructure as a function of time (normalized to $1/\Gamma_{11}^{\rm on}$). (d) Plasmon generation rate as a function of time for $N = 10$ emitters subject to the time-dependent doping of (c). The black curve stands for the case of independent emitters (*i.e.*, imposing $\Gamma_{12} = 0$), while the blue one corresponds to the fully interacting system. The plasmon generation rate is strongly enhanced by the collective superradiance effect produced by the coupling between the emitters. (e) Amount of energy released by the emitters as a function of time under the conditions of (d). Superradiance produces a considerably faster energy release.

values of Γ_{12}^{off} allow us to safely assume a system of independent emitters under off-resonance doping conditions. At this point, it is important to remark that we have not explicitly considered the coherent coupling existing between the emitters. In principle, this coupling produces a shift of the transition energies that can destroy the superradiance regime. However, for systems like ours in which all emitters are placed in symmetrically equivalent positions, the shift is the same for all, so we absorb it into the final transition energy $\hbar\omega_0$.

As a particular example to illustrate the concepts discussed here, we study the dynamics of $N = 10$ emitters controlled using the temporal doping profile shown in Fig. 3.10(c). We assume that all emitters are initially prepared in the excited state, and we normalize all rates and the time using Γ_{11}^{on}. Figure 3.10(d) shows the plasmon generation rate R. Initially, the emitters decay very slowly and independently, resulting in a negligible value of R. The situation changes dramatically when the doping is switched to the on-resonance level, with which the emitters decay faster, producing a sudden jump in the plasmon generation rate. In the independent emitters limit (black curve), the maximum rate is $R/\Gamma_{ii}^{\text{on}} = N$. In contrast, under resonant coupling (blue curves), $R/\Gamma_{ii}^{\text{on}}$ goes beyond N for $N > 2$ (superradiance regime). A high emission rate is repeatedly recovered when the doping is switched off and on at later times, thus revealing a high degree of control over the system dynamics.

Fig. 3.10(e) shows the amount of energy stored in the emitters as a function of time. As expected, this magnitude remains close to $N\hbar\omega_0$ until a resonant doping is switched on. When this happens, the emitters release their excitation energy during the time in which $E_{\text{F}} = E_{\text{F}}^{\text{on}}$.

3.5 Conclusions

In the first part of this chapter, we have presented a new approach based on the Zubarev's Green functions method for the study of the optical properties of plasmonic systems interacting with quantum emitters. This formalism describes the quantum internal evolution of such fermionic-bosonic hybrid systems beyond the perturbative regime. We have applied this method to analyze the optical properties of a system composed of a quantum emitter placed in the gap of a nanoparticle dimer.

Using realistic parameters, we have shown that the optical absorption spectrum of the dimer-quantum-emitter system can exhibit Fano resonances resulting from the interaction between the quantum emitter and the gap plasmon, in agreement with previous works [108, 109]. Our approach can be straightforwardly generalized to include more complicated interactions. This formalism is likely to become a powerful tool for the description of plasmon-exciton interactions in plasmonic transistors, modulators, and quantum information devices.

In the second part, we have fully characterized the non-linear optical response of a graphene nanodisk coupled to a quantum emitter. Because of the extraordinarily large lifetimes of graphene plasmons, this system is capable of reaching the strong-coupling regime, where a plasmon blockade effect emerges naturally in its optical response. This effect has two important consequences: (i) the optical absorption cross-section is dramatically modified and becomes strongly non-linear for large illumination intensities; and (ii) the correlation of the generated plasmons exhibits a clear non-classical behavior, as we demonstrate by studying the equal-time second-order correlation function $g^{(2)}(0)$. More precisely, non-classical plasmonic states (*i.e.*, states for which $g^{(2)}(0) < 1$) are generated due to the plasmon blockade, an effect that could be possibly detected by measuring correlations of photons emitted by radiative decay. Interestingly, we have shown that it is possible to control the optical non-linearity of the graphene-nanodisk/emitter system by tuning the plasmonic spectrum of the graphene nanodisk *via* electrostatic doping. These results open new paths for the design of novel quantum plasmonic devices with applications ranging from active metamaterials to quantum information processing.

Finally in the last part of the chapter, we have demonstrated that electrical modulation of the plasmon frequency in graphene provides an ingenious solution to achieve temporal control over the evolution of quantum emitters placed in the vicinity of a graphene nanostructure. This leads to a new paradigm in quantum information processing technologies and serves as a platform on which to test quantum phenomena controlled by means of externally applied, classical electrostatic potentials.

Chapter 4

Plasmons in graphene nanoislands

4.1 Introduction

Plasmons supported by metallic nanostructures result from the cooperative effect of many electron-hole (e-h) virtual excitations around the Fermi level. The resulting plasmon frequencies scale with the 1/2 power of the density of valence electrons [see Eq. (1.12)]. It is for this reason that massive amounts of charging are required to produce sizable frequency shifts in the plasmons supported by these nanostructures [163, 164], and therefore, their electrical control remains elusive.

This scenario has substantially changed with the arrival of graphene. As discussed in Section 1.1.3, graphene can support plasmons when it is doped, but now the plasmon frequency is proportional to the 1/4 power of the doping charge density rather than the square root of the valence electron density [31]. This behavior, which is a consequence of the peculiar electronic structure of graphene, characterized by a vanishing density of electron states at the Fermi level and a linear dispersion relation, makes possible to change the plasmon frequencies using relatively small amounts of charges.

Despite having a finite number of electrons, graphene nanostructures with dimensions of hundreds of nanometers, as the ones studied in Chapter 3, inherit

the tunability of extended graphene. This is not surprising because, due to the large number of atoms contained in these nanostructures (*e.g.*, a graphene nanodisk of 100 nm of radius contains $\approx 10^6$ atoms), their electronic structure resembles the one of extended graphene. In particular, the energy distance between the electronic states of these systems is much smaller than the typical Fermi energies. In this context, the question arises, what happens with small structures containing just hundreds of carbon atoms? Can we bring the level of doping needed to sustain plasmons in a small structure down to just a single electron?

In this chapter, we show that adding a single electron to a graphene nanoisland consisting of hundreds of atoms switches on IR plasmons that were previously absent from the uncharged structure. Remarkably, the addition of each further electron produces a dramatic frequency shift. These phenomena are highly sensitive to carbon edges. Specifically, armchair nanotriangles display sharp plasmons that are associated with intense near-field enhancement, as well as absorption cross-sections exceeding the geometrical area occupied by the graphene. In contrast, zigzag triangles do not support these plasmons.

We describe these nanotriangles using a combination of a tight-binding model for the electronic structure and the RPA [47] for the dielectric response. This methodology, explained in Section 1.2 and in Ref. [49], essentially extends to finite graphene islands what was previously reported for more extended systems by combining tight-binding and RPA. This effort was pioneered by Wallace [50] in graphene and graphite, and continued through outstanding analyses by other authors [43, 165, 31].

4.2 Plasmons in graphene nanoislands

Figure 4.1 summarizes our main finding: an electrically neutral graphene nanotriangle (with armchair edges and 7 nm side length) does not display strong polarization when illuminated by IR light; in contrast, the addition of a single electron results in the emergence of an intense plasmon mode, so that strong polarization is produced when the light is tuned to the plasmon energy (0.38 eV). A single electron can thus trigger the existence of plasmons in the structure. When further electrons are added to such armchair nanotriangle [Fig. 4.2(c)], this IR plasmon undergoes a dramatic

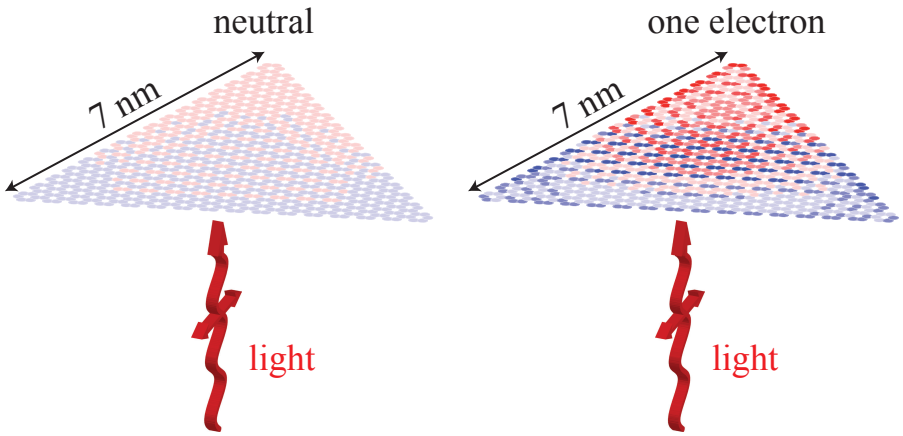

Figure 4.1: Single-electron switching of graphene plasmons. A neutral graphene nanotriangle (left) shows negligible polarization under external illumination. The same nanoisland displays a 0.38 eV plasmon resonance when it is charged with one electron, thus undergoing strong polarization (right). The density plots show the induced electron charge at the carbon sites. For comparison, the extinction cross-section is a sizable fraction of the graphene area in the resonant charged configuration and two order of magnitude smaller in the neutral island.

blue shift (in steps of ~ 0.1 eV) and it gains in strength. Notice that we denote the net charge of the structure as Q in Fig. 4.2, so that $Q < 0$ ($Q > 0$) corresponds to doping with electrons (holes).

Equally important, we find a near-IR plasmon with and without doping at an energy around ~ 0.88 eV. In contrast to the IR plasmon, this high-energy mode undergoes redshift with increasing doping. Both the IR and the near-IR plasmons give rise to large absorption cross-sections [Fig. 4.2(c)], which can reach values exceeding the geometrical area of the graphene for large doping in the IR and for low doping in the near-IR.

The plasmon shift is substantially larger than the width, thus making it clearly resolvable. Obviously, this conclusion depends on the parameter used for the intrinsic width $\hbar\tau^{-1}$ in the RPA [see Eq. (1.17)]. The main contributions to the width in extended graphene originate in optical-phonon losses, impurities, and disorder. These mechanisms are well described in extended graphene [36], and we take $\hbar\tau^{-1} = 1.6$ meV (*i.e.*, a dephasing time $\tau \sim 400$ fs) as a reasonable estimate for

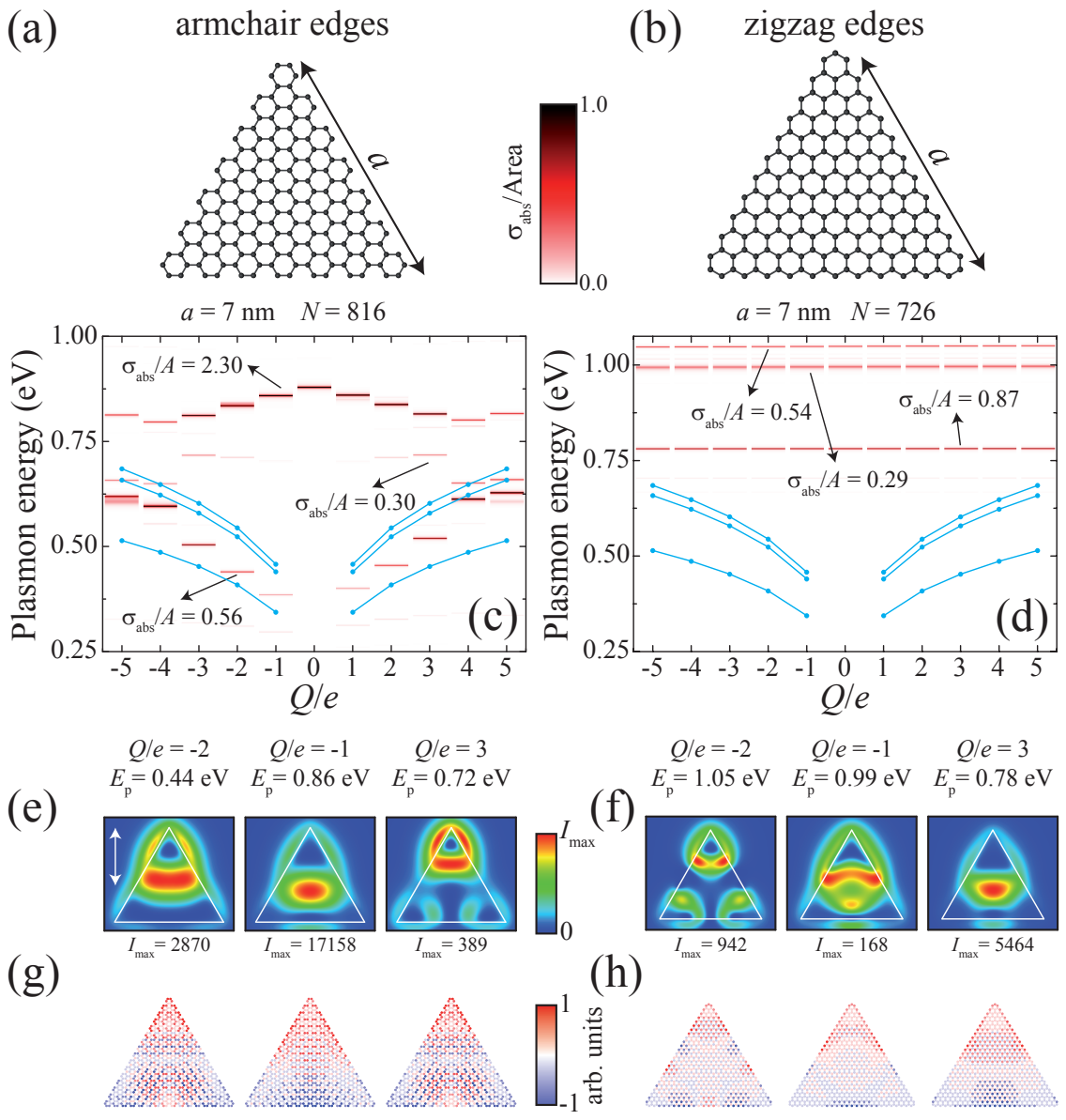

Figure 4.2: Plasmon resonances driven by single- and few-electrons or holes in graphene triangular nanoislands. We consider nanotriangles of either armchair (a) or zigzag (b) edges (side length $a = 7\,\mathrm{nm}$). (c) Absorption spectra of the ac island for various charge states Q/e, obtained from a microscopic description. The absorption cross-section (color scale) is normalized to the graphene area. The plasmon energies obtained from a classical electromagnetic description of the graphene are shown by blue curves. (d) Same as (c) for the zigzag island. (e)-(f) Near-field intensities and charge densities associated with selected plasmons of (c) and (d).

high-quality samples [46, 32]. Actually, given the small area of the islands, it should be possible to identify many of them without impurities or defects. Besides, the large shift-to-width ratios of Fig. 4.2 guarantee that our conclusions are still maintained with much higher losses up to the upper limit that is intuitively imposed by the lifetime of hot electrons ($\sim 85\,\mathrm{fs}$, as resolved from two-photon photoemission [166]). Additionally, Landau-damping is expected to be negligible for low-energy plasmons in defect-free extended graphene [167], and although plasmon decay into e-h pairs is made possible by the loss of translational symmetry in nanoislands, no substantial broadening is observed in the plasmons of armchair triangles beyond the intrinsic width $\hbar\tau^{-1}$ introduced through the RPA formula [see Eq. (1.17) and discussion below]. Actually, the plasmon energies do not overlap any intense e-h transition [see Fig. 4.5(c) below].

Incidentally, a classical electromagnetic description of the graphene (see the end of Section 1.1.3) also yields IR plasmons with similar shifts as the RPA calculations [Fig. 4.2(c), blue curve], although the plasmon energies are substantially higher in the latter due to quantum confinement [49]. However, the near-IR plasmons and their redshifts with increasing doping are completely missed by classical theory.

A completely different scenario is observed in zigzag nanotriangles [see Figs. 4.2(b),(d)] compared to armchair structures [see Figs. 4.2(a),(c)]: a single plasmon appears at $\sim 0.78\,\mathrm{eV}$ instead of the IR and near-IR plasmons; and the plasmon energy is rather independent of doping. This seems to be connected to the presence of near-zero-energy electronic states, which are known to exist near zigzag edges in a number determined by the net difference in the number of atoms in the two carbon sublattice of graphene nanoislands [168, 169, 170, 171, 172, 173] (see below). In a previous study [49], these states were found to produce plasmon dephasing in small islands. In the nanotriangle of Fig. 4.2(b), the number of such states is 24 per electron spin [see Fig. 4.3(a)]. Therefore, the addition of a few extra electrons does not substantially change the electronic structure. Moreover, as shown in Fig. 4.3(b), these states are completely confined at the edges of the nanotriangle and do not produce dipole transitions to higher-energy states [see Fig. 4.5(d)]. Therefore, they play a dummy role in the formation of plasmons. For these reasons, mid-IR plasmons are not observed in the zigzag island, and the near-IR plasmon is rather insensitive to the number of electrons added to it until the zero-energy electronic

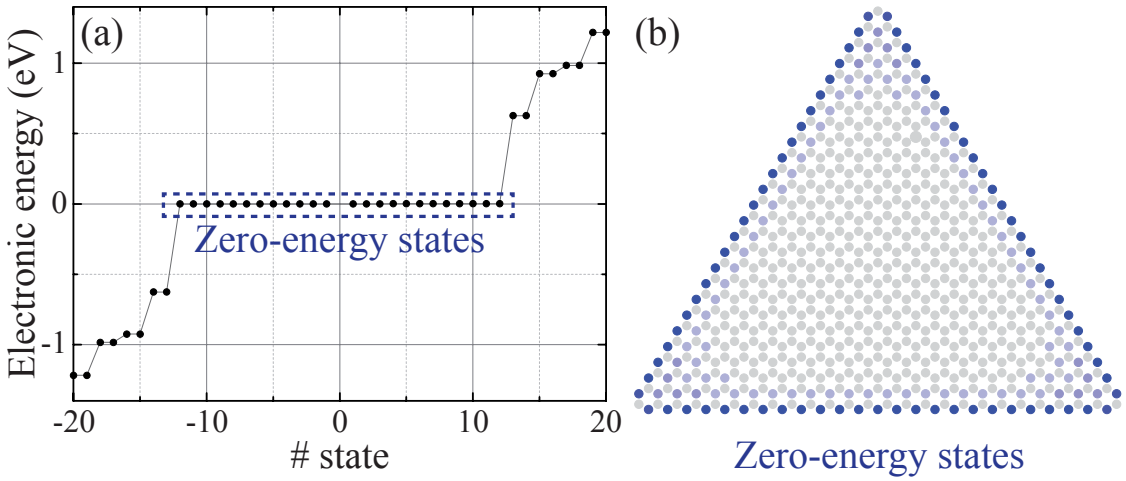

Figure 4.3: Electronic structure of a zigzag nanotriangle. (a) Electronic energies for the zigzag triangle represented in Fig. 4.2(b), showing 24 zero-energy states per electron spin at the Dirac point. (b) Spatial variation of the average probability density of the zero-energy states. These states are completely concentrated at the edges.

levels are completely filled. However, as it is shown in Fig. 4.4, when the zero-energy states are completely filled (depleted) and further electrons (holes) are added to the structure, the plasmons undergo drastic variations in energy with every new electron (hole). This is strong evidence that zero-energy states do not contribute to plasmons, and the tunability observed in graphene islands with varying doping is quenched by the presence of these states.

In extended graphene, the Dirac-cone band structure leads to a gap between intra- and inter-band e-h transitions. Long-lived plasmons exist in that gap. In nanoislands, the electron parallel momentum is not a good quantum number due to the lack of translational symmetry, but we can obtain insight into the role played by the electronic structure by analyzing the spatial Fourier transform of the electron wave functions [Figs. 4.5(a),(b)]. An incipient Dirac-cone structure is observed despite the finite size of the islands, which extends to a well defined Dirac cone in larger structures. In neutral nanostructures, all states below zero-energy are occupied, and remarkably, the density of states vanishes at the Dirac point in armchair islands (this is because both carbon sublattices have the same number

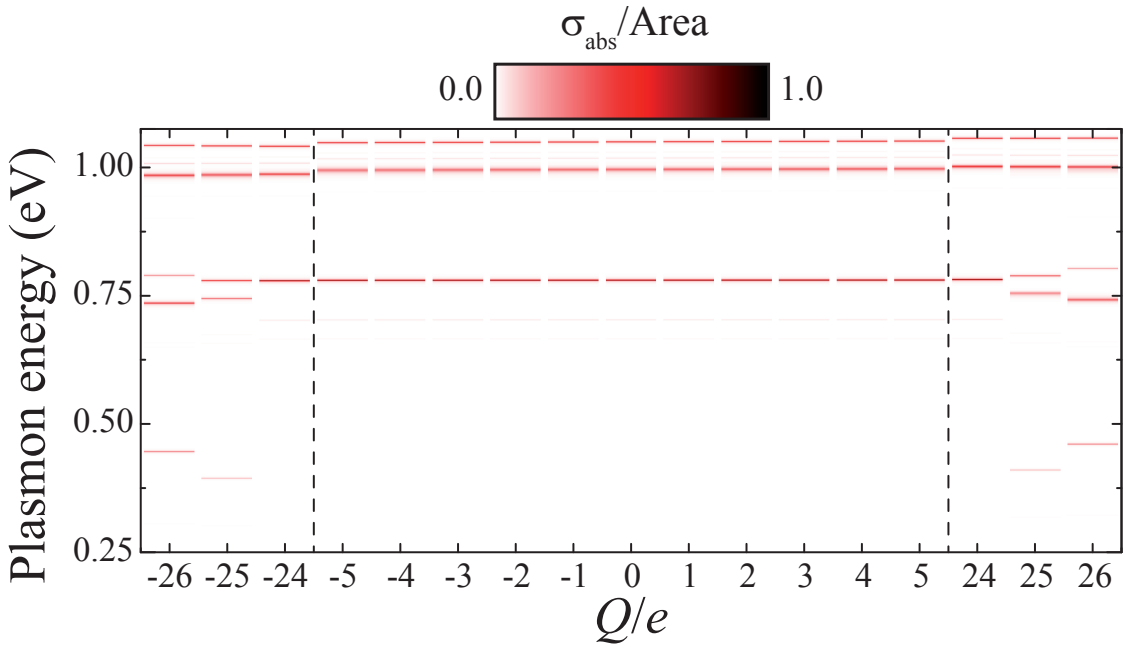

Figure 4.4: Emergence of plasmons upon filling all zero-energy electronic states in a zigzag triangle. As shown in Fig. 4.3, the zigzag triangle represented in Fig. 4.2(b) has 24 zero-energy states per electron spin at the Dirac point, half of which are occupied in the neutral configuration. No significant change in the plasmon energy and strength is observed by adding electrons (holes) until the zero-energy states are fully occupied (empty). This happens for $|Q|/e = 24$. In contrast, the addition (removal) of each further electron beyond this point produces sizable changes in the absorption cross-section.

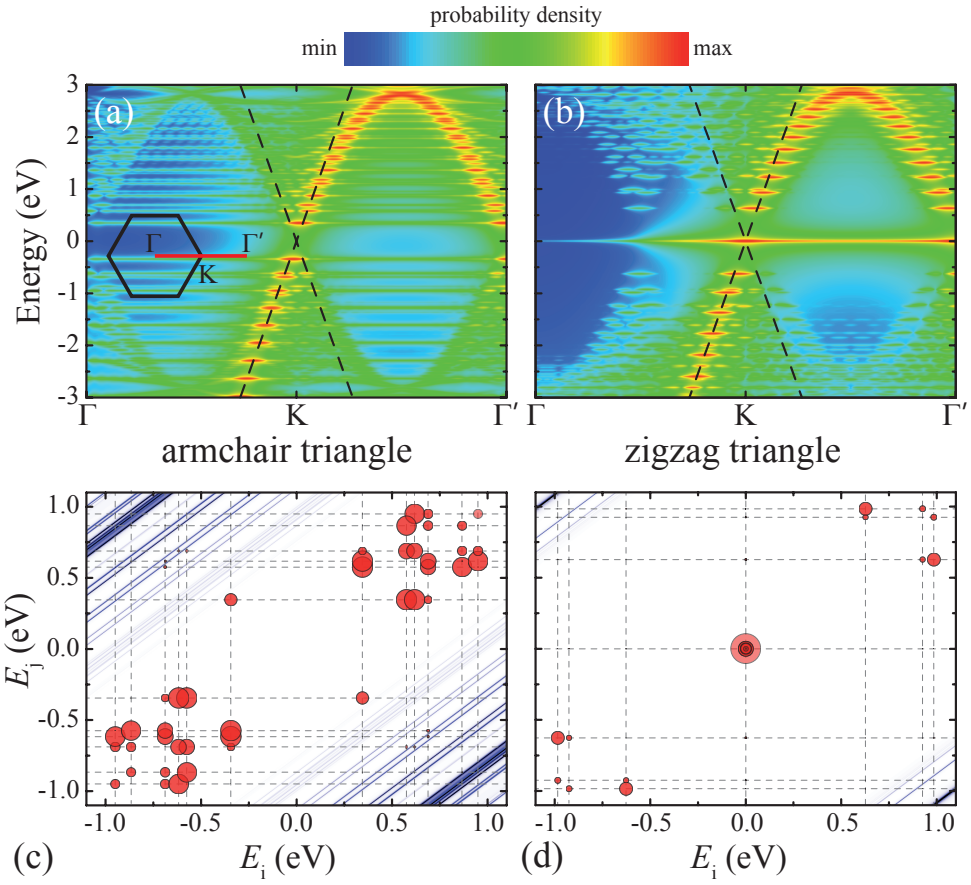

Figure 4.5: Understanding plasmons from the electronic structure. (a),(b) Intensity of the spatial Fourier transform of the electron wave functions in the same nanoislands as in Fig. 4.2. The intensity is summed over all one-electron states and it is represented as a function of energy and wave vector along the ΓK direction. The Dirac cone of extended graphene is shown by dashed lines. (c),(d) Plasmons and e-h excitations mismatch, represented through the single-electron dipole-transition matrix elements $|\langle\psi_i|x|\psi_j\rangle|^2 + |\langle\psi_i|y|\psi_j\rangle|^2$ as a function of initial (E_i) and final (E_j) electron-state energies. The area of the symbols is proportional to the squared matrix elements. The dark blue lines are obtained by setting $|E_i - E_j|$ to the plasmon energies of the islands under consideration [see Figs. 4.2(c),(d)].

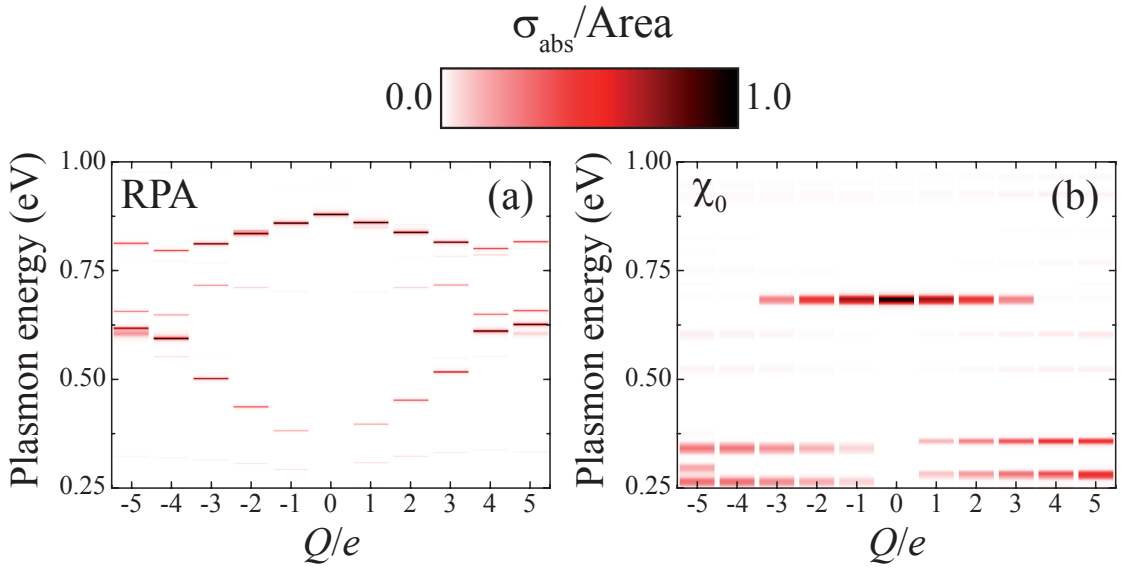

Figure 4.6: Collective character of nanotriangle plasmons. We compare the absorption spectra of the ac island of Fig. 4.2(a) calculated from the self-consistent RPA (a), with that obtained from the non-self-consistent RPA (b) for different values of Q/e.

of atoms [168]), which explains why the addition of a few electrons causes such dramatic changes in the optical response. In contrast, zigzag islands display an intense zero-energy feature associated with edge states [168], so that extra electrons do not produce significant effects in the electronic density of states, and therefore, as discussed above, the optical response is rather insensitive to the net charge of the structure until all zero-energy states are occupied.

The switching on of an IR plasmon with the addition of one electron poses the question, is this plasmon consisting of the oscillation of a single electron? The e-h excitation spectrum in the neutral armchair island has a gap $\sim 0.7\,\mathrm{eV}$, and the plasmon energies are actually not overlapping with those of intense e-h transitions, as we show in Figs. 4.5(c),(d). The observed plasmons are thus involving multiple interactions among virtual e-h excitations, leading to collective electron motion. Further evidence for this is obtained by realizing that the observed plasmon energies and their characteristics are completely missed within a non-interacting electron-gas picture. This is shown in Fig. 4.6, where we compare the full RPA

calculations described in Section 1.2 [Fig. 4.6(a)], with those obtained by removing the self-consistency in which the induced charge is computed as $\rho = \chi_0 \phi^{\text{ext}}$ [Fig. 4.6(b)]. This change leads to dramatic modifications in the plasmon spectrum: the plasmon dispersion with varying doping charge is removed, and the spectral features are now peaked at the positions of dominant electron-hole-pair transitions [see Fig. 4.5(c)], which is in contrast to the plasmonic resonances obtained from self-consistent calculations, the energies of which depend on the interaction among different electron-hole-pair virtual transitions, as a manifestation of the collective electron motion involved in these excitations. Nonetheless, despite this mounting evidence of multiple e-h interactions, the role of self-screening of each electron is still a pending issue that deserves a more detailed analysis outside the scope of the present work.

Plasmon excitations in these graphene islands produce a concentration of the electromagnetic energy down to a region $\sim 10^3$ smaller than the wavelength. This energy concentration leads to large levels of the field enhancement ($\sim 10^3$ in intensity) upon external illumination [Figs. 4.2(e),(f)], as well as absorption cross-sections larger than the geometrical area of the graphene [see Figs. 4.2(c),(d) and the scale bar]. The induced charge densities associated with these excitations are clearly showing dipolar excitation patterns with finer sign oscillations differentiating plasmons at different energies [see Figs. 4.2(g),(h)].

4.3 Conclusions

In this chapter we have studied the plasmonic response of graphene nanotriangles. We have found that the addition or removal of a single valence electron can switch on and off sharp plasmons in a structures already containing hundreds of valence electrons. A qualitatively similar conclusion is drawn by just examining the response of graphene nanoislands from a classical electrodynamics viewpoint. However, our quantum-mechanical simulations show that this intuition is strongly amended by the details of the atomic structure, to the point that the low-energy plasmons under consideration are simply absent from nanotriangles with zigzag terminations. In contrast, sharp IR plasmons appear in armchair-edge islands, although they are severely shifted with respect to classical theory. The predicted plasmons, and even

their mere existence, are thus non-trivially depending on the quantum mechanical properties of the underlying graphene fabric.

An important aspect of electrically tunable nanographene plasmons is that they can reach the near-IR regime due to the reduced size of the structures. The plasmon width in armchair nanotriangles is essentially limited by the intrinsic decoherence time. Using realistic values for this parameter, we predict absorption cross-sections exceeding the geometrical area of the graphene [see Fig. 4.2(c)]. This should allow the design of patterned graphene sheets with spacings of only a few nanometers for complete optical absorption at electrically tunable IR and near-IR frequencies [150].

Graphene nanoislands of sizes in the range of those considered here have been fabricated with different methods [174, 175, 176]. However, a major challenge is the synthesis of structures with the desired edge terminations. Although armchair edges are more energetically favorable and they are observed in experiments [177, 178], zigzag edges grow faster and dominate uncontrolled growth [179, 180]. Here, we are predicting appealing optical properties for armchair nanoislands, which are nonetheless expected to grow stably under very low or very high hydrogen chemical potential [181]. In this regard, a chemical-synthesis bottom-up approach can be beneficial to produce nanometer-sized graphene structures with well controlled edges [182, 183]. Actually, we have predicted a similar behavior in carbon molecules belonging to the group of polycyclic aromatic hydrocarbons. These molecules can be regarded as the smallest possible forms of graphene [184].

Our prediction of single-electron-induced extreme plasmon shifts relative to the plasmon widths opens new possibilities for ultrasmall sensors based upon the observation of minute amounts of charge transfer. For example, single-molecule detection should be possible by measuring the energy shift associated with the transferred charge upon absorption of donor or acceptor molecules, thus suggesting an alternative optical approach to electrical single-molecule detection in graphene [185]. However, giving the large mismatch between the wavelengths of graphene plasmons and light, plasmon readout of individual nanoislands is currently a challenge. In this respect, electrical [186] or electron-beam plasmon excitation and detection are promising options. In particular, electron beams can maximally couple to the plasmons of graphene. The large wavelength mismatch also leads to unprecedentedly high values of the Purcell factor (quality factor divided by

plasmon mode volume in units of the cubed wavelength), the field enhancement (with potential application to surface-enhanced IR absorption [187]), and the local density of optical states (reaching the strong light-matter interaction regime [7]). Tightly bound plasmons in graphene nanoislands are thus a promising tool for the investigation of fundamental optical phenomena and for applications to sensing and opto-electronics.

Chapter 5

Radiative heat transfer and friction in nanoscale systems

5.1 Introduction

Thermal and vacuum fluctuations of the electromagnetic field and the polarization of matter are responsible for many important phenomena that influence the mechanical and thermal dynamics of nanoscale systems (see Section 1.4). In particular, these fluctuations are at the origin of the blackbody radiation that mediates the radiative heat transfer (RHT) between bodies placed in vacuum and separated by large distances d compared to the thermal wavelength $\lambda_T = 2\pi\hbar c/k_{\rm B}T$. For parallel plates, this mechanism leads to a transfer rate that is independent of d. However, when $d \ll \lambda_T$, the rate is enhanced by several orders of magnitude due to the involvement of evanescent waves. Pioneering measurements [188, 189] revealed this phenomenon, which was explained within the framework of fluctuation electrodynamics [65, 190]. After a long series of experimental [191, 192] and theoretical [190, 193, 194, 195, 196, 197, 198, 64, 199, 200] studies, recent observations have accurately confirmed a $1/d^2$ dependence for sapphire plates at room temperature down to $d \sim 1\,\mu$m [192], and also a $1/d$ dependence for large silica spheres placed near a silica plate down to $d \sim 30\,$nm [201], although these laws can be substantially corrected by non-local [198], phonon [202, 203], and photonic crystal [204] effects. In this context, the

interaction of a particle with a plate has been explored both from experimental [205, 191, 201, 206] and theoretical [207, 202, 64, 208, 209, 210] fronts. Modeling heat exchange between two [211, 212, 213, 214, 215, 216, 217] or more [218] particles has been the subject of intense activity as well.

Magnetic polarization has been claimed to dominate RHT between metallic nanoparticles [213]. However, electromagnetic crossed terms (EMCTs, *i.e.*, terms mixing the electric and magnetic particle responses) have been ignored so far, although they could play a leading role in transfers within heterogeneous structures. Likewise, radiative corrections in the absorption of dielectric particles deserve further consideration, as we show below. Thus, the current level of understanding of RHT between two particles appears to be incomplete.

In the first part of this chapter, we formulate a complete solution of RHT between two nanoparticles within the assumption of dipolar response. We show that EMCTs are dominant in combinations of metallic and dielectric particles, such as gold and SiC. We introduce a relevant retardation correction beyond the customary treatment of polarization fluctuations, which results in a sizable reduction in the predicted transfer rate. Furthermore, we show that heat losses into the environment can be either dominant or negligible depending on the temperature and particle composition. An accurate description of RHT in nanostructured environments requires incorporating these effects, for which the two-particle system discussed here provides a tutorial approach as well as an estimate of the importance of EMCTs, radiative corrections, and interaction with the environment.

In addition to RHT, the thermal and vacuum fluctuations of charges and fields can also generate forces between nanostructures, as it happens with the van der Waals and Casimir interactions [64, 219]. In particular, these phenomena are at the origin of non-contact friction existing between objects set in relative uniform motion [220, 221]. This effect was first predicted for the case of two planar homogeneous surfaces, and has recently generated a heated debate [222, 223, 224, 225, 226]. Finite objects, such as particles moving parallel to surfaces [64, 227], are also expected to experience this non-contact friction. A particularly interesting case is constituted by a spinning particle, which contrarily to the previously analyzed systems, it only involves one object.

The study of such rotating system is the main objective of the second part

of this chapter. In particular, we investigate the friction experienced by rotating, neutral particles due to the interaction with the vacuum and thermal electromagnetic field. For this purpose we first follow a semiclassical approach developed within the framework of fluctuation electrodynamics [65] and therefore involving the use of the FDT (see Section 1.4). This formalism allows us to find analytical expressions for both the frictional torque and the power radiated by the particle during the stopping process. Although the semiclassical model is completely rigorous and unambiguous, one could question the validity of the FDT for a system that is out of mechanical equilibrium. In order to clarify this point, we develop a fully quantum-mechanical theory, in which the electromagnetic response of the particle is governed by bosonic excitations such as phonons and plasmons. The results of both the semiclassical and the quantum-mechanical approaches are in complete agreement, thus allowing us to obtain deeper understanding of the physical processes underlying thermal and vacuum friction. For instance, the quantum-mechanical approach provides us with a solid argument to predict, within the limits of our model, the absence of friction in non-absorbing spherical particles possessing large optical gap compared to the rotation and the thermal-radiation frequencies. In contrast, particles made of lossy materials such as metals undergo friction even at zero temperature, unlike what has been previously predicted [228, 229].

5.2 Radiative heat transfer between nanoparticles

5.2.1 Description of the model

We consider two spherical particles of radius R at temperatures T_1 and T_2 separated by a center-to-center distance d along the z direction and placed in a vacuum at temperature T_0, as shown in Fig. 5.1. We focus on small particles such that $R \ll d$, λ_T, so that their responses can be described through the polarizabilities α_1 and α_2 (see Ref. [212]). RHT between the particles and the environment is produced by fluctuations in the vacuum electromagnetic field and the particle dipoles. We simplify the notation by combining electric and magnetic field components acting

on each particle $j = 1, 2$, as well as electric and magnetic dipoles, in the vectors $\mathbf{E}_j = (E_{j,x}, E_{j,y}, E_{j,z}, H_{j,x}, H_{j,y}, H_{j,z})^\top$, and $\mathbf{p}_j = (p_{j,x}, p_{j,y}, p_{j,z}, m_{j,x}, m_{j,y}, m_{j,z})^\top$, respectively. Likewise, the polarizability tensor becomes

$$\alpha_j = \begin{pmatrix} \alpha_j^{\mathrm{E}} \mathbb{I}_3 & 0 \\ 0 & \alpha_j^{\mathrm{M}} \mathbb{I}_3 \end{pmatrix},$$

where $\mathbb{I}_3$ is the 3×3 identity matrix and the E (M) superscript refers to electric (magnetic) components.

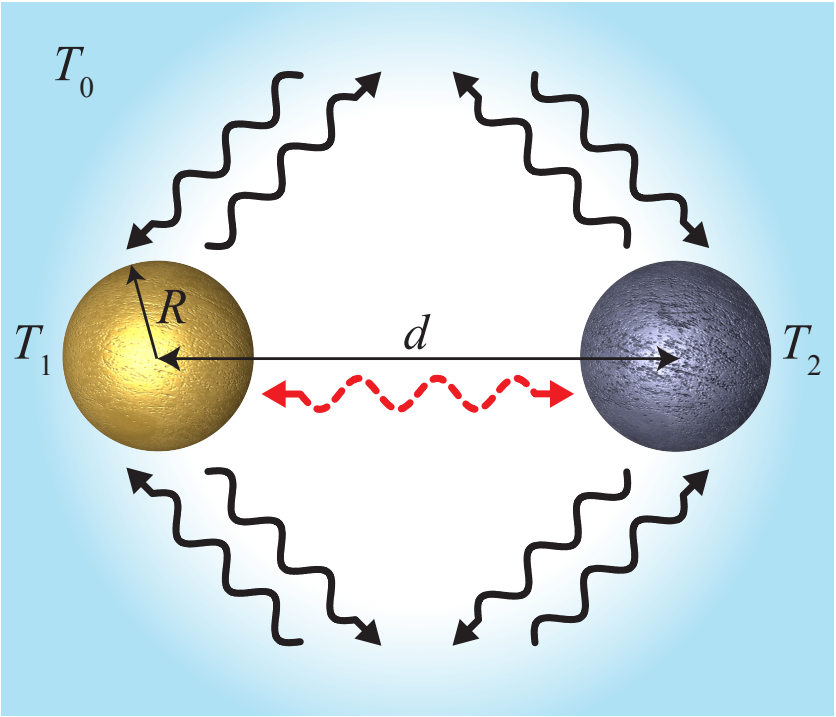

Figure 5.1: Description of the system under study. Two particles of radius R at temperatures T_1 and T_2 separated by a distance d are placed in a vacuum at temperature T_0. Each particle exchanges thermal energy with the other particle and with the surrounding vacuum.

The net power absorbed by particle 1 is the sum of dipole and field fluctuation terms,

$$\mathcal{P}_1 = \mathcal{P}_1^{\mathrm{field}} + \mathcal{P}_1^{\mathrm{dip}}.$$

More precisely,

$$\mathcal{P}_1^{\text{field}} = \int_{-\infty}^{\infty} \frac{d\omega d\omega'}{(2\pi)^2} e^{-i(\omega-\omega')t}\, \omega' \left\langle \mathbf{E}_1^{+}(\omega') \left[i\alpha^{+}(\omega') - (2k'^3/3)|\alpha(\omega')|^2 \right] \cdot \mathbf{E}_1(\omega) \right\rangle \quad (5.1)$$

represents the work exerted by the fluctuating field on particle 1. Here, $k = \omega/c$ is the wave vector of light at frequency ω. Moreover, the self-consistent fields $\mathbf{E}_j$ include the response of the system to the fluctuating source fields $\mathbf{E}_j^{\text{fl}}$ via the relations

$$\mathbf{E}_1 = \mathbf{E}_1^{\text{fl}} + \mathcal{G}_{12}\alpha_2\mathbf{E}_2, \qquad \mathbf{E}_2 = \mathbf{E}_2^{\text{fl}} + \mathcal{G}_{21}\alpha_1\mathbf{E}_1,$$

where $\mathcal{G}_{12}$ is the distance-dependent dipole-dipole inter-particle interaction,

$$\mathcal{G}_{12} = \begin{pmatrix} A & 0 & 0 & 0 & -C & 0 \\ 0 & A & 0 & C & 0 & 0 \\ 0 & 0 & B & 0 & 0 & 0 \\ 0 & C & 0 & A & 0 & 0 \\ -C & 0 & 0 & 0 & A & 0 \\ 0 & 0 & 0 & 0 & 0 & B \end{pmatrix},$$

$$\begin{aligned} A &= \exp(ikd)\,(k^2/d + ik/d^2 - 1/d^3), \\ B &= \exp(ikd)\,2(1/d^3 - ik/d^2), \\ C &= \exp(ikd)\,(k^2/d + ik/d^2), \end{aligned}$$

and $\mathcal{G}_{21}$ takes the same form as $\mathcal{G}_{12}$ with C replaced by $-C$. In Eq. (5.1), $\langle\rangle$ represents the average over field fluctuations, which we perform by applying the FDT (see Section 1.4)

$$\left\langle \left[\mathbf{E}_j^{\text{fl}}(\omega)\right]^{+} \cdot \mathbf{E}_{j'}^{\text{fl}}(\omega') \right\rangle = 4\pi\hbar\delta(\omega-\omega')\eta_{jj'}(\omega) \left[n_0(\omega) + \frac{1}{2} \right],$$

where $\eta_{12} = (1/2)\left[\text{Im}\{\mathcal{G}_{12} + \mathcal{G}_{21}\} + i\text{Re}\{\mathcal{G}_{12} - \mathcal{G}_{21}\}\right]$, $\eta_{21} = \eta_{12}^{+}$, $\eta_{11} = \eta_{22} = (2k^3/3)\mathbb{I}_6$, and $n_0(\omega) = [\exp(\hbar\omega/k_{\text{B}}T_0) - 1]^{-1}$ is the Bose-Einstein distribution at the vacuum temperature T_0.

Likewise, the contribution of fluctuating dipoles is

$$\mathcal{P}_1^{\rm dip} = \int_{-\infty}^{\infty} \frac{d\omega d\omega'}{(2\pi)^2} e^{-i(\omega-\omega')t} \left[i\omega' \left\langle \mathbf{p}_1^+(\omega') \cdot \mathcal{G}_{12}(\omega) \mathbf{p}_2(\omega) \right\rangle - \frac{2\omega^4}{3c^3} \left\langle \mathbf{p}_1^+(\omega') \cdot \mathbf{p}_1(\omega) \right\rangle \right], \tag{5.2}$$

where the first term inside the square brackets accounts for the effect of the field produced by particle 2 on particle 1, while the second term describes the interaction of the particle dipole with the vacuum. The self-consistent dipoles satisfy the relations

$$\mathbf{p}_1 = \mathbf{p}_1^{\rm fl} + \alpha_1 \mathcal{G}_{12} \mathbf{p}_2, \qquad \mathbf{p}_2 = \mathbf{p}_2^{\rm fl} + \alpha_2 \mathcal{G}_{21} \mathbf{p}_1,$$

where $p_j^{\rm fl}$ is the fluctuating source dipole at particle j. The relevant FDT now becomes (see Section 1.4)

$$\left\langle \left[\mathbf{p}_j^{\rm fl}(\omega) \right]^+ \cdot \mathbf{p}_{j'}^{\rm fl}(\omega') \right\rangle = 4\pi\hbar\delta(\omega-\omega')\delta_{jj'}\chi_j(\omega) \left[n_j(\omega) + \frac{1}{2} \right],$$

where we use

$$\chi_j = {\rm Im}\{\alpha_j\} - (2k^3/3)|\alpha_j|^2 \mathbb{I}_6, \tag{5.3}$$

rather than ${\rm Im}\{\alpha_j\}$ in order to prevent non-absorbing particles from undergoing unphysical fluctuations. We set the polarizability to $\alpha_j^\nu = (3/2k^3) t_{j,1}^\nu$ ($\nu = {\rm E}, {\rm M}$), where $t_{i,1}^\nu$ is the dipole Mie scattering coefficient [see Eqs. (1.14) and (1.15)]. This definition of α_j complies with the optical theorem condition ${\rm Im}\{\alpha_j\} \geq (2k^3/3)|\alpha_j|^2$ [230], where the equality applies to non-absorbing particles ($\chi_j = 0$). It is important to keep in mind that dipole and field fluctuations originate in different physical systems, which can have different temperatures. As a consequence of this, the correlations between the dipole and field fluctuations vanish, and therefore we do not need to consider any crossed term involving them.

Finally, using the FDT to evaluate the integrals of Eqs. (5.1) and (5.2), we find, after some lengthy but straightforward algebra,

$$\mathcal{P}_1 = \frac{2\hbar}{\pi} \sum_{\nu={\rm E,M}} \int_0^\infty \omega d\omega \; \chi_1^\nu \sum_{i=1}^{2} \left(\frac{2\Gamma_{i\perp}^\nu}{|s|^2} + \frac{\Gamma_{i\parallel}^\nu}{|t_\nu|^2} \right), \tag{5.4}$$

where

$$\Gamma^{\nu}_{1\perp} = \left[\frac{2k^3}{3}\left(|u_\nu|^2 + |w_\nu|^2\right) + \mathrm{Im}\left\{\alpha_2^{\nu}\left[Au_\nu - g_\nu C w_\nu\right]\left[Au_\nu^* + g_\nu C w_\nu^*\right]\right\}\right.$$
$$\left. + \mathrm{Im}\Big\{\alpha_2^{\nu'}\left[Aw_\nu - g_\nu C u_\nu\right]\left[Aw_\nu^* + g_\nu C u_\nu^*\right]\Big\}\right](n_0 - n_1),$$
$$\Gamma^{\nu}_{2\perp} = \left(\chi_2^{\nu}\left|Au_\nu - g_\nu C w_\nu\right|^2 + \chi_2^{\nu'}\left|Aw_\nu - g_\nu C u_\nu\right|^2\right)(n_2 - n_0),$$
$$\Gamma^{\nu}_{1\parallel} = \left[\frac{2k^3}{3} + \mathrm{Im}\left\{\alpha_2^{\nu} B^2\right\}\right](n_0 - n_1),$$
$$\Gamma^{\nu}_{2\parallel} = \chi_2^{\nu}\left|B\right|^2\ (n_2 - n_0),$$
$$u_\nu = 1 - \alpha_1^{\nu'}\alpha_2^{\nu'}A^2 + \alpha_1^{\nu'}\alpha_2^{\nu}C^2,$$
$$w_\nu = \alpha_1^{\nu'}\left(\alpha_2^{\mathrm{E}} - \alpha_2^{\mathrm{M}}\right)AC,$$
$$\mathrm{s} = 1 - \alpha_1^{\mathrm{E}}\alpha_2^{\mathrm{E}}A^2 - \alpha_1^{\mathrm{M}}\alpha_2^{\mathrm{M}}A^2 + \alpha_1^{\mathrm{E}}\alpha_2^{\mathrm{M}}C^2 + \alpha_1^{\mathrm{M}}\alpha_2^{E}C^2 + \alpha_1^{\mathrm{E}}\alpha_2^{\mathrm{E}}\alpha_1^{\mathrm{M}}\alpha_2^{\mathrm{M}}\left(A^2 - C^2\right)^2,$$
$$\mathrm{t}_\nu = 1 - \alpha_1^{\nu}\alpha_2^{\nu}B^2,$$

and $\nu' = \mathrm{M}$ (E) and $g_\nu = +1$ (-1) when $\nu = \mathrm{E}$ (M).

Neglecting the magnetic response ($\alpha_j^{\mathrm{M}} = 0$, $C = 0$), multiple scattering ($u_\nu = t_\nu = s = 1$, $w_\nu = 0$), and radiative corrections in the particles response ($\chi_j = \mathrm{Im}\{\alpha_j\}$), the above expressions reduce to

$$\mathcal{P}_1 = \frac{4\hbar}{\pi}\int_0^\infty \omega\, d\omega\ \mathrm{Im}\left\{\alpha_1^{\mathrm{E}}\right\}\ \left\{\left[k^3 + 2\mathrm{Re}\left\{\alpha_2^{\mathrm{E}}A\right\}\mathrm{Im}\{A\} + \mathrm{Re}\left\{\alpha_2^{\mathrm{E}}B\right\}\mathrm{Im}\{B\}\right]\right.$$
$$\left.\times\,(n_0 - n_1) + \mathrm{Im}\left\{\alpha_2^{\mathrm{E}}\right\}\left(|A|^2 + |B|^2/2\right)\ (n_2 - n_1)\right\},$$

where the $n_2 - n_1$ term describes direct RHT between the dimer particles and coincides with a previously reported expression [211, 213, 216]. The remaining $n_0 - n_1$ term accounts for heat exchange between particle 1 and the surrounding vacuum, partially assisted by the presence of particle 2.

5.2.2 Results and discussion

We study in Figs. 5.2 and 5.3 the heat transfer coefficient (HTC) between two particles in a dimer when particle 1 is at the same temperature as the environment

($T_1 = T_0 = T$) and particle 2 is at a slightly different temperature ($T_2 = T + \delta T$). The HTC to particle 1 is defined per unit of temperature difference as $\mathcal{P}_1/\delta T$. Under these conditions, only the terms $\Gamma^{\nu}_{2,\perp}$ and $\Gamma^{\nu}_{2,\parallel}$ contribute to the transfer. The results obtained from the above formalism (solid curves) are compared to several approximations consisting of neglecting multiple scattering between the particles (circles, calculated for $u_\nu = t_\nu = s = 1$, $w_\nu = 0$), retardation effects everywhere (dashed curves, $k = 0$), retardation effects except in the particle response χ_j defined by Eq. (5.3) (triangles), or EMCTs (dotted curves).

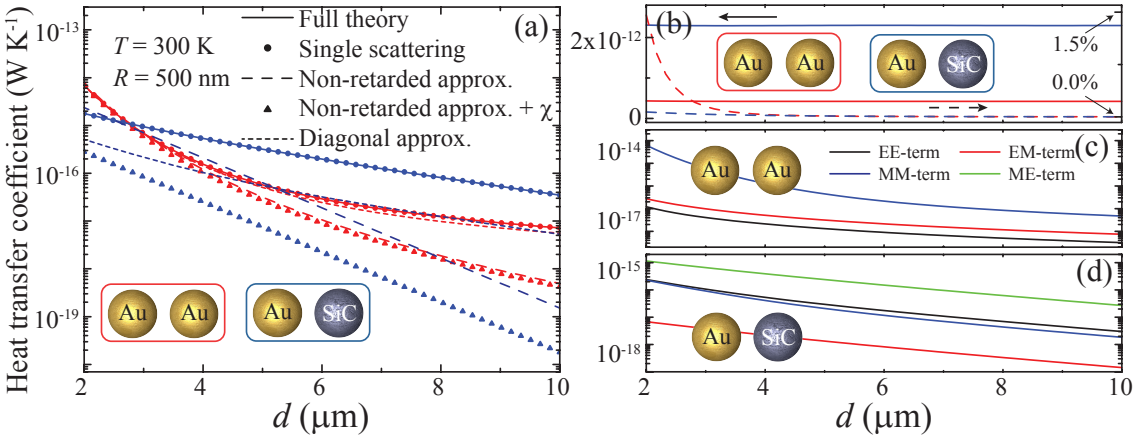

Figure 5.2: Dependence of the radiative heat transfer coefficient (HTC) on particle separation d. The HTC from particle 2 (right) to particle 1 (left) is defined as $\mathcal{P}_1/\delta T$ with $T_1 = T_0 = T$ and $T_2 = T + \delta T$ (see Fig. 5.1). (a) HTC at $T = 300\,\mathrm{K}$ obtained from our full theory (solid curves), compared to the result of neglecting multiple scattering (circles), retardation effects everywhere (dashed curves), retardation effects except in χ_j (triangles), or EMCTs (dotted curves). Gold-gold (red curves) and gold-SiC (blue curves) dimers are considered. The particles radius is $R = 500\,\mathrm{nm}$. (b) Heat power lost by particle 2 (solid curves) and fraction of that power absorbed by particle 1 (broken curves, right scale). (c),(d) Electric-electric (black), electric-magnetic (red), magnetic-magnetic (blue), and magnetic-electric (green) partial contributions to the HTC in the gold-gold (c) and gold-SiC (d) dimers.

The distance dependence of the HTC is analyzed in Fig. 5.2 for a homogeneous gold dimer and for a dimer formed by gold and SiC particles. As a first observation,

we note that multiple scattering events can be safely neglected in all cases. In contrast, retardation causes a dramatic boost in the HTC, which increases with particle distance in both types of dimers. Additionally, the $|\alpha|^2$ term of Eq. (5.3) contributes with a uniform decreasing factor in SiC particles (see Fig. 5.6). (Notice that the absorption cross-section is proportional to χ_j, whereas $\mathrm{Im}\{\alpha_j\}$ describes absorption plus scattering, so the $|\alpha|^2$ term in χ_j is removing scattering strength that is not associated with absorption.) Finally, EMCTs terms introduce additional channels of inter-particle interaction, thus resulting in higher transfer rates compared to the diagonal approximation (consisting of only including electric-electric and magnetic-magnetic terms), particularly in the heterogeneous dimer [Fig. 5.2(a)]. Figure 5.2(c) clearly shows that the magnetic-magnetic terms are dominant in the homogeneous gold dimer, in agreement with previous predictions [213], because metallic particles mainly contribute through magnetic polarization. This is unlike the heterogeneous cluster, in which magnetic-electric terms are dominant [Fig. 5.2(d)], thus picking up an important electric polarization from the SiC particle. Incidentally, the HTCs from gold to SiC and from SiC to gold are nearly identical (see Fig. 5.4).

Similar conclusions are extracted from the temperature dependence of the HTC, represented in Fig. 5.3(a) for a small distance $d = 2\,\mu\mathrm{m} \ll \lambda_T = 14\,\mu\mathrm{m}-14\mathrm{mm}$. Notice however the dramatic reduction in the transfer rate produced by retardation at high temperatures. These behavior can be understood from the spectral dependence exhibited by the integrand of Eq. (5.4) (see Fig. 5.6).

Incidentally, we are considering particle temperatures up to $\sim 1000\,\mathrm{K}$, for which the permittivities of the materials under discussion should only undergo minor thermal effects, certainly indiscernible on the logarithmic scales of the figures. Thermal effects can change the permittivity by producing volume expansion, and thus a reduction of the conduction-electron density, and also by altering the Fermi distribution near the Fermi level E_F in metals. Both of these effects are small, and in particular, we have $k_\mathrm{B}T \ll E_F$.

The full dependence on the particle temperatures for a vacuum at $T_0 = 0$ is studied in Figs. 5.3(c),(d). Interestingly, particle 1 gets cooled down (blue regions) even if particle 2 is at a higher temperature. This is due to radiation losses into the vacuum. However, particle 2 in the homogeneous cluster is rather efficient in

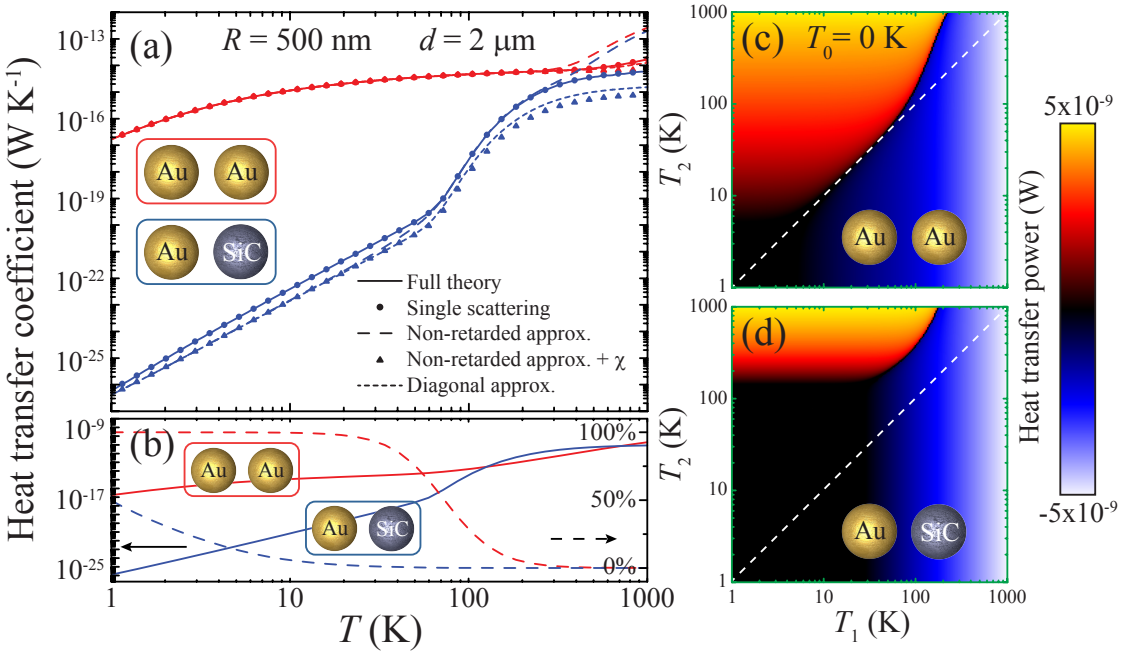

Figure 5.3: Temperature dependence of RHT. (a) HTC for the particles of Fig. 5.2. (b) Heat power lost by the right particle and fraction absorbed by the left particle. (c) Power absorbed (red-yellow scale, positive) or emitted (blue-white scale, negative) by the left particle of a gold-gold dimer as a function of T_1 and T_2 with the vacuum at $T_0 = 0$ (see Fig. 5.1). (d) Same as (c) for a gold-SiC dimer. The particle distance is $d = 2\,\mu$m and the radius is $R = 500\,$nm in all cases.

transferring energy to particle 1 and compensating for radiation losses, so that the curve separating gains (red) from losses (blue) is closer to the $T_1 = T_2$ line (dashed) in that dimer [Fig. 5.3(c)].

An important ingredient that is often overlooked in the analysis of heat transfer relates to how much energy is emitted into the surrounding vacuum. We analyze this in Figs. 5.2(b) and 5.3(b) by calculating the power escaping from a hotter particle 2. The calculation is done by reversing the particle labels, so that only the terms $\Gamma^{\nu}_{1,\perp}$ and $\Gamma^{\nu}_{1,\parallel}$ contribute in this case [see Eq. (5.4)]. For the temperature of Fig. 5.2, just a small amount of the energy emanating from particle 2 ends up in particle 1. However, this fraction increases at lower temperatures [Fig. 5.3(b)], until nearly complete heat transfer takes place below $\sim 10\,$K in the homogeneous gold

dimer. The fraction of heat transferred between the particles is thus very sensitive to temperature and particle distance (see Fig. 5.5).

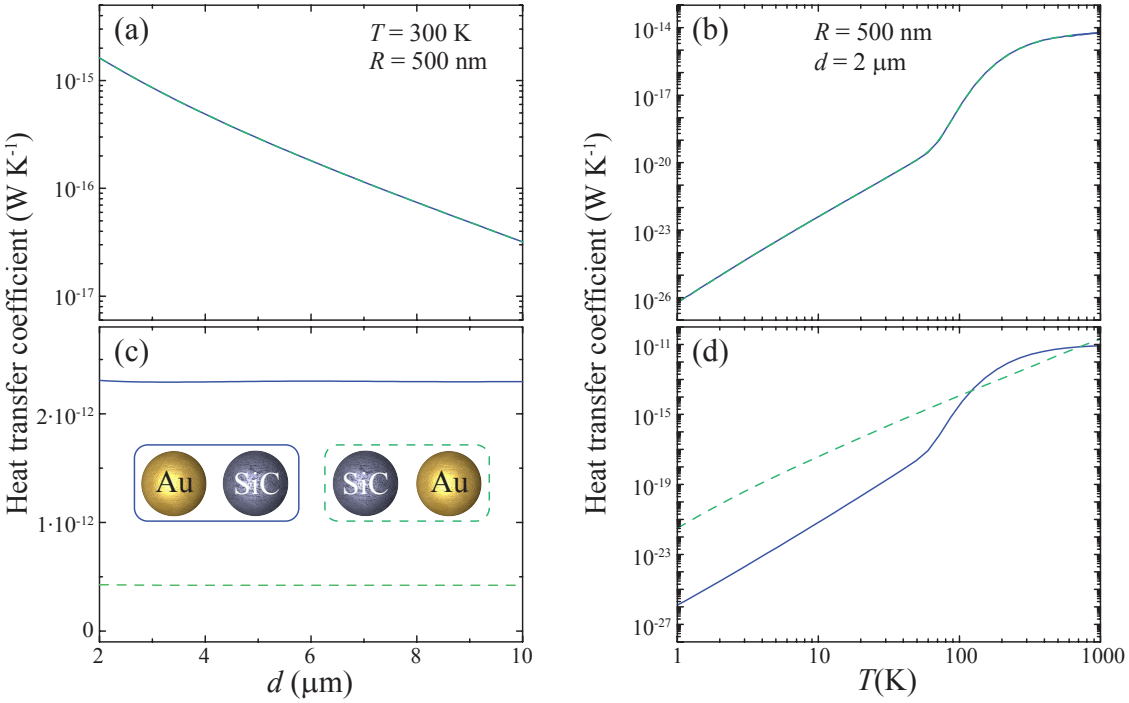

Figure 5.4: (a),(b) HTC as a function of particle distance d and temperature T for a gold-SiC dimer (solid curves) and a SiC-gold dimer (broken curves). The HTC from the right particle (2) to the left particle (1) is defined as $\mathcal{P}_1/\delta T$ with $T_1 = T_0 = T$ and $T_2 = T + \delta T$ (see insets in (c) for sketches of the dimers). (c),(d) Power emanating from the right particle in the two dimer orientations under consideration.

We show in Figs. 5.4(a),(b) the different heat transfer coefficients (HTCs) exhibited by an inhomogeneous gold-SiC dimer when the hotter particle is either SiC (solid curves) or gold (dashed curves) and the transfer is for heat absorbed by the remaining gold or SiC particle, respectively. The power transfer to the cooler particle is nearly independent on whether the hotter particle is SiC or Au. This symmetry upon permutation of particle indices ($1 \leftrightarrow 2$) is complete if we neglect multiple scattering between the particles [*i.e.*, by setting $u_\nu = 1$ and $w_\nu = 0$ in Eq. (5.4), since only $\Gamma^\nu_{2\perp}$ and $\Gamma^\nu_{2\parallel}$ terms contribute to the HTC], and indeed multiple scattering can be neglected in the clusters under consideration, as shown in Figs.

5.2 and 5.3.

In contrast, the total heat lost by the hotter particle is strongly dependent on whether this is gold or SiC [see Figs. 5.4(c),(d)]. Part of this heat is absorbed by the cooler particle, but the rest is radiated into the surrounding vacuum. At high temperatures above $\sim 100\,\mathrm{K}$, a hotter SiC particle produces larger radiation rates [Fig. 5.4(d)], rather independent of particle distance [Fig. 5.4(c)]. However, hotter gold is more capable of radiating at smaller temperatures [*cf.*, vertical scales in Figs. 5.4(b),(d)].

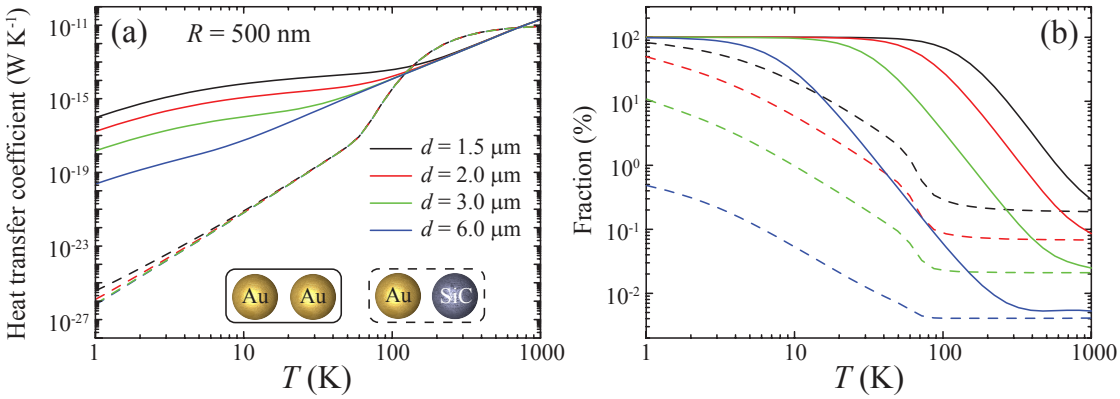

Figure 5.5: (a) Heat power lost by the right particle as a function of temperature for different particle separations. The right particle is slightly hotter than both the vacuum and the left particle, which are prepared at the same temperature, and the rate is normalized to the small temperature difference of the right particle (*i.e.*, we represent $-\mathcal{P}_2/\delta T$ for $T_0 = T_1 = T$ and $T_2 = T + \delta T$). (b) Fraction of the power lost by the right particle that ends up being absorbed by the left particle.

Heat exchange with the surrounding vacuum plays a leading role in the energy balance during radiative thermalization of a particle dimer, as shown in Fig. 5.5. We plot in Fig. 5.5(a) the power lost by the right particle when it is placed at a slightly higher temperature with respect to both the vacuum and the left particle (*i.e.*, we represent $-\mathcal{P}_2/\delta T$ for $T_0 = T_1 = T$ and $T_2 = T + \delta T$). At high temperatures, this power is rather insensitive to the presence of the neighboring particle and no significant dependence on particle separation d is observed. This happens above $T \sim 50\,\mathrm{K}$ in the inhomogeneous gold-SiC dimer and above $T \sim 300\,\mathrm{K}$ in the homogeneous gold-gold dimer. However, the accompanying left particle has a strong

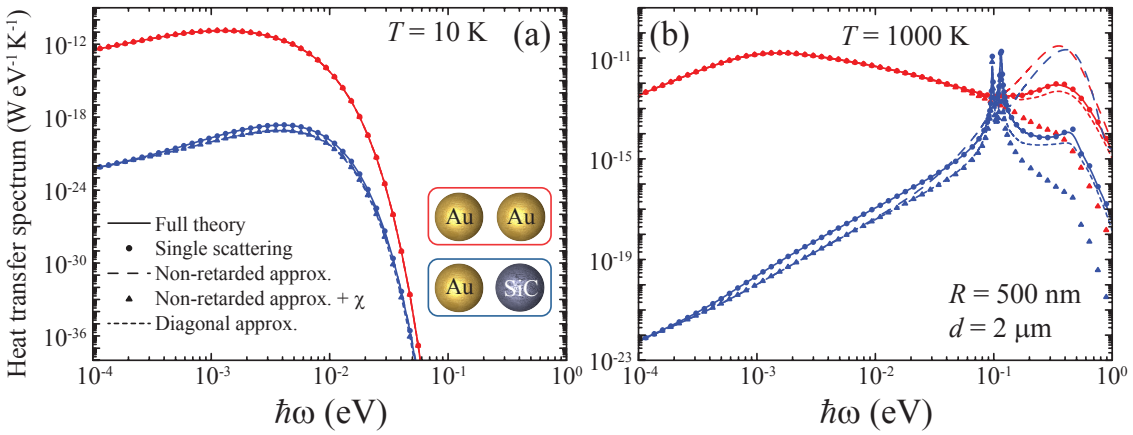

Figure 5.6: Spectral dependence of the radiative HTC for two different temperatures (see labels), obtained from our full theory (solid curves), compared to the result of neglecting multiple scattering (circles), retardation effects everywhere (dashed curves), retardation effects except in χ_j (triangles), or EMCTs (dotted curves). Gold-gold (red curves) and gold-SiC (blue curves) dimers are considered. The radius of the particles is $R = 500\,\text{nm}$ and their separation is $d = 2\,\mu\text{m}$.

influence on the power loss of the right particle at lower temperatures, specially in the homogeneous dimer. The power loss increases when the particles are placed closer together. We show next that this is partially explained by the effect of additional absorption by the left particle.

Figure 5.5(b) shows the fraction of the power lost by the right particle that is absorbed by the left particle. This fraction drops to small values at large temperatures, but it eventually approaches 100% at lower temperatures. This behavior is consistent with the distance dependence of the power lost by the right particle. Nearly full radiative heat transfer between two neighboring particles with negligible radiation into the surrounded vacuum is thus possible at sufficiently low temperatures. Specifically, in the gold-gold dimer this regime is already achieved at $\sim 100\,\text{K}$ for particles of radius $R = 500\,\text{nm}$ and a surface-to-surface separation of one radius (*i.e.*, $d = 1.5\,\mu\text{m}$). We observe that the temperature below which nearly 100% transfer between the dimer particles takes place decreases with increasing separation.

It is useful to analyze the spectral contribution from different photon energies

to the HTC [*i.e.*, the integrand of Eq. (5.4)]. At a low temperature $T = 10\,\mathrm{K}$ [Fig. 5.6(a)], the exchange is dominated by low photon energies, for which the particle polarization show a featureless behavior and χ_j almost coincides with $\mathrm{Im}\{\alpha_j\}$ for the size of the particles under discussion. At high temperature $T = 1000\,\mathrm{K}$ [Fig. 5.6(b)], optical phonons emerge as a sharp IR feature in SiC and plasmons show up as a broader near-IR feature in gold particles. Retardation effects also increase with T, as the particles appear to be large in front of λ_T.

5.3 Thermal and vacuum friction acting on rotating nanoparticles

5.3.1 Fluctuation-dissipation-theorem approach

As discussed in the introduction of this Chapter, the thermal and vacuum fluctuations of charges and fields can generate friction on spinning particles. In order to study this phenomenon we consider the system described in Fig. 5.7, which consists of an isotropic particle at temperature T_1 placed in vacuum at temperature T_0. The particle is rotating around its z axis with angular frequency Ω and interacts with the radiation field in its surroundings. This interaction produces a torque M on the particle, and it gives rise to radiation with a net power $\mathcal{P}^{\mathrm{rad}}$. As in Section 5.2, the particle radius a is assumed to be small compared to the wavelength of the involved radiation, which is controlled by the temperatures T_0 and T_1 (through the thermal radiation profile) and the rotation frequency Ω. This approximation implies that both $\Omega a/c$ and $k_{\mathrm{B}}T_j a/c\hbar$ are small compared to unity[1], thus allowing us to describe the electromagnetic response of the particle via its frequency-dependent polarizability.

Following a procedure similar to the one used to analyze RHT between nanoparticles, we have to include two separate contributions in the calculation of the torque acting on a rotating particle: (1) the fluctuations of the particle dipole and (2) the fluctuations of the electromagnetic field. The torque produced by an electric field $\mathbf{E}$

[1] These conditions are easily fulfilled in most situations encountered in practice, for instance, a particle of 100 nm in diameter requires $\Omega \ll 6 \times 10^3\,\mathrm{THz}$ and $T_j \ll 4.6 \times 10^4\,\mathrm{K}$.

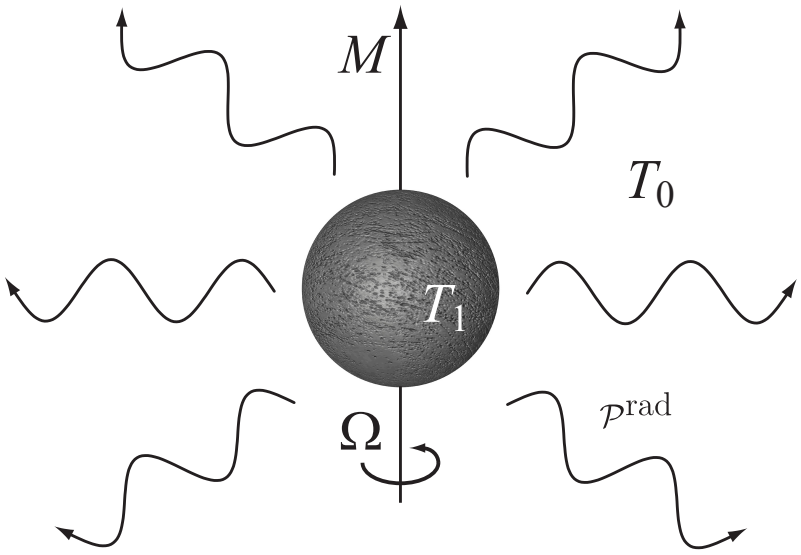

Figure 5.7: Description of the system under study. The particle is at temperature T_1 and rotates with angular frequency Ω around the z axis. The surrounding vacuum is at temperature T_0. The particle experiences a torque M and emits a power $\mathcal{P}^{\mathrm{rad}}$ in the form of radiation.

on a dipole $\mathbf{p}$ is simply given by $\mathbf{p} \times \mathbf{E}$. We can use this result to write the torque on our particle along the rotation axis $\hat{\mathbf{z}}$ as

$$M = \langle \mathbf{p}(t) \times \mathbf{E}(\mathbf{r}_0, t) \rangle \cdot \hat{\mathbf{z}},$$

where $\langle\rangle$ represents the average over fluctuations and the field is evaluated at the position of the particle $\mathbf{r} = \mathbf{r}_0$. We can separate the two contributions just described in the following way:

$$\begin{aligned} M &= \left\langle \mathbf{p}^{\mathrm{fl}}(t) \times \mathbf{E}^{\mathrm{ind}}(\mathbf{r}_0, t) + \mathbf{p}^{\mathrm{ind}}(t) \times \mathbf{E}^{\mathrm{fl}}(\mathbf{r}_0, t) \right\rangle \cdot \hat{\mathbf{z}} \\ &= M_p + M_E. \end{aligned} \tag{5.5}$$

The first term accounts for the fluctuations of the particle dipole that correlate with the resulting induced field, while the second one involves field fluctuations and the dipole that they induce. Once again, there are no cross-terms involving fluctuations of both the dipole and the field because they belong to different physical systems, so

that they are uncorrelated. It is convenient to work in frequency space ω, defined via the Fourier transform as indicated in Eq. (1.3). This allows us to express the induced field of Eq. (5.5) in terms of the fluctuating dipole by using the electromagnetic Green tensor $\mathcal{G}$ [see Eq. (1.31)]:

$$\mathbf{E}^{\mathrm{ind}}(\mathbf{r},\omega) = \mathcal{G}(\mathbf{r},\mathbf{r}_0,\omega)\mathbf{p}^{\mathrm{fl}}(\omega). \tag{5.6}$$

In a similar way, the induced dipole can be written in terms of the fluctuating field with the help of the particle polarizability tensor,

$$\mathbf{p}^{\mathrm{ind}}(\omega) = \alpha(\omega)\mathbf{E}^{\mathrm{fl}}(\mathbf{r}_0,\omega). \tag{5.7}$$

For simplicity, we assume particles with axial symmetry, for which the non-vanishing components of the polarizability tensor can be written as

$$\begin{aligned}\alpha_{xx}(\omega) &= \alpha_{yy}(\omega) = \alpha_{\perp}(\omega),\\ \alpha_{zz}(\omega) &= \alpha_{\parallel}(\omega).\end{aligned}$$

These expressions, together with Eq. (5.5), permit us writing the torque as the sum of two terms, one of them quadratic with respect to the fluctuating dipole and the other one quadratic with respect to the fluctuating field. These quadratic terms have to be averaged over fluctuations using the symmetrized version of the FDT (see Section 1.4), which in this particular case reads

$$\langle p_i^{\mathrm{fl}}(\omega) p_j^{\mathrm{fl}}(\omega')\rangle = 4\pi\hbar\delta(\omega+\omega')\mathrm{Im}\{\alpha_{ij}(\omega)\}[n_1(\omega)+\frac{1}{2}] \tag{5.8}$$

for the dipole fluctuations and

$$\langle E_i^{\mathrm{fl}}(\mathbf{r},\omega) E_j^{\mathrm{fl}}(\mathbf{r}',\omega')\rangle = 4\pi\hbar\delta(\omega+\omega')\mathrm{Im}\{\mathcal{G}_{ij}(\mathbf{r},\mathbf{r}',\omega)\}[n_0(\omega)+\frac{1}{2}] \tag{5.9}$$

for the electric-field fluctuations. The temperatures of the particle (T_1) and the vacuum (T_0) enter these expressions through the Bose-Einstein distribution functions

$$n_l(\omega) = \frac{1}{e^{\hbar\omega/k_{\mathrm{B}}T_l}-1}.$$

We first calculate the term associated with the dipole fluctuations,

$$M_p = \left\langle \mathbf{p}^{\mathrm{fl}}(t) \times \mathbf{E}^{\mathrm{ind}}(\mathbf{r}_0, t) \right\rangle \cdot \mathbf{z} = \int_{-\infty}^{\infty} \frac{d\omega d\omega'}{(2\pi)^2} e^{-i(\omega+\omega')t} \left\langle \mathbf{p}^{\mathrm{fl}}(\omega) \times \mathbf{E}^{\mathrm{ind}}(\mathbf{r}_0, \omega') \right\rangle \cdot \mathbf{z}. \tag{5.10}$$

Using Eq. (5.6) to write the induced field in terms of the fluctuating dipole, Eq. (5.10) becomes

$$\begin{aligned} M_p = \int_{-\infty}^{\infty} \frac{d\omega d\omega'}{(2\pi)^2} e^{-i(\omega+\omega')t} \Big[& p_x^{\mathrm{fl}}(\omega) \mathcal{G}_{yx}(\mathbf{r}_0, \mathbf{r}_0, \omega') p_x^{\mathrm{fl}}(\omega') + p_x^{\mathrm{fl}}(\omega) \mathcal{G}_{yy}(\mathbf{r}_0, \mathbf{r}_0, \omega') p_y^{\mathrm{fl}}(\omega') \\ & - p_y^{\mathrm{fl}}(\omega) \mathcal{G}_{xx}(\mathbf{r}_0, \mathbf{r}_0, \omega') p_x^{\mathrm{fl}}(\omega') - p_y^{\mathrm{fl}}(\omega) \mathcal{G}_{xy}(\mathbf{r}_0, \mathbf{r}_0, \omega') p_y^{\mathrm{fl}}(\omega') \Big]. \end{aligned} \tag{5.11}$$

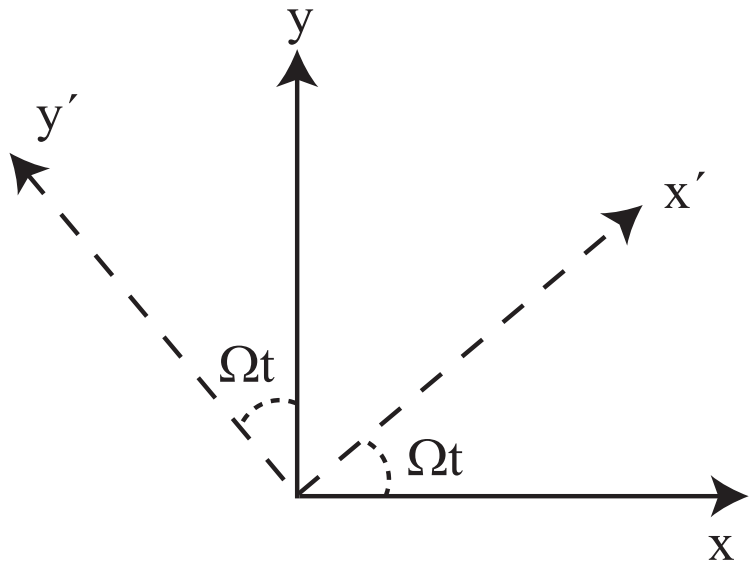

Figure 5.8: Definition of the rotating frame (dashed line) and the lab frame (solid line). The former rotates with angular frequency Ω.

So far we have expressed the fluctuating dipoles in the lab frame (see Fig. 5.8), but we need to transform them to the rotating frame in order to average over fluctuations via the FDT. The physical reason for this is that the particle polarizability can only be applied in the rotating frame, in which the electronic and

vibrational excited states that produce polarization are well defined. Furthermore, we assume that those states are unaffected by the rotational motion in the rest frame of the particle. We can express the lab-frame dipoles $\mathbf{p}$ in terms of the dipoles in the rotating frame $\mathbf{p}'$ in the following way:

$$\begin{aligned} p_x(\omega) &= \frac{1}{2}\left[p'_x(\omega_+) + ip'_y(\omega_+) + p'_x(\omega_-) - ip'_y(\omega_-)\right], \\ p_y(\omega) &= \frac{1}{2}\left[-ip'_x(\omega_+) + p'_y(\omega_+) + ip'_x(\omega_-) + p'_y(\omega_-)\right], \\ p_z(\omega) &= p'_z(\omega), \end{aligned} \tag{5.12}$$

where we have employed the compact notation $\omega_\pm = \omega \pm \Omega$. If now we introduce Eq. (5.12) into Eq. (5.11), average over fluctuations via the FDT [Eq. (5.8)], and perform the integral over ω', taking into account causality in the Green tensor [*i.e.*, $\mathcal{G}_{ij}(\mathbf{r},\mathbf{r}',-\omega) = \mathcal{G}^*_{ij}(\mathbf{r},\mathbf{r}',\omega)$], and noticing that $n_l(\omega) + 1/2$ is an odd function of ω, we obtain

$$M_p = \frac{4\hbar}{3\pi c^3}\int_0^\infty d\omega\omega^3\left[\mathrm{Im}\{\alpha_\perp(\omega_+)\}\left(n_1(\omega_+)+\frac{1}{2}\right) - \mathrm{Im}\{\alpha_\perp(\omega_-)\}\left(n_1(\omega_-)+\frac{1}{2}\right)\right], \tag{5.13}$$

where we have used the relation $\lim_{\mathbf{r}\to\mathbf{r}'}\mathrm{Im}\left\{\mathcal{G}_{ij}(\mathbf{r},\mathbf{r}',\omega)\right\} = 2k^3/3\delta_{ij}$, which can be directly obtained from the definition of $\mathcal{G}_{ij}(\mathbf{r},\mathbf{r}',-\omega)$ given in Eq. (1.31) (see Appendix B).

Equation (5.13) only contains the torque produced due to electric-dipole fluctuations. Coming back to Eq. (5.5), we still have to calculate its second term, which accounts for the torque associated with field fluctuations:

$$M_E = \left\langle \mathbf{p}^{\mathrm{ind}}(t)\times\mathbf{E}^{\mathrm{fl}}(\mathbf{r},t)\right\rangle\cdot\mathbf{z} = \int_{-\infty}^{\infty}\frac{d\omega d\omega'}{(2\pi)^2}e^{-i(\omega+\omega')t}\left[\mathbf{p}^{\mathrm{ind}}(\omega)\times\mathbf{E}^{\mathrm{fl}}(\mathbf{r},\omega')\right]\cdot\mathbf{z}. \tag{5.14}$$

In order to express the induced dipole in terms of the fluctuating field, we need to write the dipole in the rotating frame before we can apply Eq. (5.7), and then go back to the lab frame. This procedure leads to an effective polarizability for the rotating particle, whose components are: $\alpha^{\mathrm{eff}}_{xx}(\omega) = \alpha^{\mathrm{eff}}_{yy}(\omega) = 1/2\left[\alpha_\perp(\omega_+) + \alpha_\perp(\omega_-)\right]$,

$\alpha_{xy}^{\rm eff}(\omega) = -\alpha_{yx}^{\rm eff}(\omega) = \frac{i}{2}\left[\alpha_\perp(\omega_+) - \alpha_\perp(\omega_-)\right]$, and $\alpha_{zz}^{\rm eff}(\omega) = \alpha_\parallel(\omega)$. Using this effective polarizability, Eq. (5.14) becomes

$$M_E = \int_{-\infty}^{\infty} \frac{d\omega d\omega'}{(2\pi)^2} e^{-i(\omega+\omega')t} \Big[\alpha_{xx}^{\rm eff}(\omega) E_x^{\rm fl}(\mathbf{r},\omega) E_y^{\rm fl}(\mathbf{r},\omega') + \alpha_{xy}^{\rm eff}(\omega) E_y^{\rm fl}(\mathbf{r},\omega) E_y^{\rm fl}(\mathbf{r},\omega') - \alpha_{yx}^{\rm eff}(\omega) E_x^{\rm fl}(\mathbf{r},\omega) E_x^{\rm fl}(\mathbf{r},\omega') - \alpha_{yy}^{\rm eff}(\omega) E_y^{\rm fl}(\mathbf{r},\omega) E_x^{\rm fl}(\mathbf{r},\omega')\Big].$$

This expression is already prepared to perform the average over field fluctuations using the FDT [Eq. (5.9)]. By doing that, and integrating over ω', using the causality property of the polarizability $\alpha(-\omega) = \alpha^*(\omega)$ and the parity of the rest of the integrand, we obtain

$$M_E = \frac{4\hbar}{3\pi c^3} \int_0^\infty d\omega \omega^3 \left[\mathrm{Im}\left\{\alpha_\perp(\omega_-)\right\} - \mathrm{Im}\left\{\alpha_\perp(\omega_+)\right\}\right] \left[n_0(\omega) + \frac{1}{2}\right]. \tag{5.15}$$

Finally, the total torque resulting from the sum of Eqs. (5.13) and (5.15) reduces to

$$\begin{aligned} M = &- \frac{4\hbar}{3\pi c^3} \int_0^\infty d\omega \omega^3 \mathrm{Im}\left\{\alpha_\perp(\omega_-)\right\} \left[n_1(\omega_-) - n_0(\omega)\right] \\ &+ \frac{4\hbar}{3\pi c^3} \int_0^\infty d\omega \omega^3 \mathrm{Im}\left\{\alpha_\perp(\omega_+)\right\} \left[n_1(\omega_+) - n_0(\omega)\right]. \end{aligned} \tag{5.16}$$

A more compact expression can be found by playing with the integration limits:

$$M = -\frac{4\hbar}{3\pi c^3} \int_{-\infty}^\infty d\omega \omega^3 \mathrm{Im}\left\{\alpha_\perp(\omega_-)\right\} \left[n_1(\omega_-) - n_0(\omega)\right]. \tag{5.17}$$

This expression shows explicitly that, as expected, the torque vanishes for non-rotating nanoparticles.

The generalization of Eq. (5.17) to the case of anisotropic particles with principal axes along x, y, and z [*i.e.*, $\alpha_{xx}(\omega) \neq \alpha_{yy}(\omega)$] is straightforward, but it involves lengthy algebraic manipulations. We find

$$M = -\frac{4\hbar}{3\pi c^3} \int_{-\infty}^\infty d\omega \omega^3 \frac{1}{2} \mathrm{Im}\left\{\alpha_{xx}(\omega_-) + \alpha_{yy}(\omega_-)\right\} \left[n_1(\omega_-) - n_0(\omega)\right],$$

and hence, Eq. (5.17) is recovered, but understanding $\alpha_\perp(\omega)$ as the average of the polarizabilities along the x and y axes.

The interaction between the rotating particle and the surrounding field involves photon exchanges that lead to a net radiated power. We calculate this power here following a procedure similar to the one used for the torque. First we write

$$\begin{aligned}\mathcal{P}^{\rm rad} &= -\left\langle \mathbf{E}^{\rm ind}(\mathbf{r},t)\cdot\frac{\partial \mathbf{p}^{\rm fl}(t)}{\partial t} + \mathbf{E}^{\rm fl}(\mathbf{r},t)\cdot\frac{\partial \mathbf{p}^{\rm ind}(t)}{\partial t}\right\rangle \\ &= \mathcal{P}_p^{\rm rad} + \mathcal{P}_E^{\rm rad}. \end{aligned} \tag{5.18}$$

The first term on the right-hand side of Eq. (5.18) accounts for the power radiated by the particle due to fluctuations in its polarization, while the second one describes the power dissipated in the particle due to field fluctuations. The first term can be rewritten as

$$\mathcal{P}_p^{\rm rad} = -\left\langle \mathbf{E}^{\rm ind}(\mathbf{r},t)\cdot\frac{\partial \mathbf{p}^{\rm fl}(t)}{\partial t}\right\rangle = \int_{-\infty}^{\infty}\frac{d\omega d\omega'}{(2\pi)^2}e^{-i(\omega+\omega')t}(i\omega')\mathbf{E}^{\rm ind}(\mathbf{r},\omega')\cdot\mathbf{p}^{\rm fl}(\omega').$$

Now, we express the induced field in terms of the fluctuating dipole using Eq. (5.6). Then, the dipole can be written in the rotating frame with the help of Eq. (5.12) and we can apply the FDT [Eq. (5.8)] to obtain

$$\begin{aligned}\mathcal{P}_p^{\rm rad} = {}& \frac{4\hbar}{3\pi c^3}\int_0^\infty d\omega\omega^4\left(\mathrm{Im}\{\alpha_\perp(\omega_+)\}[n_1(\omega_+)+\frac{1}{2}] + \mathrm{Im}\{\alpha_\perp(\omega_-)\}[n_1(\omega_-)+\frac{1}{2}]\right) \\ & + \frac{4\hbar}{3\pi c^3}\int_0^\infty d\omega\omega^4\mathrm{Im}\{\alpha_\parallel(\omega)\}[n_1(\omega)+\frac{1}{2}], \end{aligned} \tag{5.19}$$

where we have taken advantage of the properties of the Green tensor. This result represents the power radiated by the rotating particle due to the dipole fluctuations. Notice that although the parallel component of the polarizability does not contribute to the torque, it does radiate power.

The remaining term of Eq. (5.18) represents the radiation dissipated in the particle due to the fluctuations of the external field, which can be written as

$$\mathcal{P}_E^{\rm rad} = -\left\langle \mathbf{E}^{\rm fl}(\mathbf{r},t)\cdot\frac{\partial \mathbf{p}^{\rm ind}(t)}{\partial t}\right\rangle = \int_{-\infty}^{\infty}\frac{d\omega d\omega'}{(2\pi)^2}e^{-i(\omega+\omega')t}(i\omega')\mathbf{E}^{\rm fl}(\mathbf{r},\omega)\cdot\mathbf{p}^{\rm ind}(\omega'). \tag{5.20}$$

Using the effective polarizability given in the paragraph after Eq. (5.14), the FDT [Eq. (5.9)], and the properties of the Green tensor, Eq. (5.20) becomes

$$\mathcal{P}_E^{\rm rad} = -\frac{4\hbar}{3\pi c^3}\int_0^\infty d\omega\omega^4 \left[\mathrm{Im}\left\{\alpha_\perp(\omega_+)\right\} + \mathrm{Im}\left\{\alpha_\perp(\omega_-)\right\} + \mathrm{Im}\left\{\alpha_\parallel(\omega)\right\}\right][n_0(\omega)+\frac{1}{2}]. \tag{5.21}$$

Finally, the net power radiated by the particle, which results from the difference between the power radiated by dipole fluctuations [Eq. (5.19)] and the power dissipated by the fluctuating field [Eq. (5.21)], can be written as

$$\begin{aligned}\mathcal{P}^{\rm rad} = &\frac{4\hbar}{3\pi c^3}\int_0^\infty d\omega\omega^4 \mathrm{Im}\left\{\alpha_\perp(\omega_-)\right\}[n_1(\omega_-)-n_0(\omega)] \\ &+\frac{4\hbar}{3\pi c^3}\int_0^\infty d\omega\omega^4 \mathrm{Im}\left\{\alpha_\perp(\omega_+)\right\}[n_1(\omega_+)-n_0(\omega)] \\ &+\frac{4\hbar}{3\pi c^3}\int_0^\infty d\omega\omega^4 \mathrm{Im}\left\{\alpha_\parallel(\omega)\right\}[n_1(\omega)-n_0(\omega)].\end{aligned} \tag{5.22}$$

A more compact expression is obtained by playing with the integration limits:

$$\begin{aligned}\mathcal{P}^{\rm rad} = &\frac{4\hbar}{3\pi c^3}\int_{-\infty}^\infty d\omega\omega^4 \mathrm{Im}\left\{\alpha_\perp(\omega_-)\right\}[n_1(\omega_-)-n_0(\omega)] \\ &+\frac{2\hbar}{3\pi c^3}\int_{-\infty}^\infty d\omega\omega^4 \mathrm{Im}\left\{\alpha_\parallel(\omega)\right\}[n_1(\omega)-n_0(\omega)].\end{aligned} \tag{5.23}$$

It should be noted that even if the particle is not rotating there is a net radiated power when the particle and vacuum temperatures are different.

Like in the case of the torque, we can generalize this result to anisotropic particles, and we also find that Eq. (5.23) is still valid if $\alpha_\perp(\omega)$ is understood as the average of the polarizabilities along the x and y axes.

5.3.2 Quantum-mechanical approach

One can question the suitability of the FDT to deal with a system that is out of dynamical equilibrium, such as our rotating particle when it is experiencing friction. We clarify this point and achieve deeper understanding of vacuum and thermal friction by solving the problem within the framework of quantum electrodynamics. As we show next, this procedure leads to analytical expressions for the torque and

the radiated power that are identical with the ones obtained from the FDT.

The rotation of the particle around the z axis can be described by the Hamiltonian

$$\hat{H}_{\rm rot} = \frac{L_z^2}{2I} = -\frac{\hbar^2}{2I}\frac{\partial^2}{\partial\varphi^2},$$

where I is the particle moment of inertia. Accordingly, the rotational part of the eigenfunction can be written

$$\Psi_R(\varphi,t) = \frac{1}{\sqrt{2\pi}} e^{im\varphi} e^{(-i\hbar m^2/2I)\,t}, \tag{5.24}$$

which describes a rotation of frequency $\Omega = \hbar m/I$, as obtained from the condition of stationary phase[2]. This wave function satisfies the equation

$$\hat{H}_{\rm rot}\Psi_{\rm rot}(\varphi) = E_{\rm rot}\Psi_{\rm rot}(\varphi),$$

where $E_{\rm rot} = \hbar^2 m^2/2I$ is the rotational energy.

The complete system (particle plus field) can be adequately described by states $|k_j\, m\, l_i\rangle$, where k_j is the number of particle bosonic excitations of energy ε_j in the particle internal state (*e.g.*, phonons or plasmons), m is the rotational azimuthal number, and l_i describes the field state through the number of photons in mode i. The energy of this state is $k_j\varepsilon_j + \hbar^2 m^2/2I + l_i\hbar\omega_i$.

Using Fermi's golden rule [see Eq. (1.22)] to account for the particle-radiation coupling to first order, the transition probabilities between states like the one defined above can be written as

$$P_{|k_j' m' l_i'\rangle \leftarrow |k_j m l_i\rangle} = \frac{2\pi}{\hbar}\left|\langle k_j' m' l_i'|\, \hat{H}_{\rm int}\, |k_j m l_i\rangle\right|^2 \delta\left(\Delta k_j\varepsilon_j + \hbar^2\frac{m'^2 - m^2}{2I} + \Delta l_i\hbar\omega_i\right),$$

where $\Delta k_j = k_j' - k_j$ and $\Delta l_i = l_i' - l_i$. Here, $\hat{H}_{\rm int}$ is the Hamiltonian that describes the interaction between the particle and the radiation field, which, as discussed in Section 1.3.1 [see Eq. (1.21)], can be written as $\hat{H}_{\rm int} = -\hat{\mathbf{p}}\cdot\hat{\mathbf{E}}$ within the dipolar approximation.

[2]The condition of stationary phase can be expressed as $\left[\frac{\partial}{\partial k}\eta(k,x)\right]_{k=k_0} = 0$, where $\eta(k,x)$ represents the phase of a wave packet. This expression allows one to identify where the maximum of the wave packet is situated.

Assuming that dipolar response of the particle is dominated by bosonic excitations (*e.g.*, phonons or plasmons) the dipole operator $\hat{\mathbf{p}}$ can be expressed in terms of bosonic creation and annihilation operators $\hat{b}^+$ and b as [see the discussion preceding Eq. (1.20)]

$$\hat{\mathbf{p}} = \sum_j \mathbf{p}_j \left[\hat{b}_j + \hat{b}_j^+\right], \tag{5.25}$$

where $\mathbf{p}_j$ is the dipole moment associated with the bosonic mode j. On the other hand, the electric-field operator can be written in terms of photon creation and annihilation operators $\hat{a}^+$ and a using the expression derived in Eq. (1.18).

In the dipolar approximation, we can take $e^{i\mathbf{k}\cdot\mathbf{r}} \approx 1$, which, together with Eq. (5.24), allows us to write the relation

$$\langle k_j' m' l_i' |\, \hat{H}_{\rm int} \,| k_j m l_i \rangle = -i\sqrt{\frac{2\pi\hbar\omega_i}{V}} N \int \left(\mathbf{p}_j \cdot \mathbf{e}_i\right) \frac{e^{i(m-m')\varphi}}{2\pi} d\varphi, \tag{5.26}$$

for the transition matrix elements. Here, N is the matrix element corresponding to the bosonic and photonic degrees of freedom, which produces four possible transitions depending on the change of the bosonic ($\Delta k_j = \pm 1$) and photonic ($\Delta l_i = \pm 1$) numbers. More precisely,

$$\langle k_j - 1 l_i - 1 |\, \hat{b}_j \hat{a}_i \,| k_j l_i \rangle \to N = \sqrt{k_j l_i}, \tag{5.27}$$

$$\langle k_j + 1 l_i + 1 |\, \hat{b}_j^+ \hat{a}_i^+ \,| k_j l_i \rangle \to N = \sqrt{(k_j+1)(l_i+1)}, \tag{5.28}$$

$$\langle k_j + 1 l_i - 1 |\, \hat{b}_j^+ \hat{a}_i \,| k_j l_i \rangle \to N = \sqrt{(k_j+1) l_i}, \tag{5.29}$$

$$\langle k_j - 1 l_i + 1 |\, \hat{b}_j \hat{a}_i^+ \,| k_j l_i \rangle \to N = \sqrt{k_j (l_i+1)}. \tag{5.30}$$

Now, the integration over φ in Eq. (5.26) requires expressing the dipole moment in the particle frame using the relations $p_x = p_x' \cos\varphi - p_y' \sin\varphi$, $p_y = p_x' \sin\varphi + p_y' \cos\varphi$, and $p_z = p_z'$, where the primed (non-primed) quantities refer to the rotating (lab) frame. From here we have

$$\begin{aligned}\langle k_j' m' l_i' |\, H_I \,| k_j m l_i \rangle = -i\sqrt{\frac{2\pi\hbar\omega_i}{V}} \frac{N}{2} \Big[& \delta_{m,m'+1} \left(p_{j,x}' - i p_{j,y}'\right)\left(e_{i,x} + i e_{i,y}\right) \\ & + \delta_{m,m'-1} \left(p_{j,x}' + i p_{j,y}'\right)\left(e_{i,x} - i e_{i,y}\right) + 2 p_{j,z}' \delta_{m,m'} e_{i,z} \Big], \end{aligned} \tag{5.31}$$

where $e_{i,j}$ are the Cartesian components of the polarization vector $\mathbf{e}_i$ [see Eq. (1.18)]. The Kronecker delta functions appear as a result of the φ integration in Eq. (5.26). From this equation we conclude that there is no contribution to the torque coming from the dipole component along the rotation axis z, because it conserves the rotation number m.

Each of the four possible transitions discussed in Eqs. (5.27)-(5.30) contributes to the torque through the rate of change in the rotational energy. More precisely,

$$M = \frac{1}{\Omega}\frac{dE_{\rm rot}}{dt} = -\sum_{j,m',i}\frac{\pm\varepsilon_j \pm \hbar\omega_i}{\Omega}P_{|k_j \pm 1 m' l_i \pm 1\rangle \leftarrow |k_j m l_i\rangle},$$

where the signs depend on the particular transition and we are summing over all possible final states. Replacing the sum over the photonic states by an integral ($\sum_i \to \int dS \sum_\varsigma \frac{V}{(2\pi)^3}\frac{1}{c^3}\int_0^\infty \omega^2 d\omega$) and using Eq. (5.31), we find

$$M = \frac{-2\hbar}{3\Omega c^3}\sum_{j,m'}\int_0^\infty d\omega N^2\omega^3(\pm\varepsilon_j \pm \hbar\omega)\left\{|p_{j,x}+ip_{j,y}|^2\delta_{m',m-1} + |p_{j,x}-ip_{j,y}|^2\delta_{m',m+1}\right\}$$
$$\times\,\delta(\pm\varepsilon_j \pm \hbar\omega + \hbar^2\frac{m'^2-m^2}{2I}). \tag{5.32}$$

The factors $\delta_{m',m\pm1}$ allow writing

$$\hbar^2\frac{(m'^2-m^2)}{2I} = \hbar^2\frac{(m\pm1)^2-m^2}{2I} \approx \pm\hbar\Omega \tag{5.33}$$

(with $\Omega = \hbar m/I$), where we use the non-recoil approximation ($|m| \gg 1$). Using this expression and defining $p_j^2 = |p_{j,x} \pm ip_{j,y}|^2$, we can rewrite Eq. (5.32) as

$$M = -\frac{4\hbar}{3c^3}\sum_j\int_0^\infty d\omega N^2\omega^3 p_j^2\left[\delta(\pm\varepsilon_j \pm \hbar\omega - \hbar\Omega) - \delta(\pm\varepsilon_j \pm \hbar\omega + \hbar\Omega)\right]. \tag{5.34}$$

Finally, the total torque is the sum of the contributions from the four transitions described in Eqs. (5.27)-(5.30).

At this point, we assume that both the radiation field and the particle are in thermodynamic equilibrium at temperatures T_0 and T_1, respectively. Then, we have to average over the number of bosons k_j and photons l_i in the system, which appear in the factor N. Using the Bose-Einstein statistics, $\langle k_j\rangle = \left[e^{\varepsilon_j/k_{\rm B}T_1}-1\right]^{-1} = n_1(\varepsilon_j)$

and $\langle l_i \rangle = \left[e^{\hbar\omega_i / k_{\rm B} T_0} - 1 \right]^{-1} = n_0(\omega_i)$ the averaged torque reduces to

$$M = \frac{4\hbar}{3c^3} \sum_j \int_0^\infty d\omega \omega^3 p_j^2 \left\{ \left[\delta(\varepsilon_j - \hbar\omega_+) - \delta(\varepsilon_j + \hbar\omega_+) \right] \left[n_1(\omega_+) - n_0(\omega) \right] \right.$$
$$\left. - \left[\delta(\varepsilon_j - \hbar\omega_-) - \delta(\varepsilon_j + \hbar\omega_-) \right] \left[n_1(\omega_-) - n_0(\omega) \right] \right\} . \tag{5.35}$$

The net radiated power can be calculated in a way similar to the torque. Once again, there are four separate contributions associated with the transitions of Eqs. (5.27)-(5.30). Two of them involve the emission of a photon (with $\Delta l_i = 1$ and $\Delta k_j = \pm 1$), thus producing a positive contribution, whereas the other two describe photon absorption ($\Delta l_i = -1$ and $\Delta k_j = \pm 1$), giving rise to a negative contribution. The net radiated power can then be written as

$$\mathcal{P}^{\rm rad} = \sum_{j,m',i} \hbar\omega_i \left[\mathcal{P}_{|k_j+1 m' l_i+1\rangle \leftarrow |k_j m l_i\rangle} + \mathcal{P}_{|k_j-1 m' l_i+1\rangle \leftarrow |k_j m l_i\rangle} \right.$$
$$\left. - \mathcal{P}_{|k_j+1 m' l_i-1\rangle \leftarrow |k_j m l_i\rangle} - \mathcal{P}_{|k_j-1 m' l_i-1\rangle \leftarrow |k_j m l_i\rangle} \right] . \tag{5.36}$$

Following the same steps as in Eqs. (5.32)-(5.35), we find

$$\mathcal{P}^{\rm rad} = \frac{4\hbar}{3c^3} \sum_j \int_0^\infty d\omega \omega^4 p_j^2 \left\{ \left[n_1(\omega_+) - n_0(\omega) \right] \left[\delta(\varepsilon_j - \hbar\omega_+) - \delta(\varepsilon_j + \hbar\omega_+) \right] \right.$$
$$+ \left[n_1(\omega_-) - n_0(\omega) \right] \left[\delta(\varepsilon_j - \hbar\omega_-) - \delta(\varepsilon_j + \hbar\omega_-) \right]$$
$$\left. + \left[n_1(\omega) - n_0(\omega) \right] \left[\delta(\varepsilon_j - \hbar\omega) - \delta(\varepsilon_j + \hbar\omega) \right] \right\} . \tag{5.37}$$

It should be noted that, unlike the torque, the radiated power contains a contribution from the dipole component parallel to the rotation axis.

5.3.3 Equivalence of the fluctuation-dissipation-theorem and the quantum-mechanical approaches

In order to compare the expressions for the torque and the net radiated power obtained within the two different approaches, we have to introduce the particle polarizability α in the quantum-mechanical formalism. From the customary definition

[144]

$$\alpha(\omega) = \sum_j p_j^2 \left[\frac{1}{\varepsilon_j - \hbar\omega - i\gamma} + \frac{1}{\varepsilon_j + \hbar\omega + i\gamma} \right],$$

and using the identity

$$\mp\, \delta(x) = \frac{1}{\pi} \mathrm{Im} \left\{ \frac{1}{x \pm i\gamma} \right\},$$

where $\gamma \to 0^+$, we can write the imaginary part of the polarizability as

$$\mathrm{Im}\left\{\alpha(\omega)\right\} = \pi \sum_j p_j^2 \left[\delta(\varepsilon_j - \hbar\omega) - \delta(\varepsilon_j + \hbar\omega)\right].$$

This allows us to directly recast the torque and the radiated power given by Eqs. (5.35) and (5.37) into exactly the same form as in Eqs. (5.16) and (5.22), respectively. The only difference is that we have focused on isotropic particles in the quantum-mechanical approach, although the generalization to anisotropic particles can be easily done through the dipole moment of the bosonic excitations, $\mathbf{p}_j$ [see Eq. (5.25)].

Therefore, we find that the FDT and the quantum-mechanical approaches lead to exactly the same results. An additional conclusion from the quantum-mechanical derivation is that isotropic particles with no allowed internal excitations (*i.e.*, non-absorbing particles) cannot experience any torque, within the limits of our model.

5.3.4 Metallic particles

As an illustrative example of the theory derived in the previous pages, we analyze the thermal and vacuum friction acting on a metallic particle. From the discussion carried out in Section 1.1.1, we know that at low photon frequencies ω below the interband transitions region, metals can be well described by the Drude model, characterized by a DC electric conductivity σ_0 and a dielectric function $\epsilon = 1 + \mathrm{i}\, 4\pi\sigma_0/\omega$ [21]. Furthermore, in the quasi-static regime the polarizability of a spherical particle of radius a can be approximated as $\alpha = a^3(\epsilon - 1)/(\epsilon + 2)$ [see Eq. (1.11)], and consequently

$$\mathrm{Im}\{\alpha(\omega)\} = 3\omega a^3/4\pi\sigma_0. \tag{5.38}$$

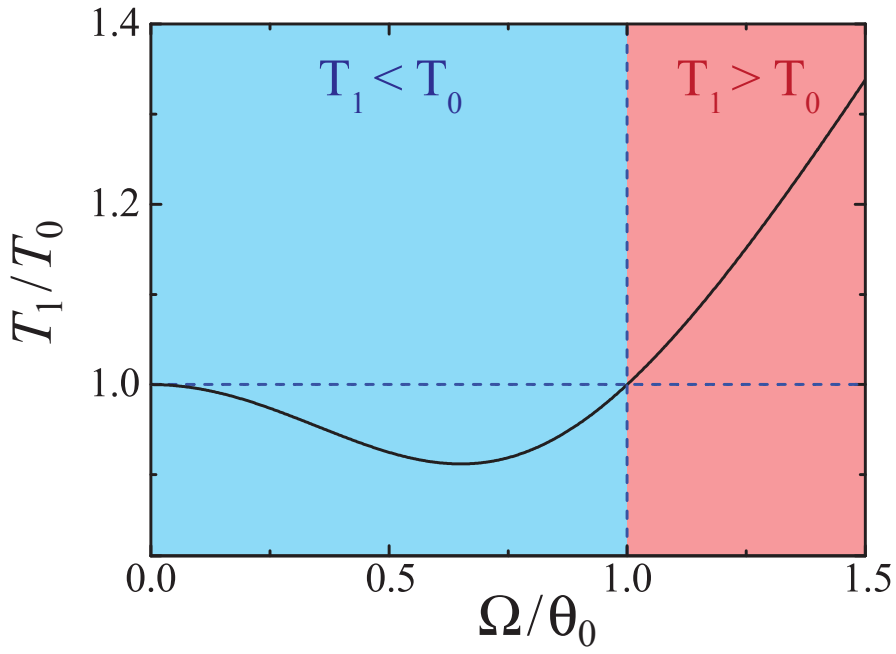

Figure 5.9: Normalized particle temperature at equilibrium (T_1/T_0) as a function of Ω/θ_0, where $\theta_0 = 2\pi k_B T_0/\hbar$.

Therefore, using this relation into Eqs. (5.17) and (5.23) we find the following closed-form expressions

$$\mathcal{P}_{\rm D}^{\rm rad} = \frac{\hbar a^3}{60\pi^2 c^3 \sigma_0}\left[2\Omega^6 + 5\Omega^4\theta_1^2 + 3\Omega^2\theta_1^4 + \frac{5}{14}(\theta_1^6 - \theta_0^6)\right] \tag{5.39}$$

and

$$M_{\rm D} = \frac{-\hbar a^3 \Omega}{120\pi^2 c^3 \sigma_0}\left[6\Omega^4 + 10\Omega^2\theta_1^2 + \theta_0^4 + 3\theta_1^4\right], \tag{5.40}$$

where the subscript D refers to the Drude model and

$$\theta_j = 2\pi k_B T_j/\hbar.$$

Equations (5.39) and (5.40) show that thermal and vacuum friction is always producing stopping ($M\Omega < 0$), whereas the balance of radiation exchange between

particle and free space can change sign depending on their relative temperatures. At low Ω, the torque scales as Ω, while a steeper Ω^5 dependence is observed at faster velocities. Interestingly, a non-zero torque $M \propto \Omega^5$ is predicted at $T_0 = T_1 = 0$, despite the axial symmetry of the particle.

The power absorbed by the particle in the form of thermal heating $\mathcal{P}^{\rm abs}$ can be obtained from energy conservation, expressed by the identity $-M\Omega = \mathcal{P}^{\rm rad} + \mathcal{P}^{\rm abs}$, where the left-hand side represents mechanical energy dissipation (stopping power). Using Eqs. (5.39) and (5.40), we find

$$\mathcal{P}^{\rm abs}_{\rm D} = \frac{\hbar a^3}{120\pi^2 c^3 \sigma_0}\left[2\Omega^6 + \Omega^2(\theta_0^4 - 3\theta_1^4) + \frac{5}{7}(\theta_0^6 - \theta_1^6)\right]. \tag{5.41}$$

The particle equilibrium temperature is determined by the condition $\mathcal{P}^{\rm abs} = 0$, and it is stable because $\partial\mathcal{P}^{\rm abs}/\partial T_1 < 0$ [this inequality is obvious from Eq. (5.41), but it can be easily derived in the general case from Eqs. (5.17)-(5.23)]. Unlike conventional friction of a spinning object immersed in a fluid, thermal and vacuum friction is not always leading to particle heating, as shown in Fig. 5.9 from the solution of $\mathcal{P}^{\rm abs}_{\rm D} = 0$. Actually, $T_1 < T_0$ for finite temperatures and rotation velocities below $\Omega = \theta_0$, whereas particle heating occurs at higher Ω. The crossing point between these two types of behavior is independent of particle size a and conductivity σ_0.

At $T_0 = 0$, we find $\theta_1 \approx 0.867\,\Omega$, so that the Ω^5 dependence of $M_{\rm D}$ is maintained with the particle at equilibrium temperature. The loss of mechanical energy is then fully converted into a radiated power $\mathcal{P}^{\rm rad}_{\rm D} \approx 0.013\,\hbar a^3\Omega^6/c^3\sigma_0$.

5.3.5 Stopping times of interstellar dust

At low rotation velocity and finite temperature, the frictional torque acting on a metallic particle is proportional to Ω [see Eq. (5.40)]. The correction to the particle equilibrium temperature [$\theta_1 \approx \theta_0 - (7/15)\Omega^2/\theta_0$] can be then neglected to first order in Ω, so the torque becomes $M \approx -\beta\Omega$, where $\beta = \hbar a^3\theta_0^4/30\pi^2c^3\sigma_0$. From Newton's second law, we find an $\Omega(t) = \Omega(0)\exp(-t/\tau)$ time dependence of the rotation velocity, where $\tau = I/\beta$ is the characteristic stopping time and I is the moment of

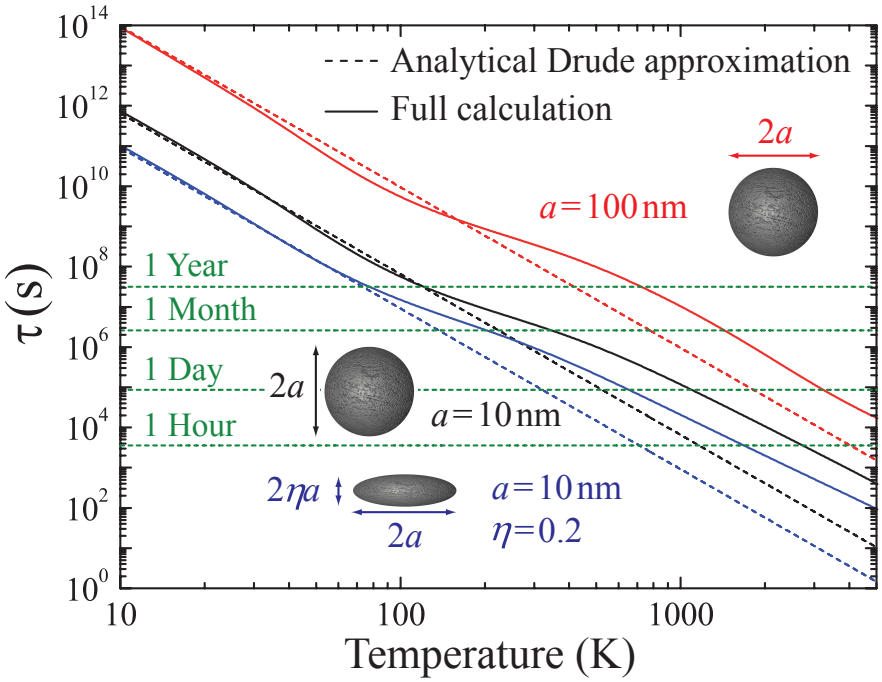

Figure 5.10: Characteristic stopping time of spinning graphite particles as a function of the environment temperature. Solid curves: full calculation using measured dielectric functions for the graphite particles [231]. Broken curves: analytical Drude approximation [Eq. (5.42)]. Various particle sizes and shapes are considered: spheres of radius 10 nm and 100 nm, and an oblate ellipsoid of radius 10 nm and aspect ratio $\eta = 0.2$. Low rotation velocities $\Omega \ll k_{\rm B}T_0/\hbar$ are assumed (*e.g.*, $\Omega \ll 21\,{\rm GHz}$ at $T_0 = 1\,{\rm K}$).

inertia. For a spherical Drude particle, we find

$$\tau = \frac{(\hbar c)^3}{\pi}\frac{\rho a^2 \sigma_0}{(k_{\rm B}T_0)^4}, \tag{5.42}$$

where ρ is the particle density.

Graphite particles are abundant in interstellar dust [232], so we focus on them as an important case to study the rotation stopping time. The frequency-dependent dielectric function of graphite is taken from optical data [231], tabulated for different particle sizes, which differ due to non-local corrections. The low-ω behavior is well approximated by the Drude model with $\sigma_0 = 2.3 \times 10^4$ $(2.0 \times 10^5)\,\Omega^{-1}{\rm m}^{-1}$ for

spherical particles of radius $a = 10\,(100)\,\mathrm{nm}$, where the response has been averaged over different crystal orientations. Plugging this into Eq. (5.42), we obtain the results shown in Fig. 5.10 by broken lines. Interband transitions become important in the response of graphite at frequencies above $\hbar\omega \sim 10^{-2}\,\mathrm{eV}$, so we expect a deviation from Drude behavior at temperatures above $\sim 100\,\mathrm{K}$ in this material. This is indeed confirmed by numerically integrating Eq. (5.17) with the full tabulated response of graphite to obtain τ (Fig. 5.10, solid curves). For the particle sizes under consideration, stopping times are small on cosmic scales within the plotted range of temperatures, which are often encountered in hot dust regions [232]. In cooler areas ($T_0 = 2.7\,\mathrm{K}$), 100 nm graphite particles have a stopping time $\tau \sim 0.6$ billion years.

Dust particles can adopt non-spherical shapes. In particular, for oblate ellipsoids Eq. (5.38) [$\mathrm{Im}\{\alpha(\omega)\}$] must be corrected by a factor $\eta/9L^2$, where η is the aspect ratio (see inset in Fig. 5.10) and L is the depolarization factor for equatorial polarization, approximately linear in η [3]. Also, I is linear in η, thus leading to a $\tau \propto \eta^2$ dependence for fixed radius. We show in Fig. 5.10 the case $a = 10\,\mathrm{nm}$ and $\eta = 0.2$, which exhibits a significant reduction in τ compared to spherical particles of the same radius. In a related context, translational motion leads to thermal drag [233], only at non-zero temperature and with similar stopping times.

5.4 Conclusions

In the first part of this chapter, we have presented a complete model to describe RHT between two nanoparticles within the assumption of dipolar response. We have shown that crossed magnetic-electric terms and radiative corrections produce modifications in the transfer rate by up to several orders of magnitude, which cannot be overlooked. Furthermore, we have presented an analysis of how much heat is released from a dimer into a cooler vacuum revealing a large dependence on composition and temperature (it is strongly suppressed at low temperatures and dominant in hot environments). Our results for gold-SiC dimers suggest the experimental exploration of these effects via, for example, in-vacuum particle levitation, or by attaching one of the particles to a nanoscale tip and the other one to an insulating substrate. As an interesting direction, we note that RHT can be strongly modified by the presence of additional mirrors and dielectrics that distort

the exchanged electromagnetic fields.

We believe that these results are of highly technological importance since heat dissipation in nanostructured devices is becoming a limiting factor in the design of microchips and is expected to play a major role in nanoelectronics, nanophotonics, and photovoltaics. In such context radiative losses provide a convenient way of handling the excess of heat produced in these devices [234].

In the second part of this chapter, we have developed a comprehensive semiclassical model based upon the FDT to describe the vacuum and thermal friction acting on rotating particles. We have presented analytical expressions both for the torque exerted on the rotating particle and for the net power that it radiates due to friction. We have also proved that the results derived within the semiclassical approach are in full agreement with those obtained through a quantum-mechanical derivation, in which the particle and the external field are described using combined states that include the internal state of the particle, which can host a number of bosonic excitations (*e.g.*, phonons or plasmons), the rotational state, and the electromagnetic field in the photon-number representation. The coupling between the mechanical rotation and the vacuum photon field is mediated by internal excitations of the particle. Using Fermi's golden rule to evaluate the different possible transitions between those states, we calculate the torque and the net radiated power.

The present results can be relevant to study the distribution of rotation velocities of cosmic nanoparticles, which could be eventually examined through measurements of rotational frequency shifts [235, 236]. Besides, relatively small stopping times are predicted for graphite nanoparticles, which ask for experimental corroboration (for example, using in-vacuo optical trapping setups). By analogy to the Purcell effect [237], the frictional torque can be altered due to the presence of physical boundaries that modify density of photonic states, thus opening new possibilities for controlling the degree of friction. For instance, as we have shown recently [238], the friction can be enhanced by placing the rotating particle close to a surface.

In a more fundamental direction, our results provide solid theoretical support for a semiclassical treatment of fluctuations using the FDT. The presented methodology can be useful to deal with friction in other situations such as sliding surfaces, a particle moving near a surface, and neutral particles in relative contactless motion. An interesting scenario is presented by Casimir-bound objects, orbiting around

each other, so that spin-orbit interaction (*i.e.*, coupling between rotational and translational degrees of freedom) can play a significant role.

Chapter 6

Conclusions

The research presented in this thesis has been devoted to study different aspects of light-matter interactions at the nanoscale. We have covered topics ranging from the design and characterization of plasmonic devices, to more fundamental concepts involving interactions with vacuum. The main contributions of our work can be summarized as follows:

(i) the identification of gap plasmons supported by metallic wire pairs as suitable candidates to guide signals in information processing devices,

(ii) the theoretical study of hybrid systems resulting from the interaction between quantum emitters and localized plasmons,

(iii) the prediction of a plasmon blockade effect associated with the interaction of a graphene nanodisk and a quantum emitter,

(iv) the proposal of a new scheme to control the temporal evolution of quantum emitters using graphene nanostructures,

(v) the theoretical study of the plasmonic response of small graphene nanoislands, showing its sensitivity to single electrons,

(vi) the development of a complete theory of radiative heat transfer between nanoparticles,

(vii) the prediction of a frictional torque acting upon rotating nanoparticles, originated from the fluctuations of the electromagnetic vacuum.

The first of these contributions has been extensively exposed in Chapter 2, where we have presented a novel plasmonic waveguide formed by pairs of metallic nanowires placed in silica. We have shown that the gap plasmons supported by these systems are excellent candidates to guide signals over tens of microns. These modes are quite robust against both unintended variations of wire cross-section and curvature in short turns. Furthermore, gap modes are highly confined to the gap region, so that inter-mixing between neighboring wire pairs can be minimized, enabling the design of highly-integrated plasmonic circuits in three dimensional spaces. We have also studied the interaction between gap plasmons confined in different wire pairs, finding a complex structure of hybridized modes including non-avoided crossings, which has led us to design an efficient gap plasmon coupler.

Chapter 3 has been devoted to study hybrid systems composed of quantum emitters interacting with the localized plasmons supported by metallic and graphene nanostructures. We have presented a novel methodology, based on Zubarev's Green functions, to describe the absorption spectrum of these systems. As an illustrative example, we have applied this method to study the optical response of a quantum emitter placed in the gap of a metallic dimer, finding a very rich spectral behavior, including narrow Fano resonances.

Analyzing the plasmonic response of a graphene nanodisk, we have predicted the existence of a plasmon blockade effect arising from the interaction of the plasmons supported by this system and a quantum emitter. This effect results in a strongly non-linear absorption cross-section and the generation of non-classical plasmon states, which we have characterized by studying the equal-time second-order correlation function. In contrast to the photon blockade effect, observed in experiments of cavity quantum electrodynamics, plasmon blockade can be tuned by modifying the doping level of the graphene nanodisk.

Taking advantage of the tunability of graphene plasmons, we have developed a novel strategy for controlling the temporal evolution of ensembles of quantum emitters. The method proposed here is based on controlling the plasmon-emitter interaction through the modulation of the doping level of the graphene nanostructure. We have provided realistic simulations demonstrating excellent control over

the decay of individual and interacting dots.

In Chapter 4, we have studied the plasmonic response of small graphene nanotriangles composed of hundreds of atoms, showing that the addition or the removal of a single electron switches on infrared plasmons that were previously absent from the uncharged structure. We have shown that this effect is highly sensitive to the type of edges of the nanostructure. Specifically, armchair nanotriangles display sharp plasmons that are associated with intense near-field enhancement, as well as absorption cross-sections exceeding the geometrical area occupied by the graphene. In contrast, zigzag triangles do not support these plasmons due to the existence of zero-energy states.

In Chapter 5, we have presented a theoretical model to describe the radiative heat transfer between nanoparticles. This model incorporates the full electromagnetic particle response, heat exchange with the environment, and important radiative corrections, both in the distance dependence of the fields and in the particle absorption coefficients, that where absent in previous studies and can be dominant in the interaction between commonly available nanoparticles.

Finally, we have predicted the existence of a frictional torque acting upon rotating nanoparticles. This torque originates in the fluctuations of the vacuum electromagnetic field and the particle polarization. Our results are based on two different methodologies leading to the same results, namely a semiclassical approach, which relies on the fluctuation-dissipation theorem, and a full quantum electrodynamic calculation. Using the developed theory, we have studied the stopping time of graphite nanoparticles, which are abundant in cosmic dust.

In conclusion, we honestly hope that the research presented in this thesis has contributed to advance the knowledge of light-matter interaction at the nanoscale. We are confident that this knowledge will open new horizons to develop novel applications in the field of nanophotonics.

Appendix A

Zubarev's Green functions

Derivation of the optical absorption spectrum in terms of Zubarev's Green functions

Within the approximation of linear response, the absorption cross-section of a certain system can be obtained from Fermi's Golden rule [see Eq. (1.22)] according to

$$\sigma(\omega) \propto \sum_f \left| \langle fn-1 | \, \hat{H}^{\text{int}} \, | in \rangle \right|^2 \delta(\varepsilon_f - \hbar\omega), \tag{A.1}$$

where $|i\rangle$ represents the initial ground state of the system under consideration; $|f\rangle$ is the corresponding final state, separated from the former by an energy difference ε_f; n is the number of external photons with frequency ω; and $\hat{H}^{\text{int}}$ is the Hamiltonian that couples the system to the external photon field, which is given by the expression

$$\hat{H}^{\text{int}} \propto \hat{R}\hat{a}^+ + \hat{R}^+\hat{a}. \tag{A.2}$$

Here, $\hat{a}$ and $\hat{R}$ ($\hat{a}^+$ and $\hat{R}^+$) are annihilation (creation) operators for the external photons and the excitations of the system, respectively, and therefore, $\hat{R}$ connects the initial and final states, governing the optical absorption properties.

Using the Hamiltonian of Eq. (A.2) and the identity

$$\delta(x) = \frac{1}{\pi}\text{Im}\left\{\frac{1}{x - i0^+}\right\},$$

we can recast Eq. (A.1) into

$$\sigma(\omega) \propto \mathrm{Im}\left\{\sum_f \frac{\langle in|\,\hat{H}^{\mathrm{int}}\,|fn-1\rangle\,\langle fn-1|\,\hat{H}^{\mathrm{int}}\,|in\rangle}{\varepsilon_f - \hbar\omega - i0^+}\right\}.$$

Then, taking into account the action of the photon annihilation operator ($\hat{a}\,|n\rangle = \sqrt{n}\,|n-1\rangle$) and the orthogonality of the photonic states ($\langle n|\,|n'\rangle = \delta_{n,n'}$), we obtain

$$\sigma(\omega) \propto \mathrm{Im}\left\{\sum_f \frac{\langle i|\,\hat{R}\,|f\rangle\,\langle f|\,\hat{R}^+\,|i\rangle}{\varepsilon_f - \hbar\omega - i0^+}\right\}. \tag{A.3}$$

At this point, we assume that $\hat{R}^+$ connects the initial ground state with a set of final states that present a common energy ε_f. This is a good approximation for the systems considered in this thesis, in which the external photons couple through excitations of single mode plasmons. Therefore, we can extract the denominator of Eq. (A.3) from the sum over final states, and using the closure relation for final states $\sum_f |f\rangle\langle f| = \mathbb{I}$ (within the ε_f reachable-energy shell), the optical absorption spectrum reduces to

$$\sigma(\omega) \propto \mathrm{Im}\left\{\frac{\langle i|\,\hat{R}\hat{R}^+\,|i\rangle}{\varepsilon_f - \hbar\omega - i0^+}\right\}, \tag{A.4}$$

where $\langle i|\,\hat{R}\hat{R}^+\,|i\rangle$ is the expectation value of $\hat{R}\hat{R}^+$ in the initial ground state.

We now consider the definition of the retarded Zubarev Green function for the operators that annihilate and create a system excitation [see Eq. (1.23)]:

$$\langle\langle \hat{R}; \hat{R}^+\rangle\rangle_{\omega+i0^+} = -\frac{i}{\hbar}\int_0^\infty dt e^{i(\omega+i0^+)t}\left[\left\langle \hat{R}(t)\hat{R}^+(0)\right\rangle - \eta\left\langle \hat{R}^+(0)\hat{R}(t)\right\rangle\right], \tag{A.5}$$

where we have switched to the Heisenberg picture, and therefore, the free evolution of the operator $\hat{R}$ is given by the Heisenberg equation of motion [54], which for fixed excitation energy ε_f leads to

$$\hat{R}(t) = \hat{R}(0)e^{-i\varepsilon_f t/\hbar}. \tag{A.6}$$

This is consistent with the noted assumption of a single final-state energy ε_f.

Equation (A.6) allows us to solve the integral of Eq. (A.5). We find

$$\langle\langle \hat{R}; \hat{R}^{+} \rangle\rangle_{\omega+i0^{+}} = -\frac{\left\langle \hat{R}(0)\hat{R}^{+}(0) \right\rangle}{\varepsilon_f - \hbar\omega - i0^{+}}, \tag{A.7}$$

where we have taken into account that the second term of Eq. (A.5) vanishes when the system is in the ground state. Finally, noticing that $\langle i| \hat{R}\hat{R}^{+} |i\rangle$ and $\left\langle \hat{R}(0)\hat{R}^{+}(0) \right\rangle$ are both the same magnitude in the Schrödinger and the Heisenberg picture, respectively, we can substitute Eq. (A.7) into Eq. (A.4) to obtain the desired expression [see Eq. (1.24)].

Derivation of the equation of motion for the retarded Zubarev's Green functions

The retarded Zubarev's Green function in the time domain can be obtained from the Fourier transform of Eq. (1.23), as

$$\langle\langle \hat{R}(t); \hat{S}(0) \rangle\rangle = -\frac{i}{\hbar}\theta(t) \left\langle \left[\hat{R}(t), \hat{S}(0) \right]_{\eta} \right\rangle.$$

Differentiating with respect to the time, we find

$$i\frac{d}{dt}\langle\langle \hat{R}(t); \hat{S}(0) \rangle\rangle = \frac{1}{\hbar}\frac{d\theta(t)}{dt} \left\langle \left[\hat{R}(t), \hat{S}(0) \right]_{\eta} \right\rangle + \langle\langle i\frac{d\hat{R}(t)}{dt}; \hat{S}(0) \rangle\rangle,$$

which can be simplified using the Heisenberg equation of motion [54] to yield

$$i\hbar\frac{d}{dt}\langle\langle \hat{R}(t); \hat{S}(0) \rangle\rangle = \delta(t) \left\langle \left[\hat{R}(t), \hat{S}(0) \right]_{\eta} \right\rangle + \langle\langle [\hat{R}(t), \hat{H}]; \hat{S}(0) \rangle\rangle. \tag{A.8}$$

Here, $\hat{H}$ is the Hamiltonian of the system. Finally, taking the Fourier transform of Eq. (A.8), we readily obtain the desired equation of motion for the retarded Zubarev's Green functions [see Eq. (1.25)].

Appendix B

Derivation of the fluctuation-dissipation theorem

The fluctuation-dissipation theorem (FDT) [66, 67] connects the fluctuations of the product of two operators with the dissipation expressed through the imaginary part of their response function. Here we provide a simple derivation of this result with a notation that is appropriate to deal with fluctuations of vacuum fields and particle polarizations. Let us start by considering a Hamiltonian $\hat{H}_0$ perturbed by a term

$$\hat{H}'(t) = -\varphi(t)\hat{q}(t),$$

where $\varphi(t)$ is a time-dependent function, $\hat{q}(t)$ is an operator in the Heisenberg representation, related to its Schrödinger representation $\hat{q}_{\rm S}$ through the expression $\hat{q}(t) = \hat{U}^{+}(t,t_0)\hat{q}_{\rm S}\hat{U}(t,t_0)$, where $\hat{U}(t,t_0) = \exp(-i\hat{H}_0(t-t_0)/\hbar)$. In the Heisenberg representation, Schrödinger's equation becomes $\hat{H}'\left|\phi\right\rangle = i\hbar\partial\left|\phi\right\rangle/\partial t$, and we have $\left|\phi\right\rangle = \hat{U}^{+}(t-t_0)\left|\phi_{\rm S}(t)\right\rangle$.

Under the condition $\hat{H}'(t)\xrightarrow[t\to-\infty]{}0$, the eigenstates of the total Hamiltonian become

$$\begin{aligned}\left|\phi_m(t)\right\rangle &= \left|m\right\rangle - \frac{i}{\hbar}\int_{-\infty}^{t} dt' H'(t')\left|\phi_m(t')\right\rangle \\ &\approx \left|m\right\rangle - \frac{i}{\hbar}\int_{-\infty}^{t} dt' H'(t')\left|m\right\rangle,\end{aligned}$$

where the last line corresponds to first-order perturbation theory, and $|m\rangle$ is a state of the unperturbed Hamiltonian with energy ε_m (*i.e.*, $\hat{H}_0 |m\rangle = \varepsilon_m |m\rangle$).

The expected value of another operator $\hat{p}(t)$ is simply given by

$$\begin{aligned}\langle \hat{p}(t) \rangle &= \frac{1}{Z} \sum_m e^{-\varepsilon_m / k_{\mathrm{B}} T} \langle \phi_m(t) | \hat{p}(t) | \phi_m(t) \rangle \\ &\approx \frac{1}{Z} \sum_m e^{-\varepsilon_m / k_{\mathrm{B}} T} \left[\langle m | \hat{p}(t) | m \rangle + \frac{i}{\hbar} \int_{-\infty}^{t} dt' \varphi(t') \langle m | [\hat{p}(t), \hat{q}(t')] | m \rangle \right], \quad \text{(B.1)}\end{aligned}$$

where we have assumed that the system is at equilibrium at temperature T, being $Z = \sum_m e^{-\varepsilon_m / k_{\mathrm{B}} T}$ the system partition function. The first term in Eq. (B.1) reduces to $\langle m | \hat{p}(t) | m \rangle = \langle m | \hat{p}_{\mathrm{S}} | m \rangle$, and from here, we can recast Eq. (B.1) as

$$\langle \delta \hat{p}(t) \rangle \equiv \langle \hat{p}(t) - \hat{p}(-\infty) \rangle = \int dt' \chi(t - t') \varphi(t'),$$

where

$$\chi(t - t') = \frac{i}{\hbar} \theta(t - t') \frac{1}{Z} \sum_m e^{-\varepsilon_m / k_{\mathrm{B}} T} \langle m | [\hat{p}(t), \hat{q}(t')] | m \rangle \quad \text{(B.2)}$$

is a susceptibility function. Now, using the closure relation $|n\rangle \langle n| = I$, we can write

$$\begin{aligned}\langle m | [\hat{p}(t), \hat{q}(t')] | m \rangle = \sum_n \Big[&\langle m | \hat{p}_{\mathrm{S}} | n \rangle \langle n | \hat{q}_{\mathrm{S}} | m \rangle e^{i(\varepsilon_m - \varepsilon_n)(t - t')/\hbar} \\ &- \langle m | \hat{q}_{\mathrm{S}} | n \rangle \langle n | \hat{p}_{\mathrm{S}} | m \rangle e^{-i(\varepsilon_m - \varepsilon_n)(t - t')/\hbar} \Big].\end{aligned}$$

Inserting this back into Eq. (B.2), and taking the time Fourier transform to work in frequency space we find[1]

$$\chi(\omega) = \int dt \chi(t) e^{i\omega t} = \frac{-1}{Z} \sum_{m,n} \langle m | \hat{p}_{\mathrm{S}} | n \rangle \langle n | \hat{q}_{\mathrm{S}} | m \rangle \frac{e^{-\varepsilon_m / k_{\mathrm{B}} T} - e^{-\varepsilon_n / k_{\mathrm{B}} T}}{\hbar\omega + \varepsilon_m - \varepsilon_n + i0^+}.$$

[1] Notice that $\int_0^\infty dt e^{i\Delta t} = \frac{i}{\Delta + i0^+}$.

Finally, the dissipation associated with χ can be written as

$$\mathrm{Im}\left\{\chi(\omega)\right\} = \left(1 - e^{-\hbar\omega/k_{\mathrm{B}}T}\right)\frac{\pi}{Z}\sum_{m,n} e^{-\varepsilon_m/k_{\mathrm{B}}T}\left\langle m\right|\hat{p}_{\mathrm{S}}\left|n\right\rangle\left\langle n\right|\hat{q}_{\mathrm{S}}\left|m\right\rangle\delta(\hbar\omega + \varepsilon_m - \varepsilon_n). \tag{B.3}$$

Similarly, we can write the average over fluctuations as

$$\begin{aligned} S(t-t') \equiv \langle\hat{p}(t)\hat{q}(t')\rangle &= \frac{1}{Z}\sum_{m,n} e^{-\varepsilon_m/k_{\mathrm{B}}T}e^{i(\varepsilon_m-\varepsilon_n)(t-t')/\hbar}\left\langle m\right|\hat{p}_{\mathrm{S}}\left|n\right\rangle\left\langle n\right|\hat{q}_{\mathrm{S}}\left|m\right\rangle \\ &= \int\frac{d\omega}{2\pi}S(\omega)e^{-i\omega(t-t')}, \end{aligned}$$

where

$$S(\omega) = \frac{2\pi\hbar}{Z}\sum_{m,n} e^{-\varepsilon_m/k_{\mathrm{B}}T}\left\langle m\right|\hat{p}_{\mathrm{S}}\left|n\right\rangle\left\langle n\right|\hat{q}_{\mathrm{S}}\left|m\right\rangle\delta(\hbar\omega + \varepsilon_m - \varepsilon_n). \tag{B.4}$$

The relation between $S(\omega)$ and $\mathrm{Im}\left\{\chi(\omega)\right\}$ that one obtains by comparing Eqs. (B.3) and (B.4) constitutes the general form of the fluctuation-dissipation theorem:

$$S(\omega) = 2\hbar[n(\omega,T)+1]\mathrm{Im}\left\{\chi(\omega)\right\}, \tag{B.5}$$

where $n(\omega,T) = \left[e^{\hbar\omega/k_{\mathrm{B}}T} - 1\right]^{-1}$ is the Bose-Einstein distribution function. We can formulate a more useful relation by noticing that $\langle\hat{p}(t)\hat{q}(t')\rangle$ is a function of $t-t'$, so that its double Fourier transform satisfies

$$\begin{aligned} \langle\hat{p}(\omega)\hat{q}(\omega')\rangle &= \int dtdt' e^{i\omega t + i\omega' t'}S(t-t') \\ &= \int d\tau e^{i\omega\tau}S(\tau)\int dt' e^{i(\omega+\omega')t'} = 2\pi\delta(\omega+\omega')S(\omega), \end{aligned}$$

and from here we find the expression

$$\langle\hat{p}(\omega)\hat{q}(\omega')\rangle = 4\pi\hbar[n(\omega,T)+1]\mathrm{Im}\left\{\chi(\omega)\right\}\delta(\omega+\omega'). \tag{B.6}$$

Proceeding like above, the Fourier transform of the fluctuation $\langle\hat{q}(t')\hat{p}(t)\rangle$ reads

$\langle \hat{q}(\omega')\hat{p}(\omega)\rangle = \exp(-\hbar\omega/k_{\rm B}T)\, S(\omega)$, which together with Eq. (B.5) leads to

$$\langle \hat{q}(\omega')\hat{p}(\omega)\rangle = 4\pi\hbar n(\omega,T)\mathrm{Im}\left\{\chi(\omega)\right\}\delta(\omega+\omega'). \tag{B.7}$$

Finally, it should be noticed that $\hat{p}(\omega)\hat{q}(\omega')$ is not an observable in general, but the symmetrized product is Hermitian, and therefore, an observable. From Eqs. (B.6) and (B.7), we find

$$\frac{1}{2}\langle \hat{p}(\omega)\hat{q}(\omega') + \hat{q}(\omega')\hat{p}(\omega)\rangle = 4\pi\hbar\left[n(\omega,T)+\frac{1}{2}\right]\mathrm{Im}\left\{\chi(\omega)\right\}\delta(\omega+\omega'). \tag{B.8}$$

Equations (B.6)-(B.8) are general forms of the FDT. Next, we formulate specific applications for dipole and electric-field fluctuations.

FDT for fluctuations of the dipole moment

Now, we can apply the above general expressions of the FDT to dipole-dipole fluctuations, with the identifications

$$\begin{aligned}
\hat{p}(t) &\to p_i(t),\\
\hat{q}(t) &\to p_j(t),\\
\chi(t) &\to \alpha_{ij}(t),\\
\varphi(t) &\to E_j(t),
\end{aligned}$$

where p_i and p_j are components of the dipole moment along directions i and j, respectively, E_j is the electric field along j at the position of the dipole, and α_{ij} is the (i,j) component of the polarizability tensor. The interaction Hamiltonian is $\hat{H}'(t) = -E_j(t)p_j(t)$, where E_j is regarded as a time-dependent function and p_j as an operator. The susceptibility acts in frequency space according to $\langle \delta p_i(\omega)\rangle = \alpha_{ij}(\omega)E_j(\omega)$. With these substitutions, the FDT [Eqs. (B.6)-(B.8)] takes the forms

$$\begin{aligned}
\langle p_i(\omega)p_j(\omega')\rangle &= 4\pi\hbar[n(\omega,T)+1]\mathrm{Im}\left\{\alpha_{ij}(\omega)\right\}\delta(\omega+\omega'),\\
\langle p_j(\omega')p_i(\omega)\rangle &= 4\pi\hbar n(\omega,T)\mathrm{Im}\left\{\alpha_{ij}(\omega)\right\}\delta(\omega+\omega'),\\
\frac{1}{2}\langle p_i(\omega)p_j(\omega') + p_j(\omega')p_i(\omega)\rangle &= 4\pi\hbar\left[n(\omega,T)+\frac{1}{2}\right]\mathrm{Im}\left\{\alpha_{ij}(\omega)\right\}\delta(\omega+\omega').
\end{aligned}$$

The same expression is valid for the FDT for fluctuations of the magnetic dipole, with α_{ij} being, in that case, the magnetic polarizability.

FDT for fluctuations of the electric field

Similarly, the fluctuations of the electric field can be analyzed with the substitutions

$$\begin{aligned}
\hat{p}(t) &\to E_i(\mathbf{r},t),\\
\hat{q}(t) &\to E_j(\mathbf{r}',t),\\
\chi(t) &\to \mathcal{G}_{ij}(\mathbf{r},\mathbf{r}',t),\\
\varphi(t) &\to p_j(t),
\end{aligned}$$

where $E_i(\mathbf{r},t)$ and $E_j(\mathbf{r}',t)$ are components of the electric field along directions i and j at positions $\mathbf{r}$ and $\mathbf{r}'$, respectively, and $\mathcal{G}_{ij}(\mathbf{r},\mathbf{r}',t)$ is the Green tensor of the electromagnetic field [see Eq. (1.31)]. The interaction Hamiltonian is again $\hat{H}'(t) = -p_j(t)E_j(t)$, but now p_j is a time-dependent function and E_j is an operator. The susceptibility acts as $\langle \delta E_i(\omega)\rangle = \mathcal{G}_{ij}(\mathbf{r},\mathbf{r}',\omega)\, p_j(\omega)$, which is consistent with the definition of Eq. (1.31) [18]. The FDT takes the forms

$$\begin{aligned}
\langle E_i(\mathbf{r},\omega)E_j(\mathbf{r}',\omega')\rangle &= 4\pi\hbar[n(\omega,T)+1]\mathrm{Im}\left\{\mathcal{G}_{ij}(\mathbf{r},\mathbf{r}',\omega\right\}]\\
&\quad\times\delta(\omega+\omega'),\\
\langle E_j(\mathbf{r}',\omega')E_i(\mathbf{r},\omega)\rangle &= 4\pi\hbar n(\omega,T)\mathrm{Im}\left\{\mathcal{G}_{ij}(\mathbf{r},\mathbf{r}',\omega)\right\}]\\
&\quad\times\delta(\omega+\omega'),\\
\frac{1}{2}\left\langle E_i(\mathbf{r},\omega)E_j(\mathbf{r}',\omega')+E_j(\mathbf{r}',\omega')E_i(\mathbf{r},\omega)\right\rangle &= 4\pi\hbar\left[n(\omega,T)+\frac{1}{2}\right]\\
&\quad\times\mathrm{Im}\left\{\mathcal{G}_{ij}(\mathbf{r},\mathbf{r}',\omega)\right\}\delta(\omega+\omega').
\end{aligned}$$

Interestingly, in the limit $\mathbf{r}=\mathbf{r}'$ we have $\mathrm{Im}\left\{\mathcal{G}_{ij}(\mathbf{r},\mathbf{r},\omega)\right\} = (2\pi^2\omega/3)\rho^0\delta_{ij}$, where ρ^0 is the photonic local density of states [1] ($\rho^0 = \omega^2/\pi^2c^3$ in vacuum).

Due to the symmetries of Maxwell's equations, the expressions given above represent also the FDT for the fluctuations of the magnetic field. Furthermore, using Maxwell-Faraday's law [first expression of Eq. (1.4)], it is straightforward to derive the FDT for the electric-magnetic and the magnetic-electric field fluctuations.

List of publications and contributions to conferences

The research performed during the development of this thesis has led to the following publications and contributions to international conferences:

Articles in which the thesis is based

1. A. Manjavacas, S. Thongrattanasiri, and F. J. García de Abajo.
Plasmons driven by single electrons in graphene nanoislands
Nanophotonics **2**, 139 (2013). Selected for the cover of Vol. 2, Iss. 2, 2013.

2. A. Manjavacas, S. Thongrattanasiri, D. E. Chang, and F. J. García de Abajo.
Temporal quantum control with graphene.
New Journal of Physics **14**, 123020 (2012).

3. A. Manjavacas, and F. J. García de Abajo.
Radiative heat transfer between neighboring particles.
Physical Review B **86**, 075466 (2012).

4. A. Manjavacas, P. Nordlander, and F. J. García de Abajo.
Plasmon blockade in nanostructured graphene.
ACS Nano **6**, 1724 (2012).

5. A. Manjavacas, F. J. García de Abajo, and P. Nordlander.
Quantum plexcitonics: strongly interacting plasmons and excitons.
Nano Letters **11**, 2318 (2011). Highlighted in Nanotechweb.

6. A. Manjavacas, and F. J. García de Abajo.
Thermal and vacuum friction acting on rotating particles.
Physical Review A **82**, 063827 (2010). Highlighted in Physics Synopsis and New Scientist

7. A. Manjavacas, and F. J. García de Abajo.
Vacuum friction in rotating particles.
Physical Review Letters **105**, 113601 (2010).

8. A. Manjavacas, and F. J. García de Abajo.
Coupling of gap plasmons in multi-wire waveguides.
Optics Express **17**, 19401 (2009).

9. A. Manjavacas, and F. J. García de Abajo.
Robust plasmon waveguides on nanowire arrays.
Nano Letters **9**, 1285 (2009). Selected for the cover of Vol. 9, Iss. 4, 2009.

Articles related to the thesis

1. A. Manjavacas, and F. J. García de Abajo.
Optical response of single-monolayer gold nanodisks.
In preparation.

2. A. Manjavacas, F. Marchesin, S. Thongrattanasiri, P. Koval, P. Nordlander, D. Sánchez-Portal, and F. J. García de Abajo.
Tunable molecular plasmons in polycyclic aromatic hydrocarbons.
ACS Nano **7**, 3635 (2013).

3. I. Silveiro, A. Manjavacas, S. Thongrattanasiri, and F. J. García de Abajo.
Plasmonic energy transfer in periodically doped graphene.
New Journal of Physics **15**, 033042 (2013).

4. S. Thongrattanasiri, A. Manjavacas, P. Nordlander, and F. J. García de Abajo.
Quantum junction plasmons in graphene dimers.
Laser and Photonics Reviews **7**, 297 (2013).

5. A. Asenjo-Garcia, A. Manjavacas, V. Myroshnychenko, and F. J. García de Abajo.
Magnetic polarization in the optical absorption of metallic nanoparticles.
Optics Express **20**, 28142 (2012).

6. R. Zhao, A. Manjavacas, F. J. García de Abajo, and J. B. Pendry.
Rotational quantum friction.
Physical Review Letters **109**, 123604 (2012). Highlighted as Editor's Suggestion.

7. V. Myroshnychenko, A. Stefanski, A. Manjavacas, M. Kafesaki, R. I. Merino, V. M. Orera, D. A. Pawlak, and F. J. García de Abajo.

Interacting plasmon and phonon polaritons in aligned nano- and microwires. Optics Express **20**, 10879 (2012).

8. S. Thongrattanasiri, A. Manjavacas, and F. J. García de Abajo. *Quantum finite-size effects in graphene plasmons.* ACS Nano **6**, 1766 (2012).

9. J. Christensen, A. Manjavacas, S. Thongrattanasiri, F. H. L. Koppens, and F. J. García de Abajo. *Graphene plasmon waveguiding and hybridization in individual and paired nanoribbons.* ACS Nano **6**, 431 (2012).

10. A. Asenjo-Garcia, A. Manjavacas, and F. J. García de Abajo. *Stimulated light emission and inelastic scattering by a classical linear system of rotating particles.* Physical Review Letters **106**, 213601 (2011).

11. A. G. Curto, A. Manjavacas, and F. J. García de Abajo. *Near-field focusing with optical phase antennas.* Optics Express **17**, 17801 (2009). Selected for the cover video of Vol. 17, Iss. 20 - Sep. 28, 2009.

Contributions to international conferences

1. A. Manjavacas, P. Nordlander, and F. J. García de Abajo. *Plasmon blockade in nanostructured graphene.* SPP6, Ottawa, Canada. May 26-31, 2013. Oral contribution.

2. A. Manjavacas, F. Marchesin, S. Thongrattanasiri, P. Koval, P. Nordlander, D. Sánchez-Portal, and F. J. García de Abajo. *Tunable molecular plasmons in polycyclic aromatic hydrocarbons.* SPP6, Ottawa, Canada. May 26-31, 2013. Oral contribution.

3. A. Manjavacas, P. Nordlander, and F. J. García de Abajo. *Plasmon blockade in nanostructured graphene.* Nanometa 2013, Seefeld in Tirol, Austria. January 3-6, 2013. Oral contribution.

4. A. Manjavacas, P. Nordlander, and F. J. García de Abajo. *Plasmon blockade in nanostructured graphene.* Nanometa 2013, Seefeld in Tirol, Austria. January 3-6, 2013. Oral contribution.

5. A. Manjavacas, S. Thongrattanasiri, P. Nordlander, D. E. Chang, and F. J. García de Abajo. *Graphene plasmons and quantum emitters: from plasmon blockade to temporal control.* Quantum Science Syposium-2012, Cambridge, United Kingdom. November 1-2, 2012. Oral contribution.

6. A. Manjavacas, S. Thongrattanasiri, P. Nordlander, D. E. Chang, and F. J. García de Abajo. *Graphene plasmons and quantum emitters: from plasmon blockade to temporal control.* CEN 2012, Carmona, Spain. October 1-4, 2012. Oral contribution.

7. A. Manjavacas, P. Nordlander, and F. J. García de Abajo. *Plasmon blockade in nanostructured graphene.* NFO12, San Sebastian, Spain. September 3-7, 2012. Oral contribution.

8. A. Manjavacas, P. Nordlander, and F. J. García de Abajo. *Plasmon blockade in nanostructured graphene.* SPIE - Optics + Photonics 2012, San Diego, United States. August 12-16, 2012. Oral contribution.

9. A. Manjavacas, and F. J. García de Abajo. *Graphene plasmonics.* QuoDTPhe, Madrid, Spain. June 29, 2012. **Invited talk**.

10. A. Manjavacas, and F. J. García de Abajo. *Quantum friction and radiative transfer.* TaCoNa Photonics, Bad Honnef, Germany. October 25-28, 2011. **Invited talk**.

11. A. Manjavacas, F. J. García de Abajo, and P. Nordlander. *A quantum-mechanical approach to light-plasmon interaction.* SPP5, Busan, South Korea. May 15-20, 2011. Oral contribution.

12. A. Manjavacas, and F. J. García de Abajo. *Deterministic single-photon generation in a linear waveguide.* SPP5, Busan, South Korea. May 15-20, 2011. Oral contribution.

13. A. Manjavacas, and F. J. García de Abajo. *Quantum plasmonics with nanoparticles.* MRS Spring Meeting 2011, San Francisco, United States. April 26-29, 2011. **Invited talk**.

14. A. Manjavacas, and F. J. García de Abajo. *Vacuum can stop spinning particles.* Nanometa 2011, Seefeld in Tirol, Austria. January 3-6, 2011. Oral contribution.

15. A. Manjavacas, and F. J. García de Abajo. *Deterministic single-photon generation in a linear waveguide.* Nanometa 2011, Seefeld in Tirol, Austria. January 3-6, 2011. Oral contribution.

16. A. Manjavacas, and F. J. García de Abajo. *Vacuum friction in rotating particles.* SPIE - Optics + Photonics 2010, San Diego, United States. August 1-5, 2010. Oral contribution.

17. A. Manjavacas, and F. J. García de Abajo. *Vacuum and thermal friction in rotating nanoparticles.* CEN 2010, Segovia, Spain. June 15-18, 2010. Oral contribution.

18. A. Manjavacas, and F. J. García de Abajo. *Electromagnetic friction in rotating nanoparticles.* SPIE Europe 2010, Brussels, Belgium. April 12-16, 2010. Oral contribution.

19. A. Manjavacas, and F. J. García de Abajo. *Coupling of gap plasmons in multi-wire waveguides.* Meta 10 - Nato Advanced Research Workshop, Cairo, Egypt. February 22-25, 2010. Oral contribution.

20. A. Manjavacas, and F. J. García de Abajo. *Gap-plasmon waveguides.* ChinaNano 2009, Beijing, China. September 1-3, 2009. Oral contribution.

21. A. Manjavacas, and F. J. García de Abajo. *Gap plasmons in neighburing metal wires.* SPIE Optics and Optoelectronics 2009, Prague, Czech Republic. April 20-23, 2009. Oral contribution.

22. A. Manjavacas, and F. J. García de Abajo. *Robust plasmon waveguides in nanowire arrays.* SPIE - Optics + Photonics 2008, San Diego, United States. August 10-14, 2008. Oral contribution.

23. A. Manjavacas, and F. J. García de Abajo. *Robust plasmon waveguides in nanowire arrays.* Meta 08 - Nato Advanced Research Workshop, Marrakech, Morocco. May 7-10, 2008. Oral contribution.

24. A. Manjavacas, and F. J. García de Abajo. *Robust plasmon waveguides in nanowire arrays.* SPIE Europe 2008, Strasbourg, France. April 7-10, 2008. Oral contribution.

Additionally, the work performed during the thesis had led to 20 poster contributions presented by A. Manjavacas, and 12 poster contributions, 4 oral contributions, 3 invited talks, and 1 keynote talk presented by other coauthors.

Bibliography

[1] L. Novotny and B. Hecht. *Principles of Nano-Optics*. Cambridge University Press, New York, 2006.

[2] I. Freestone, N. Meeks, M. Sax, and C. Higgitt. The lycurgus cup - a roman nanotechnology. *Gold Bulletin*, 40:270–277, 2007.

[3] V. Myroshnychenko, J. Rodríguez-Fernández, I. Pastoriza-Santos, A. M. Funston, C. Novo, P. Mulvaney, L. M. Liz-Marzán, and F. J. García de Abajo. Modelling the optical response of gold nanoparticles. *Chem. Soc. Rev.*, 37:1792–1805, 2008.

[4] H. Raether. *Surface Plasmons on Smooth and Rough Surfaces and on Gratings*, volume 111 of *Springer Tracks in Modern Physics*. Springer-Verlag, Berlin, 1988.

[5] S. A. Maier. *Plasmonics: Fundamentals and Applications*. Springer, New York, 2007.

[6] A. K. Geim and K. S. Novoselov. The rise of graphene. *Nat. Mater.*, 6:183–191, 2007.

[7] F. H. L. Koppens, D. E. Chang, and F. J. García de Abajo. Graphene plasmonics: A platform for strong light-matter interactions. *Nano Lett.*, 11:3370–3377, 2011.

[8] H. Xu, E. J. Bjerneld, M. Käll, and L. Börjesson. Spectroscopy of single hemoglobin molecules by surface enhanced raman scattering. *Phys. Rev. Lett.*, 83:4357–4360, 1999.

[9] C. E. Talley, J. B. Jackson, C. Oubre, N. K. Grady, C. W. Hollars, S. M. Lane, T. R. Huser, P. Nordlander, and N. J. Halas. Surface-enhanced Raman scattering from individual au nanoparticles and nanoparticle dimer substrates. *Nano Lett.*, 5:1569–1574, 2005.

[10] R. A. Álvarez-Puebla, L. M. Liz-Marzán, and F. J. García de Abajo. Light concentration at the nanometer scale. *J. Phys. Chem. Lett.*, 1:2428–2434, 2010.

[11] M. W. Knight, H. Sobhani, P. Nordlander, and N. J. Halas. Photodetection with active optical antennas. *Science*, 332:702–704, 2011.

[12] K. R. Catchpole and A. Polman. Plasmonic solar cells. *Opt. Express*, 16:21793–21800, 2008.

[13] H. A. Atwater and A. Polman. Plasmonics for improved photovoltaic devices. *Nat. Mater.*, 9:205–213, 2010.

[14] D. P. O'Neal, L. R. Hirsch, N. J. Halas, J. D. Payne, and J. L. West. Photothermal tumor ablation in mice using near infrared-absorbing nanoparticles. *Cancer Lett.*, 209:171–176, 2004.

[15] C. Loo, A. Lowery, N. J. Halas, J. L. West, and R. Drezek. Inmunotargeted nanoshells for integrated cancer imaging and therapy. *Nano Lett.*, 5:709–711, 2005.

[16] R. Zia, J. A. Schuller, A. Chandran, and M. L. Brongersma. Plasmonics: The next chip-scale technology. *Mater. Today*, 9:20–27, 2006.

[17] J. C. Maxwell. *Treatise on Electricity and Magnetism*. reprint by Dover, New York, 1891.

[18] J. D. Jackson. *Classical Electrodynamics*. Wiley, New York, 1999.

[19] F. J. García de Abajo. Nonlocal effects in the plasmons of strongly interacting nanoparticles, dimers, and waveguides. *J. Phys. Chem. C*, 112:17983–17987, 2008.

[20] J. Zuloaga, E. Prodan, and P. Nordlander. Quantum description of the plasmon resonances of a nanoparticle dimer. *Nano Lett.*, 9:887–891, 2009.

[21] N. W. Ashcroft and N. D. Mermin. *Solid State Physics*. Harcourt College Publishers, New York, 1976.

[22] F. J. García de Abajo. Optical excitations in electron microscopy. *Rev. Mod. Phys.*, 82:209–275, 2010.

[23] P. B. Johnson and R. W. Christy. Optical constants of the noble metals. *Phys. Rev. B*, 6:4370–4379, 1972.

[24] G. Mie. Beiträge zur optik trüber medien, speziell kolloidaler metallösungen. *Ann. Phys. (Leipzig)*, 25:377–445, 1908.

[25] C. F. Bohren and D. R. Huffman. *Absorption and Scattering of Light by Small Particles*. Wiley-Interscience, New York, 1983.

[26] F. J. García de Abajo. Relativistic energy loss and induced photon emission in the interaction of a dielectric sphere with an external electron beam. *Phys. Rev. B*, 59:3095–3107, 1999.

[27] A. García-Etxarri, R. Gómez-Medina, L. S. Froufe-Pérez, C. López, L. Chantada, E. Scheffold, J. Aizpurua, M. Nieto-Vesperinas, and J. J. Sáenz. Strong magnetic response of submicron silicon particles in the infrared. *Opt. Express*, 19:4815–4826, 2011.

[28] A. Asenjo-Garcia, A. Manjavacas, V. Myroshnychenko, and F. J. García de Abajo. Magnetic polarization in the optical absorption of metallic nanoparticles. *Opt. Express*, 20:28142–28152, 2012.

[29] F. J. García de Abajo and A. Howie. Relativistic electron energy loss and electron-induced photon emission in inhomogeneous dielectrics. *Phys. Rev. Lett.*, 80:5180–5183, 1998.

[30] F. J. García de Abajo and A. Howie. Retarded field calculation of electron energy loss in inhomogeneous dielectrics. *Phys. Rev. B*, 65:115418, 2002.

[31] A. H. Castro Neto, F. Guinea, N. M. R. Peres, K. S. Novoselov, and A. K. Geim. The electronic properties of graphene. *Rev. Mod. Phys.*, 81:109–162, 2009.

[32] K. S. Novoselov, A. K. Geim, S. V. Morozov, D. Jiang, M. I. Katsnelson, I. V. Grigorieva, S. V. Dubonos, and A. A. Firsov. Two-dimensional gas of massless Dirac fermions in graphene. *Nature*, 438:197–200, 2005.

[33] C. F. Chen, C. H. Park, B. W. Boudouris, J. Horng, B. Geng, C. Girit, A. Zettl, M. F. Crommie, R. A. Segalman, S. G. Louie, and F. Wang. Controlling inelastic light scattering quantum pathways in graphene. *Nature*, 471:617–620, 2011.

[34] J. Chen, M. Badioli, P. Alonso-González, S. Thongrattanasiri, F. Huth, J. Osmond, M. Spasenović, A. Centeno, A. Pesquera, P. Godignon, A. Zurutuza Elorza, N. Camara, F. J. García de Abajo, R. Hillenbrand, and F. H. L. Koppens. Optical nano-imaging of gate-tunable graphene plasmons. *Nature*, 487:77–81, 2012.

[35] Z. Fei, A. S. Rodin, G. O. Andreev, W. Bao, A. S. McLeod, M. Wagner, L. M. Zhang, Z. Zhao, M. Thiemens, G. Dominguez, M. M. Fogler, A. H. Castro Neto, C. N. Lau, F. Keilmann, and D. N. Basov. Gate-tuning of graphene plasmons revealed by infrared nano-imaging. *Nature*, 487:82–85, 2012.

[36] M. Jablan, H. Buljan, and M. Soljačić. Plasmonics in graphene at infrared frequencies. *Phys. Rev. B*, 80:245435, 2009.

[37] L. Ju, B. Geng, J. Horng, C. Girit, M. Martin, Z. Hao, H. A. Bechtel, X. Liang, A. Zettl, Y. R. Shen, and F. Wang. Graphene plasmonics for tunable terahertz metamaterials. *Nat. Nanotech.*, 6:630–634, 2011.

[38] Z. Fei, G. O. Andreev, W. Bao, L. M. Zhang, A. S. McLeod, C. Wang, M. K. Stewart, Z. Zhao, G. Dominguez, M. Thiemens, M. M. Fogler, M. J. Tauber, A. H. Castro-Neto, C. N. Lau, F. Keilmann, and D. N. Basov. Infrared nanoscopy of dirac plasmons at the graphene–sio_2 interface. *Nano Lett.*, 11:4701–4705, 2011.

[39] H. Yan, X. Li, B. Chandra, G. Tulevski, Y. Wu, M. Freitag, W. Zhu, P. Avouris, and F. Xia. Tunable infrared plasmonic devices using graphene/insulator stacks. *Nat. Nanotech.*, 7:330–334, 2012.

[40] H. Yan, T. Low, W. Zhu, Y. Wu, M. Freitag, X. Li, F. Guinea, P. Avouris, and F. Xia. Damping pathways of mid-infrared plasmons in graphene nanostructures. *Nat. Photon.*, 2013.

[41] S. A. Mikhailov and K. Ziegler. New electromagnetic mode in graphene. *Phys. Rev. Lett.*, 99:016803, 2007.

[42] Z. Fang, S. Thongrattanasiri, A. Schlather, Z. Liu, L. Ma, Y. Wang, P. M. Ajayan, P. Nordlander, N. J. Halas, and F. J. García de Abajo. Gated tunability and hybridization of localized plasmons in nanostructured graphene. *ACS Nano*, 7:2388–2395, 2013.

[43] B. Wunsch, T. Stauber, F. Sols, and F. Guinea. Dynamical polarization of graphene at finite doping. *New J. Phys.*, 8:318, 2006.

[44] E. H. Hwang and S. Das Sarma. Dielectric function, screening, and plasmons in two-dimensional graphene. *Phys. Rev. B*, 75:205418, 2007.

[45] L. A. Falkovsky and A. A. Varlamov. Space-time dispersion of graphene conductivity. *Eur. Phys. J. B*, 56:281, 2007.

[46] K. S. Novoselov, A. K. Geim, S. V. Morozov, D. Jiang, Y. Zhang, S. V. Dubonos, I. V. Grigorieva, and A. A. Firsov. Electric field effect in atomically thin carbon films. *Science*, 306:666–669, 2004.

[47] D. Pines and P. Nozières. *The Theory of Quantum Liquids*. W. A. Benjamin, Inc., New York, 1966.

[48] L. Hedin and S. Lundqvist. Effects of electron-electron and electron-phonon interactions on the one-electron states of solids. volume 23 of *Solid State Physics*, pages 1 – 181. Academic Press, 1970.

[49] S. Thongrattanasiri, A. Manjavacas, and F. J. García de Abajo. Quantum finite-size effects in graphene plasmons. *ACS Nano*, 6:1766–1775, 2012.

[50] P. R. Wallace. The band theory of graphite. *Phys. Rev.*, 71:622–634, 1947.

[51] R. Loudon. *The Quantum Theory of Light*. Oxford University Press, Oxford, 2000.

[52] P. W Milonni. *The quantum vacuum: an introduction to quantum electrodynamics*. Academic Press, San Diego, 1994.

[53] M. O. Scully and M. S. Zubairy. *Quantum optics*. Cambridge University Press, Cambridge, 1997.

[54] A. Messiah. *Quantum Mechanics*. North-Holland, New York, 1966.

[55] D. Dzsotjan, A. S. Sörensen, and M. Fleischhauer. Quantum emitters coupled to surface plasmons of a nanowire: A Green's function approach. *Phys. Rev. B*, 82:075427, 2010.

[56] A. Archambault, F. Marquier, J. J. Greffet, and C. Arnold. Quantum theory of spontaneous and stimulated emission of surface plasmons. *Phys. Rev. B*, 82:035411, 2010.

[57] K. Rzazewski and R. W. Boyd. Equivalence of interaction hamiltonians in the electric dipole approximation. *Journal of Modern Optics*, 51:1137–1147, 2004.

[58] D N Zubarev. Double-time green functions in statistical physics. *Soviet Physics Uspekhi*, 3:320, 1960.

[59] M. Tsukada and W. Brenig. Theory of optical excitation of adsorbed rare gas atoms. *Surface Science*, 151:503 – 520, 1985.

[60] E R Pike and S Swain. A general approach to nonequilibrium quantum statistics. *Journal of Physics A: General Physics*, 4:555, 1971.

[61] P. Nordlander and PH. Avouris. Structure of adsorbate inverse photoemission spectra: A model hamiltonian study. *Surface Science Letters*, 177:L1004 – L1010, 1986.

[62] P. Meystre and M. Sargent. *Elements of Quantum Optics*. Springer, New York, 1999.

[63] Z. Ficek and R. Tanas. Entangled states and collective nonclassical effects in two-atom systems. *Physics Reports*, 372(5):369 – 443, 2002.

[64] A. I. Volokitin and B. N. J. Persson. Near-field radiative heat transfer and noncontact friction. *Rev. Mod. Phys.*, 79:1291–1329, 2007.

[65] S. M. Rytov. *Theory of Electrical Fluctuation and Thermal Radiation.* Academy of Science of USSR, Moscow, 1953.

[66] H. Nyquist. Thermal agitation of electric charge in conductors. *Phys. Rev.*, 32:110–113, 1928.

[67] H. B. Callen and T. A. Welton. Irreversibility and generalized noise. *Phys. Rev.*, 83:34–40, 1951.

[68] D. Sarid. Long-range surface-plasma waves on very thin metal films. *Phys. Rev. Lett.*, 47:1927–1930, 1981.

[69] P. Berini. Plasmon-polariton waves guided by thin lossy metal films of finite width: Bound modes of symmetric structures. *Phys. Rev. B*, 61:10484–10503, 2000.

[70] P. Berini. Plasmon-polariton waves guided by thin lossy metal films of finite width: Bound modes of asymmetric structures. *Phys. Rev. B*, 63:125417, 2001.

[71] E. Ozbay. Plasmonics: Merging photonics and electronics at nanoscale dimensions. *Science*, 311:189–193, 2006.

[72] J. Takahara, S. Yamagishi, H. Taki, A. Morimoto, and T. Kobayashi. Guiding of a one-dimensional optical beam with nanometer diameter. *Opt. Lett.*, 22:475–477, 1997.

[73] S. I. Bozhevolnyi, V. S. Volkov, E. Devaux, J. Y. Laluet, and T. W. Ebbesen. Channel plasmon subwavelength waveguide components including interferometers and ring resonators. *Nature*, 440:508–511, 2006.

[74] E. Moreno, S. G. Rodrigo, S. I. Bozhevolnyi, L. Martín-Moreno, and F. J. García-Vidal. Guiding and focusing of electromagnetic fields with wedge plasmon polaritons. *Phys. Rev. Lett.*, 100:023901, 2008.

[75] G. Veronis and S. Fan. Guided subwavelength plasmonic mode supported by a slot in a thin metal film. *Opt. Lett.*, 30:3359–3361, 2005.

[76] S. I. Bozhevolnyi, J. Erland, K. Leosson, P. M. W. Skovgaard, and J. M. Hvam. Waveguiding in surface plasmon polariton band gap structures. *Phys. Rev. Lett.*, 86:3008–3011, 2001.

[77] J. R. Krenn, A. Dereux, J. C. Weeber, E. Bourillot, Y. Lacroute, J. P. Goudonnet, G. Schider, W. Gotschy, A. Leitner, F. R. Aussenegg, and C. Girard. Squeezing the optical near-field zone by plasmon coupling of metallic nanoparticles. *Phys. Rev. Lett.*, 82:2590–2593, 1999.

[78] S. A. Maier, P. G. Kik, H. A. Atwater, S. Meltzer, E. Harel, B. E. Koel, and A. A. G. Requicha. Local detection of electromagnetic energy transport below the diffraction limit in metal nanoparticle plasmon waveguides. *Nat. Mater.*, 2:229–232, 2003.

[79] R. F. Oulton, V. J. Sorger, D. A. Genov, D. F. P. Pile, and X. Zhang. A hybrid plasmonic waveguide for subwavelength confinement and long-range propagation. *Nat. Photon.*, 2:496–500, 2008.

[80] M. Danckwerts and L. Novotny. Optical frequency mixing at coupled gold nanoparticles. *Phys. Rev. Lett.*, 98:026104, 2007.

[81] M. U. Gonzalez, J. C. Weeber, A. L. Baudrion, A. Dereux, A. L. Stepanov, J. R. Krenn, E. Devaux, and T. W. Ebbesen. Design, near-field characterization, and modeling of 45° surface-plasmon bragg mirrors. *Phys. Rev. B*, 73:155416, 2006.

[82] L. M. Liz-Marzán. Tailoring surface plasmon through the morphology and assembly of metal nanoparticles. *Langmuir*, 22:32–41, 2006.

[83] H. T. Miyazaki and Y. Kurokawa. Squeezing visible light waves into a 3-nm-thick and 55-nm-long plasmon cavity. *Phys. Rev. Lett.*, 96:097401, 2006.

[84] J. A. Conway, S. Sahni, and T. Szkopek. Plasmonic interconnects versus conventional interconnects: A comparison of latency, crosstalk and energy costs. *Opt. Express*, 15:4474–4484, 2007.

[85] F. J. García de Abajo and M. Kociak. Probing the photonic local density of states with electron energy loss spectroscopy. *Phys. Rev. Lett.*, 100:106804, 2008.

[86] D. P. Fussell, R. C. McPhedran, and C. Martijn de Sterke. Three-dimensional green's tensor, local density of states, and spontaneous emission in finite two-dimensional photonic crystals composed of cylinders. *Phys. Rev. E*, 70:066608, 2004.

[87] F. J. García de Abajo, A. G. Pattantyus-Abraham, N. Zabala, A. Rivacoba, M. O. Wolf, and P. M. Echenique. Cherenkov effect as a probe of photonic nanostructures. *Phys. Rev. Lett.*, 91:143902, 2003.

[88] E. D. Palik. *Handbook of Optical Constants of Solids*. Academic Press, San Diego, 1985.

[89] F. J. García de Abajo and M. Kociak. Electron energy-gain spectroscopy. *New J. Phys.*, 10:073035, 2008.

[90] P. Nordlander, C. Oubre, E. Prodan, K. Li, and M. I. Stockman. Plasmon hybridizaton in nanoparticle dimers. *Nano Lett.*, 4:899–903, 2004.

[91] J. C. Ashley and L. C. Emerson. Dispersion relations for non-radiative surface plasmons on cylinders. *Surf. Sci.*, 41:615–618, 1974.

[92] L. D. Landau and E. M. Lifshitz. *Quantum Mechanics: Non-Relativistic Theory*. Pergamon Press, Oxford, 1981.

[93] I. N. Levine. *Molecular Spectroscopy*. Wiley-Interscience, London, 1975.

[94] P. R. McIsaac. Symmetry-induced modal characteristics of uniform waveguides - i: Summary of results. *IEEE Trans. Microwave Theory Tech.*, 23:421–429, 1975.

[95] P. R. McIsaac. Symmetry-induced modal characteristics of uniform waveguides - ii: Theory. *IEEE Trans. Microwave Theory Tech.*, 23:429–433, 1975.

[96] G. Veronis and S. Fan. Crosstalk between three-dimensional plasmonic slot waveguides. *Opt. Express*, 16:2129–2140, 2008.

[97] V. Myroshnychenko, A. Stefanski, A. Manjavacas, M. Kafesaki, R. I. Merino, V. M. Orera, D. A. Pawlak, and F. J. García de Abajo. Interacting plasmon and phonon polaritons in aligned nano- and microwires. *Opt. Express*, 20:10879–10887, 2012.

[98] A. Vakil and N. Engheta. Transformation optics using graphene. *Science*, 332:1291–1294, 2011.

[99] A. Y. Nikitin, F. Guinea, F. J. García-Vidal, and L. Martín-Moreno. Fields radiated by a nanoemitter in a graphene sheet. *Phys. Rev. B*, 84:195446, 2011.

[100] J. Christensen, A. Manjavacas, S. Thongrattanasiri, F. H. L. Koppens, and F. J. García de Abajo. Graphene plasmon waveguiding and hybridization in individual and paired nanoribbons. *ACS Nano*, 6:431–440, 2012.

[101] N. J. Halas, S. Lal, W. Chang, S. Link, and P. Nordlander. Plasmons in strongly coupled metallic nanostructures. *Chemical Reviews*, 111(6):3913–3961, 2011.

[102] A. Aubry, D. Y. Lei, S. A. Maier, and J. B. Pendry. Plasmonic hybridization between nanowires and a metallic surface: A transformation optics approach. *ACS Nano*, 5(4):3293–3308, 2011.

[103] W. Zhang, A. O. Govorov, and G. W. Bryant. Semiconductor-metal nanoparticle molecules: Hybrid excitons and the nonlinear fano effect. *Phys. Rev. Lett.*, 97:146804, 2006.

[104] R. D. Artuso and G. W. Bryant. Optical response of strongly coupled quantum dot-metal nanoparticle systems: Double peaked fano structure and bistability. *Nano Lett.*, 8(7):2106–2111, 2008.

[105] A. Trügler and U. Hohenester. Strong coupling between a metallic nanoparticle and a single molecule. *Phys. Rev. B*, 77:115403, 2008.

[106] Y. B. Zheng, Y. Yang, L. Jensen, L. Fang, B. K. Juluri, A. H. Flood, P. S. Weiss, J. F. Stoddart, and T. J. Huang. Active molecular plasmonics: Controlling plasmon resonances with molecular switches. *Nano Lett.*, 9(2):819–825, 2009.

[107] P. Banerjee, D. Conklin, S. Nanayakkara, T. Park, M. J. Therien, and D. A. Bonnell. Plasmon-induced electrical conduction in molecular devices. *ACS Nano*, 4(2):1019–1025, 2010.

[108] S. Savasta, R. Saija, A. Ridolfo, O. Di Stefano, P. Denti, and F. Borghese. Nanopolaritons: Vacuum Rabi splitting with a single quantum dot in the center of a dimer nanoantenna. *ACS Nano*, 4:6369–6376, 2010.

[109] X. Wu, S. K. Gray, and M. Pelton. Quantum-dot-induced transparency in a nanoscale plasmonic resonator. *Opt. Express*, 18:23633–23645, 2010.

[110] R. D. Artuso and G. W. Bryant. Strongly coupled quantum dot-metal nanoparticle systems: Exciton-induced transparency, discontinuous response, and suppression as driven quantum oscillator effects. *Phys. Rev. B*, 82:195419, 2010.

[111] A. Ridolfo, O. Di Stefano, N. Fina, R. Saija, and S. Savasta. Quantum plasmonics with quantum dot-metal nanoparticle molecules: Influence of the Fano effect on photon statistics. *Phys. Rev. Lett.*, 105:263601, 2010.

[112] G. Kyas and V. May. Density matrix based microscopic theory of molecule metal-nanoparticle interactions: Linear absorbance and plasmon enhancement of intermolecular excitation energy transfer. *The Journal of Chemical Physics*, 134(3):034701, 2011.

[113] W. Zhang and A. O. Govorov. Quantum theory of the nonlinear fano effect in hybrid metal-semiconductor nanostructures: The case of strong nonlinearity. *Phys. Rev. B*, 84:081405, 2011.

[114] B. K. Juluri, N. Chaturvedi, Q. Hao, M. Lu, D. Velegol, L. Jensen, and T. J. Huang. Scalable manufacturing of plasmonic nanodisk dimers and cusp

nanostructures using salting-out quenching method and colloidal lithography. *ACS Nano*, 5(7):5838–5847, 2011.

[115] H. Duan, H. Hu, K. Kumar, Z. Shen, and J. K. W. Yang. Direct and reliable patterning of plasmonic nanostructures with sub-10-nm gaps. *ACS Nano*, 5:7593–7600, 2011.

[116] P. Van Dorpe and J. Ye. Semishells: Versatile plasmonic nanoparticles. *ACS Nano*, 5(9):6774–6778, 2011.

[117] D. E. Chang, A. S. Sörensen, E. A. Demler, and M. D. Lukin. A single-photon transistor using nanoscale surface plasmons. *Nat. Phys.*, 3:807–812, 2007.

[118] M. S. Tame, C. Lee, J. Lee, D. Ballester, M. Paternostro, A. V. Zayats, and M. S. Kim. Single-photon excitation of surface plasmon polaritons. *Phys. Rev. Lett.*, 101:190504, 2008.

[119] S. Fasel, M. Halder, N. Gisin, and H. Zbinden. Quantum superposition and entanglement of mesoscopic plasmons. *New Journal of Physics*, 8(1):13, 2006.

[120] B. Luk'yanchuk, N. I. Zheludev, S. A. Maier, N. J. Halas, P. Nordlander, H. Giessen, and C. Chong. The fano resonance in plasmonic nanostructures and metamaterials. *Nat. Mater.*, 9:707–715, 2010.

[121] U. Fano. Effects of configuration interaction on intensities and phase shifts. *Phys. Rev.*, 124:1866–1878, 1961.

[122] A. V. Akimov, A. Mukherjee, C. L. Yu, D. E. Chang, A. S. Zibrov, P. R. Hemmer, H. Park, and M. D. Lukin. Generation of single optical plasmons in metallic nanowires coupled to quantum dots. *Nature*, 450:402–406, 2007.

[123] R. Kolesov, B. Grotz, G. Balasubramanian, R. J. Stöhr, A. A. L. Nicolet, P. R. Hemmer, F. Jelezko, and J. Wrachtrup. Wave-particle duality of single surface plasmon polaritons. *Nat. Phys.*, 5:470–474, 2009.

[124] J. P. Reithmaier, G. Sek, A. Löffler, C. Hofmann, S. Kuhn, S. Reitzenstein, L. V. Keldysh, V. D. Kulakovskii, T. L. Reinecke, and A. Forchel. Strong

coupling in a single quantum dot-semiconductor microcavity system. *Nature*, 432:197–200, 2004.

[125] K. Hennessy, A. Badolato, M. Winger, D. Gerace, M. Atatüre, S. Gulde, S. Fält, E. L. Hu, and A. Imamoglu. Quantum nature of a strongly coupled single quantum dot-cavity system. *Nature*, 445:896–899, 2007.

[126] A. Imamoglu, H. Schmidt G. Woods, and M. Deutsch. Strongly interacting photons in a nonlinear cavity. *Phys. Rev. Lett.*, 79:1467–1470, 1997.

[127] K. M. Birnbaum, A. Boca, R. Miller, A. D. Boozer, T. E. Northup, and H. J. Kimble. Photon blockade in an optical cavity with one trapped atom. *Nature*, 436:87–90, 2005.

[128] J. M. Fink, M. Göppl, M. Baur, R. Bianchetti, P. J. Leek, A. Blais, and A. Wallraff. Climbing the jaynes-cummings ladder and observing its nonlinearity in a cavity qed system. *Nature*, 454:315–318, 2008.

[129] K. F. Mak, M. Y. Sfeir, Y. Wu, C. H. Lui, J. A. Misewich, and T. F. Heinz. Measurement of the optical conductivity of graphene. *Phys. Rev. Lett.*, 101:196405, 2008.

[130] J. I. Cirac, P. Zoller, H. J. Kimble, and H. Mabuchi. Quantum state transfer and entanglement distribution among distant nodes in a quantum network. *Phys. Rev. Lett.*, 78:3221–3224, 1997.

[131] J. M. Amini, H. Uys, J. H. Wesenberg, S. Seidelin, J. Britton, J. J. Bollinger, D. Leibfried, C. Ospelkaus, A. P. VanDevender, and D. J. Wineland. Toward scalable ion traps for quantum information processing. *New J. Phys.*, 12:033031, 2010.

[132] S. Ritter, C. Nolleke, C. Hahn, A. Reiserer, A. Neuzner, M. Uphoff M. Mucke, E. Figueroa, J. Bochmann, and G. Rempe. An elementary quantum network of single atoms in optical cavities. *Nature*, 484:195–200, 2012.

[133] T. D. Ladd, F. Jelezko, R. Laflamme, Y. Nakamura, C. Monroe, and J. L. O'Brien. Quantum computers. *Nature*, 464:45–53, 2010.

[134] E. Togan, Y. Chu, A. S. Trifonov, L. Jiang, J. Maze, L. Childress, M. V. G. Dutt, A. S. Sörensen, P. R. Hemmer, A. S. Zibrov, and M. D. Lukin. Quantum entanglement between an optical photon and a solid-state spin qubit. *Nature*, 466:730–734, 2010.

[135] S. J. van Enk, J. I. Cirac, and P. Zoller. Ideal quantum communication over noisy channels: A quantum optical implementation. *Phys. Rev. Lett.*, 78:4293–4296, 1997.

[136] Z. Q. Li, E. A. Henriksen, Z. Jian, Z. Hao, M. C. Martin, P. Kim, H. L. Stormer, and D. N. Basov. Dirac charge dynamics in graphene by infrared spectroscopy. *Nat. Phys.*, 4:532–535, 2008.

[137] L. M. Duan and C. Monroe. Robust probabilistic quantum information processing with atoms photons, and atomic ensembles. volume 55 of *Advances In Atomic, Molecular, and Optical Physics*, pages 419–463. Academic Press, 2008.

[138] N. Yamamoto, S. Ohtani, and F. J. García de Abajo. Gap and mie plasmons in individual silver nanospheres near a silver surface. *Nano Lett.*, 11:91–95, 2011.

[139] N. T. Fofang, T. Park, O. Neumann, N. A. Mirin, P. Nordlander, and N. J. Halas. Plexcitonic nanoparticles: Plasmon-exciton coupling in nanoshell-j-aggregate complexes. *Nano Lett.*, 8(10):3481–3487, 2008.

[140] F. J. García de Abajo. Multiple scattering of radiation in clusters of dielectrics. *Phys. Rev. B*, 60:6086–6102, 1999.

[141] S. A. Empedocles, D. J. Norris, and M. G. Bawendi. Photoluminescence spectroscopy of single cdse nanocrystallite quantum dots. *Phys. Rev. Lett.*, 77:3873–3876, 1996.

[142] V. Myroshnychenko, E. Carbó-Argibay, I. Pastoriza-Santos, J. Pérez-Juste, L. M. Liz-Marzán, and F. J. García de Abajo. Modelling the optical response of highly faceted metal nanoparticles with a fully 3d boundary element method. *Adv. Mater.*, 20:4288–4293, 2008.

[143] S.J Oldenburg, R.D Averitt, S.L Westcott, and N.J Halas. Nanoengineering of optical resonances. *Chem. Phys. Lett.*, 288:243–247, 1998.

[144] P. W. Milonni and Robert W. Boyd. Influence of radiative damping on the optical-frequency susceptibility. *PRA*, 69:023814, 2004.

[145] P. G. Eliseev, H. Li, A. Stintz, G. T. Liu, T. C. Newell, K. J. Malloy, and L. F. Lester. Transition dipole moment of inas/ingaas quantum dots from experiments on ultralow-threshold laser diodes. *Appl. Phys. Lett.*, 77:262–264, 2000.

[146] M. Kroner, A. O. Govorov, S. Remi, B. Biedermann, S. Seidl, A. Badolato, P. M. Petroff, W. Zhang, R. Barbour, B. D. Gerardot, R. J. Warburton, and K. Karrai. The nonlinear fano effect. *Nature*, 451:311–314, 2008.

[147] H. Shao, D. C. Langreth, and P. Nordlander. Many-body theory for charge transfer in atom-surface collisions. *Phys. Rev. B*, 49:13929–13947, 1994.

[148] E.T. Jaynes and F.W. Cummings. Comparison of quantum and semiclassical radiation theories with application to the beam maser. *Proc. IEEE*, 51:89–109, 1963.

[149] F. P. Laussy, E. del Valle, M. Schrapp, A. Laucht, and J. J. Finley. Climbing the jaynes-cummings ladder by photon counting. *J. Nanophoton.*, 6:061803–061803, 2012.

[150] S. Thongrattanasiri, F. H. L. Koppens, and F. J. García de Abajo. Complete optical absorption in periodically patterned graphene. *Phys. Rev. Lett.*, 108:047401, 2012.

[151] H. J. Kimble, M. Dagenais, and L. Mandel. Photon antibunching in resonance fluorescence. *Phys. Rev. Lett.*, 39:691–695, 1977.

[152] A. G. Curto, G. Volpe, T. H. Taminiau, M. P. Kreuzer, R. Quidant, and N. F. van Hulst. Unidirectional emission of a quantum dot coupled to a nanoantenna. *Science*, 329:930–933, 2010.

[153] M. Andreas Lieb, James M. Zavislan, and Lukas Novotny. Single-molecule orientations determined by direct emission pattern imaging. *J. Opt. Soc. Am. B*, 21:1210–1215, 2004.

[154] P. Kukura, H. Ewers, C. Muller, A. Renn, A. Helenius, and V. Sandoghdar. High-speed nanoscopic tracking of the position and orientation of a single virus. *Nat. Meth.*, 6:923–927, 2009.

[155] T. Ung, L. M. Liz-Marzán, and P. Mulvaney. Optical properties of thin films of au@sio$_2$ particles. *J. Phys. Chem. B*, 105:3441–3452, 2001.

[156] W. K. Wootters. Entanglement of formation of an arbitrary state of two qubits. *Phys. Rev. Lett.*, 80:2245–2248, 1998.

[157] P. A. Huidobro, A. Y. Nikitin, C. González-Ballestero, L. Martín-Moreno, and F. J. García-Vidal. Superradiance mediated by graphene surface plasmons. *Phys. Rev. B*, 85:155438, 2012.

[158] R. H. R. H. Dicke. Coherence in spontaneous radiation processes. *Phys. Rev.*, 93:99–110, 1954.

[159] N. Skribanowitz, I. P. Herman, J. C. MacGillivray, and M. S. Feld. Observation of dicke superradiance in optically pumped hf gas. *Phys. Rev. Lett.*, 30:309–312, 1973.

[160] M. Gross, C. Fabre, P. Pillet, and S. Haroche. Observation of near-infrared dicke superradiance on cascading transitions in atomic sodium. *Phys. Rev. Lett.*, 36:1035–1038, 1976.

[161] M. Gross and S. Haroche. Superradiance: An essay on the theory of collective spontaneous emission. *Phys. Rep.*, 93(5):301–396, 1982.

[162] S. Inouye, A. P. Chikkatur, D. M. Stamper-Kurn, J. Stenger, D. E. Pritchard, and W. Ketterle. Superradiant rayleigh scattering from a bose-einstein condensate. *Science*, 285:571–574, 1999.

[163] R. Chapman and P. Mulvaney. Electro-optical shifts in silver nanoparticle films. *Chem. Phys. Lett.*, 349:358–362, 2001.

[164] T. Hirakawa and P. V. Kamat. Photoinduced electron storage and surface plasmon modulation in ag@tio$_2$ clusters. *Langmuir*, 20:5645–5647, 2004.

[165] L. Brey and H. A. Fertig. Elementary electronic excitations in graphene nanoribbons. *Phys. Rev. B*, 75:125434, 2007.

[166] N. Armbrust, J. Güdde, P. Jakob, and U. Höfer. Time-resolved two-photon photoemission of unoccupied electronic states of periodically rippled graphene on ru(0001). *Phys. Rev. Lett.*, 108:056801, 2012.

[167] N. M. R. Peres, R. M. Ribeiro, and A. H. Castro Neto. Excitonic effects in the optical conductivity of gated graphene. *Phys. Rev. Lett.*, 105:055501, 2010.

[168] J. Fernández-Rossier and J. J. Palacios. Magnetism in graphene nanoislands. *Phys. Rev. Lett.*, 99:177204, 2007.

[169] M. Ezawa. Metallic graphene nanodisks: Electronic and magnetic properties. *Phys. Rev. B*, 76:245415, 2007.

[170] A. R. Akhmerov and C. W. J. Beenakker. Boundary conditions for dirac fermions on a terminated honeycomb lattice. *Phys. Rev. B*, 77:085423, 2008.

[171] Z. Z. Zhang, Kai Chang, and F. M. Peeters. Tuning of energy levels and optical properties of graphene quantum dots. *Phys. Rev. B*, 77:235411, 2008.

[172] M. Wimmer, A. R. Akhmerov, and F. Guinea. Robustness of edge states in graphene quantum dots. *Phys. Rev. B*, 82:045409, 2010.

[173] M. Zarenia, A. Chaves, G. A. Farias, and F. M. Peeters. Energy levels of triangular and hexagonal graphene quantum dots: A comparative study between the tight-binding and dirac equation approach. *Phys. Rev. B*, 84:245403, 2011.

[174] Y. L. Luo, Y. S. Shiao, and Y. F. Huang. Transforming c_{60} molecules into graphene quantum dots. *Nat. Nanotech.*, 6:247–252, 2011.

[175] D. Subramaniam, F. Libisch, Y. Li, C. Pauly, V. Geringer, R. Reiter, T. Mashoff, M. Liebmann, J. Burgdörfer, C. Busse, T. Michely, R. Mazzarello,

M. Pratzer, and M. Morgenstern. Wave-function mapping of graphene quantum dots with soft confinement. *Phys. Rev. Lett.*, 108:046801, 2012.

[176] S. Kim, S. W. Hwang, M.-K. Kim, D. Y. Shin, D. H. Shin, C. O. Kim, S. B. Yang, J. H. Park, E. H., S.-H. Choi, G. Ko, S. Sim, C. Sone, H. J. Choi, S. Bae, and B. H. Hong. Anomalous behaviors of visible luminescence from graphene quantum dots: Interplay between size and shape. *ACS Nano*, 6:8203–8208, 2012.

[177] Y. Kobayashi, K.-I Fukui, T. Enoki, K. Kusakabe, and Y. Kaburagi. Observation of zigzag and armchair edges of graphite using scanning tunneling microscopy and spectroscopy. *Phys. Rev. B*, 71:193406, 2005.

[178] J. Tian, H. Cao, W. Wu, Q. Yu, and Y. P. Chen. Direct imaging of graphene edges: Atomic structure and electronic scattering. *Nano Lett.*, 11:3663–3668, 2011.

[179] C. Ö. Girit, J. C. Meyer, R. Erni, M. D. Rossell, C. Kisielowski, L. Yang, Cheol-Hwan Park, M. F. Crommie, M. L. Cohen, S. G. Louie, and A. Zettl. Graphene at the edge: Stability and dynamics. *Science*, 27:1705–1708, 2009.

[180] H. Shu, X. Chen, X. Tao, and F. Ding. Edge structural stability and kinetics of graphene chemical vapor deposition growth. *ACS Nano*, 6:3243–3250, 2012.

[181] C. K. Gan and D. J. Srolovitz. Analysis of the dielectric constants of the ag_2o film by spectroscopic ellipsometry and single-oscillator model. *Phys. Rev. B*, 81:125445, 2010.

[182] Jishan Wu, Wojciech Pisula, and Klaus Müllen. Graphenes as potential material for electronics. *Chem. Rev.*, 107:718–747, 2007.

[183] X. Feng, M. Liu, W. Pisula, M. Takase, J. Li, and K. Müllen. Supramolecular organization and photovoltaics of triangle-shaped discotic graphenes with swallow-tailed alkyl substituents. *Adv. Mater.*, 20:2684–2689, 2008.

[184] A. Manjavacas, F. Marchesin, S. Thongrattanasiri, P. Koval, P. Nordlander, D. Sánchez-Portal, and F. J. García de Abajo. Tunable molecular plasmons in polycyclic aromatic hydrocarbons. *ACS Nano*, ASAP, 2013.

[185] F. Schedin, A. K. Geim, S. V. Morozov, E. W. Hill, P. Blake, M. I. Katsnelson, and K. S. Novoselov. Detection of individual gas molecules adsorbed on graphene. *Nat. Mater.*, 6:652–655, 2007.

[186] P. Bharadwaj, A. Bouhelier, and L. Novotny. Electrical excitation of surface plasmons. *Phys. Rev. Lett.*, 106:226802, 2011.

[187] J. Kundu, F. Le, P. Nordlander, and N. J. Halas. Surface enhanced infrared absorption (seira) spectroscopy on nanoshell aggregate substrates. *Chem. Phys. Lett.*, 452:115–119, 2008.

[188] C. M. Hargreaves. Anomalous radiative transfer between closely-spaced bodies. *Phys. Lett.*, 30A:491–492, 1969.

[189] G. A. Domoto, R. F. Boehm, and C. L. Tien. Experimental investigation of radiative transfer between metallic surfaces at cryogenic temperatures. *J. Heat Transfer*, 92:412–416, 1970.

[190] D. Polder and M. Van Hove. Theory of radiative heat transfer between closely spaced bodies. *Phys. Rev. B*, 4:3303–3314, 1971.

[191] A. Narayanaswamy, S. Shen, L. Hu, X. Chen, and G. Chen. Breakdown of the planck blackbody radiation law at nanoscale gaps. *Appl. Phys. A*, 96:357–362, 2009.

[192] R. S. Ottens, V. Quetschke, S. Wise, A. A. Alemi, R. Lundock, G. Mueller, D. H. Reitze, D. B. Tanner, and B. F. Whiting. Near-field radiative heat transfer between macroscopic planar surfaces. *Phys. Rev. Lett.*, 107:014301, 2011.

[193] J. J. Loomis and H. J. Maris. Theory of heat transfer by evanescent electromagnetic waves. *Phys. Rev. B*, 50:18517–18524, 1994.

[194] R. Carminati and J. J. Greffet. Near-field effects in spatial coherence of thermal sources. *Phys. Rev. Lett.*, 82:1660–1663, 1999.

[195] A. V. Shchegrov, K. Joulain, R. Carminati, and J. J. Greffet. Near-field spectral effects due to electromagnetic surface excitations. *Phys. Rev. Lett.*, 85:1548–1551, 2000.

[196] A. I. Volokitin and B. N. J. Persson. Radiative heat transfer between nanostructures. *Phys. Rev. B*, 63:205404, 2001.

[197] A. Narayanaswamy and G. Chen. Surface modes for near field thermophotovoltaics. *Appl. Phys. Lett.*, 82:3544–3546, 2003.

[198] A. I. Volokitin and B. N. J. Persson. Resonant photon tunneling enhancement of the radiative heat transfer. *Phys. Rev. B*, 69:045417, 2004.

[199] M. I. Mishchenko. Multiple scattering, radiative transfer, and weak localization in discrete random media: Unified microphysical approach. *Rev. Geophys.*, 46:RG2003, 2008.

[200] S. Basu, Z. M. Zhang, and C. J. Fu. Review of near-field thermal radiation and its application to energy conversion. *Int. J. Energy Res.*, 33:1203–1232, 2009.

[201] E. Rousseau, A. Siria, G. Jourdan, S. Volz, F. Comin, J. Chevrier, and J. J. Greffet. Radiative heat transfer at the nanoscale. *Nat. Photon.*, 3:514–517, 2009.

[202] J. P. Mulet, K. Joulain, R. Carminati, and J. J. Greffet. Nanoscale radiative heat transfer between a small particle and a plane surface. *Appl. Phys. Lett.*, 78:2931–2933, 2001.

[203] M. Prunnila and J. Meltaus. Acoustic phonon tunneling and heat transport due to evanescent electric fields. *Phys. Rev. Lett.*, 105:125501, 2010.

[204] A. W. Rodriguez, O. Ilic, P. Bermel, I. Celanovic, J. D. Joannopoulos, M. Soljačić, and S. G. Johnson. Frequency-selective near-field radiative heat transfer between photonic crystal slabs: A computational approach for arbitrary geometries and materials. *Phys. Rev. Lett.*, 107:114302, 2011.

[205] A. Kittel, W. Müller-Hirsch, J. Parisi, S. A. Biehs, D. Reddig, and M. Holthaus. Near-field heat transfer in a scanning thermal microscope. *Phys. Rev. Lett.*, 95:224301, 2005.

[206] S. Shen, A. Narayanaswamy, and G. Chen. Surface phonon polarities mediated energy transfer between nanoscale gaps. *Nano Lett.*, 9:2909–2913, 2009.

[207] J. B. Pendry. Radiative exchange of heat between nanostructures. *J. Phys. Condens. Matter*, 11:6621–6633, 1999.

[208] P. O. Chapuis, M. Laroche, S. Volz, and J. J. Greffet. Near-field induction heating of metallic nanoparticles due to infrared magnetic dipole contribution. *Phys. Rev. B*, 77:125402, 2008.

[209] M. Krüger, T. Emig, and M. Kardar. Nonequilibrium electromagnetic fluctuations: Heat transfer and interactions. *Phys. Rev. Lett.*, 106:210404, 2011.

[210] C. Otey and S. Fan. Numerically exact calculation of electromagnetic heat transfer between a dielectric sphere and plate. *Phys. Rev. B*, 84:245431, 2011.

[211] G. Domingues, S. Volz, K. Joulain, and J. J. Greffet. Heat transfer between two nanoparticles through near field interaction. *Phys. Rev. Lett.*, 94:085901, 2005.

[212] A. Narayanaswamy and G. Chen. Thermal near-field radiative transfer between two spheres. *Phys. Rev. B*, 77:075125, 2008.

[213] P. O. Chapuis, M. Laroche, S. Volz, and J. J. Greffet. Radiative heat transfer between metallic nanoparticles. *Appl. Phys. Lett.*, 93:201906, 2008.

[214] A. Pérez-Madrid, J. M. Rubí, and L. C. Lapas. Heat transfer between nanoparticles: Thermal conductance for near-field interactions. *Phys. Rev. B*, 77:155417, 2008.

[215] A. Pérez-Madrid, L. C. Lapas, and J. M. Rubí. Heat exchange between two interacting nanoparticles beyond the fluctuation-dissipation regime. *Phys. Rev. Lett.*, 103:048301, 2009.

[216] G. V. Dedkov and A. A. Kyasov. Radiative heat transfer of spherical particles mediated by fluctuation electromagnetic field. *J. Comput. Theor. Nanosci.*, 7:2019–2023, 2010.

[217] R. Messina and M. Antezza. Scattering-matrix approach to casimir-lifshitz force and heat transfer out of thermal equilibrium between arbitrary bodies. *Phys. Rev. A*, 84:042102, 2011.

[218] P. Ben-Abdallah, S. A. Biehs, and K. Joulain. Many-body radiative heat transfer theory. *Phys. Rev. Lett.*, 107:114301, 2011.

[219] C. Henkel, K. Joulain, J. P. Mulet, and J. J. Greffet. Radiation forces on small particles in thermal near fields. *Journal of Optics A: Pure and Applied Optics*, 4:S109, 2002.

[220] J. B. Pendry. Shearing the vacuum - quantum friction. *J. Phys. Condens. Matter*, 9:10301–10320, 1997.

[221] A. I. Volokitin and B. N. J. Persson. Theory of friction: The contribution from a fluctuating electromagnetic field. *J. Phys. Condens. Matter*, 11:345–359, 1999.

[222] T. G. Philbin and U. Leonhardt. No quantum friction between uniformly moving plates. *New Journal of Physics*, 11:033035, 2009.

[223] G.V. Dedkov and A.A. Kyasov. Conservative-dissipative forces and heating mediated by fluctuation electromagnetic field: Two plates in relative nonrelativistic motion. *Surface Science*, 604:562 – 567, 2010.

[224] J. B. Pendry. Quantum friction-fact or fiction? *New J. Phys.*, 12:033028, 2010.

[225] U. Leonhardt. Comment on "Quantum friction-fact or fiction?". *New J. Phys.*, 12:068001, 2010.

[226] J. B. Pendry. Reply to comment on "Quantum friction-fact or fiction?". *New J. Phys.*, 12:068002, 2010.

[227] A. I. Volokitin and B. N. J. Persson. Theory of the interaction forces and the radiative heat transfer between moving bodies. *Phys. Rev. B*, 78:155437, 2008.

[228] Y. Pomeau. Friction on a spinning piece of matter. *Journal of Statistical Physics*, 121:1083–1095, 2005.

[229] Y. Pomeau. Friction of the qed vacuum on spinning matter. *Europhys. Lett.*, 74:951, 2006.

[230] H. C. van de Hulst. *Light Scattering by Small Particles.* Dover, New York, 1981.

[231] B. T. Draine. Scattering by interstellar dust grains. ii. x-rays. *Astrophys. J.*, 598:1026–1037, 2003.

[232] F. Hoyle and N. C. Wickramasinghe. On graphite particles as interstellar grains. *Monthly Not. Royal Astron. Soc.*, 124:417–433, 1962.

[233] V. Mkrtchian, V. A. Parsegian, R. Podgornik, and W. M. Saslow. Universal thermal radiation drag on neutral objects. *Phys. Rev. Lett.*, 91:220801, 2003.

[234] C. J. Fu and Z. M. Zhang. Nanoscale radiation heat transfer for silicon at different doping levels. *Int. J. Heat Mass Tran.*, 49:1703–1718, 2006.

[235] I. Bialynicki-Birula and Z. Bialynicka-Birula. Rotational frequency shift. *Phys. Rev. Lett.*, 78:2539–2542, 1997.

[236] M. Michalski, W. Hüttner, and H. Schimming. Experimental demonstration of the rotational frequency shift in a molecular system. *Phys. Rev. Lett.*, 95:203005, 2005.

[237] E. M. Purcell. Spontaneous emission probabilities at radio frequencies. *Phys. Rev.*, 69:681, 1946.

[238] R. Zhao, A. Manjavacas, F. J. García de Abajo, and J. B. Pendry. Rotational quantum friction. *Phys. Rev. Lett.*, 109:123604, 2012.